THE UNIVERSITY OF HULL

The static and dynamic structural bulk properties of fibrous media

being a Thesis submitted for the Degree of PhD

In the Department of Engineering, the University of Hull

by

Mr. Ho-Chul Shin, MSc (Korea Advanced Institute of Science and Technology)

February 2004

Acknowledgements

First and foremost, I would like to express my deepest gratitude to my supervisor, Prof. Alan Cummings, not only for his guidance during the course of the research and the preparation of this thesis, but also for opening a new window of opportunity for me. I would like to thank Dr. Chris Truman for his advice and encouragement on the project and thesis. I would like to thank Prof. Keith Attenborough for giving me a chance to work with him and his help with this thesis. I would also like to thank Dr. Philippe Leclaire for introducing me to some of works in this thesis and his willingness to share his experience.

I would like to acknowledge the financial support from the Engineering and Physical Sciences Research Council under grant number GR/M43555.

Finally, I would like to share this moment of achievement with my parents, sister and brother.

Abstract

The structural bulk properties of fibrous materials are investigated. Theoretical models are developed and their predictions are compared to measured data. The properties under both static loading and dynamic excitation are studied.

Macro-scale experimental models are constructed to represent the idealised microscopic structure and to investigate its static behaviour under compression. As a result, the dominant mechanisms of deflection and nonlinearity are respectively identified as bending and the increase in the number of inter-fibre contacts under compression. Exploratory investigations concerning friction and electric contact resistance are conducted on macro-scale models.

As an effective means of representing its structural characteristic, a transversely isotropic structure of stacked cylinders is employed to model a bulk fibrous material. Based on this, static bending models are formulated to describe the structural nonlinear stress-strain behaviour of bulk fibrous media under static compression. In these models, the increase in the number of inter-fibre contacts is related to the shortening of fibre links, and is also further examined in terms of "connectivity" inside a medium. Similarities to, and differences from, percolation theory are noted.

The dynamic structural bulk properties of fibrous materials are also investigated. Their nonlinear behaviour is dealt with mainly in terms of dependence on the amplitude of excitation, and is characterised by shifts in the measured transmissibility and the corresponding complex Young's modulus.

As in the case of the static properties, the dynamic behaviour of a fibrous material is also investigated by means of idealised models, which show that the nonlinear mechanism is similar to that in the static case.

A novel method is proposed to improve the efficacy in measuring the dynamic properties of a bulk fibrous material. The new method combines the advantages of two conventional techniques, the transfer function method and the mechanical impedance method.

Finally, a nonlinear governing partial differential equation is derived for the dynamic behaviour of a bulk fibrous material. Its analogy to nonlinear equations in other types of media is observed. And the nonlinear behaviour, especially regarding the occurrence of harmonic components, is predicted in the theory as well as being confirmed by experiment.

List of Symbols

Chapter 1

Not applicable

Chapter 2

Roman symbols

a	Distance from the welded end of the rod to the contact point with the adjacent rod
A	Location on a rod
B	Location on a rod
C	Location on a rod
C_1	Coefficient
C_2	Coefficient
C_3	Coefficient
C_4	Coefficient
d	Diameter of a rod
D	Location on a rod
D_h	Distance for a hanger in 3-D model
E	Young's modulus of a material
EI	Flexural rigidity, or Bending stiffness
F	Force applied to a structure
F_a	Contact (or reaction) force at the location A
F_b	Contact (or reaction) force at the location B
F_c	Force applied at the location C
F_d	Contact (or reaction) force at the location D
F_H	Contact force in a Hertzian contact
F_p	Weight of a top loading plate
F_w	Weight applied to a structure

I	Second moment of area of a beam about its neutral axis.
j	Summation index, which also denotes each layer
L	Length of a rod link which deflects
L_a	Length of a rod from its origin to the location A
L_b	Length of a rod from its origin to the location B
L_c	Length of a rod from its origin to the location C
L_d	Length of a rod from its origin to the location D
m	A total number of deflectable layers
M	External moment
M_0	Moment at the origin
M_b	Bending moment in a rod
n	Exponent
N_j	Number of contacts in the j-th layer
N_l	Number of deflected layers
P	Axial load applied to a beam
P_i	Load at the location i
P_{cr}	Critical load
R_0	Reaction force at the origin
R_a	Reaction force at the location A
sf	Sliding factor
U	Elastic energy of an elastic system
U^c	Total complementary energy of an elastic system
U^p	Potential energy of an elastic system
x	Cartesian coordinate
y	Cartesian coordinate

Greek symbols

δ	Deflection of a bulk model
δ_a	Deflection at the location A
δ_b	Deflection at the location B
δ_B	Deflection by bending effect
δ_d	Deflection at the location C

δ_F	Deflection contributed by a force loading
δ_{gap}	Gap between the loading bar and target bar, before the contact is made.
δ_H	Deflection by Hertzian contact
δ_{Hi}	Initial Hertzian deflection by a top plate
δ_i	In-line deflection at the location i
δ_M	Deflection contributed by a moment loading
θ_1	Initial angle between the loading bar and the bottom plate
θ_2	Angle between the loading bar and the bottom plate, after the first coming-to-contact
θ_3	Initial angle between the loading bar and the bottom plate, after the second coming-to-contact
ν	Poisson's ratio

Chapter 3

Roman symbols

a	Radius of a circular contact area
a_a	Radius of a-spot
A	Real contact area
A_b	Load bearing area
A_{cd}	Conducting area
A_e	End surface
A_{rod}	Cross-sectional area of a rod
b	Half-width of a rectangular contact area
c	Coefficient
d	Diameter
E	Young's modulus
F	Force applied to a structure
F_μ	Friction force
H	Hardness of a material
l	Length of a cylinder
l_R	Distance along a beam between its origin and the contact location
L	Length of a beam

L_1	Length of rod links
L_2	Length of rod links
L_{rod}	Length of a rod
n	Exponent
N	Normal force
r	Radius of a cylinder
R	Resistance
R_1	Resistances of rod link 1
R_2	Resistances of rod link 2
R_c	Constriction resistance
R_{c1}	Constriction resistances of members 1
R_{c2}	Constriction resistances of members 2
R_{ct}	Contact resistance
R_f	Film resistance
R_l	Reaction force at the contact
R_r	Rig resistance, accompanied by integer subscripts
R_{rod}	Resistance of a rod
R_s	Sample resistance, accompanied by integer subscripts
S	Shear strength
t	Thickness of an alien film
Y	Yielding pressure for a material deforming plastically

Greek symbols

ε	Strain
μ	Coefficient of friction
ν	Poisson's ratio
ξ	Coefficient
ρ	Electrical resistivity
ρ_f	Resistivity of an alien film
σ	Stress
σ_f	Resistance of an alien film

Chapter 4

Roman symbols

a	Parameter for the original MNBM with offset
A	Surface area of a bulk model
b	Parameters for the original MNBM with offset
d	Diameter of a cylindrical rod.
E	Young's modulus of a material
E_b	Bulk Young's modulus
F	Force applied to the centre of a rod link
F_{ext}	External force applied to a bulk model
l	Link length of a rod
I	Second moment of a cross sectional area of a rod about the neutral axis
M_0	Additional moment
M_b	Bending moment
n	Number of measured data
N_l	Number of layers
p	Exponent
q	Proportional constant
S	Sum of squared residual
t	Thickness of a bulk model
V	Bulk volume (fibres plus voids)
W	Elastic energy of a link

Greek symbols

α	Parameter for the generalised MNBM
β	Parameter for the generalised MNBM
β	Ratio of the width to the length of a cell frame (not confused with parameter β)
γ	Dimensionless parameter
δ	Deflection of each layer
Δ	Total deflection of a bulk model
ε	Strain
ε_c	Elastic collapse strain

ε_d	Densification strain
ε_i	Measured Strain
ε_{th}	Threshold strain
ε_x	Strain in x- direction
ε_y	Strain in y- direction
ε_z	Strain in z- direction
ζ	Dimensionless parameter for MNBM
ν_b	Bulk Poisson's ratio
ρ_b	Bulk density
ρ_s	Density of a fibre material
σ	Stress
σ_c	Elastic collapse stress
σ_i	Stress representing each reading
Ψ	Varying solid fraction
Ψ_0	Initial solid fraction

Chapter 5

Roman symbols

A	Proportionality constant
B	Proportionality constant
d	Fibre diameter
E_b	Young's modulus
l	Fibre link length
p	Probability
p_c	Critical probability widely
P	Exponent
Q	Proportionality constant
X	Substitute variable
X_c	Critical exponent
Y	Percolation quantity

Greek symbols

ε_{th}	Threshold strain
ζ	Dimensionless parameter for MNBM
κ	Effective elastic constant
κ_0	Proportionality constant
σ_e	Electrical conductivity
τ	Critical exponent
Ψ	Solid volume fraction
Ψ_0	Initial solid fraction
Ψ_c	Critical Solid volume fraction
Ψ_{th}	Threshold solid fraction

Chapter 6

Roman symbols

a	Velocity propagating through a sample
a_0	Accleration at the bottom end of a sample
a_l	Accleration at the top end of a sample
A	Acceleration
c	Complex wave velocity
D	Vibration displacement
E_0	Real part of Young's modulus
E_1	Bulk Young's modulus at the first resonance
E_d	Dynamic bulk Young's modulus
E_p	Bulk Young's modulus at the p-th resonance
F	Force propagating through a sample
F_0	Force at the bottom end of a sample
F_1 and F_2	Measured forces associated with the mass m_1 and m_2, respectively
F_l	Force at the top end of a sample
F_+ and F_-	Forces propagating in the positive and negative direction, respectively
$\hat{F}_+$ and $\hat{F}_-$	Mangitude of forces
j	Imaginary unit $\sqrt{-1}$

k	Complex wave number
K	Scale factor for calibrating a force transducer
l	Length of a sample
m	Loading mass including a top plate and an accelerometer
m_0	Extra mass contributed by the bottom plate and accelerometer on it
m_1 and m_2	Known weights
M	Mass of a sample
M_d	Dynamic mass of a system
r_F	Force reflection coefficient
r_k	Ratio of the attenuation constant and the phase constant
S	Cross-sectional area of a sample
t	Time
T	Transfer function or Transmissibility
$T_{calibration}$	Transfer function for calibration
$T_{compensated}$	Compensated transfer function
$T_{measured}$	Measured transfer function
$\lvert T \rvert$	Magnitude of transfer function
$\lvert T_1 \rvert$	Magnitude of the transfer function at the first resonance
$\lvert T_p \rvert$	Magnitude of the transfer function at the p-th order resonance
v	Velocity propagating through a sample
v_0	Velocity at the bottom end of a sample
v_l	Velocity at the top end of a sample
v_+ and v_-	Velocities propagating in the + and – direction, respectively
$\hat{v}_+$ and $\hat{v}_-$	Mangitude of velocities
V	Velocity
x	Dimension
Z	Mechanical characteristic impedance

Greek symbols

α	Attenuation constant.
β	Phase constant
$(\beta l)_p$	p-th solution of the equation (6.7c)

Δf_p	Resonance bandwidth measured at $\lvert T_p \rvert / \sqrt{2}$, at p-th order
η	Loss factor
η_1	Loss factor at the first resonance
η_p	Loss factor at the p-th resonance
ξ	Displacement of a sample under longitudinal excitation
ρ	Static density of a sample
ρ_d	Dynamic bulk density
ϕ	Phase of transfer function
ω	Angular frequency
ω_1	Angular frequency at the first resonance
ω_p	Angular frequency at the p-th resonance

Chapter 7

Not applicable

Chapter 8

Roman symbols

a	Coefficient
A	Coefficient
A_1	Amplitude of the fundamental displacement component
A_2	Amplitude of the second harmonic displacement
b	Coefficient
B	Coefficient
c	Coefficient
c:	Propagation speeds in a solid structure (not confused with coefficient c)
c_0	Wave speed in the linear regime in the case of the fluid
C	Coefficient
d	Coefficient
D	Coefficient
e	Coefficient
E	Young's modulus of a material

E_b	Bulk Young's modulus
E_c	Complex Young's modulus
E_x	Young's modulus in the x-direction
f	Coefficient
$F_{v,x}$	Viscous force in the x-direction
g	Coefficient
G	Modulus of elasticity in shear, or the modulus of rigidity.
$J_n(\ )$	Bessel function of the first kind of order n
k	Wave number
K_2 and K_3	Conventional combinations of the second and third order elastic constants in orthotropic directions in crystal lattices
l	Coefficient
m	Coefficient
n	Coefficient
p	Acoustic pressure
p	Coefficient (not confused with acoustic pressure p)
q	Coefficient
r	Coefficient
r_G	Radius of gyration about the direction of the propagation
s	Condensation
s	Coefficient (not confused with condensation s)
S	Elastic constant which is inversely proportional to elastic modulus
t	Time
V_0	Amplitude of a particle velocity
x	Cartesian coordinate
x^*	Discontinuity distance
y and z	Cartesian coordinates

Greek symbols

α	Nonlinear parameter
β	Coefficient of nonlinearity, $\beta \equiv -2\beta^*$
β^*	Coefficient of nonlinearity
γ	Shear strain
γ	Ratio of principal specific heats (not confused with shear strain γ)

ε	Normal strain
ζ	Parameter from the MNBM
η	Structural coefficient of viscosity
θ	Substitution variable, $\theta \equiv kx - \omega t$
λ	Lamé constant
ν	Poisson's ratio of a material
ξ	Particle displacement
$\hat{\xi}$	Displacement amplitude
ξ_0, ξ_1 and ξ_2	Terms of displacement in a perturbation analysis.
ρ	Density of a material
ρ_0	Density at the equilibrium state
σ	Normal stress
τ	Shear stress
Ψ_0	Initial solid fraction
ω	Forcing angular frequency

Chapter 9

E	Young's modulus of a fibre material
E_b	Bulk Young's modulus
Ψ_0	Initial solid fraction

Table of Contents

Chapter 3

Chapter 4

Chapter 5

Chapter 6

Chapter 7

Chapter 8

Chapter 9

Chapter 1

Introduction

Many solid materials, both naturally occurring and manufactured, contain internal cavities, or "pores", that are filled with a fluid. Such porous materials are extremely common and include wood, cork, sponges, sand, rocks, snow, concrete, brick, popcorn and expanded polystyrene. Porous media are usually of the cellular, granular or fibrous type. A cellular material may be composed of closed or open cells in a solid frame structure, usually containing a fluid within the cells. A granular material is composed of discrete particles, which may or may not be fused together or bound together by an adhesive. A fibrous material consists of long, thin, rod-like structures, usually interwoven, which are termed fibres. These may, or may not, be treated with a binding agent. In this thesis, it is fibrous materials that are of primary interest.

There is an enormous variety of fibrous materials in commercial and industrial use, and in everyday life. Textiles, cloths, cotton wool, rope, fibre-reinforced solid materials, paper and optical fibre for communication are all examples of these. Some are natural, such as vegetable fibres, fibres covering fruits, human and animal hair, but others are manufactured, such as glass fibre blanket, felted textile, and wire wool. Although fibrous materials in general have many purposes, they have three main roles in engineering applications: as vibration isolation materials, sound absorbing materials, and thermal insulation materials. Particularly in the case of vibration isolation, the structural properties of fibrous media are clearly of paramount importance. It is these structural properties which will form the main topic of this thesis. "Multifunctional" roles for fibrous media are, however, also possible. For example, an internal acoustic lining within an air duct also bestows thermal insulation to the duct wall, even though its thermal properties may not be optimal. And, conversely, the thermal insulation blanket in an aircraft fuselage structure also conveys the benefit of acoustic damping. Most of the

examples above – even human hair – can be analysed by a physical or engineering approach, if they are formed so as to constitute an interconnected bulk structure of fibres.

Porous media in general can also be grouped in different ways. For example, an acoustical classification is based on the thickness of a layer of the material, which can be regarded as a "sheet" or a "bulk material" depending on the acoustic wavelength of interest. Categorisation may also be made according to the structural nature of the solid frame of the material. The earliest models describing sound propagation in porous media are based on the assumption that the solid skeleton of the material is rigid and therefore does not move [1]. This may be a valid assumption when the bulk modulus of the solid frame is very much greater than that of the interstitial fluid, which is usually air. The density of frame material could be important, especially for an elastic frame material. Such materials are discussed in the next category. The dilatational fluid wave is considered dominant, and thus such models are also known as "equivalent fluid" models. Because of their simplicity, "rigid frame" models have long been favoured in acoustic modelling and associated design techniques for sound absorbing systems. The very simplicity of such models requires only the complex characteristic impedance and the complex propagation coefficient (or two other equivalent complex parameters) to describe the acoustical properties of the medium fully.

Another category of porous materials which has, in recent years, attracted much attention in the literature, is one in which motion of the solid frame is appreciable [2]. Porous media with bulk frame moduli of the same order as those of the fluids in the pores fall in this group. Because of the relative motion of the elastic frame and the interstitial fluid, wave propagation within the material is much more complex than that in a single-wave rigid-frame material. Thus, the understanding of the structural behaviour of the frame becomes essential.

A final – but less well recognised – category of porous materials is that in which the bulk modulus of the frame is significantly less than that of air. Such media are termed "limp frame" materials, which are, for example, light and unconstrained fibrous materials [3]. Although the solid phase can move, the fluid-borne wave usually tends to be

dominant (depending on the frequency and material parameters), because of the difference in moduli between the two phases. The material behaves like a distribution of "limp mass", the motion of which may be rather loosely coupled to the fluid motion.

Because of the simplicity of the equivalent fluid model for poroelastic materials, their structural behaviour has traditionally been suppressed in analyses. The acoustic behaviour of porous materials has been studied in detail since Lord Rayleigh, in the early part of the nineteenth century [4], modelled them as parallel straight capillary tubes containing a viscous, heat-conducting fluid. His approach has generally been regarded as the simplest geometrical form of model by which a porous material may be analysed, whilst retaining the salient physical effects.

Zwikker and Kosten [5] extended the Rayleigh model to include an inclination angle of the capillary tubes to the direction of the incident sound. Based on the fact that the compressibility and inertia of the porous medium govern the wave propagation, the complex effective, frequency-dependent, density and bulk modulus were introduced.

Johnson, Koplik and Dashen [6] defined the dynamic tortuosity as the ratio between the effective density and the equilibrium density of the fluid in the pores. They also introduced a characteristic length. Attenborough [7] and Allard [1] derived expressions for the effective density for idealised porous materials. Champoux and Allard [8] derived an effective bulk modulus based on the work of Johnson et al.

Delany and Bazley [9] conducted experiments in which the bulk acoustic properties – characteristic impedance and propagation constant – of various fibrous materials were measured, and showed that the two bulk quantities can be represented as functions of a single fluid/acoustical frequency parameter, the steady viscous flow resistivity multiplied by frequency and divided by fluid density.

Biot's salient work [10, 11] showed the importance of the solid phase in poroelastic materials. He showed theoretically that there exist two dilatational waves and a rotational wave in a porous material which is assumed to have a flexible frame. He specified both types of wave in the solid phase, together with a dilatational wave only in

the interstitial fluid phase. The fluid-solid coupling effect was shown to play a significant role.

In this case, the structural characteristics of porous materials are important, since structural motion can strongly couple with the fluid-borne wave in certain frequency ranges and influence the acoustic behaviour of the material. Structural/acoustic coupling in porous media has received increasing attention in recent decades. Kawasima [12] proposed an air-fibre composite medium model, with fibres vibrating in air. Resonant behaviour was theoretically predicted but not experimentally confirmed.

Dahl, Rice and Groesbeck [13] investigated the anisotropy of a fibrous material, where measurements both normal to and parallel to the fibre layers were conducted. Resonant effects in the acoustic properties was observed when a fibrous material was exposed to the normally incident sound wave. However, the resonance frequency of fibres was not fully modelled, and was simply adjusted by observing its effect on the measured impedance.

Lambert [14] proposed a one-dimensional fibre-resonance model different from those by Kawasima and Dahl et al. His predictions and measurements showed acoustic resonance effects deviating from those forecast by a rigid frame model. However, the resonance frequency was obtained from an adjusted fibre-resonance parameter based on experiments. These resonance models by Kawasima, Dahl et al., and Lambert were all derived based on the idea that only portions of fibres could resonate. Parameters representing the moving structural components were introduced, and their extreme values were related to the rigid-frame model.

Watson and Cummings [15] measured the bulk acoustic properties of lightweight fibrous media under different degrees of static compression. The data showed very pronounced structural resonance effects, the resonance frequencies increasing with the static loading. The evidence of significant amplitude dependence was also reported. Wilson, Cummings and Rice [16] gave experimental data on the dynamic elastic properties and damping of fibrous media, which also showed significant nonlinearity.

It is worth noting that, in references [12~16], no attempt was made to develop comprehensive models of the bulk structural properties of fibrous materials, for use in vibroacoustic formulations for these media. However, such models are necessary for the complete modelling of fibrous materials and for a proper understanding of the various aspects of sound transmission in flexible-framed materials. The purpose of the present investigation is to make some progress toward meeting this need.

Most of the reported investigations concerning the structural or coupled structural/acoustic behaviour of fibrous materials have been confined to the linear regime. Because of increasing interest in the extreme environmental conditions to which poroelastic materials can be exposed (e.g., in vehicle exhaust silencers), it is advantageous to understand the mechanisms by which they react to high sound pressure amplitudes or other forcing functions. Understanding the "static" structural nonlinearity of fibrous materials can be a step forward in this connection. The static behaviour of cellular materials have been extensively studied [17, 18], but this is not the case for fibrous materials. The static nonlinear behaviour of granular materials should also be investigated. Unconsolidated granular materials might experience densification under high-intensity sound and this could affect their dynamic performance.

Sides, Attenborough and Mulholland [19] idealised a fibrous material by means of "stacked-cylinder model". Since bending was prohibited by the stacking configuration, the model was analysed in terms of Hertzian contact deformation.

Rosen, Bagchi and Kibler [20] proposed a "space-frame material model" to investigate the three dimensional structural behaviour of fibrous thermal insulation materials. Fibres were represented by trusses in four vertical planes and a horizontal plane. The static behaviour of the model was formulated on the basis of the axial deformation of fibres. However, the model predicted an incorrect nonlinear stress/strain relationship.

Sherwood and Van Damme [21] investigated the static compression of flat clay plates. The deformation of each plate was assumed small enough to behave linearly. Both numerical simulation and controlled experiments were conducted to investigate the nonlinear behaviour of deposited plates. It was observed that, as the compression progressed, the number of inter-particle contacts per plate increased and the bulk structure became gradually stiffer and showed structural nonlinearity.

Baudequin, Ryschenkow and Roux [22] investigated the nonlinear elastic behaviour of a light fibrous material. Fibre elongation and compression were ignored, and only the linear bending of individual fibres was taken into account. The bulk nonlinearity was attributed to the creation of new contacts between fibres and a corresponding increase in the number of contacts when the material is subjected to compression, rather than to Hertzian deformation (which also shows a degree of nonlinearity). Certain other factors such as friction, sliding and damage, apparently likely to exist in a fibrous material, were not taken into account. By means of a scale transformation, a power-law relation was identified between the applied compressive stress and the corresponding strain in the high-strain region. However, this model was not applicable in the low-strain region.

In Chapter 4 of this thesis, static bending models will be developed to describe the nonlinear stress-strain relationship of bulk fibrous materials under static compression. Several specific models will be presented and their applicability will be discussed in terms of the strain range and the type of fibrous structure. Regarding the development of static models, in Chapter 2, the main physical mechanisms governing their bulk elastic behaviour will be investigated by means of experimental macro-scale elastic rod structures. In Chapter 3, the feasibility of extending the microscopic models will be studied in terms of contact friction and electric contact resistance. And in Chapter 5, the change in the number of inter-fibre contacts will be further investigated in terms of "connectivity" inside the fibrous material.

In their "dynamic" applications, bulk fibrous materials and other poroelastic media have been widely used for vibration isolation. The most effective way to control an undesirable vibration is of course to tackle it at source, but this is not always possible. Thus, engineers often have to design a structure in which the transmitted response from a vibration source is minimised. There are several different approaches in such methods of passive vibration control. They are related to overall structural design, material selection, localised additions, added damping and resilient isolation [23]. Among these, a fibrous material may often find its role as a resilient isolation element. Its role will be principally to isolate the source of vibration from its supporting structure by being physically placed between the two [24, 25]. The supporting structure is usually regarded as the receiver, to be protected from the unwanted vibration. A quantitative measure of vibration transmission is therefore a prime parameter in the evaluation of the efficacy of vibration isolation treatment.

Traditional vibration isolation techniques have often been based on "lumped-parameter" models, in which the source is usually represented as a point mass and the isolator as a (usually massless) spring [24~27]. Such simplification has been well established in an elementary understanding of vibration isolation, but there are limitations to its practical application. For example, it cannot explain resonance phenomena ("surging") caused by wave motion in the spring at the higher frequencies, and is limited to the fundamental resonance of the mass and the spring [25]. Thus, a frequency-domain dynamic structural analysis becomes essential in understanding vibration transmission through the isolator. This is particularly important if the isolator material is nonlinear in its dynamic properties.

The dynamic structural properties of fibrous and other poroelastic materials have frequently been represented by the complex modulus of elasticity, characteristic impedance, propagation constant and complex density, only two of which quantities are independent. They are often experimentally determined. Perhaps because of applications in vibration isolation, experimental determination (and theoretical understanding) of the structural properties of poroelastic materials are often closely related to those employed

in the case of vibration isolation mounts such as solid rubber. Harrison, Sykes and Martin [28] investigated longitudinal wave motion in isolation mounts in terms of the force transmissibility. They observed that the properties of isolation mounts could be affected by wave motion which is not explained on the basis of lumped-parameter models. Pritz [29, 30] investigated a method, involving a complex transfer function, for determining the propagation constant, which was obtained by solving a transcendental equation. The propagation constant was then converted into a dynamic modulus. However, this method was based on the assumption that the density of a material was a fixed, real, quantity equal to the static value. Wilson and Cummings [31] proposed a method to measure the dynamic mechanical properties of a porous material without prior knowledge of its density. In doing so, they measured the mechanical impedance between the velocity input and the force transmitted at the other end of a sample. It was equivalent to the two-thickness method [32~34] for measuring the characteristic acoustic properties of porous media. Instead of a transfer function and the mechanical impedance, the stiffness of a sample can also be measured to evaluate the bulk Young's modulus. Sahraoui, Mariez and Etchessahar [35] calculated the elastic modulus of an open-cell polymer material by measuring its compressional stiffness and Poisson's ratio in the quasi-static frequency range. Langlois, Panneton and Atalla [36] also developed a quasi-static compression test method. A polynomial relation based on compressional stiffness and shape factor was proposed to evaluate the elastic properties such as Young's modulus, Poisson's ratio, and the loss factor. These methods are, however, restricted to isotropic materials.

In Chapter 6, a series of experimental methods is reviewed. In particular, the transfer function method is described in detail. A novel method to measure the dynamic structural properties of a fibrous material is then proposed. Its advantage and limitations are also discussed. In particular, numerous measurements of the nonlinear dynamic behaviour of fibrous materials are presented in Chapter 7.

In much published work, the structural and acoustic behaviour of porous materials has been mainly investigated in the linear region, in which the amplitude of excitation is assumed to be very small. In cases, wave propagation in these materials could be explained by the use of linearisation which leads to the development of a wave equation. Traditionally, most applications have been investigated under such an assumption, with the benefit of a straightforward solution resulting from the linearity of the wave equation. These solutions have been understood on the basis of harmonic motion such as a pure sine wave. However, with finite amplitude excitation, a nonlinear version of each governing partial differential equation is inevitable because the first order approximation for a linear equation no longer holds. Such nonlinear equations have been reported for the propagation of finite amplitude wave through ideal gases, other fluids and solids [38, 40, 41, 42]. Solutions for those situations have shown the occurrence of higher-order harmonic components of the excitation frequency and the distortion of a sine wave as it propagates through the medium.

Crystals often experience anharmonic effects such as a structural instability and higher harmonics when their surface atoms are exposed to high amplitudes of vibration [38]. Melngailis, Maradudin, and Seeger [39] showed the distortion of an initially sinusoidal ultrasonic wave with finite amplitude as it propagates through anharmonic crystals. Breazeale and Ford [40] showed the distortion of a sine wave as well as the occurrence of a second harmonic component when an ultrasonic wave passes through a solid. Melngailis and Breazeale's solution was obtained by means of a perturbation analysis. Keck and Beyer [42] presented a theory concerning the generation of harmonic components as a finite-amplitude ultrasonic wave propagates in ideal gas and liquids. They also introduced a solution by Fubini, whose work was not known widely in this context. A series of specific applications concerns a closed or open ended pipe, excited at the other end by an oscillating piston. Betchov [43] theoretically studied the nonlinear motion of air trapped in a closed pipe. He predicted the distortion of a waveform and the generation of a shock wave. Cruikshank [44] obtained experimental data in good qualitative agreement with the theoretical work by Chester [45], who predicted distortion

and discontinuities in waveforms at high amplitude in a closed tube. Jimenez theoretically [46] and Sturtevant experimentally [47] studied nonlinear oscillation of a gas in a tube, and showed that good agreement between the two sets of results could be achieved by adjusting the effective length of the tube and the reflection coefficient at the end.

Such nonlinear phenomena have also been reported for the structural behaviour of porous materials. Belyaeva, Ostrovsky and Zaitsev [48] showed that the second harmonic amplitude had a quadratic dependence on that of the fundamental frequency in a fluid-filled unconsolidated granular material and a porous material made from a polymer. However, this nonlinear dependence has not been reported for fibrous materials to the best knowledge of the present author.

In Chapter 8 of this thesis, the structural behaviour of fibrous materials is studied by developing a governing nonlinear partial differential equation for this particular purpose. The analogy of this equation to those for other types of media is discussed. Finally, an analytical solution and experimental confirmation of this is presented, describing the occurrence of a second harmonic component in the case of a fibrous material.

Chapter 2

Idealised macro-scale static models

As an exploratory, initial, part of this investigation, a series of large-scale structures, or "macro-models" of fibrous media were constructed and tested experimentally. The object was to study, at a convenient physical scale, some of the structural effects that were thought to be potential causes of nonlinearity in the static mechanical behaviour of the bulk material. These macro-models were kept as simple as possible and efforts were made to build, into each, the particular effects that required investigation, e.g. Hertzian contact deflection of fibres in contact or "coming-to-contact" behaviour of nearby fibres. The macro-models were, on the whole, "modular" in that they constituted small, but representative, regions of much larger overall fibrous structures. The starting-point of the macro-model phase of the research was to examine a range of fibrous media visually by the use of a scanning electron microscope. This was done with differing degrees of mechanical compression applied, so that the salient physical effects of this compression could be examined. For comparison, similar tests were also applied to certain cellular media such as polyurethane foam. Then an experimental and numerical study of Hertzian contact effects between crossing fibres was carried out, with the object of establishing the importance of these effects and, if appropriate, eliminating them from the subsequent investigation. Following the conclusions from this part of the study, fibre bending effects were examined, in a suitably configured stack of fibres, both by the finite element method and by the use of Euler beam bending theory. A series of "coming-to-contact" models was next designed and tested, to investigate nonlinear effects brought about by increased inter-fibre contacts as a material is compressed. These models contained only a few "macro-fibres", and were sufficiently simple for theoretical modelling to be carried out without difficulty. Finally, some effects caused by the longitudinal loading of fibres

were studied, on the basis that these could be of possible importance in complex three-dimensional structures.

2.1 SEM photographs

At the outset of this research a range of practical fibrous materials, together with polyurethane foams, were examined microscopically by the use of a scanning electron microscope (SEM, Cambridge Instrument Stereoscan 200). Some fibrous media were found to contain "shot" – solid spheres or other shaped particles of the fibre material, see the circular objects in Figure 2.1, middle – and in some cases there was evidence of the presence of a binder at the contact points between fibres. Open-celled polyurethane foams typically have cells that appear regular and uniform (Figure 2.1, bottom left), a feature which might prove advantageous in any structural modelling effort. In the case of fibrous media, however, there is usually a distribution in fibre diameter, and some of these materials have an arrayed planar configuration (Figure 2.1, top left), whereas others have a "tangled" three-dimensional geometry (Figure 2.1, middle).

In addition to visual investigations of unloaded materials, porous media deformed by static compression were also examined here. For example, the top left and top right pictures in Figure 2.1 show the same fibrous material without compression normal to the planes of fibres (left) and with compression of about 0.7 strain (right). The SEM photos under compression clearly signify the difference in structure between the two states of this material. When compressed, the fibrous material is seen to become denser and to have more inter-fibre contacts (the key mechanism for nonlinearity, to be discussed later in this thesis).

The bottom left and right pictures in Figure 2.1 show the same polyurethane foam material without static compression (left) and with static compression of about 0.7 strain (right). Evidence not only of an increase in density of the structure, but also of buckling and twisting of the structural members is clearly visible here.

Apart from illustrating some essential differences between the behaviour, under compression, of the structure of fibrous and cellular materials, the five SEM photographs shown here also reveal two very significant features in the case of fibrous media: the increase in material density (which would, of course, be expected), and the increase in the number of inter-fibre contacts per unit volume. These two effects will, as shown later in this thesis, help to form the basis of a predictive model for the bulk static compressional behaviour of layered fibrous media.

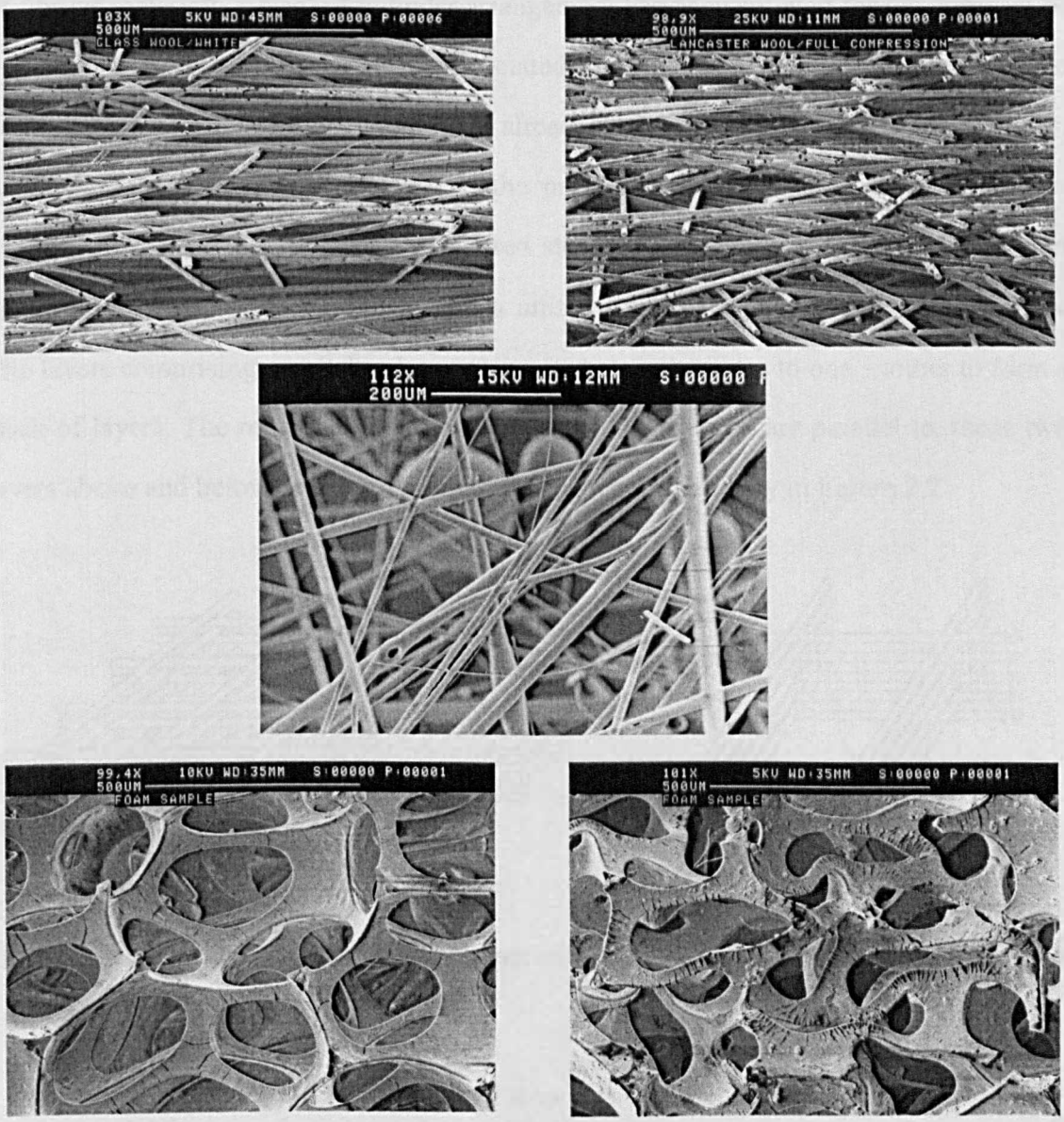

Figure 2.1 Microscopic views of a fibrous material and a polyurethane foam taken by the SEM. Top left, unloaded fibrous material; Top right, fibrous material under compression; Middle, "tangled" structure of a 3D fibrous material; Bottom left, unloaded polyurethane foam; Bottom right, polyurethane foam under compression.

2.2 Hertzian deflection of a stacked cylinder model

2.2.1 General nature of the model

A rectangular lattice may be considered as one of the simplest idealisations of the structure of a layered fibrous material. Thus as a first step to represent the microstructure of fibrous materials, a stacked cylinder arrangement has been adopted for the purposes of modelling and, on a macro scale, for associated experiments. The Hertzian characteristic of inter-fibre contacts in this model has already been described in the work of Sides, Attenborough and Mulholland [19]. In the present chapter its static behaviour is re-examined. The model is basically a layered structure of cylindrical rods. Each layer is composed of rods, placed parallel, with a uniform interval between adjacent members. The layers comprising parallel rods are orientated at right angles to one another to form a stack of layers. The rods in every layer lie directly above, and are parallel to, those two layers above and below. The arrangement is shown schematically in Figure 2.2.

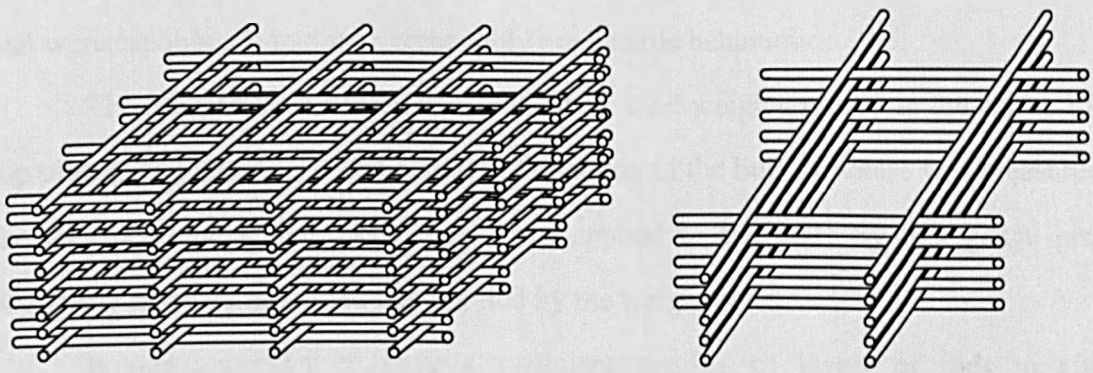

Figure 2.2 Schematic view for Hertzian contact model. Left, general layout; right, simplest model.

In the laboratory tests, the stacked structure was constructed from straight silver-steel rods 3 *mm* in diameter and about 335 *mm* in length. Both values are nominal and here the lengths of the rods do not have any real significance in the analysis. The construction of the bulk structure was achieved by building up each layer from a thick

steel base plate and it was finished by placing another thick steel plate on top of the stack, to act as a support for a series of loading weights. In building up the structure for the Hertzian deformation test, the simplest model can be constructed by layers having only two rods, which are sufficient to keep each layer stable and in balance (Figure 2.2). Thus each layer with two rods is in contact with other layers having the same number of the rods, so the layer will have four contact points on each contact plane, which is an imaginary common tangent plane running through the contact points. (Clearly, this does not apply to the top and bottom layers of two rods.) Throughout the layers, the contact points were aligned vertically to prevent any bending behaviour, which would have caused a spurious additional deflection.

Initially a silicon sealant was used to glue each rod and layer to form the bulk structure, but later this idea was abandoned because it was suspected the sealant itself was likely to contribute a greater deflection than the Hertzian deformation between the rods. Instead, a commercial adhesive tape was used to fix the position of each rod and hence each layer. Strips of the tape, of about 3 *mm* width, were put circumferentially around the rod near the contact points solely to restrict the horizontal degree of freedom (DOF) of the rods (See Figure 2.3). Thus, the clean Hertzian contact areas were exposed and were capable of yielding a reasonably predictable behaviour.

The compressional force was applied by steel weights placed in the centre of the top plate (See Figure 2.3). The resulting deflection of the bulk structure was measured by the use of a dial gauge. (The very force applied to the plate by this gauge proved negligibly small compared to that applied by the weights.)

It was necessary to have a sufficient number of layers of rods to give a measurable deflection, in view of the inherently small deflection related to Hertzian contact. Accordingly, 51 layers of silver steel rods were employed in the bulk structure and 50 Hertzian contact planes were thereby generated, with a total number of 200 contact points. Only one of the four narrow vertical regions encompassing the aligned contact points in the various layers is required for prediction of the Hertzian deflection in the model. It is worth pointing out that the contact planes generated by the top and

bottom steel plates and the adjacent rods are not taken into account. Those two planes are also exposed to a general Hertzian contact situation. However, the main difference is that the contact deflections are too small to contribute significantly to the total deflection, because they are line-contacted rather than point-contacted [49, 50].

2.2.2 Analysis

When two solid bodies having curved surfaces come into contact with each other, the initial point/line contact changes to circular/rectangular area contact [49, 50]. The stresses develop in the contact region and the corresponding strains cause a deformation to generate the contact area and hence to produce a deflection perpendicular to the contact plane. The most general case of this situation occurs when the two solid bodies have radii of curvature. This situation was theoretically analysed by Hertz and has been named after him. Perhaps the best known case among a number of applications is that where two spheres are in contact. The case of interest here may be treated in this way, because two cylindrical rods in contact at right angles may be shown to produce a circular contact area. In many engineering applications, the area of contact is of more interest than the perpendicular deflection, because the area is directly related to the contact stress or pressure, which will be linked to the strength or safety of the structure such as gear teeth and valve cams [49]. Here, however, as far as the compressional behaviour of the model is concerned, only the vertical or perpendicular deflection is of importance. The "vertical" direction in the case of an upright structure is the direction perpendicular to the contact plane.

It is well known that the deformation in a single Hertzian contact between two identical spherical materials is given by [19, 49]

$$\delta_H = \left(\frac{3}{\sqrt{2}} \cdot \frac{1-\nu^2}{E \cdot \sqrt{d}} \cdot F_H \right)^{2/3}, \qquad (2.1)$$

where F_H is the contact force, ν is Poisson's ratio, d is the diameter and E is the Young's modulus of the material. Poisson's ratio and Young's modulus were chosen as those typical of stainless steel. They are 0.3 and 200 GN/m^2, respectively [51].

In the experimental tests conducted here, the initial Hertzian deflection of the stack of rods, caused by the top loading plate (of mass 6 *kg*) was taken into account. Masses of up to 8 *kg* were added, by 1 *kg* increments, to the top plate, and the tests were repeated twelve times. The spatial resolution of the dial gauge was 0.01 *mm*.

In Figure 2.3, measurement apparatus is illustrated. The entire 51 layers are not shown for the sake of the simplicity and space, but the four contact points per layer in the actual model are implied in the side view.

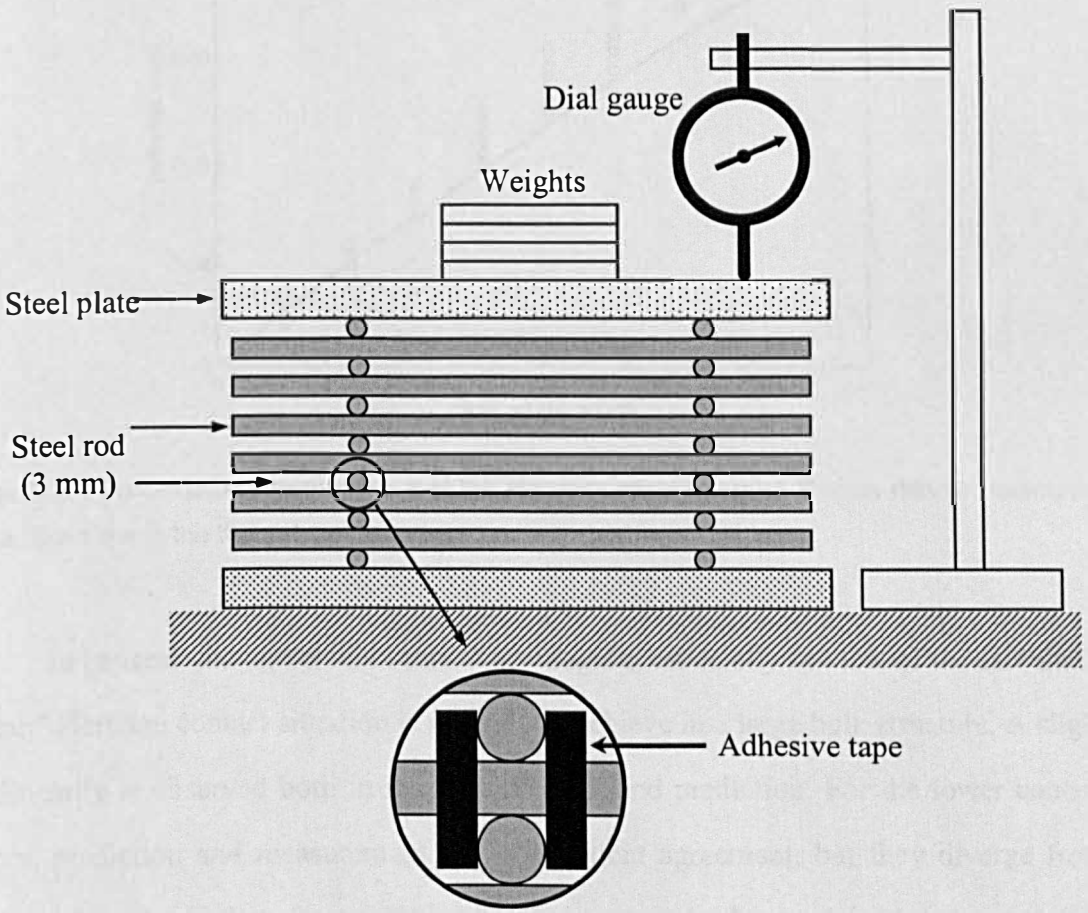

Figure 2.3 Schematic view of the experimental apparatus for measurement of the Hertzian contact deflection of a stack of cylindrical rods. The enlarged circle shows how the horizontal DOF is constrained by a strip of adhesive tape.

Figure 2.4 shows a comparison between the predicted and measured Hertzian deflection of the bulk model as a function of the applied force, which excludes the weight of the top loading plate. It is worth noting that, because of the nonlinear characteristic of Hertzian deflection, the contact force is not linearly related to the deflection. The deflection in the ordinate and the contact force in the abscissa represent the effect of the *additional* weight, over and above that of the top loading plate. Thus the effect of the loading plate cannot be envisaged by a linear extension of this plot.

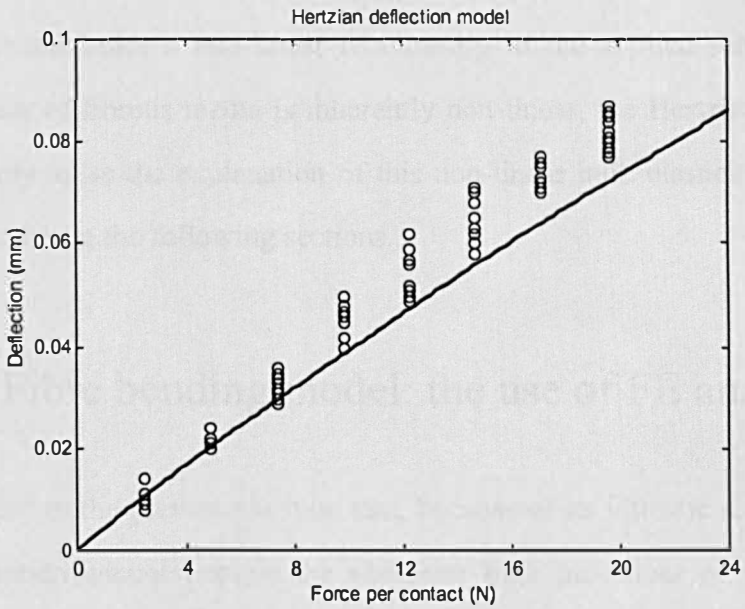

Figure 2.4 Force-deflection behaviour of the Hertzian contact model. Circles denote measured data. Solid line is the theoretical deflection.

In general, the agreement seems encouraging, especially in view of the fact that a "clean" Hertzian contact situation is not easy to achieve in a large bulk structure. A slight nonlinearity is observed both in the measurement and prediction. For the lower contact forces, prediction and measurement are in excellent agreement, but they diverge from one another for higher forces. This discrepancy might be explained by a possible instability of the model under the prevailing conditions. This occurs because the model owes its upright bulk structure to the horizontal DOF restriction imposed solely by the tapes around the circumferences of the rods near the contact points. It is thus possible that the horizontal constraint might be less than perfect, particularly in the upper parts of

the structure, and will be more significant at heavier loads. When the instability occurs, the contact points of the rods will be placed off a vertical axis. In this case, strictly speaking, the conditions of the current model become invalid. However, the effect of the instability was thought to be small and it was not investigated in detail.

As discussed, Hertzian deformation is expected to take place wherever inter-fibre contact occurs. In a realistic configuration, however, its contribution is likely to be very small because the deflection is inherently restricted by the fibre diameter, which is normally only a few microns or tens of microns in a typical fibrous material. Although Hertzian deflection bears a non-linear relationship to the applied force and the bulk elastic behaviour of fibrous media is inherently non-linear, the Hertzian deformation of fibres is unlikely to be the explanation of this non-linear bulk elasticity, which will be investigated further in the following sections.

2.3 Fibre bending model: the use of FE analysis

It was concluded in the previous section that, because of its intrinsic small contribution, Hertzian deflection cannot explain the nonlinear bulk behaviour of fibrous materials when they are compressed. Rather, it is the bending of individual fibres that is much more likely to be responsible for the bulk compressional behaviour of a fibrous medium [22]. As a first step, a fibrous structure that has inherently *linear* bulk elastic behaviour is investigated here, both by beam bending theory and by numerical analysis. The use of a finite element method – very widely used in structural analysis – is described in this section.

2.3.1 Analysis

A commercial FE code, ANSYS 5.5, was used to carry out the numerical simulation. Before proceeding with the main analysis, the validity of an element (a 3D 8-noded structural solid element) in a "macro bending model" was checked. In this process, a

single beam of length 100 *mm* and diameter 3 *mm* was analysed by the FE code and by beam bending theory. The beam was clamped at both ends and a force was applied at its centre. The beam deflection in the FE simulation and the bending theory agreed to within 1 %.

In the pre-processing of a "full model", depicted in Figure 2.5, 20 layers of rods were assembled, each link having a length of 100 *mm* and a diameter of 3 *mm*. In contrast to the Hertzian macro model of Section 2.2, each layer of rods in the bending model was displaced laterally by half the rod spacing in order to permit bending deflection. This was done in both plan coordinate dimensions. The arrangement is shown in Figure 2.5 and in more detail in Figure 2.6. Thus, a different number of contacts were created in each contact plane, because of the finite plan dimensions of the model. They are 9, 12 and 16 and this pattern is repeated throughout the fibre stack. The nodes of the lowest rods adjacent to the bottom plate were fixed in all possible degrees of freedom. The shared nodes of adjacent rods were merged. The nodes on the vertical centre plane of each rod were prevented from moving in the horizontal directions, which assumption is justified by the fact that the external force is applied vertically to induce a purely vertical deflection. Although the full structure was assembled in the pre-processing procedure, only a quarter of it was actually analysed in the simulation, because of its symmetry.

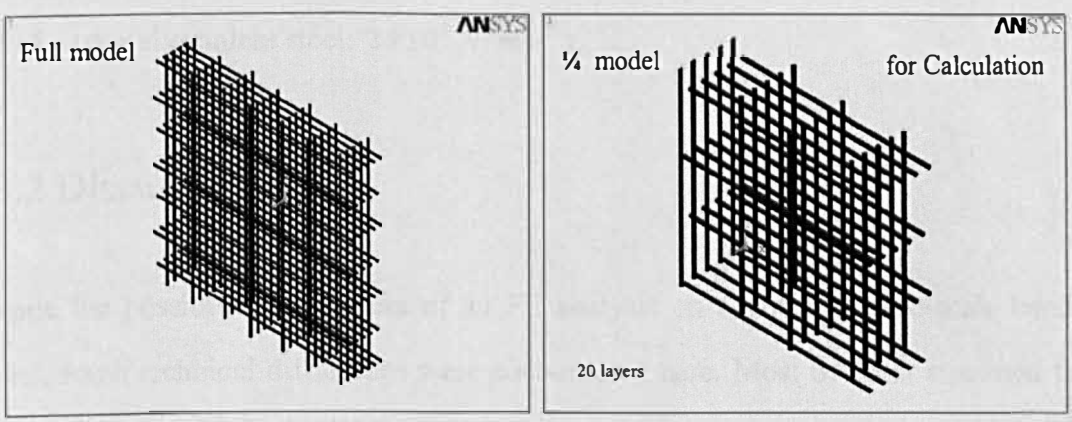

Figure 2.5 Geometry of the bending model created in the pre-processing for FE analysis.

In the simulation, a *constant* force of 5 *kgf* (49 *N*) was applied to an imaginary top plate. The choice of a 5 *kgf* force is arbitrary. Other values could be tried as long as consistent with a linear deflection. The force was divided equally amongst the 9 contact points that were formed by the two top layers. It was evident that the simulated result did not produce uniform deflection across a horizontal plane. This was explained by an "end effect" caused by the finite geometry of the simulated structure, which was not taken into account in the beam bending theory. The deflections at the 9 contact points of the top layer were averaged to produce a representative figure, based on the symmetrical geometry of the structure.

It is believed that the linear bending behaviour of a virtual macro-scale bending model could be well analysed by an FE code. That is because, when the vertical deflection (0.635 *mm*) of the simulation is obtained by averaging, it is found to be only about 1 % different from the theoretical deflection δ (0.641 *mm*) obtained by beam bending theory [50],

$$\delta = N_l \frac{F}{3\pi E} \frac{L^3}{d^4}, \tag{2.2}$$

where N_l is the number of deflected layers (18 here, because the top and bottom layers are not deflected), F is the force applied to the centre of the structure, L is the spacing between rods, d is the rod diameter and E is the Young's modulus (selected here to be that of a typical stainless steel, $2\times10^5\ N/mm^2$).

2.3.2 Discussion

Despite the possibility of success of an FE analysis on a virtual macro-scale bending model, some technical difficulties were encountered here. Most of them stemmed from the geometrical complexity of the model and eventually led to a question of efficiency and even the possibility of a more complex FE analysis for the model. Technically, the difficulties appeared in the form of an error in degrees of freedom (DOF) and the warning of a large negative pivot value, which could make the matrix singular. The effort

to overcome these problems turned out to be a time and resource-consuming procedure without a significant promise of success.

Selection of the type of element used was related to the above problems. The use of a 3D structural element led to a great increase in the number of the elements in comparison to the use of a 2D beam element, and created the problem of insufficient boundary conditions or restrictions. However, the selection of a 2D beam element was dismissed in the first instance, although such an element is specifically designed for bending behaviour. The reason for this was that – because its intrinsic two-dimensionality – the 2D beam element was not suitable to mimic certain essential features of the lattice structure of a virtual macro-scale bending model, such as a cylindrical geometry of each idealised rod and the "crossed" formation of the lattice.

The adoption of a 3D element certainly contributed to the instability of the virtual model. However, the fundamental cause of this may be the particular geometrical features of this model for example the high aspect ratio of each rod, incurred by its large length to diameter ratio. In the model, long rods with many elements are connected to one another just by a few nodes at the contact points. Forces are also transmitted through those few merged nodes. Because the whole model is sustained by a few nodes, a shortage of constraints or boundary conditions is inevitable. Thus one can encounter the problem of a DOF error when one tries to establish a matrix system to solve. Although it can be overcome, there is still the possibility of a warning of a large negative pivot value.

Modelling only bending deformation is evidently not straightforward, and thus there seems to be little hope of including Hertzian contact deflection in the virtual model. The Hertzian contribution is, of course, likely to be too small to be significant. However, both bending and Hertzian contact models cannot coexist in the same pre-process and analysis phases. To establish a well-conditioned matrix system for bending simulation, the contact nodes of adjacent rods need to be shared to keep the number of DOF as small as possible. But to run the code for Hertzian deformation the nodes must not be merged [52], otherwise, the contact (or attack) surface cannot penetrate the target surface,

because the merged node moves as one; this would prevent Hertzian deflection occurring in the simulation.

In summary, based on the various difficulties encountered here, any notion of the further adoption of FE analysis was discarded in the cases of other, more complicated, structures. The quarter model of the full structure described above required 73500 elements and 93240 nodes. This number of nodes is close to the limit (128000) imposed in the version 5.5 of ANSYS installed on a Pentium 4 machine with 512*MB* of RAM and a CPU speed of 500*MHz*. Therefore a microscopic FE formulation of a realistic fibrous material or even its idealisation would be a challenging procedure because of (a) a lack of computing resources and (b) vulnerability to the large number of DOF.

2.4 Linear bending model for a system of stacked cylinders

The concept of a stacked cylinder model was used again to investigate the bending behaviour of the bulk structure. The model was identical to that described in section 2.3, with alternate layers of rods offset by half the rod spacing in order to permit bending. In this case, however, the extent of the theoretical model in the planes of the rod layers was unspecified, and it could tacitly be assumed to be infinite. The rod layout is shown schematically in Figure 2.6. A perspective view is shown in the upper figure, showing the offset arrangement of the rods.

The measurement was carried out in a similar manner to that in the case of the Hertzian model described in Section 2.2. Steel weights were placed in the centre of the top plate to produce the compressional force. The deflection was detected by a dial gauge with a resolution of 0.01 *mm*. The experimental arrangement is depicted in Figure 2.6. The main parts of the apparatus are common to those in the Hertzian model experiments, so only the idealised bulk structure is illustrated. Eight layers are shown, with four links per layer as used in the actual experiments. The rods whose axes are in the plane of the paper are shown as grey or black. The black rods are all in the same vertical plane, as are the grey rods, though black and grey rods are laterally offset from one another by half the

rod spacing. To constrain the horizontal degrees of freedom, small pieces of "Blu Tack" adhesive were placed alongside the rods near the contact points, and these are indicated schematically by the elliptical shapes in Figure 2.6.

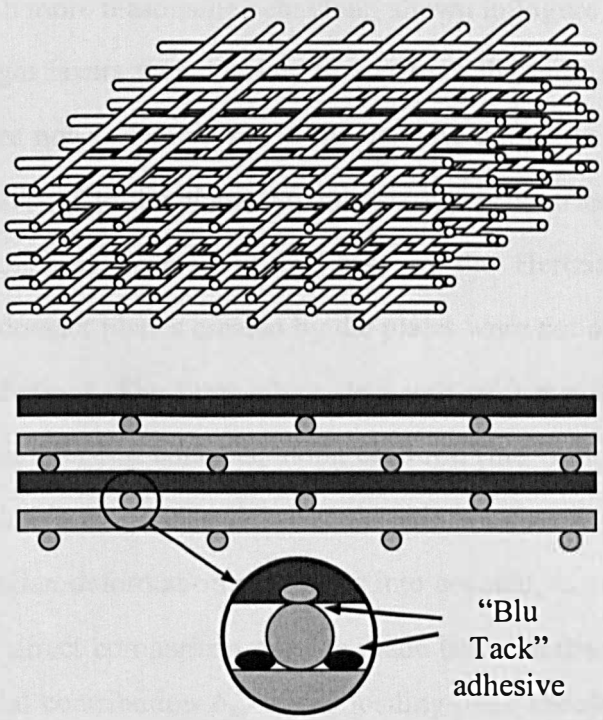

Figure 2.6 Schematic view of the bending model. Top, general model with infinite number of rods; Bottom, experimental arrangement. Note that rods are shifted by half the rod spacing to ensure bending.

The initial test produced a significant discrepancy between prediction and measurement, and the causes were identified as follows. The bottom and top plates departed significantly from flatness on a length scale equal to the length of a bar. Moreover, most of the steel rods were found to be bent because of frequent and heavy loading in the previous experiment such as the Hertzian deflection tests. The degree of curvature caused by previous loading was probably small for a single rod, but the cumulative effect was thought to be significant when a bulk structure was made. Certainly, initial gaps (in the unloaded stack of rods) between individual rods and between the plates and rods were noted. Thus the actual deflection, under load, of the stack of rods would be significantly greater than expected on the basis of complete inter-rod contacts. To compensate for the effects of these initial gaps in the bending behaviour,

additional rods were inserted between the layers. The deflection was then measured under load to evaluate the additional, spurious, deflection that occurred before the rods came fully into contact with one another. The subtraction of this value from the original data produced a much more reasonable behaviour, shown in Figure 2.7.

A total of eight layers were stacked to construct the bulk structure. The two top and bottom layers are not accounted for in the bending deflection calculations, because they were directly attached to the plates. So only six layers contribute to the bending, but seven contact planes were formed in the case of the Hertzian component of the deflection. The two contact planes created by the plates were not counted either, because of their small contributions. The same silver steel rods of 3 *mm* in diameter were used. The distance between inter-rod contacts, along each rod (the "link length") was taken to be 100 *mm*. The Young's modulus and Poisson's ratio were treated as previously. In the predictions, the Hertzian deformation was taken into account, in addition to the bending deflection, so that a direct comparison may be made between the two. As mentioned in Section 2.2, the initial contribution δ_{Hi} of the loading plate should be considered in the case of the Hertzian deflection. Thus the predicted deflection δ is composed of both bending and Hertzian effects, δ_B [50] and δ_H [49], respectively.

$$\delta = \delta_B + \delta_H = \sum_j^m \frac{F_w/N_j}{3\pi E} \cdot \frac{L^3}{d^4} + \sum_i^{m+1} \cdot \left(\frac{3}{\sqrt{2}} \cdot \frac{1-\nu^2}{E \cdot \sqrt{d}} \cdot \frac{F_w + F_p}{N_j} \right)^{2/3} - \delta_{Hi} . \quad (2.3)$$

Here, F_w is the applied weight and F_p is the weight of the top loading plate, N_j is the number of contacts in the j-th layer (corresponding in the present case to 9, 12, and 16). m is the number of deflectable layers (6 in the present case), and L is the length of a deflectable rod link. Euler beam bending theory with (effectively) clamped boundary conditions is employed in evaluating δ_B in equation (2.3). Although the actual boundary condition is simply-supported, symmetry in an effectively infinite stack of cylinders will prevent any rotation of structural elements at the contact points.

The Hertzian deflection is negligible as compared to the bending deflection, as one may see from Figure 2.7. The Hertzian contribution amounts to about 1% of that of

bending. The thick solid line, which includes both deflections, is hard to distinguish from the thin dashed line for bending deflection only. Both measurement and prediction indicate that the model behaves linearly and there is good agreement between them. Although a discrepancy may be observed at higher loads, it is fairly small. The nonlinearity in the Hertzian deflection is, not surprisingly, impossible to distinguish in Figure 2.7.

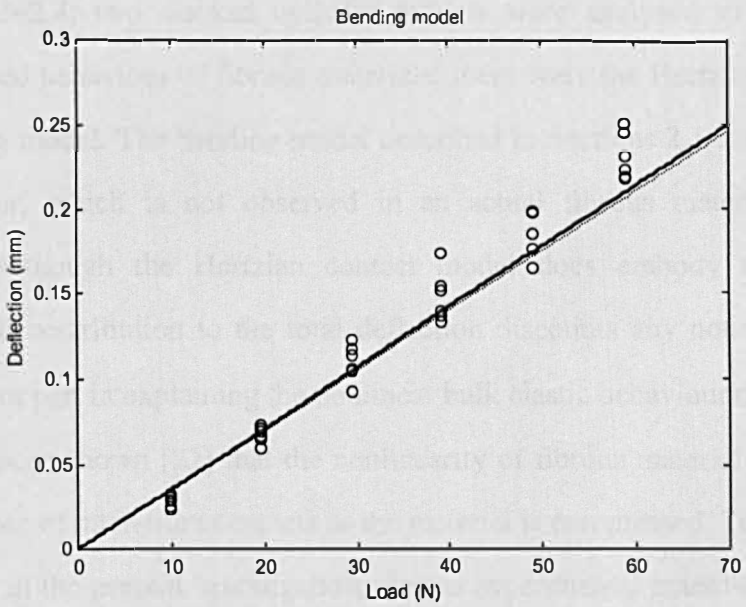

Figure 2.7 Deflection/force behaviour of the linear bending model. Circles represent the measured data. Solid lines are predictions. The thick line includes both linear bending and Hertzian deflections. The thin dashed line is for linear bending deflection only.

So far, one may observe that the stacked cylinder models yield good agreement between theoretical prediction and measured data, both in case of the bending model and in the Hertzian model. However, the deflection caused by bending is definitely more representative of a realistic fibrous material than that from purely Hertzian deflection. However, its linearity is not representative of the observed elastic behaviour of actual bulk fibrous media: it is well known that a fibrous material deflects nonlinearly under compression. One mechanism for this non-linearity is the increase in the numbers of inter-fibre contacts as the material is compressed [22]. Therefore, as will be seen in Chapter 4, real fibrous materials behave nonlinearly throughout the strain range of static

compression, even though it is usual to assume fibrous materials have a linear stress-strain behaviour under small strain and that any nonlinearity is not significant in this region.

2.5 Coming-to-contact models

In Sections 2.2~2.4, two stacked cylinder models were analysed to investigate the possible idealised behaviour of fibrous materials; these were the Hertzian contact model and the bending model. The bending model described in Sections 2.3 and 2.4 involves a linear behaviour, which is not observed in an actual fibrous material under static compression. Although the Hertzian contact model does embody nonlinearity, its inherently small contribution to the total deflection discounts any notion that it would play a significant part in explaining the nonlinear bulk elastic behaviour of fibrous media. Instead, it has been shown [22] that the nonlinearity of fibrous material is related to the increased number of inter-fibre contacts as the material is compressed. To verify this idea experimentally in the present investigation, simple experimental macro-model structures related to the previous idealised silver steel structures were developed. They were made up of crossed rods with different initial gaps between them (Figures 2.8 and 2.13) and are referred to here as "coming-to-contact" models. Two different arrangements were constructed, the first of which involved a single coming-to-contact event between two structural members, as a force was applied to the structure, and the second of which involved two coming-to-contact events. The two models otherwise shared some general geometric features. It is worth mentioning that mechanisms other than the nonlinear fibre-contact are not pursued at this stage. For example, "fibre fracturing" is not addressed here. Such fracturing is unlikely with silver steel rods, however, it could occur in glass fibre. Such occurrences will be addressed implicitly in Section 4.4.3.

Three different terms will be used here for rods forming structural elements in a coming-to-contact model. A "loading rod" is one to which an external force is applied. A "target rod" is one which is to make contact with a loading rod. Thus new contacts are

made when the loading rod and the target rod meet one another. Finally a "supporting rod" is one which supports the target rod(s), to allow space for the target rod to deflect. These are illustrated in Figure 2.8.

2.5.1 Single new contact model

As a means of investigating the effects of the increase in the number of inter-rod contacts with compressive strain, a "single new contact" model was first developed. It was made up of crossed cylindrical rods with different initial gaps between them, as depicted in Figure 2.8. Supporting rods were glued to the base plate and one end of the loading rod was also glued to it by the use of a resilient silicone adhesive, permitting some degree of rotation but little translation of the end of the rod. The boundary conditions at that end were therefore taken to be those appropriate to a simply supported end. A single new contact was designed to occur in this structure. The arrows in Figure 2.8 show the reference position where the force was applied and the deflection measured. Silver stainless steel rods of 3 *mm* diameter were used to construct this coming-to-contact model. Rods of this 3 *mm* diameter were used because they are readily available. The choice of diameter is not important here since it is not intended to produce a scale model of a fibrous material. Despite its geometric simplicity, it is believed that this model embodies one important feature of the local behaviour of an area of a real, transversely isotropic, fibrous material with a laminar configuration.

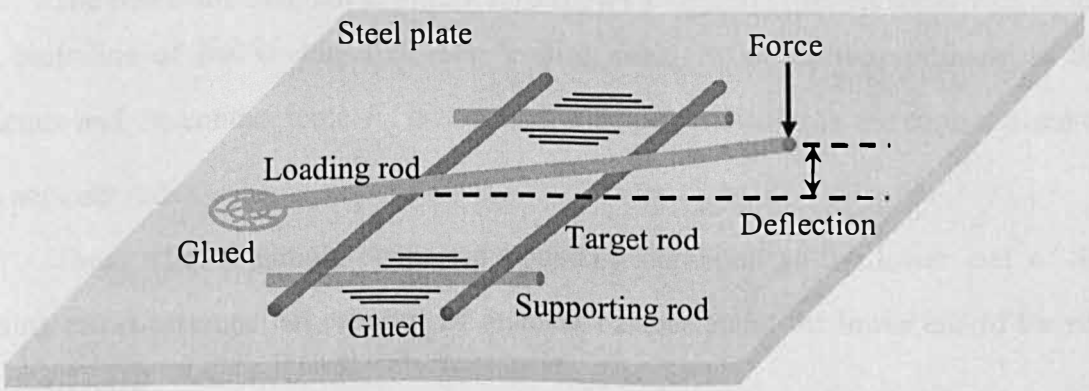

Figure 2.8 Schematic diagram showing a single-new-contact coming-to-contact model.

In the actual experimental arrangement, three further, identical, coming-to-contact structural modules were added to make a total of four modules, as depicted in Figure 2.9. They were placed at the corners of a square, to maintain the balance and symmetry of the whole structure. Then a steel plate was placed over the four modules, supported by the tips of the loading bars. The measurement was then conducted in a manner similar to those described in Sections 2.2 and 2.3. Steel weights were placed on the centre of the loading plate to produce the compressive force, which was distributed evenly between the four loading bars. The dial gauge was used to measure the vertical deflection of the four structures.

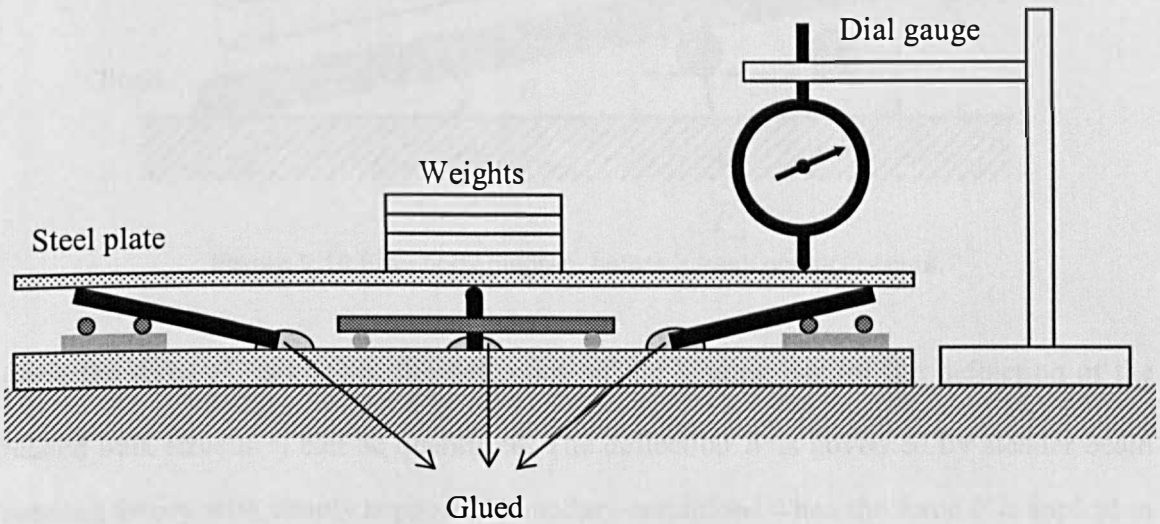

Figure 2.9 Schematic view of the experimental arrangement for the single coming-to-contact model. The fourth element is not seen in this view, because it is obstructed by the element in the centre.

The schematic diagram in Figure 2.10 shows a vertical cross-sectional view along the centreline of the loading rod. The loading force F_c is applied vertically to the structure and the contact force F_a is assumed to be perpendicular to the contact plane of two adjacent rods.

Thus, when a simply supported boundary condition at the lower end of the loading rod is assumed, an equation of moment balance about the lower end of the rod may be written:

$$L_a \cdot F_a = \left(L_c - d \cdot \tan\theta_1\right) \cdot \cos\theta_1 \cdot F_c . \qquad (2.4)$$

From this, one can find the contact force F_a applied to the target rod. The other parameters except the loading force F_c can be obtained from the geometry of the structure. The dimensions of the experimental model were as follows, L_c being the length of the loading bar and L being the link length of the target bars (measured between junctions with the supporting bars):

$$L_a = 70\ mm,\ L_b \approx 80\ mm,\ L_c = 83\ mm, L = 120\ mm, d = 3\ mm. \tag{2.5}$$

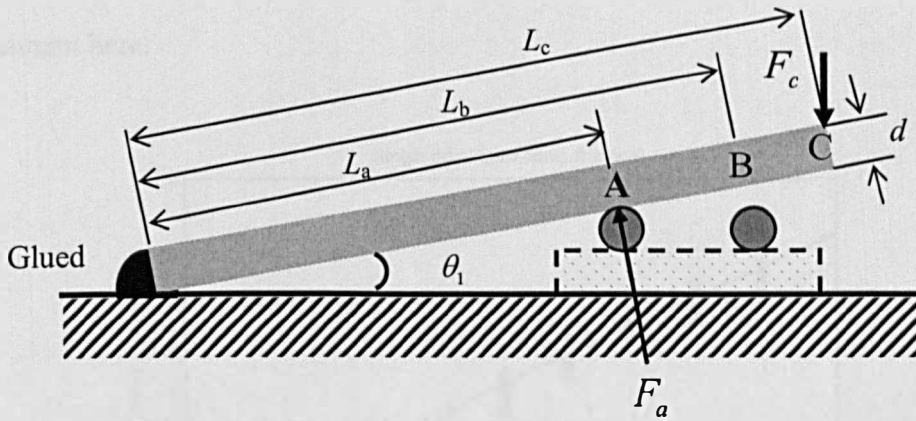

Figure 2.10 Free body diagram before a fresh contact occurs.

Once the force F_a is known, the deflection of the loading bar (or the deflection of the related bulk structure) can be quantified. The deflection δ is governed by slender beam bending theory with simply supported boundary conditions when the force F is applied in the vertical plane of the central axis of the target rod with Young's modulus E and diameter d [50]:

$$\delta = \frac{4FL^3}{3\pi d^4 E}. \tag{2.6}$$

At this stage, the value for F is equal to that of F_a. In contrast to the both-ends-clamped situation in the bending model, the target bars here are free to rotate, but rest on the supporting rods. The deflection given by equation (2.6) accounts for the first, linear, part of the predicted deflection/load relationship (see Figure 2.11). It is worth noting that Hertzian contact behaviour has not been accounted for. That is mainly because it would not make a significant contribution, and this assertion is supported by the previous cases previously described in this chapter.

It may be noted that the contact force F_a is not constant, because the angle θ_1 is changing according to the level of deflection. However, because of the particular geometry, the change of this angle is small enough for it to be neglected. Thus, F_a is also assumed constant and fixed at the initial value until the next contact is generated. The loading rod L_c is assumed to remain straight. Some small degree of bending would occur in this rod at the point A but, because of the particular dimensions of the model (see (2.5)), this would be small and is neglected. Bending deflection in the target rod would be dominant here.

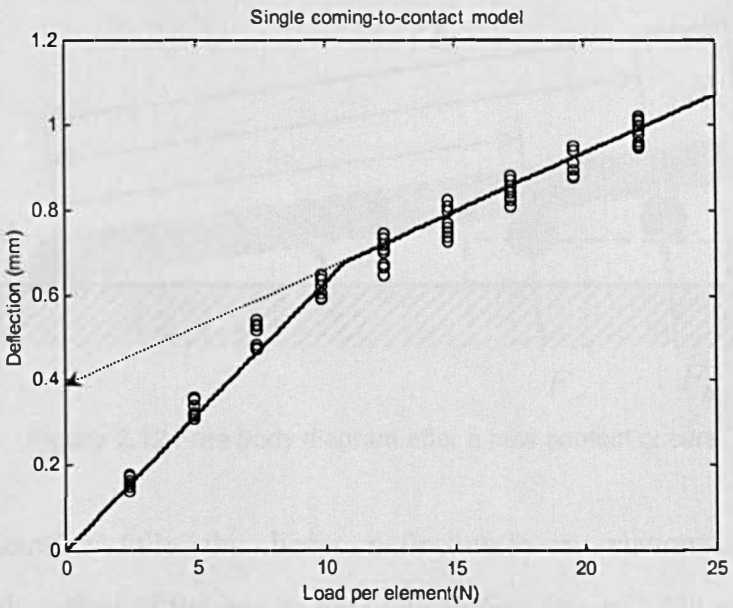

Figure 2.11 Deflection/load behaviour of the single-new-contact coming-to-contact model. The circles denote measured data. The solid line represents prediction. The dotted line and its arrow indicate the "offset" of the second linear line. Here the "load per element" is equal to F_c in Figure 2.12. And "deflection" is equal to the vertical movement at point C.

Once the new contact has occurred (Figure 2.12), the previous moment equilibrium (equation. 2.4) is no longer valid, and a new equation applies:

$$L_a \cdot F_a + L_b \cdot F_b = \left(L_c - d \cdot \tan\theta_1\right) \cdot \cos\theta_2 \cdot F_c . \qquad (2.7)$$

The assumption that the loading bar is straight will lead to the condition,

$$\frac{L_b}{L_a} = \frac{\delta_b}{\delta_a} = \frac{F_b}{F_a}, \tag{2.8}$$

where the deflections at points A and B are denoted by δ_a and δ_b, respectively. Thus the two contact forces F_a and F_b can be identified from the equations (2.7) and (2.8). Even while the structure deflects further, the angle θ_2 is assumed constant. Once both contact forces have been found, the deflection of the loading bar can be quantified by the deflection of either of the two target bars, which are related by the above equation. This deflection explains the slope of the second line, but not the offset on the ordinate in Figure 2.11.

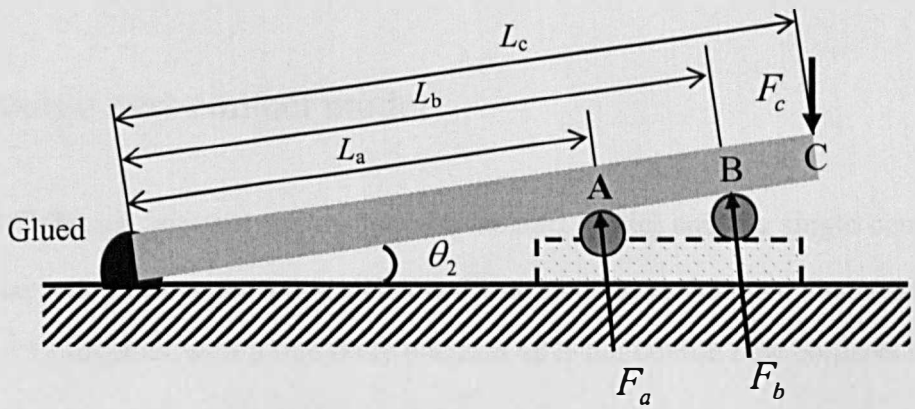

Figure 2.12 Free body diagram after a new contact occurs.

To determine fully the linear deflection/force relationship for the new configuration, the offset of the line in the ordinate (see Figure 2.11) needs to be found. This is related to the point at which coming to contact occurs. In the model, it is assumed that the additional contact is generated when, at point B, the initial gap is equal to the deflection of the loading rod. The initial gap δ_{gap} may be approximated by

$$\delta_{gap} \approx L_b \cdot \tan\theta_1 - (d + d/\cos\theta_1). \tag{2.9}$$

If angular changes are assumed small, the deflection at the point B may be obtained from that at the point A:

$$\delta_b = \frac{L_b}{L_a} \cdot \delta_a . \tag{2.10}$$

When the loading begins, the deflection δ_b is less than the gap δ_{gap}, but when the loading bar meets the second target bar (See Figure 2.12), δ_b will be equal to δ_{gap}. Thus,

the magnitude of the force responsible for the additional contact can be identified. This force will determine the offset of the second linear part of the deflection/load curve (see Figure 2.11), and so the piecewise linear behaviour of the coming-to-contact model can be fully explained.

Measured data and the predictions of equations 4, 6, 8, 9 and 10 in Figure 2.11 are in good agreement, and a stiffening, piecewise linear, characteristic is apparent as expected. This confirms that the overall nonlinearity can be explained adequately by increased contacts rather than by Hertzian deflection (which, as previously mentioned, is not accounted here because of its relatively small value).

2.5.2 Double new contact model

The only difference between the double new contact model and the single contact new model is that one more target rod is added to the structure. A schematic diagram is shown in Figure 2.13 together with a free body diagram after the double new contacts in Figure 2.14.

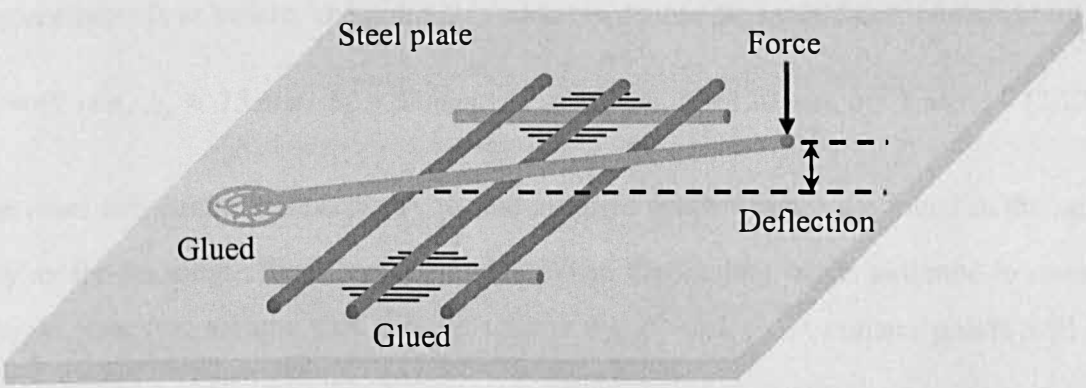

Figure 2.13 Schematic diagram showing the double-new-contact coming-to-contact model. Target rods are attached to the supporting rods by the use of silicone adhesive.

It can be seen that the geometry is very similar to that of the single-new-contact coming-to-contact model. The moment equilibrium is identical for the first two contacts (one existing and one new contacts). Thus the magnitude of the force determining the onset of

the first new contact is also found by the same procedure. For the second additional contact, the moment may be balanced by the following equation when a simple supported boundary condition is imposed at the lower end of the loading bar (all parameters except forces are known from the geometry of the structure):

$$L_a \cdot F_a + L_b \cdot F_b + L_d \cdot F_d = \left(L_c - d \cdot \tan\theta_2\right) \cdot \cos\theta_3 \cdot F_c . \tag{2.11}$$

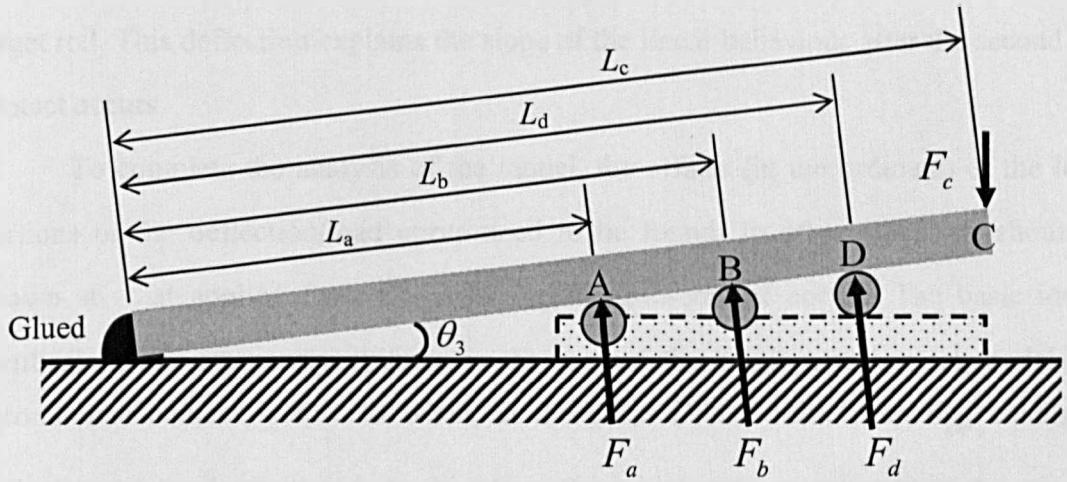

Figure 2.14 Free body diagram after a second new contact occurs.

The experimental model was constructed with the following dimensions (the nomenclature is as before, and point D is added to denote the second new contact point):

$$L_a = 62\ mm,\ L_b \approx 75\ mm,\ L_c = 83\ mm,\ L_d \approx 82\ mm, L = 120\ mm, d = 3\ mm. \tag{2.12}$$

The other two conditions necessary to find all three contact forces are found in the same way as for the single fresh contact model. When the loading bar is assumed to remain straight, one can assume that the deflections δ_a, δ_b and δ_d at contact points will be proportional according to geometrical compatibility:

$$\frac{L_b}{L_a} = \frac{\delta_b}{\delta_a} = \frac{F_b}{F_a} \tag{2.13a}$$

$$\frac{L_d}{L_a} = \frac{\delta_d}{\delta_a} = \frac{F_d}{F_a} \tag{2.13b}$$

Equations (2.11) and (2.13a,b) enable the three contact forces F_a, F_b and F_d to be determined. Once all the contact forces are evaluated, the deflection of the loading bar can be quantified by the deflections of any of the three target bars (these are related to one another). The deflection is obtained in the same way as that of the single new contact model, by the use of slender beam theory with simply supported boundary conditions at the ends of the rods, the force being applied in the vertical plane of the central axis of the target rod. This deflection explains the slope of the linear behaviour after the second new contact occurs.

To complete the analysis of the model, the offsets (in the ordinate) of the linear portions of the deflection/load curve need to be found. In other words, it should be known at what applied force the second coming-to-contact occurs. The basic idea is identical to that previously outlined in the case of the single new contact model. The second new contact is formed when, at the point D, the initial gap δ_{gap} equals the deflection of the loading rod. In this case, the initial gap corresponds to the gap that remains immediately after the first new contact has occurred. It may be approximated by

$$\delta_{gap} \approx L_d \cdot \tan\theta_2 - (d + d/\cos\theta_2)\,. \tag{2.14}$$

The subscript for angles is '2' not '3', because the gap is determined by the stage before the contact is created. When the assumption of small angular variation is made, the deflection at the point D may be obtained from the value at the point A via geometric compatibility (equations (2.13a,b)). Thus the magnitude of the force at that point will determine the offset of the piecewise linear curve after the second new contact.

In the measurements, the bulk structure and the test method were arranged in a similar way to that in the case of the single-coming-to-contact model. A total of four modules were built up and placed at the four corners of a square, as before. The arrangement resembled that in Figure 2.9, except for the different number of target bars. Measured data and prediction at compared in Figure 2.15, and are in reasonable agreement. The onset of nonlinearity is clearly evident.

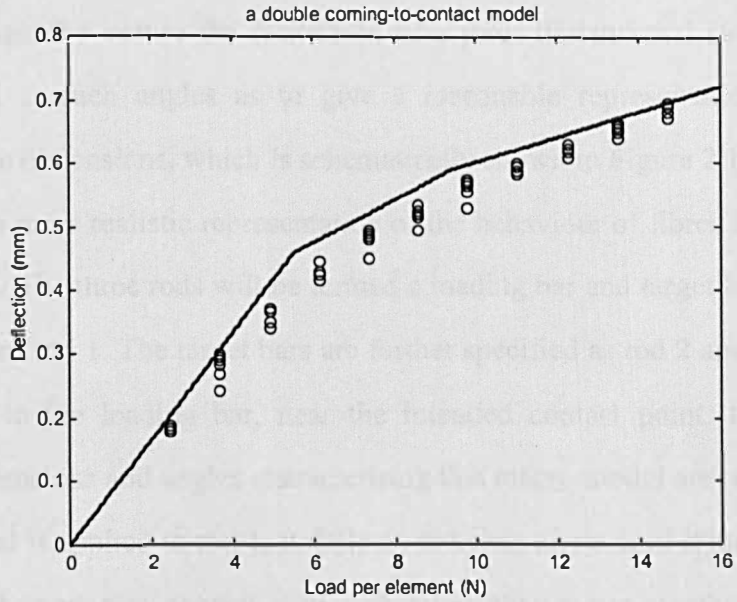

Figure 2.15 Deflection/load behaviour of a double-new-contact coming-to-contact model. The circles denote the measured data. The solid represents the prediction.

The two "coming-to-contact" models described here offer convincing support for the idea that an increased number of inter-fibre contacts is responsible for the non-linear compressional elastic behaviour characteristic of real fibrous materials. However these models still require further development in order to be applicable to realistic materials. The geometric simplicity of the essentially laminar configuration of these models is likely to limit their application to planar layered media, and the modelling therefore needs to be made more general.

2.6 Three-dimensional contact model

As one may infer from the central SEM image in Figure 2.1, some fibrous materials have a structure composed of "tangled" fibres which is more three-dimensional in nature than the essentially laminar structures discussed in Sections 2.2~2.5. To investigate the idealisation of such media, an experimental macro-scale model was developed with three-dimensionally arranged rods. The model was composed of three silver steel rods of diameter 3 *mm*. The rods were welded to a brass base plate of thickness 5 *mm*. As far as the number of contacts is concerned, it was designed to make two successive contacts

across initial gaps. To ensure the realisation of a three-dimensional structure, the rods were orientated at such angles as to give a reasonable representation of a general structure in three dimensions, which is schematically shown in Figure 2.16. Thus it might be regarded as a more realistic representation of the behaviour of fibres in an actual bulk fibrous medium. The three rods will be termed a loading bar and target bars. The loading bar is also termed rod 1. The target bars are further specified as rod 2 and rod 3. Rod 2 is situated closer to the loading bar, near the intended contact point, than rod 3. The appropriate dimensions and angles characterising this macro-model are recorded in Table 2.1. When a load is applied to rod 1, it deflects or bends alone until it meets rod 2. Since rod 1 and rod 2 come into contact with each other, they move together, as the load in increased, until the rod 2 meets rod 3. Finally the three rods move in unison.

	Length (*mm*)	Angle of inclination to base plate (°)	Distance *a* (*mm*)
Rod 1	143	53	79
Rod 2	97	42	87
Rod 3	101	37	N/A

Table 2.1 Characteristic dimensions of the three-dimensional model.
The distance "*a*" is from the welded end of the rod to the contact point with the adjacent rod. The value for Rod 3 is not required in the analysis, because Rod 4 is not present.

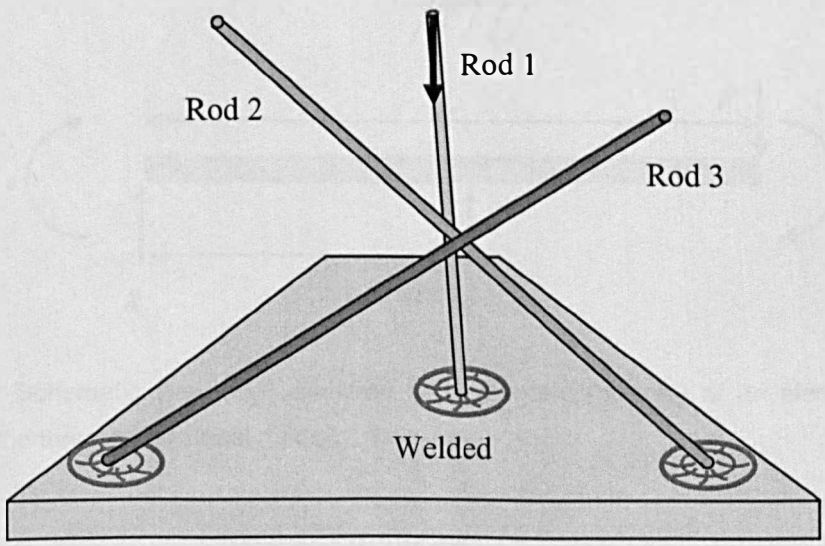

Figure 2.16 Schematic view of the three-dimensional model. The arrow shows the location and direction of the applied force.

2.6.1 Behaviour of an elemental modular structure

To analyse this particular three-dimensional model, especially once a new contact has been made, it is necessary to interpret the behaviour of the generic cantilever beam shown in the schematic and free-body diagrams in Figure 2.17. That is because, when the loading rod meets the first target rod and makes a new contact, it has an additional support together with the original built-in (welded) boundary condition. The support can be defined by a simply supported boundary condition, and there is also the possibility of sliding motion between the loading rod and the target rod. This newly generated situation appears to be relatively simple to analyse and may be solved by the superposition of several known solutions. It could be the case that the reaction R_a is known a priori, by superposing the deflections resulting from the external force F, the external moment M and the reaction R_a. However, the problem should be solved step by step, because the reaction R_a is, in general, unknown.

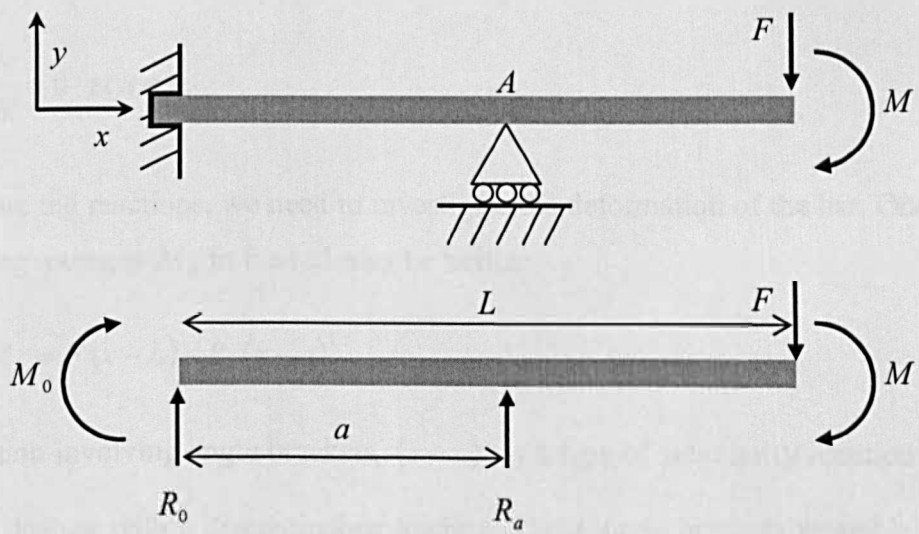

Figure 2.17 Schematic view (top) and free body diagram (bottom) of an elementary beam structure in the three dimensional model.

We need to find the reaction force R_a applied to the target bar, and the deflection at the end of the target bar. From the equilibrium of forces and moments (about the left-hand end of the bar; see Figure 2.17), the following two conditions may be written:

$$R_0 + R_a = F, \tag{2.15a}$$

$$M_0 + M = a R_a - F L\ . \tag{2.15b}$$

This is a "statically indeterminate system" [51], however, because only two equations are available for three unknowns, R_0, R_a and M_0. Nevertheless, this setback can be overcome by the application of the "force-deformation relationship". The boundary conditions usually include both "force equilibrium conditions" and "geometric compatibility conditions". The equilibrium conditions will involve restrictions on the shear and bending moment at certain points. The geometric conditions will involve restrictions on the deflection and slope at certain points:

$$y = 0 \ \text{ at } x = 0 \text{ and } x = a, \tag{2.16a}$$

$$\frac{dy}{dx} = 0 \ \text{ at } x = a. \tag{2.16b}$$

To evaluate the reactions, we need to investigate the deformation of the bar. Once again, the bending moment M_b in the rod may be written,

$$M_b = F(x - L) - R_a\langle x - a\rangle^1. \tag{2.17}$$

The function involving angle brackets, $\langle x - a\rangle$, is a type of singularity function which is useful in dealing with a discontinuous loading. These angle brackets resemble ordinary brackets except that the function is always zero when the argument is negative. When the exponents are -1 and -2 (these numbers are placed as a subscript for attention), the function equals zero everywhere except at $x = a$. These functions are integrated according to the following rules [51]:

$$\int_{-\infty}^{x} \langle x-a \rangle^{n} dx = \frac{\langle x-a \rangle^{n+1}}{n+1} \quad \text{when } n \geq 0, \tag{2.18a}$$

$$\int_{-\infty}^{x} \langle x-a \rangle_{-2} dx = \langle x-a \rangle_{-1} \text{, and} \tag{2.18b}$$

$$\int_{-\infty}^{x} \langle x-a \rangle_{-1} dx = \langle x-a \rangle^{0}. \tag{2.18c}$$

When bending is involved in the deflection of a structure, the bending moment may be related to the deflection by [51],

$$EI\frac{d^2y}{dx^2} = M_b, \tag{2.19}$$

where E and I denote, respectively, the Young's modulus and the second moment of area of the beam about its neutral axis. Their product EI represents the "flexural rigidity" or "bending stiffness".

While equation (2.19) is integrated twice to find the deflection, the specific boundary conditions (equation (2.16a,b)) can be evaluated together. By doing this, one may find the reaction R_a in the present model,

$$R_a = \frac{F}{2a}(3L-a) + \frac{3}{2a}M. \tag{2.20}$$

If this reaction is inserted back into equation (2.17), the bending moment in the specific beam of interest is completely represented by

$$M_b = F(x-L) - \left(\frac{F}{2a}(3L-a) + \frac{3}{2a}M\right)\langle x-a \rangle^{1}. \tag{2.21}$$

To evaluate the deflection at the end of the bar, an energy method may be successfully adopted. "Castigliano's theorem" states that if the total complementary energy U^c of a loaded elastic system is expressed in terms of the loads, the in-line deflection δ_i at any particular loading point is obtained by the partial derivatives of U^c with respect to the load P_i at that point [51],

$$\delta_i = \frac{\partial U^c}{\partial P_i}. \tag{2.22}$$

To apply Castigliano's theorem it is necessary to determine the total elastic energy of the system in terms of the loads that are parallel to the required deflection. In a linear elastic system, it is obvious that its complementary energy is equal in magnitude to the potential energy U^p. It has been widely accepted that the potential energy rather than its complementary counterpart in such a system is used. Therefore, for a linear-elastic system, the term "elastic energy" U will be adopted to express the potential energy or the complementary energy. When a bending moment exists in a structure, the elastic energy may be represented by integrating the bending moment along the characteristic dimension, which is usually the length of a beam [51],

$$U = \int_0^L \frac{M_b^2}{2EI} dx. \tag{2.23}$$

When the bending stiffness EI is assumed constant, the elastic energy will be expressed by

$$U = \frac{F^2}{6EI}\left\{L^3 - \frac{a}{4}(3L-a)^2\right\} + \frac{FM}{2EI}\left\{L^2 - \frac{a}{2}(3L-a)\right\}. \tag{2.24}$$

Thus, according to Castigliano's theorem, the deflection at the end of a bar may be written

$$\delta_L = \frac{\partial U}{\partial F} = \frac{F}{3EI}\left\{L^3 - \frac{a}{4}(3L-a)^2\right\} + \frac{M}{2EI}\left\{L^2 - \frac{a}{2}(3L-a)\right\}. \tag{2.25}$$

For the particular model in Figure 2.16, the moment M in Figure 2.17 is related to the force F (see Figure 2.19), because of the idealisation of the load-bearing shape as a straight rod (see Section 2.6.3). Finally, relations (2.20) and (2.25) for the reaction force and the deflection will be used to evaluate the contact force and the deflection of each rod after a fresh contact in the analysis of the three-dimensional model.

2.6.2 Deflection by a longitudinal force

So far only transverse forces on the rods have been investigated. This limitation could be justified in many cases such as a planar geometry, because transverse forces are dominant. However, for a more complicated situation having a more or less three-dimensional geometry, it might be necessary to include the contribution by longitudinal forces. When a load with multiple components is applies to the beam illustrated in Figure 2.18, its deflection may be predicted [51]

$$y(x) = C_1 + C_2 x + C_3 \sin(\sqrt{\frac{P}{EI}} x) + C_4 \cos(\sqrt{\frac{P}{EI}} x), \tag{2.26}$$

where C_1~C_4 are coefficients to be determined from the boundary conditions and P is the axial load applied to the beam.

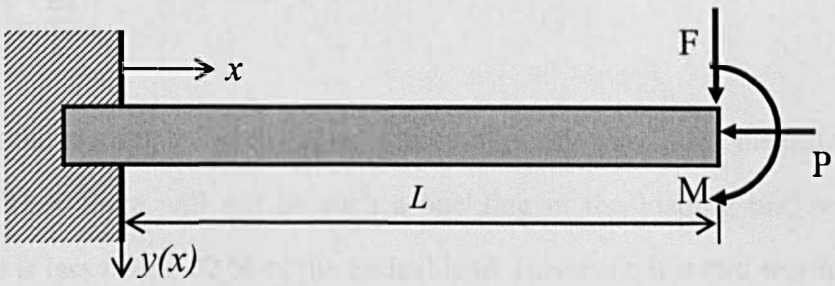

Figure 2.18 Schematic view of a beam under a multi-component load. Clamped boundary condition is applied at x = 0.

Equation (2.26) is obtained by solving a series of load-deflection differential equations which include equation (2.19). When the boundary conditions are applied to (2.26), its coefficients may be obtained. Two geometric-compatibility conditions and two load-equilibrium conditions are:

$$y = 0 \text{ and } \frac{dy}{dx} = 0 \text{ at } x = 0, \tag{2.27a}$$

$$EI\frac{d^2y}{dx^2} = -M \text{ and } \frac{d}{dx}\left(EI\frac{d^2y}{dx^2}\right) = F \text{ at } x = L. \tag{2.27b}$$

Thus the following coefficients are determined for the deflection equation (2.26).

$$C_1 = \frac{F}{P}\sqrt{\frac{EI}{P}}\tan(\sqrt{\frac{P}{EI}}L)+\frac{M}{P}\sec(\sqrt{\frac{P}{EI}}L) \tag{2.28a}$$

$$C_2 = -\frac{F}{P} \tag{2.28b}$$

$$C_3 = \frac{F\sqrt{EI}}{P\sqrt{P}} \tag{2.28c}$$

$$C_4 = -C_1. \tag{2.28d}$$

When a compressive force is applied longitudinally to a long slender beam structure, buckling can often occur. The "critical load" P_{cr} (also known as a buckling load) of a beam with built-in boundary conditions may be expressed as [51]

$$P_{cr} = \frac{\pi^2}{4}\frac{EI}{L^2}. \tag{2.29}$$

For the case of the loading bar in the current three-dimensional model, the critical load is about 13 *kN*. Thus there will not be such a buckling in the loading bar, because the maximum load is less than 0.02 % of the critical load. However, it is still worth analysing the deflection by longitudinal forces, which are evaluated to contribute about 3% to the deflection. This is the result of the current three-dimensional geometry, where a greater proportion of the force is applied in the longitudinal direction than in the case of a laminar geometry (where this proportion is negligibly small). Nevertheless, bending deflection by a transverse force is about 30 times greater than that by a longitudinal force, for this exaggerated three-dimensional geometry. Thus, one may conclude that it is not always necessary to consider the effect by a longitudinal force in the majority of situations.

2.6.3 Analysis

In the three-dimensional macro-model for an experiment, the load-bearing rod has a hooked end to bear a load, but it can be modelled as a straight rod with the appropriate force and moment at the loading location (Figure 2.19).

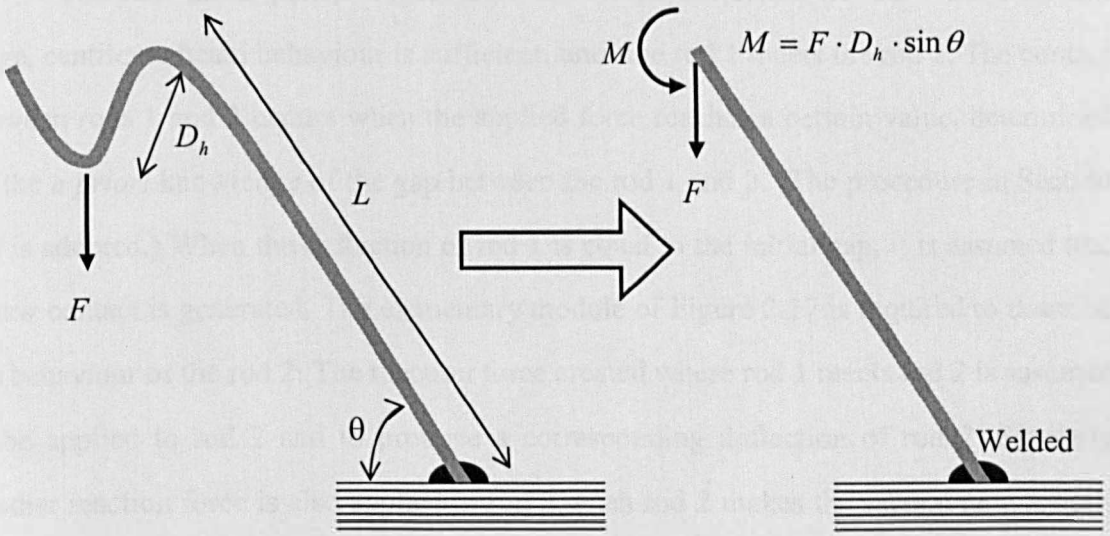

Figure 2.19 Free body diagram of the three dimensional model. The right-hand diagram shows an idealisation of the left-hand structure. A clamped boundary condition is assumed at the lower end of the rod due to a welding.

The deflection of the loading rod results from the contributions of both the force and the moment at loaded end. These contributions are denoted by δ_F and δ_M, respectively. These may be written in the following forms, where a circular cross section with a diameter of d is assumed [50, 51]:

$$\delta = (\delta_M + \delta_F)\cos\theta, \tag{2.30a}$$

$$\delta_M = \frac{M L^2}{2EI} = \frac{32 L^2}{\pi E d^4} F D_h \sin\theta, \text{ and} \tag{2.30b}$$

$$\delta_F = \frac{F \sin\theta L^3}{3EI} = \frac{64 L^3}{3\pi E d^4} F \sin\theta. \tag{2.30c}$$

Table 2.1 lists the values for L and θ. A Young's modulus of $2\times10^5\ N/mm^2$ was used. The behaviour of the loading bar (or the 3-D bulk structure) is governed by equations (2.30a~c) until a new contact occurs between the loading bar and rod 2 (the first target rod). Thus they explain the behaviour of the first region of the piecewise linear curves in Figure 2.20.

The first linear part in Figure 2.20 shows the deflection of rod 1 only. At this stage, cantilever beam behaviour is sufficient, until the rod 1 meets the rod 2. The contact between rods 1 and 2 occurs when the applied force reaches a certain value, determined by the *a priori* knowledge of the gap between the rod 1 and 2. (The procedure in Section 2.5 is adopted.) When the deflection of rod 1 is equal to the initial gap, it is assumed that a new contact is generated. The elementary module of Figure 2.17 is required to describe the behaviour of the rod 2. The reaction force created where rod 1 meets rod 2 is assumed to be applied to rod 2 and to produce a corresponding deflection of rod 2. Similarly another reaction force is also applied to rod 3 when rod 2 makes the second new contact on rod 3. Finally all three rods are connected to one another by contacts, and rod 3 moves downward according to cantilever beam behaviour because there is no further contact. Of course, the pre-determined gap between rods 2 and 3 is required to determine the load at which the second contact occurs. During the intermediate states between contacts, the forces are assumed to be invariant.

The deflection of the three-dimensional macro-model was measured under a vertical downward load, which was applied to a hanger hooked to the upper end of the loading rod. A travelling microscope with a resolution of 0.01 *mm* was used to read the deflection at each loading step. The measured results, shown in Figure 2.20, display an intrinsic non-linearity brought about by the increased number of contacts, although this is not as marked as it is in the laminar cases of Figures 2.11 and 2.15, because the rod links between contact points in the 3-D model are not long enough to produce a significant deflection (See Figure 2.16). Good agreement is noted between the measured data and prediction. However, it should be noted that a discrepancy between prediction and measurement was initially observed in the third piecewise linear region (Figure 2.21),

and hence an "adjustment" procedure was adopted to fit the measured data. In this three-dimensional situation, sliding motion between the rods was suspected of being more important than in the case of laminar structure, because of the significant tangential force inherently incurring upon contact in a three-dimensional geometry. (A plot is shown in Figure 2.21 to illustrate this behaviour, and this will be explained later in this section.)

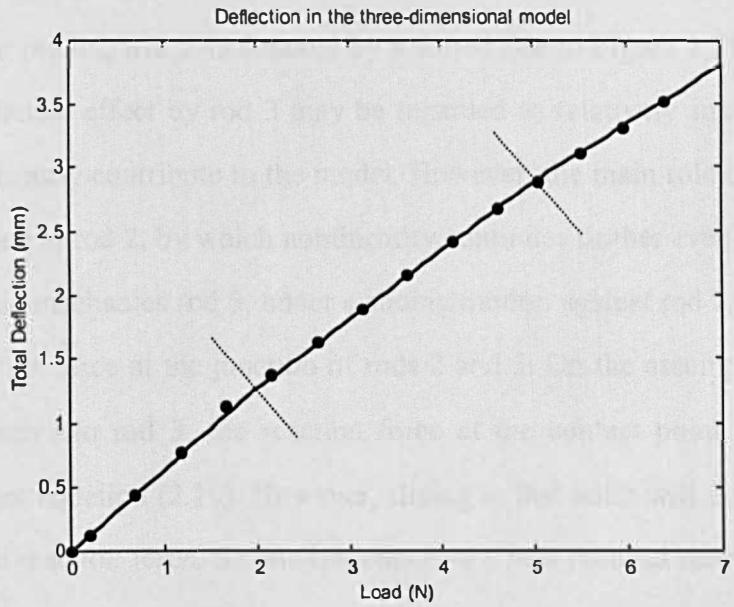

Figure 2.20 Deflection/force behaviour of the three-dimensional contact model. Circles represent the measured data and the solid line is the predicted curve. Dot lines separate three piecewise linear regions.

The aforementioned discrepancy was observed only after the second contact was made. This was thought to be caused by a possible relative sliding motion between rods 2 and 3 at their contact point. From the configuration of the 3D-contact model, it may easily be seen (although it is not certain in Figure 2.16) that the relative sliding motion is more likely to happen at the second contact than at the first contact. That is because the plane formed by rods 2 and 3, when they meet each other, is not too far from perpendicular (78°) to the bottom plate, whereas rods 1 and 2 make a plane with an angle of 58°. In the present model, therefore, the sliding effect needs to be taken into account.

The sliding process itself may be understood in the sense that sliding may be related to a reduction of resistance, not necessarily in the form of conventional friction.

For the particular geometry of the three-dimensional contact model, because of the almost upright orientation of the imaginary plane formed by rod 2 and 3, it seems likely that rod 3 would not give a significant resisting contribution to rod 2. Thus rod 2 could well move downward with little resistance, such that simply-supported contact in position *A* (see Figure 2.17) is appropriate. This could be confirmed by the fact that the third piecewise linear region in Figure 2.20 is close to a simple elongation of the second piecewise linear region, which is denoted by a dotted line in Figure 2.21. In other words, the further nonlinear effect by rod 3 may be regarded as relatively small, because rod 3 does not significantly contribute to the model. However, the main role of rod 3 is to give a small resistance to rod 2, by which nonlinearity continues further even if it is very small. In terms of static mechanics rod 3, under a sliding motion against rod 2, may be acting to reduce the contact force at the junction of rods 2 and 3. On the assumption that rod 2 is not sliding relative to rod 3, the reaction force at the contact point may be obtained analytically from equation (2.20). However, sliding at that point will eventually lead to a reduction in the reaction force. So one can conceive a new reduced reaction force, simply by the following recurrence:

$$R_a \equiv (1 - sf) R_a \quad \text{and} \quad 0 \leq sf \leq 1. \tag{2.31}$$

Here, the sf is a so-called "sliding factor", which is not necessarily a conventional coefficient of friction. It could be related to the angle of contact, however this is not pursued further. Its extreme values represent a fixed/non-sliding situation for $sf = 0$, and a non-resisting case for $sf = 1$. The latter coincides with the situation where there is no further contact and nonlinearity. According to these ideas, this simple relation would affect the behaviour of rod 2. For the current three-dimensional model, the sf was adjusted to fit the measurement data and was found to be 0.2.

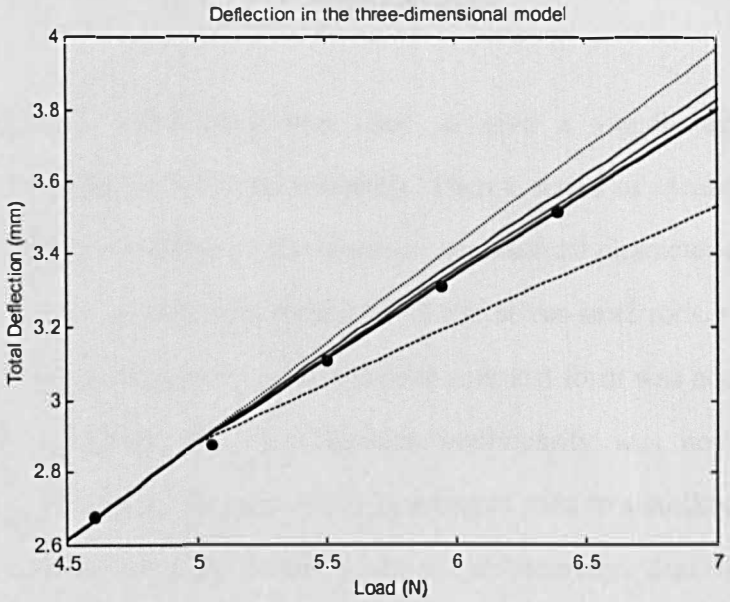

Figure 2.21 "Zoomed" plot of the third piecewise linear region of Figure 2.20. The thick solid line is the "adjusted" curve, the dashed line is the original non-adjusted curve, the dotted line represents the elongation of the second piecewise linear region (i.e., for a sliding factor of zero) and the two thin sold lines are for coefficients of friction in place of sliding factor. The one closer to the adjusted line is for a value 0.17 and the other is for 0.12.

Although the sliding factor *sf* is not a coefficient of friction, it has been found, in the case of the present model, that a coefficient of friction works quite well as the sliding factor when it is inserted in place of the sliding factor. In other words, the measured coefficient of friction obtained was quite similar in value to the adjusted sliding factor. However, it does not necessarily follow that the two are related. The same silver steel rods with a diameter of 3 *mm* were tested for their coefficient of friction. The values of 0.12 and 0.17 were obtained, based on the actual testing method. The former value was recorded when a standard 120° tip slider was used, and the latter was of the case for a round-tip slider. More information (including tip sliders) about the friction measurement is given in Section 1 of Chapter 3. It may be observed, in Figure 2.21, that both these values for the coefficient of friction produce similar nonlinear behaviour to that derived from the adjusted sliding factor.

2.7 Summary

A scanning electronic microscope was used to give a visual impression of the microstructure of cellular and fibrous materials. Then a series of idealised macroscopic models were constructed to describe the essential geometrical characteristics of a fibrous material. They were constructed by means of elastic silver-steel rods. One of them has been known as a "stacked cylinder model", whose simplest form was adopted to describe Hertzian contact deflection. But, the Hertzian nonlinearity was not regarded to be dominant due to its negligible amount. Then, bending of rods in a stacked cylinder model was investigated numerically by ANSYS and experimentally. Significant amount of deflection was confirmed in bending models, however whose linear behaviour was in contrast to a nonlinear nature of bulk fibrous materials. Such nonlinearity was taken into account by constructing "coming-to-contact models" which experienced the increase of inter-rods contacts. Two models were successively built for single and double fresh contacts. Due to their planar structures, a three-dimensional contact models was also constructed. These idealised macro-scale models confirmed that bending deflection and an increase in the number of contacts are likely to be the mechanism of nonlinear behaviour of bulk fibrous materials.

Although the several idealised macroscopic models representing the microscopic characteristic of fibrous materials produced reasonable explanations of how fibrous materials behave nonlinearly, the limitations of this approach should be highlighted at this stage, especially in the case of a realistic bulk structure. When one considers the results of Sections 2.3 (on FE analysis), 2.5 (coming-to-contact planar models) and 2.6 (the coming-to-contact three-dimensional model), it can be concluded that any attempt to describe the performance of a bulk fibrous material by means of its microscopic modular behaviour could prove extremely problematical. It was shown how computationally intensive the FE analysis is in the simulation of bending behaviour of even a simple geometry without consideration of new contacts. When new contact behaviour was included, it was necessary to know the initial gaps between structural members and the

locations of the new contacts. This process is not practically achievable for a real bulk fibrous material with a very great number of contacts. For the three dimensional models, apart from an *a priori* knowledge of gaps, the issue of the statically indeterminate nature of the problem was enough to make the situation difficult to tackle. In real bulk fibrous materials, such a statically indeterminate system could make the problem impossible to solve. This statically indeterminate issue could be related to the restriction of DOF and the large negative pivot value in FE analysis. Therefore, to understand better the structural behaviour of a bulk fibrous material, a macroscopic approach including the macroscopic parameters at the outset is believed to be more feasible than a macro-scale model of microscopic structure. This topic will be discussed in Chapter 4, in which several static models are proposed. In Chapter 3, a macro-scale approach to the microscopic structure will be further investigated particularly in respect of contact friction and electric contact resistance. Its conclusion gives further support for the macroscopic approach in Chapter 4.

Chapter 3

Contact Friction and Resistance

By means of macro-scale models with silver-steel rods, the mechanisms of structural behaviour of fibrous materials under static compression have been investigated. Bending behaviour has been identified as determining the performance of fibrous media. However, in one of models, which has a three-dimensional configuration rather than a two-dimensional or laminar structure, it has revealed that bending theory might lead to a discrepancy from what could be observed. Thus, it seems necessary to account for sliding contact between the rods. And this requires a coefficient of friction. In this chapter, first some of the theoretical background on friction is reviewed, the choice of model is explained and corresponding results are discussed.

While bending provides a dominant "linear" deflection, the increase in the number of contact between rods was found out to play a key role and to introduce "nonlinear" behaviour. Other than in an idealised model, however, it is not certain how to determine the number of contacts, let alone the exact location. For the special case of conducting fibrous materials, one may match those numbers to the electric resistance. It is a common sense that the more compressed a fibrous material, the more conducting it is. In this chapter, a review of theory for electric contact resistance is followed by a methodology for idealised structures of silver-steel rods. It will be shown how the resistance at a contact responds to the force of contact. In addition, measurements have been made on steel wool (a conducting fibrous material) to see if it is possible to extend from knowledge of the resistance of idealised contacts on a macro-scale model to the conducting properties of a bulk material.

3.1 Contact Friction

3.1.1 Review on Friction

Friction forces between two objects resist relative motion between them, and then slow the motion once the objects are moving relative to each other. The causes of friction are extremely complicated in nature. However the effects of friction in many cases can be described by simple equations with empirical constants.

There are two main types in friction. "Contact friction" is generated when one solid object is set into motion across the surface of another. "Fluid friction" is observed when a solid object moves through a fluid. Contact friction is usually represented by a coefficient of friction, and fluid friction, which is also known as a drag, is quantified by a coefficient of viscosity.

Historically, contact friction has been explained by means of three classical laws of friction. Leonardo da Vinci found that the friction is independent of the area of contact (Law of Leonardo). Amontons found that friction F_μ is proportional to the normal force (Law of Amontons) and independent of the apparent area of contact as Leonardo did. Coulomb revealed that the friction is independent of the velocity, if the speed is not too large or too small (Law of Coulomb) [53]. These classical laws of friction is mainly represented by Amontons' law,

$$F_\mu = \mu N, \tag{3.1}$$

with the coefficient of friction μ and the normal force N.

The normal force is actually a pair of forces which the objects exert on each other when they are in contact. According to Newton's third law, they are of the same magnitude and are in opposite direction normal to the contact surface. The coefficient of friction is determined by the specific conditions of the surfaces in contact. The contact friction is specified further into the static and kinetic cases. Usually it has been

recognised that the kinetic friction force is smaller than its static equivalent, and the coefficient of kinetic friction is smaller than that for static friction.

In the 1950s, Bowden and Tabor [54] established a "cohesion theory" which is also known as the adhesion model or plastic junction model. The theory postulated that the real (or true) area of contact was a small fraction of the apparent (or visible) area of contact.

Even highly polished surfaces may be regarded rough on a molecular-size scale. Such surfaces are composed of irregular asperities that comprise a very small part of the total surface area. According to the cohesion theory [54, 55], the contact is made only at the tips of these asperities. During contact, therefore it is highly likely that the pressure in the extremely small contact area is well beyond the yield strength causing plastic flow. The plastic flow enlarges the real contact area and continues until the pressure falls back below the yielding point and the normal force is supported elastically. This plastic behaviour causes the so-called cold-welding between metal objects. This is one of the causes of static friction, together with interlocking of asperities. To set the object into motion, a tangential force is required to overcome these cold-weld junctions. In this situation, Amontons' law can be generalised [56, 57],

$$F = S\,A = S\left(N/Y\right) = \left(S/Y\right)N = \mu N\,, \tag{3.2}$$

based on the shear strength S and the real contact area A, which is proportional to the normal force N and is inversely proportional to the yielding pressure Y for materials deforming plastically.

When the objects are set into motion, cold welds are supposed to be broken [53, 54]. It leads to the decrease in the amount of a cold welding and further leads to the fact that the coefficient of kinetic friction is usually smaller than that of static friction. Deformation of the asperities also explains why the friction force seems independent of the apparent contact surface (Law of Leonardo). Under the smaller contact surface, large deformations of the asperities are created microscopically. Conversely, small deformations of the asperities are generated when the larger contact surfaces are formed.

In both cases, microscopically, the real contact area is regarded essentially the same, provided that the normal force remains equal.

Due to its significance, the true area of contact deserves a further consideration. The definition of contact area and surface condition such as roughness and cleanness are some of aspects shared by the mechanical friction and electric contact, because they are established by a physical contact. The true area of contact is also preferably known as a "load bearing area" and "a-spots" especially in the electric contact. They are regarded as a sum of all these real contact spots/asperities, which actually carry a load and maintain a physical contact. As far as an electric resistance is concerned, only the portion of the load bearing area may be electrically conducting. That is because it is often composed of (quasi-) metallic area plus insulating film area. Thus, one can imagine an inequality in terms of their size, saying that a "conducting area" is usually smaller than a load-bearing area which is mostly smaller than an apparent contact area.

The load bearing area may be determined theoretically from the load between two members in contact, provided that the contact surface is perfectly clean and smooth. If the deformation at the contact junction is produced purely elastically at a load smaller than the yielding pressure of the members, the load bearing area can be evaluated. For the ideal case of two cylinders at a right angle, the radius a of a circular contact area is given by the Hertzian formula [49, 50, 58],

$$a = \sqrt[3]{\frac{3}{4} N \left(\frac{1-\nu_1^2}{E_1} + \frac{1-\nu_2^2}{E_2} \right) \Big/ \left(\frac{1}{r_1} + \frac{1}{r_2} \right)} \,, \tag{3.3}$$

and the corresponding load bearing area will be $A_b = \pi a^2$. For two cylinders in parallel contact, the half-width b of a rectangular contact area may be expressed as [49, 50, 58],

$$b = \sqrt{\frac{4N}{\pi l} \left(\frac{1-\nu_1^2}{E_1} + \frac{1-\nu_2^2}{E_2} \right) \Big/ \left(\frac{1}{r_1} + \frac{1}{r_2} \right)} \,, \tag{3.4}$$

The corresponding load bearing area will be $A_b = 2\pi bl$. Here N is the contact force generated between two members with radius r distinguished by subscript 1 and 2. The Poisson's ratio and Young's modulus are denoted by ν and E, respectively. The length

of the cylinder is indicated by l. However, when the load is large enough to produce a permanent deformation even after the removal of a force, the elastic behaviour implied by Hertz formula is no longer valid. Instead, if the hardness H of a material is known, the load N may be related to its load bearing area A_b as follows [58],

$$N = \xi H A_b . \tag{3.5}$$

Any value of ξ between 0 and 1 is possible.

In many cases, Amontons' law is known to hold for metals [54]. However failure of Amontons' law has been reported in the textile industry [55, 56, 57, 59]. For materials with a high elastic modulus such as metals, a plastic flow is experienced on microscopic asperities because the elastic deformation is not enough to enlarge the real contact area. This case can be analysed according to the Amontons' law. However, for materials with a relatively lower elastic modulus, the elastic deformation may be regarded enough to secure enlarged contact area. In this case, the contact area is related to the normal force raised to some exponent. It is straightforward to find out, from equations (3.3) and (3.4), that the contact area is related to $N^{2/3}$ for two cylinders at a right angle and to $N^{1/2}$ for two parallel cylinders. Thus, for non-metals, Amontons' law may be replaced by a new empirical relationship of

$$F = S A \propto S N^n = c N^n , \tag{3.6}$$

with adjustable constants c and n [55, 56, 57, 59]. Amontons' law corresponds to special case of $n = 1$ (See also equation (3.5) for $A \sim N^1$) for materials with plastically-deforming asperities such as metals.

Silver steels, which are the subject of this chapter, are known to have a high elastic modulus which makes the Amontons' law applicable.

3.1.2 Measurement method

The coefficient of kinetic friction for a pair of materials may be measured through a system of a block and a plane, in which a block with a mass slides down an inclined plane [53]. The critical angle at which the block slides down the plane at constant speed can be related to the coefficient of kinetic friction. The coefficient of static friction may be measured in a similar way in terms of the angle just before the motion starts.

However, because of their cylindrical shape, the traditional method is inappropriate for measuring the coefficient of friction for silver steel rods which constructed the idealised macro-scale model described in Chapter 2. Instead, a so-called "friction and scratch hardness apparatus" well established in the surface-engineering area has been adopted [60].

The apparatus consists of a pivoted beam, a counterbalance, slider, load cell, weight platform, and moving stage. It is represented schematically in Figure 3.1. Weights are placed on to the weight platform which is connected vertically to the slider and horizontally to the load cell. The weight platform is joined with the pivoted beam proper through the load cell located inside the beam. The beam is pivoted by roller bearings and supported by upright structure and hence is allowed to rotate and to move vertically to adjust its height. The specimen is clamped horizontally on to the stage which is mounted on a traverse basement. The basement is driven by an electric motor via a worm and nut system. Thus the slider connected to the load cell and beam proper is fixed and the specimen on the moving stage is travelling horizontally and reciprocally. The weight, slider and specimen are lined vertically to make sure that the load is transmitted along the vertical axis through the contact formed by the slider and specimen.

Before the main round of the tests, the load cell needs to be calibrated. During this procedure, it is not necessary for the specimen and slide to be present. The weight platform is set horizontal. Usually the slider is replaced by a screw to which a nylon string is tied. The signal from the load cell is recorded when weights are applied downward to the string passing over a pulley wheel.

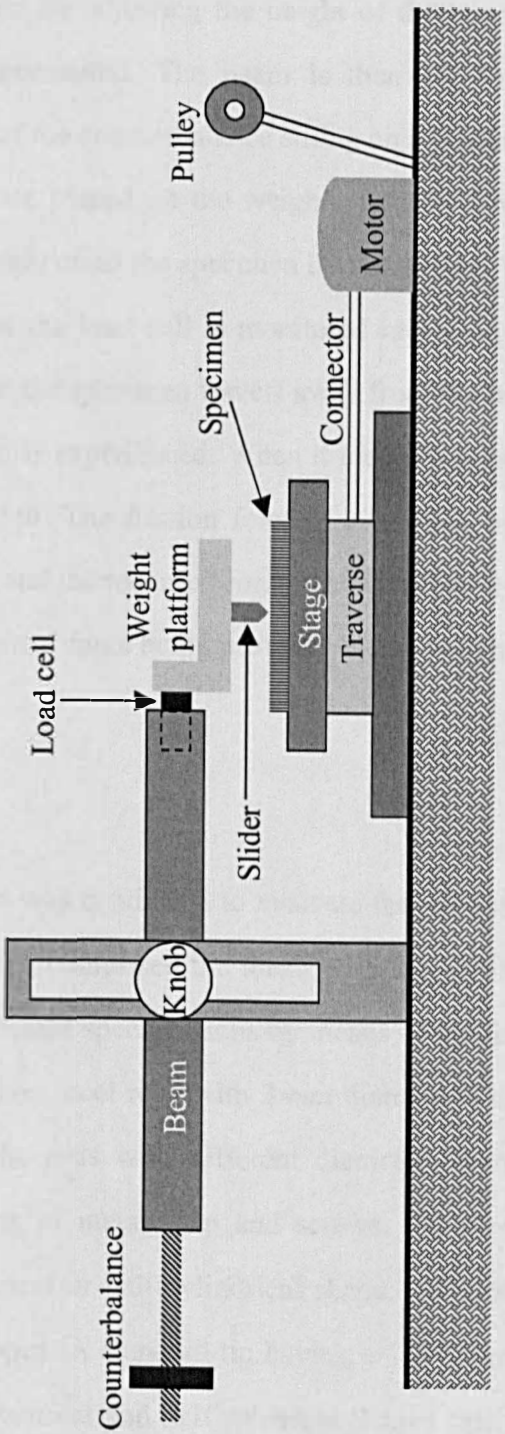

Figure 3.1 Schematic diagram for the friction and scratch hardness apparatus. More details are given elsewhere [60].

During the main test, the specimen is clamped on to the horizontal stage. The slider is set normal to the specimen by adjusting the height of the beam. A spirit level is used to check whether it is horizontal. The beam is then pivot-tightened and balanced by adjusting the distance of the counterbalance sitting on a treaded rod. Loads are applied by metal weights which are placed on the weight platform directly above the slider. The slider is then placed softly on to the specimen by the weight. Then, the motor is activated. The output signal from the load cell is monitored into a digital oscilloscope through a charge amplifier. When the specimen travels away from the beam and parallel to the axis of the load cell, tension is experienced. When it moves toward the beam, compression is recorded by the load cell. The friction force is quantified by comparing the calibrated data from the load cell and the recorded force. The coefficient of friction is obtained from Amontons' law, the normal force being provided by the weight.

3.1.3 Analysis

A friction measurement was conducted to evaluate the friction coefficient on the surface of silver-steel rods which comprised the idealised macro-scale models. A series of tests were followed with different specifications by means of the friction and scratch hardness apparatus. Although silver steel rods with 3 *mm* diameter were used in the construction of the idealised models, rods with different diameters were also clamped on to the moving stage by means of metal strip and screws. Samples were of 3, 6, 9, 12 *mm* diameter with a cylindrical or half-cylindrical shape. Sliders were also chosen to have various types of tip shapes. A standard tip having a 120° conical end was used together with sliders with a cylindrical and half-spherical shaped tips. For the latter two sliders, the dimension of the tips was adjusted to have the same radius of the specimen. The same material of silver steel was selected for the sliders. Two different distances for the moving specimen were tried. The shorter travelling distance was about 11 *mm*, and the longer distance was of 27 *mm*. However, the travelling speed of the specimen was not

varied, to have a fixed speed of about 3.7 *mm/s*. This represents an averaged speed, because the reciprocal movement hinders the instantaneous speed from being constant.

A series of measurements with different specifications were accomplished. Although the results were not identical, there were no significant differences among them. However, a considerable consistency has not been observed between the various specifications of measurements.

Some data are displayed in Figure 3.2. Generally, periodical peaks were recorded. The peak indicates the static-friction required to break the cold welding, but the corresponding value of its coefficient evaluated from these data is often more than unity. This is also reported for a certain pairs of contact surfaces for the coefficient of static friction [53]. The normal force, which is exerted by the weight on the platform, ranged from 0.5 to 2.5 N in steps of 0.5 N. As expected, there was no significant difference monitored, depending on the normal force in terms of the coefficient of friction. (The results for different normal forces are not shown here. Only the 2.5 N case is presented). Oscillations in the data in some plots may be related to successive measurements on the same specimen. Often they were accompanied by an audible high-frequency noise. Thus the contact areas of the specimens were consistently relocated and the surface was polished with a soft cloth soaked with acetone to reduce the symptom. In this noisy situation, the peaks were also observed to have a bigger value than usual, and hence were conjectured to be related to the surface roughness.

The plots (a) and (b) in Figure 3.2 shows results obtained by using several rods with different diameter as specimens. A consistent pattern is not easy to recognise. At a glance, the coefficient seems to increase as the diameter increases, but for the 12 *mm* rod, this trend is overturned. Secondly in the plots (a) and (c), the effect of using different tips on the slider are presented. For a 3-*mm* diameter rod, in this example, the cylindrically-tipped slider seems to produce a significantly bigger friction coefficient. But for 6-*mm* diameter rod, however, the difference is not repeated. Instead, the cylindrical tip makes more wiggles in the data. It may be because more contact areas are involved for the cylindrical and spherical tip than for the standard 120° conical tip slider. Although the

size of the contact area does not affect the value of the coefficient in the ideal situation, in reality it may produce such wiggles or unstable data. Therefore, the patterns may be said to be similar to one another without regard to the types of tips. The plots (a) and (d) presents the behaviour for two different moving distances. It is observed that the coefficient of kinetic friction is not constant during the sliding and is gradually decreasing after reaching its maximum. This is the case for the longer travelling distance. However, for the shorter-distance, the values seem to be more stable. Therefore, representative values for the coefficient of kinetic friction were evaluated, using the higher values for the longer distance and the stable values for the shorter distance, both of which yield a similar value. It may be reasonable to say the coefficient of kinetic friction is about between 0.1 to 0.2 depending on the cases selected. Figure 3.3 gives an enlarged view of Figure 3.2. Overall compromise values were deduced as 0.12 or 0.17 from the averaged combination of several other cases, which are not presented here. They were used as the friction coefficient when evaluating the behaviour of the three-dimensional model described in Section 6 of Chapter 2.

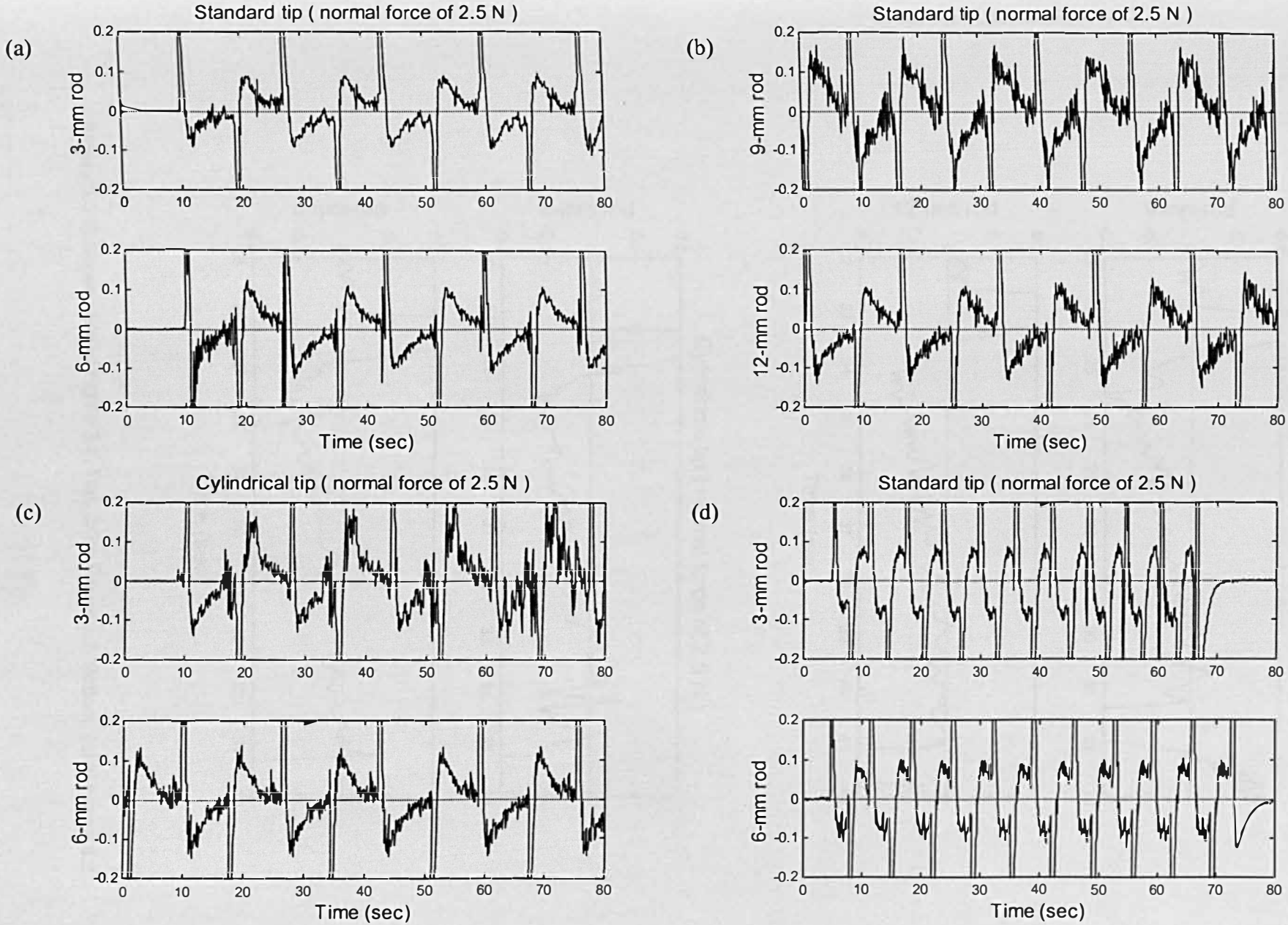

Figure 3.2 Friction coefficient of silver-steel rods. Effect of different diameter (a and b), slider tip (a and c), and travelling distance (a and d) is illustrated.

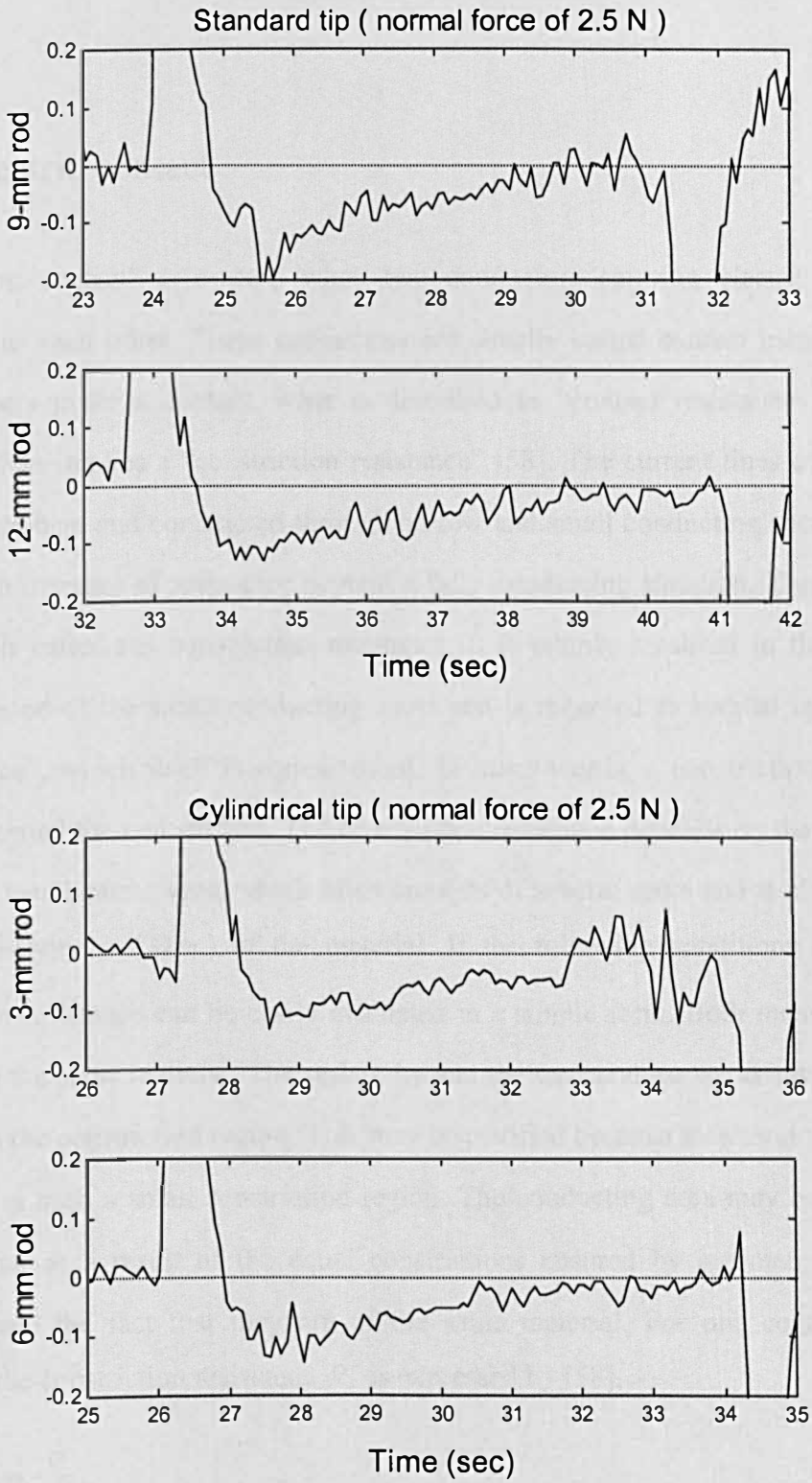

Figure 3.3 Enlarged view of Figure 3.2. Top, (b) in Figure 3.2; Bottom, (c) in Figure 3.2.

3.2 Contact Resistance

3.2.1 Electric contact

An "electric contact" is created when two conductors carrying electric current are connected to each other. These conductors are usually called contact members. When two members make a contact, what is described as "contact resistance" in an ideal situation often implies a "constriction resistance" [58]. The current lines of flow in the members are bent and constricted through narrow and small conducting spots and hence it causes an increase of resistance beyond a fully conducting situation. This increase of resistance is called the constriction resistance. It is mainly localised in the immediate neighbourhood of the small conducting spots and is regarded as limited by a so-called "end surface", which itself is equipotential. In other words, a constriction is assumed unlikely beyond the end surface. The constriction resistance depends on the size and the shape of a load bearing area, which often consists of several spots and is also a function of the resistivity ρ (Ωm) of the material. If the following conditions are met, the constriction resistance can be easily evaluated in a simple form. Both members may be selected as the same material. The resistivity and the temperature are assumed to remain constant in the constriction region. This may be justified because structural variations are negligible in such a small constriction region. The conducting area may be regarded as equipotential as a result of the equal constrictions ensured by symmetry of the two members and the fact that they are of the same material. For one contact member, therefore, the constriction resistance R_c is expressed by [58],

$$R_c = \frac{\rho}{4a}, \tag{3.7}$$

assuming a flat circular contact area with a radius a.

In addition to the constriction resistance, an alien film in the contact may contribute to an additional resistance called a "film resistance" R_f [58],

$$R_f = \frac{\sigma_f}{A_{cd}} = \frac{\rho_f t}{A_{cd}}. \tag{3.8}$$

The film may be characterised by its resistance σ_f, resistivity ρ_f, and thickness t, when it is assumed to prevail uniformly throughout the conducting area A_{cd}, which is smaller than the load bearing area in the presence of an alien film.

Therefore the contact resistance R_{ct}, in a practical situation, is likely to consist of both a constriction resistance R_c and a film resistance R_f. Since the constriction extends into both contact members, then

$$R_{ct} = R_{c1} + R_{c2} + R_f. \tag{3.9}$$

When a film resistance is present, the constriction resistance in both members, R_{c1} and R_{c2}, are not quite independent of R_f, because the presence of alien films affects the real conducting area related to the constriction. If two cylindrical contact members are chosen as the ones with same material and same diameter, the total constriction resistance will be simply twice as that in equation (3.7),

$$R_c = \frac{\rho}{2a}, \tag{3.10}$$

when the effect of R_f is negligible. This is for an ideal situation with a whole conducting area composed of a single, preferably circular, spot. However, for a realistic situation where there are several a-spots, the constriction resistance will be defined in a different way.

The load bearing area may be calculated, from the measured electric resistance (3.10), when the load is small enough to create only an elastic deformation and the area is ideally clean and smooth, and circular or elliptical. However, only measurements in vacuum have been reported to confirm the Hertzian deformation [58]. In air, metals are supposed to be covered by layers of oxygen, which increase the resistance. Moreover in reality, the surfaces are likely to have thick alien films, which contribute to the increase of observed resistance and hamper the evaluation of a load bearing area according to the Hertz formula. Thus, a cleaning procedure should precede the measurement of electric

contact. Thick alien films such as grease or lubricants can be removed by using a volatile liquid such as acetone. A metallic surface can also be cleaned by the aid of heating in vacuum and by the means of ultrasonic cleaning.

3.2.2 Single cross-rod contact

As a modular test on the electric contact resistance, a cross rod contact is often investigated [58]. Two cylinders, preferably with a same diameter, with a same conducting material are chosen and placed crosswise to produce a reasonable symmetry having a circular contact surface.

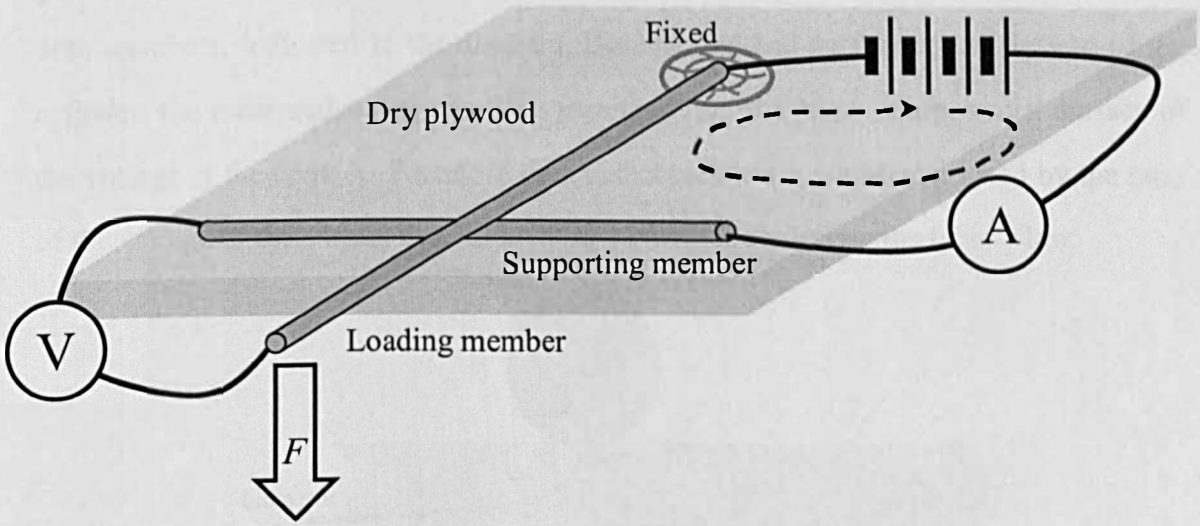

Figure 3.4 Schematic measurement setting of a cross-rod contact situation and its circuit diagram with a loading force.

In the situation of cross-rod contact, a system may be mechanically constructed and electrically wired, which is shown in the schematic diagram in Figure 3.4. 'A' and 'V' denote a current and voltage meters, which were replaced by two separate multimeters The particular multimeter used (Thurlby 1905 intelligent multimeter) has precisions of $1\mu V$, $1nA$ and $1m\Omega$ for voltage, current and resistance measurements, respectively. Although the internal resistance of the multimeter is not known, the value is assumed to be negligible. The electric circuit is formed to have its current flow around

the dashed line in the direction of the arrow. The electrical source was a $1.5V$ dry battery. Electric cables of a type usually deployed in an audio system were used. Wires were soldered to the ends of the rod. To produce a variable load at the contact, the loading member is clamped at one end and is supported at the contact by a supporting member. A series of weights are placed at the other end of the loading member. The contact force is evaluated as the reaction force at the contact.

When the contact is made, the electric circuit generates the equipotential surfaces in each cylinder, illustrated in Figure 3.5. In the immediate neighbourhood of the contact area, the equipotential surfaces are likely to be concentric ellipsoids. But, beyond this, the surface A_e in the diagram may be regarded as the end surface of the constriction generated in the cross rod contact. The voltage will be measured between the ends of both members, indicated in the diagram. Because the end surface meets the end of the cylinder, the measured voltage will be essentially on the same equipotential surface of the voltage at the contact. Therefore the contact resistance can be evaluated by the ratio of the voltage to the current measured in the system, according to the Ohm's law.

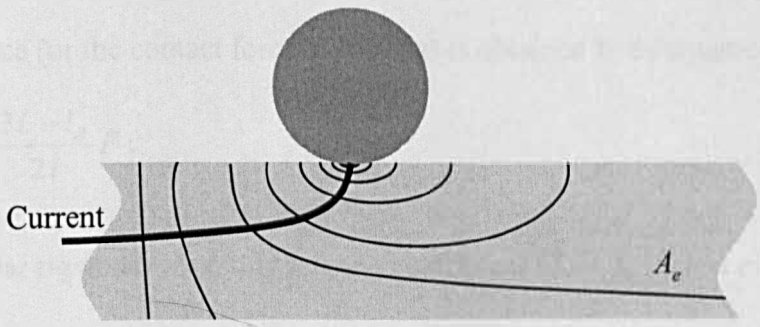

Figure 3.5 Equipotential surface in the contact area of crossed rods. Thin lines represent equipotential surfaces, and A_e is the end surface, which extends to a voltage meter. The thick line is the path of the current flow and is extended to a current meter.

To evaluate how the contact resistance is related to the varying contact force, it is necessary to (a) measure the resistivity of the conducting member, (b) calculate the contact force from a load, and (c) find out how the load bearing area is changed according to the contact force.

(a) To evaluate the electrical resistivity ρ, the voltage and the current across a single rod were measured in a simple circuit (which is not shown here) where wires are connected to both ends of the rod. The resistance R_{rod} was obtained by the ratio of the measured voltage drop to the current, and the resistivity was obtained by [53],

$$R_{rod} = \frac{\rho \cdot L_{rod}}{A_{rod}}, \tag{3.11}$$

where L_{rod} is the length of the rod, A_{rod} is the cross-sectional area of the rod. The value of 20.7×10^{-8} Ωm was obtained for the particular silver-steel rod used in the system. The 330 *mm*-long rod with 3-*mm* diameter was installed, so it was assumed that the lines of current flow were parallel and the equipotential lines were perpendicular to the length and hence the potential constriction was localised to each end of the rod and was negligible.

(b) In the measurement, the weights were hung at the end of a loading rod and they produced the contact force between two rods. A free-body-diagram associated with the loading rod is seen in Figure 3.6, which is similar to the situation in Figure 2.17. Thus, the reaction force (or the contact force of this rig) is obtained from equation (2.20),

$$R_l = \frac{3L - l_R}{2l} F. \tag{3.12}$$

For the particular rig under investigation, the coefficient $(3L - l_R)/2l$ is evaluated as 2.04.

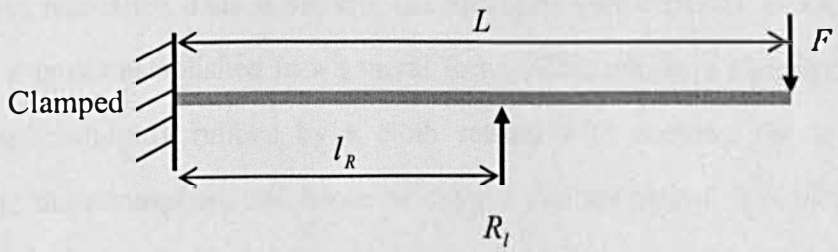

Figure 3.6 Free body diagram of a cantilever beam which is featured in the particular setting of a cross rod contact situation.

(c) Based on the equation (3.3), the radius a of the circular Hertzian contact area can be further simplified into,

$$a = \sqrt[3]{\frac{3d(1-\nu^2)R_l}{8E}}, \tag{3.13}$$

for two identical contact cylinders of diameter d . ν is the Poisson's ratio, E is the Young's modulus.

These results together with the equation for the constriction resistance (3.7) lead to the dependence of the resistance R on the load F given by,

$$R \propto F^{-1/3}. \tag{3.14a}$$

When the indentation behaves plastically, the load bearing will be related to the hardness of a material (3.5). The resistance-load dependence is,

$$R \propto F^{-1/2}. \tag{3.14b}$$

Thus, regardless of an elastic or plastic deformation, it is possible to evaluate the qualitative dependence of the constriction resistance on the contact force as long as the surface is smooth and clean.

Finally, in Figures 3.7 and 3.8 are the result of the experiment and corresponding calculation. Different points are allocated for several readings of measurement. Each reading seems to be fluctuating especially for lower loads, but a stable dependency is observed across several readings. The solid line is for the predicted resistance. A significant discrepancy is observed. In fact the calculated resistance is only the constriction resistance. That is because the film resistance depends on a specific situation and thus it is not established in a general form. Although, as a cleaning procedure, the rods were thoroughly rubbed by a cloth soaked with acetone, the tested rods were exposed to the atmosphere and hence to oxygen contamination. It is likely also that the surfaces are not perfectly smooth and with a lot of asperities. In this situation, the constriction resistance should be evaluated by [58],

$$R_c = \frac{\rho}{4\sum a_a} \tag{3.15}$$

with the radii a_a of each a-spot, which is usually smaller than the circular contact area of a Hertzian contact. This will increase the constriction resistance by a significant amount. Without knowledge of a microstructure of the surface, it is impractical to determine the number and size of all the a-spots. Nevertheless, the effects induced by films and asperities are believed to cause the discrepancy.

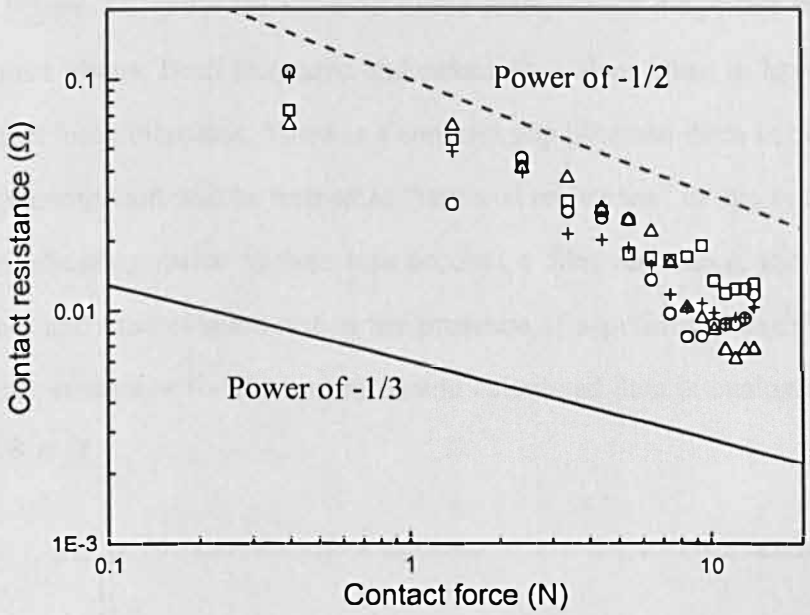

Figure 3.7 Contact resistance in the log-log domain for a cross rod contact situation. Discrete symbols are obtained by different sets of measurements. The solid line is of a prediction of a constriction resistance for elastic deformation. The dashed line shows only the slope of a constriction resistance for plastic deformation.

In Figure 3.7, where results are plotted as log-log domain, the solid line shows the power of -1/3 dependence between the resistance and the load predicted for elastic deformation by equation (3.14a). The dashed line shows the power-law of -1/2 dependence between resistance and load for plastic deformation predicted by equation (3.14b). In terms of magnitude, the solid line is actually predicted by the combination of equations (3.10) and (3.13). But, the dashed line is shifted arbitrarily to a location in the plot where the power dependence is easily identified, because the parameter ξ is not known in equation (3.5). The data for lower loads seems to fall between these two slopes, but to be closer to the power of -1/2. This finding of a plastic behaviour also justifies the use of Amontons' law for the silver-steel rods in Section 3.1. Recall that the normal force

in the friction test was varied from 0.5 to 2.5 N, and in this range the measured resistances seem to follow the power of -1/2 in Figure 3.7. However, under higher loads, the measured resistance is seen to deviate significantly from either power-law dependence. The reason is not clear apart from that the extra resistances may play a bigger role at higher loads than at lower loads.

In Figure 3.8, plots are made in linear scale, which magnifies the behaviour for higher contact forces. Both measured and calculated values seem to have a similar trend as the contact force increases. There is a constant gap between them in higher loads. This empirical phenomenon will be termed as "terminal resistance" in this section, and will be used as an adjusting factor to take into account a film resistance, the effect of plastic deformation, and the deviation due to the presence of asperities. The difference between the terminal resistances for the measured and calculated data is evaluated, ranging from 6.35 to 7.98 $m\Omega$.

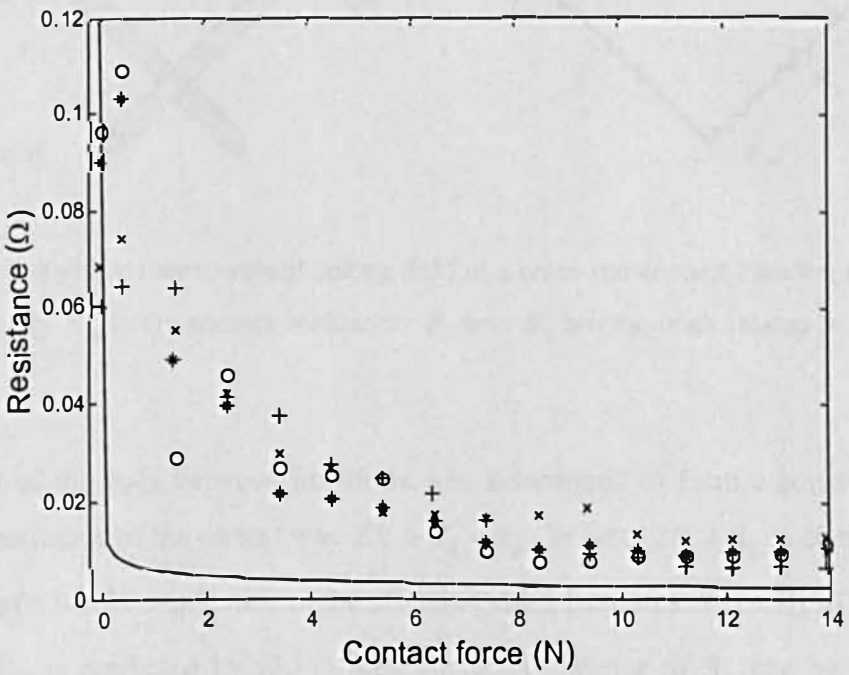

Figure 3.8 Linear scale representation of Figure 3.7. The line conforms with the solid line in the previous figure.

3.2.3 A network of cross-rod contact

As an extension of a single cross rod contact, a four-junction network was constructed by the use of four silver-steel rods placed in the form of a square with four electric contacts. The corresponding resistance was measured when it was wired through a voltage and ampere meters to a battery. The contact force for each contact point was evaluated as a quarter of the weights on a dry wooden plate which was placed on the top of the circuit members. A schematic view of arrangement is drawn in Figure 3.9 together with the corresponding circuit diagram.

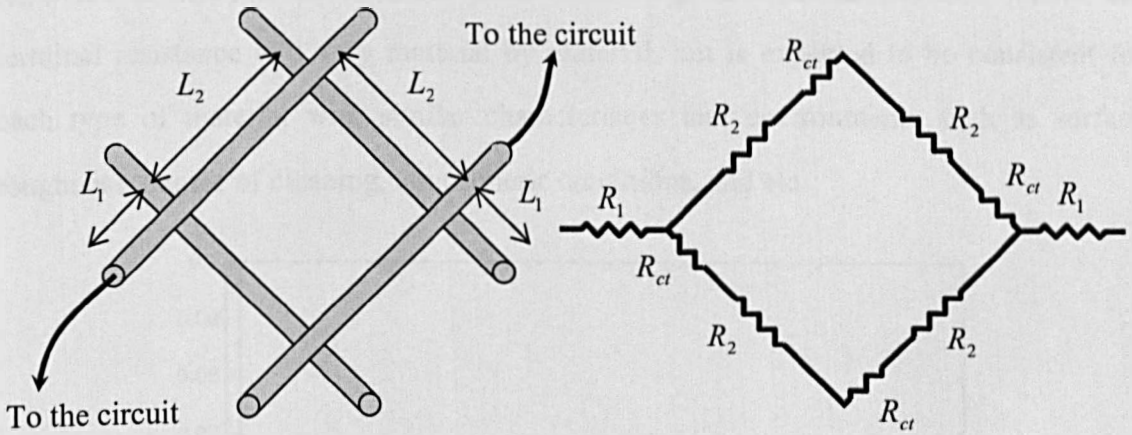

Figure 3.9 Schematic measurement setting (left) of a cross rod contact situation and its circuit diagram (right). R_{ct} is the contact resistance. R_1 and R_2 are the ones related to the length of rods.

The length of the rods between junctions was determined to form a square so that the effective resistance of the circuit was $2R_1 + R_2 + R_{ct}$. In fact, $2R_1 + R_2$ is equivalent to the resistance of a whole single rod, so the effective value becomes $R_{rod} + R_{ct}$. The resistance of a rod R_{rod} is predicted by (3.11). The contact resistance of R_{ct} can be predicted by equation (3.9), if the constriction resistance and film resistance are known. However, the results of the measurements on a single rod contact suggest that these resistances are not predicted accurately. The corresponding discrepancy was treated as a terminal resistance at a higher load.

In the result for the network resistance in Figure 3.10, an overall discrepancy, denoted by a dashed line, is initially found throughout the loads. Measured data fluctuate for lower loads, but become stable in the higher load region, where the terminal resistance is observed as introduced in the previous section. After accounting for the terminal resistance, a good agreement, represented by a solid line, is achieved for the higher loads. A value of 7.0 $m\Omega$ from the previous section was adopted for the contact. It was found that the discrepancy was between 6.88 and 7.18 $m\Omega$, in this four-junction test. These results justify the use of terminal resistance to take into account the non-constriction resistance for a structure of silver steel rods. The concept of a terminal resistance is likely to be valid for other conducting materials as well. Of course, the terminal resistance will vary material by material, but is expected to be consistent for each type of material with similar characteristics and environments such as surface roughness, degree of cleaning, atmospheric conditions, and etc.

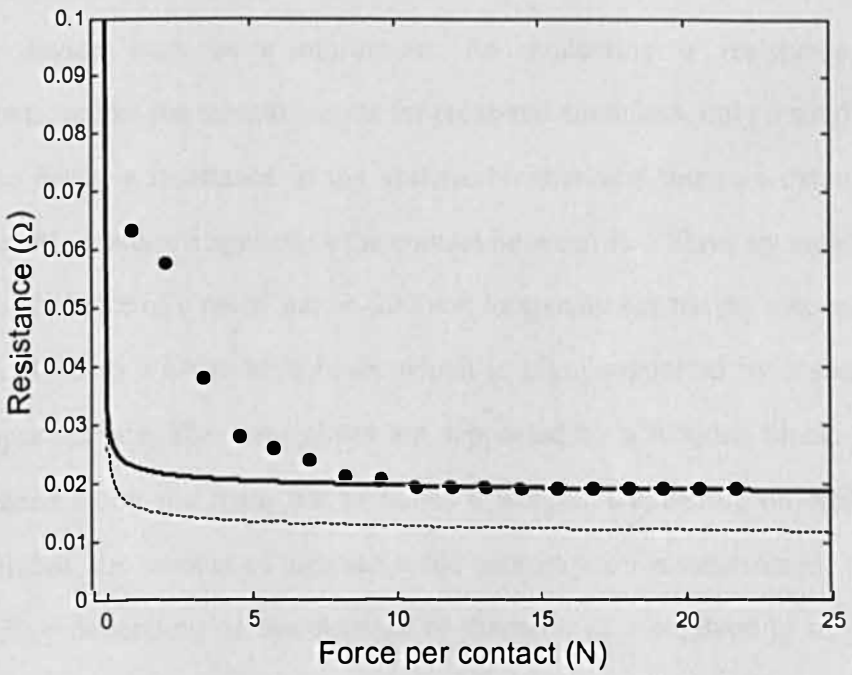

Figure 3.10 Measured and predicted resistance of a four-junction network of rods. The filled circles represent the data. The dashed line represents the constriction resistance prediction only. The solid line is the prediction after including "terminal resistance".

3.2.4 Single fibre conductivity test

As a result of the findings with the silver-steel rod models, it is clear that the contact resistance is a function of a contact force. When a bulk fibrous material is under compression, the contact force at each contact point is supposed to change and so does the contact resistance. Information on how the contact force and resistance are related to a real single fibre of a conducting bulk fibrous material is necessary to work out the number of inter-fibre contacts by means of resistance. However, the "variable" contact resistance is one of major difficulties when it comes to the understanding of the structure of a bulk fibrous material in terms of a resistance.

For this purpose, a rig has been designed to measure the contact resistance of single fibres. It is mainly composed of bronze bars with a diameter of 1.6 *mm* and supporting blocks as depicted in Figure 3.11. Electric current is supposed to travel through the metal bars and the contact between the test wires in order to reach a measuring device such as a multimeter for evaluating a resistance. For these measurements, unlike the measurements for cross-rod situations, only a single multimeter was used to detect a resistance in the system. Neither was there an external electrical source. Variable loads are applied to the contact between two fibres by means of a knife-edge pivoted balance of a metal bar. A 200-*mm* long main bar having a counterbalance at one end is glued to a knife-edge blade which is pivot-supported by a steel plate with smooth upper surface. The steel plates are supported by a wooden block. Grooves are equally spaced along the main bar to house a weight. Depending on which groove a weight is placed, the amount of the load at the contact point is determined. Weights of 1, 5, 20 and 50 g depending on the strength or diameter of a conducting subject (fibre or wire) were placed and shifted along the grooves of the main bar. Near the other end of the main bar, a three-soled bronze frame is soldered to accommodate a conducting subject stretched at both ends. Another three-soled bronze frame, holding a conducting subject is fixed on a wooden block at right-angles and face-to-face to the upper frame making contact between the test subjects.

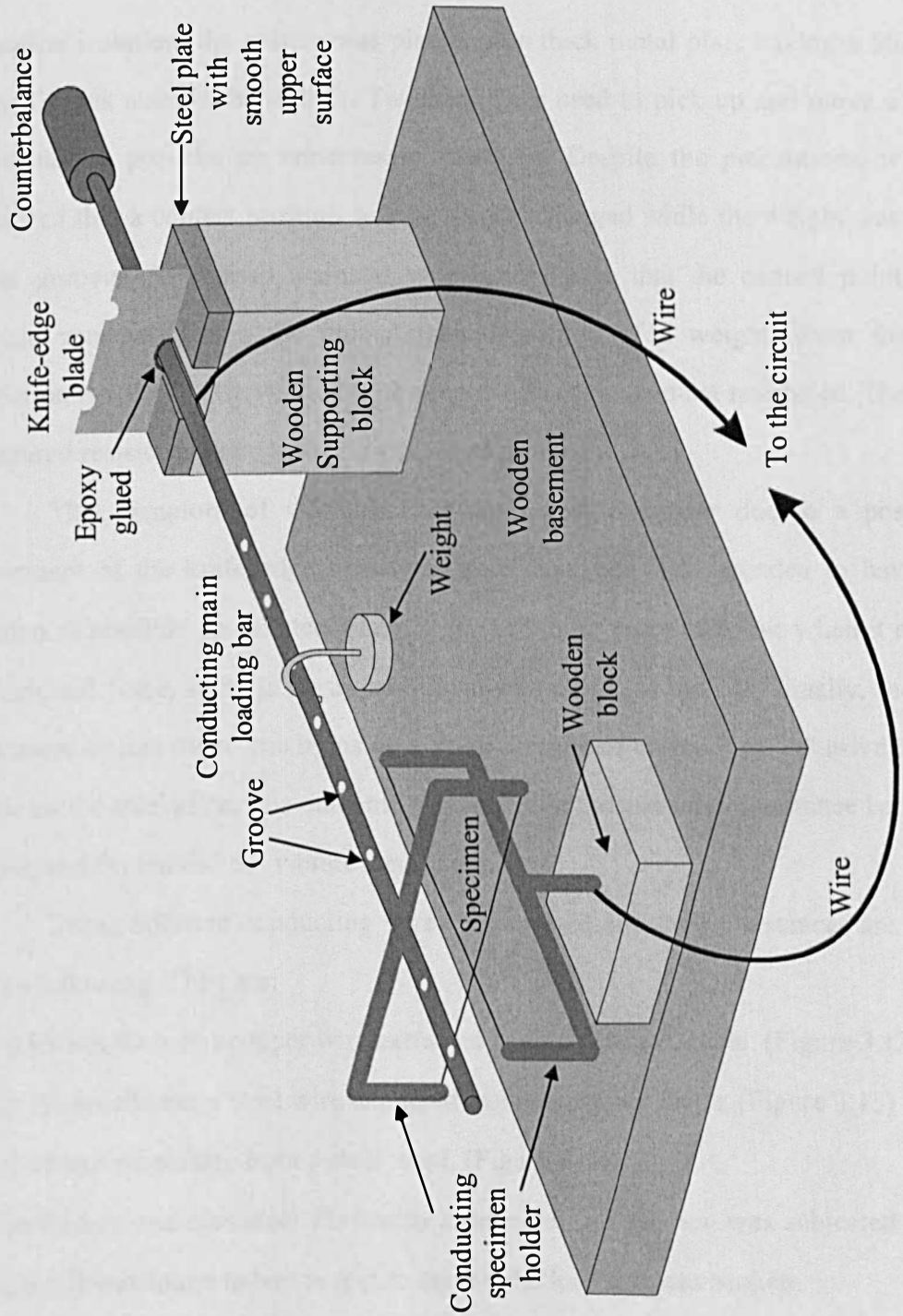

Figure 3.11 Schematic bird's eye view of a single-fibre conductivity test rig. The wooden supporting blocks are not glued to the wooden basement to allow positions to be adjusted.

In the experiment, however, when a conducting fibres or wires were placed to make contact with each other, the main bar was observed to vibrate. As a method of vibration isolation, the system was placed on a thick metal plate having a 50-*mm* thick glass fibrous material beneath it. Tweezers were used to pick up and move a weight in order not to provoke an unnecessary vibration. Despite the precautions, it has been observed that a contact position was frequently changed while the weight was moved to other grooves. The small diameter wire used means that the contact point does not remain constant during the unloading and loading of a weight. Even the slightest deviation has been observed to make a big difference in contact resistance. Therefore the measured resistance were unstable and unrepeatable.

This symptom of vibration was suspected to appear due to a possible free movement of the knife edge blade. Because the blade was intended to have as little friction as possible on the steel plate, it seemed to be prone to move when it exposed to an external force, such as an up-and-down movement of the bar. Finally, the problem was more or less overcome by using a small amount of epoxy resin adhesive to hold the blade on the steel plate. The outcome was such that the measured resistance became more stable, and the bar did not vibrate significantly.

Three different conducting wires were tested and their resistances are illustrated in the following. They are:

1) 0.85-*mm* diameter copper wire extracted from an electric cable. (Figure 3.12)
2) 0.19-*mm* diameter steel wire extracted from an electric cable. (Figure 3.13)
3) 0.08-*mm* steel fibre from a steel wool. (Figure 3.14)

Much thinner stainless-steel fibre with a diameter of 0.02 *mm* was subjected to the test also, but it was found to be too thin to endure the load and was broken.

In Figure 3.12 the "total resistance" label of the ordinate means that the value is not for the contact resistance only, but of the whole circuit. As stated before, the internal resistance of a multimeter is assumed to be negligible. Despite the fact that the contact resistance is of interest, it is worth displaying the total resistance measured in the system because, in reality, the contact resistance is not the only factor to be captured in an

electric circuit of a material. However, if any variability depending on a load were observed, it would be related to the contact resistance rather than other types of resistance related to the structure of the measuring rig, which is supposed to be constant. So, the behaviour of contact resistance could be identified easily.

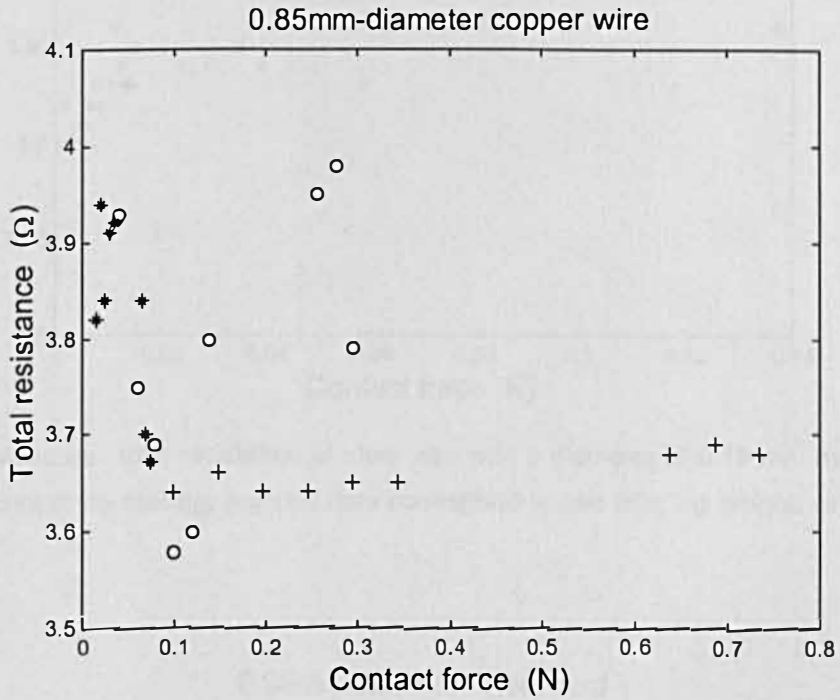

Figure 3.12 Measured total resistance of a copper wire with a diameter of 0.85 *mm* by means of a single fibre conductivity test rig. Asterisk data correspond to use of a 1-*g* weight; circle, 5-*g*; and cross, 20-*g*.

As expected, for the copper wire, the resistance seems to decrease with contact force when the load is small. Some abruptly high values (circles) in Figures 3.12 and 3.13 may be related to an unwanted change in the contact position when a weight is shifted. However at high loads, the contact resistance appears to be practically invariant for both the 0.85-*mm* copper and 0.19-*mm* steel wires. The data for the 0.08-*mm* steel wool shown in Figure 3.14 seems to decrease monotonously with increasing load but the associated contact forces are much smaller than those used with the other two. The 0.15 Ω reduction for 0.01 *N* increase in force is large compared with the 0.1 Ω change in about 10 *N* for the 3-*mm* silver steel test (Figure 3.8). But, provided that the resistivity is similar, it seems to be related to the fact that the contact area of steel wool is much

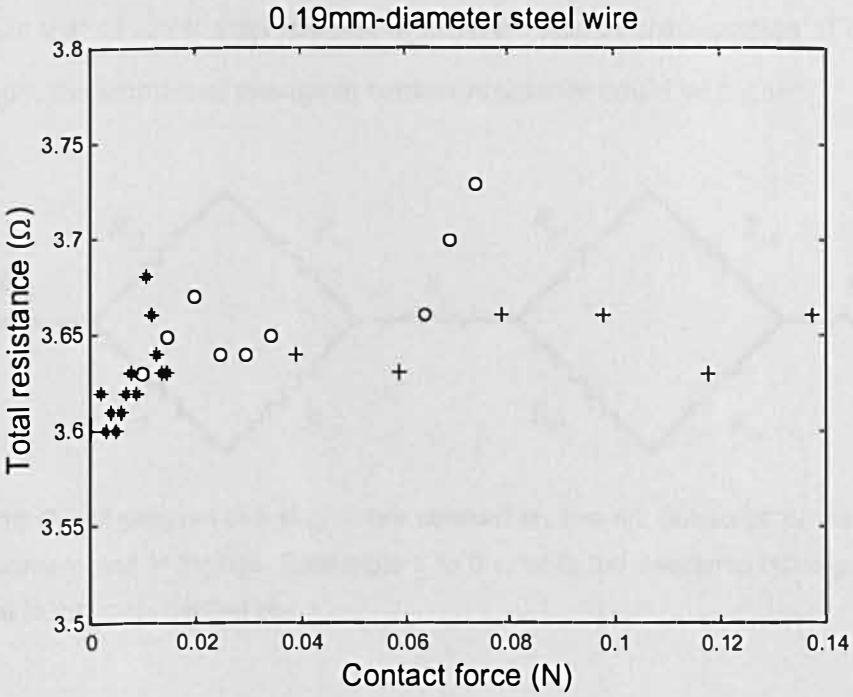

Figure 3.13 Measured total resistance of steel wire with a diameter of 0.19 *mm* by means of a single fibre conductivity test rig. Asterisk data correspond to use of a 1-*g* weight; circle, 5-*g*; and cross, 20-*g*.

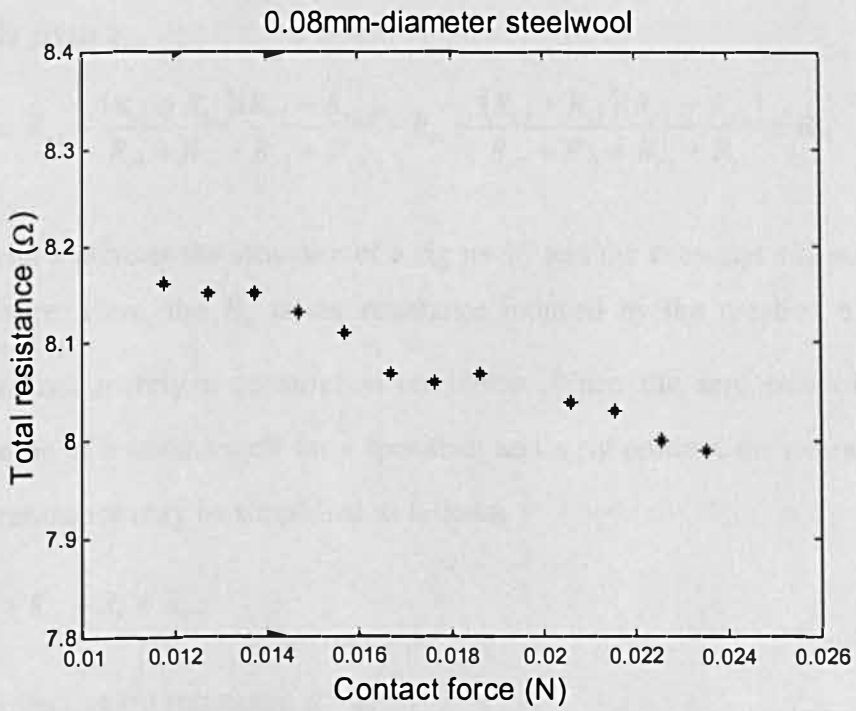

Figure 3.14 Measured total resistance of steel wool with a diameter of 0.08 *mm* by means of a single fibre conductivity test rig. Only a 1-*g* weight was used.

smaller than that of silver steel rod due to different size of cross section of both samples. Accordingly, the amount of change in contact resistance could be higher.

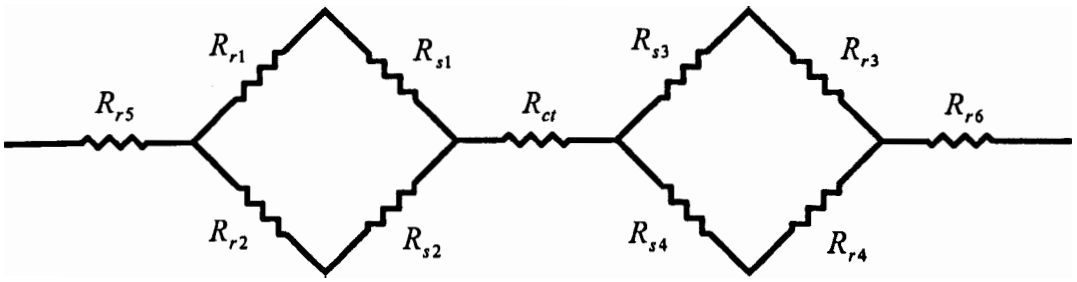

Figure 3.15 Circuit diagram of a single-fibre conductivity test rig. Subscript 'ct' means contact; 's' for specimen; and 'r' for rigs. Subscripts 1 to 5 refer to the specimen holding frames, and subscript 6 to the main loading bar.

Although the total resistance was displayed in the preceding figures, the contact resistance itself can be evaluated. Here, it will be discussed how much of the total resistance is contributed by the contact resistance. For this purpose, a circuit diagram for the rig (Figure 3.15) is considered. The resistance is measured as the ratio of the voltage to current is given by,

$$R = R_{r5} + \frac{(R_{r1}+R_{s1})(R_{r2}+R_{s2})}{R_{r1}+R_{s1}+R_{r2}+R_{s2}} + R_{ct} + \frac{(R_{r3}+R_{s3})(R_{r4}+R_{s4})}{R_{r3}+R_{s3}+R_{r4}+R_{s4}} + R_{r6}. \qquad (3.16a)$$

The subscript r denotes the structure of a rig itself, and the subscript s is allocated for a specimen wire. Here, the R_{ct} is the resistance induced by the creation of an electric contact, but not merely a constriction resistance. When the segments of 1 to 4 are arranged to be of a same length for a specimen and a rig portion, the expression for the measured resistance may be simplified as follows,

$$R = R_{ct} + R_r + R_s, \qquad (3.16b)$$

where the effective rig resistance R_r is,

$$R_r = R_{r5} + R_{r6} + R_{r0}, \qquad (3.16c)$$

with

$$R_{r0} \equiv R_{r1} = R_{r2} = R_{r3} = R_{r4}. \tag{3.16d}$$

The contribution in resistance of the sample is,

$$R_s \equiv R_{s1} = R_{s2} = R_{s3} = R_{s4}. \tag{3.16e}$$

It is very likely that the other resistances (sample and rig resistances) are much smaller than the contact resistance. These sample and rig resistances have been measured by the same method used for the resistivity of a silver steel rod. The values of these associated resistances are shown in Table 3.1.

	Resistivity ρ	Sample resistance R_s	Rig resistance R_r
Copper wire	3.06×10^{-8} Ωm	0.8 $m\Omega$	6.18 $m\Omega$
Steel wire	2.69×10^{-8} Ωm	14.3 $m\Omega$	
Steel wool	4.57×10^{-7} Ωm	1.36 Ω	

Table 3.1 Electric resistivity and resistances of sample and rig required for the evaluation of the contact resistance out of the directly measured total resistance of the system.

This conjecture about the relative resistances is valid for relatively thick copper and steel wire, but it may be controversial for the very thin wire from a bulk steel wool. According to the table and the plots, the contributions to total resistance by the sample and rig are negligible in the cases of the first two wires, as less than 0.5 % of the amount is affected. However, the steel wool itself when stretched on the rig is confirmed to produce as much as 15 % of the total resistance measured. This may be due to the combination of its high resistivity and relatively long length compared to the diameter (See equation (3.11)). Thus it may not be straightforward to observe the behaviour of the contact resistance for this type of material, because the non-contact types of resistance appear to make a significant contribution.

In a bulk material, however, the situation may be different for a high load, due to a much-shortened fibre length which will also reduce the resistance related to the length,

while the contact resistance is not much affected by the shortening. But, the much more complicated network of an equivalent electric circuit would make it difficult to deduce the behaviour of contact resistance and thereby to estimate the number of inter-fibre contacts. Therefore, it is not practical to extend the knowledge on a single fibre to a bulk fibrous material. Despite the difficulty, the behaviour of resistance in a bulk conducting material under compression is considered in the next section.

3.2.5 Bulk steel wool test

The bulk resistance of steel wool was measured as a function of the load. The wool sample was placed between two wooden plates and was loaded by the weights on the top plate. Two series of resistance measurements were made, for one the mechanical strain (Figure 3.16) was recorded as well. The resistance was measured directly by a single multimeter rather than using separate meters for voltage and current. The multimeter was then wired to top and bottom layers of the sample using cables and crocodile clips. The mechanical stress and strain behaviour was measured by reading the deflection through a travelling microscope with a resolution of 0.01 *mm*.

Although they were extracted from the same larger sample of steel wool, the two tested samples were suspected to have different bulk structures, since their structures were likely to be altered unintentionally, when they were extracted from the bulk. In other words, it was not simple to produce samples with a repeatable structure for this particular type of flexible steel wool.

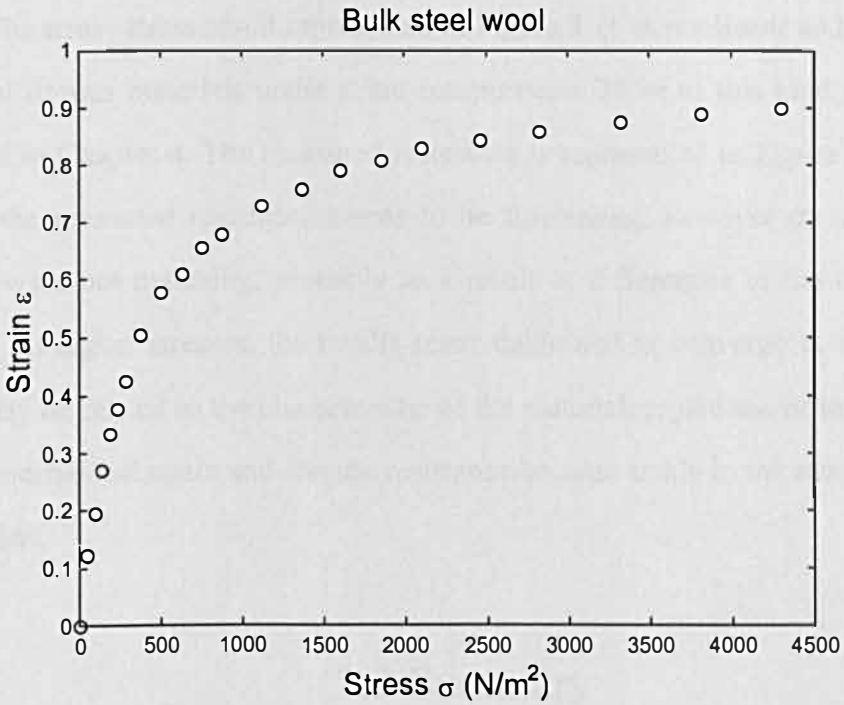

Figure 3.16 Structural stress-strain relationship of a steel wool under static compression which is obtained in parallel with an electric resistance test. The result shows the steel wool behaves as a typical fibrous material.

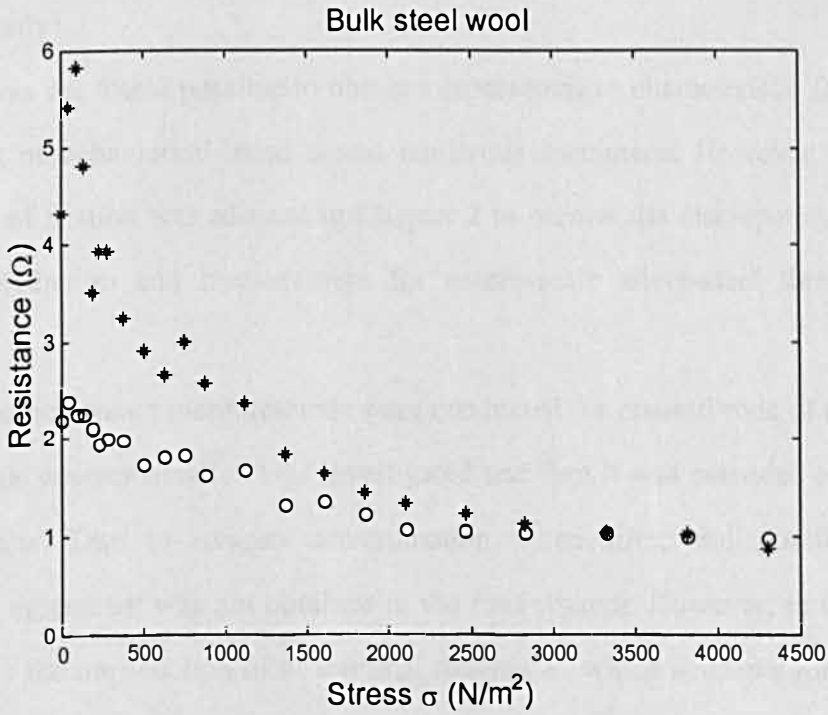

Figure 3.17 Electric resistance measured for a steel wool. Two readings were obtained for samples from different parts of the bulk material. The circled data was obtained for the sample whose stress-strain compressional behaviour is shown in Figure 3.16.

The strain-stress result represented in Figure 3.16 is nonlinear and looks like that of typical fibrous materials under static compression. More of this kind of data will be presented in Chapter 4. The measured resistance is represented in Figure 3.17. At lower stresses the measured resistance seems to be fluctuating, however the results for two samples were not matching, probably as a result of differences in the structure of the samples. At higher stresses, the results seem stable and to converge to a certain value, which may be related to the characteristic of the material, regardless of the sample. Note that the mechanical strain and electric resistance become stable in the stress region of the same order.

3.3 Summary

Methods of predicting and measuring contact friction and electric contact resistance and their measurements have been reviewed briefly. Measurements have been conducted for macro-scale specimens (for friction and resistance) and a realistic fibrous material (for resistance only).

It was not found possible to obtain a representative characteristic for friction due to the lack of behavioural trend across numerous specimens. However, the measured coefficient of friction was adopted in Chapter 2 to narrow the discrepancy in agreement between prediction and measurement for macro-scale silver-steel three-dimensional model.

Electric contact measurements were conducted for crossed rods of silver steel. At first, a single contact situation was investigated and then it was extended to a network of four contacts. Due to oxygen contamination, alien film, and possible asperities, reasonable agreement was not obtained in the first attempt. However, in the end, it was achieved by the introduction of a "terminal resistance" which accounts for those factors. A single wire or fibre was tested as well. The results for the resistance and force have shown the same trend as those observed for bigger silver steel rods. Measurements on a bulk fibrous material (steel wool) have yielded a reasonable resistance-force pattern.

However, due to the complex geometry and electric circuit, it seems to be difficult to extend what has been learned from macro-scale and single-fibre contacts to a bulk fibrous material.

Therefore, the idea of relating the electric contact resistance to the number of inter-fibre contacts inside the fibrous materials has not been investigated further. As a consequence, as also mentioned in the concluding remark in Chapter 2, a "macroscopic" approach has been adopted to describe the nonlinear structural behaviour of fibrous material under compression, rather than applying what is known in a microscopic scale to a bulk fibrous material. These models will be detailed in Chapter 4.

Chapter 4

Static models for the bulk compressional elastic properties of fibrous media

A series of macro-scale models representing the microscopic structure of fibrous materials (Chapter 2) has suggested that the structural behaviour, in compression, of such media is principally governed by bending rather than Hertzian contact deflection. These models have also demonstrated that the nonlinearity is likely to be brought about by the creation of further inter-fibre contacts as the material is compressed. The possible role of inter-fibre friction was raised, especially for a structure with considerable randomness of fibre orientation (Section 2.6). But the friction effect appeared to be small for a laminar structure in compression, and certainly a large part, if not the greater part, of fibrous media in common use are of essentially laminar structure. It was also discovered that the frictional behaviour of the fibre material was difficult to measure (Section 3.1). The possibility of using an electrical resistance technique to determine the number of inter-fibre contacts per unit volume in a conducting fibrous material was also investigated (Section 3.2). Despite its successful application to idealised macro-scale models, a full extension to a realistic fibrous material was abandoned because of the complicated nature of the electrical network. The same conclusion was also reached concerning the applicability of structural modules to a bulk fibrous material because of geometric irregularity and complexity in a realistic fibrous material (see Chapter 2). In other words, an understanding of the structural behaviour of a bulk fibrous medium from the details of its microscopic structure turned out to be impracticable. Instead, the possibility of an "equivalent continuum" approach, incorporating the essential physical features of the simple structural models of Chapter 2, has been raised.

4.1 Review

Several models have been appeared in the literature, related to the analysis of fibrous and other porous materials with a related structure. Sides, Attenborough and Mulholland [19] investigated a structural lattice in the form of a "stacked-cylinder model", in which Hertzian contact deformation was the sole governing factor in the bulk elastic behaviour, since bending effects were prohibited by the stacking configuration. Their model had the same configuration as that of the Hertzian contact model in Chapter 2 (see Figure 2.2). In a realistic situation, however, the contribution of Hertzian contact effects is likely to be very small because the deflection is inherently restricted by the fibre diameter, which is normally only a few microns or tens of microns (see Section 2.2). Although Hertzian deflection bears a nonlinear relationship to the applied force, it is unlikely to be the explanation of the observed nonlinear bulk elasticity of fibrous media, as was pointed out in Chapter 2.

In addition to the Hertzian stacked-cylinder model of Sides et al., other models describing the structural behaviour of fibrous media have been reported. A so-called "space-frame material model" was reported by Rosen, Bagchi and Kibler [20]. This was intended to represent the three dimensional structural behaviour of a random fibre network, particularly in fibrous thermal insulation materials for aerospace applications. Fibres in the model were represented by trusses in four vertical planes, together with a horizontal plane of trusses. One of the four vertical planes of trusses is depicted in Figure 4.1. The model is physically an approximate model and mathematically a discrete representation of a continuous actual material, because of the limited number of trusses used. The three most basic ideas of the space frame model are the transformation matrix (equation 117 in reference [61]), the effective Young's modulus, and the principle of virtual work. By the use of the transformation matrix and the principle of virtual work, the strain component in the microscopic fibre direction can be linked to its macroscopic counterpart. The effective Young's modulus itself contains the microscopic fibre stress component and hence yields nonlinear relationships between the bulk stresses and

strains. However, the space frame model was only based on the "axial" behaviour of its fibre components. No bending mechanism or change in the number of contacts between fibres was embodied in the space-frame model (these effects will be the main theme in this chapter). Most notably of all, the model predicted an incorrect stress-strain relationship which yielded the result that a fibrous material becomes softer under static compression and stiffer under static tension, which is contrary to experience and runs counter to the results presented in this chapter. However, the concept of adopting the transformation matrix and the principle of virtual work may be useful in application to the microscopic structural behaviour of fibrous materials.

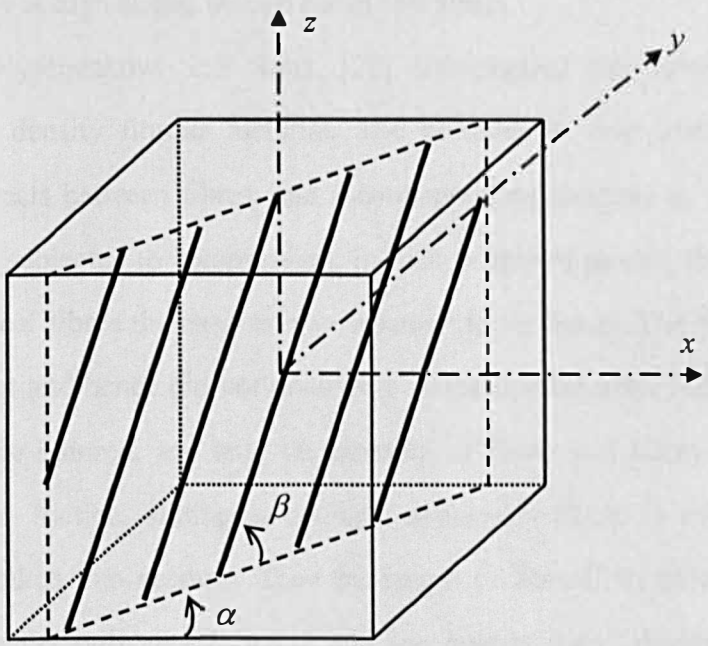

Figure 4.1 Schematic view of a hypothetical vertical plane containing trusses in the space frame material model of Rosen et al. [20]. Angle α is the orientation of the plane and β is the inclination angle of the trusses.

Sherwood and Van Damme [21] investigated deposited compaction of flat clay plates which can be related to the compression over a long time scale, such as a geological time scale in the case of clays deposited on the bottom of the sea. The deformation of each plate was assumed small enough to be governed by the linear biharmonic equation. In a simulation, a discrete two-dimensional lattice was proposed. The plates were added at random positions of the lattice. Compaction was generated by

the weight of the plates. Throughout the compression, each plate was allowed to deform until equilibrium was reached. The number of structural contacts per clay plate was also considered. As the compression proceeded, the number of contacts per node of the lattice was observed to increase and the bulk structure becomes gradually stiffer. However, the friction and related sliding between plates were not taken into account in their simulation. In an experiment, a pack of drawing papers was piled up to emulate a quasi two-dimensional bulk structure. In addition to gravitational forces, external forces were applied vertically to the paper pile. When the compressive stress and corresponding void ratio (porosity/solid fraction) were evaluated, a power law relationship between the two was observed to apply at high stress, though not at low stress.

Baudequin, Ryschenkow and Roux [22] investigated the nonlinear elastic behaviour of a low density fibrous material. The nonlinearity was attributed to the creation of new contacts between fibres, and a corresponding increase in their number, when the material is subjected to compression. In their proposed model, the mechanical behaviour of individual fibres themselves was assumed to be linear. The fibre diameter was assumed constant and hence did not contribute to the nonlinearity. Fibre elongation and compression were ignored, and only the bending of fibres was taken into account. Other factors such as friction, sliding or damage, apparently likely to exist in fibrous materials, were not taken into account. Thus the length of fibre links between contacts was presumed to be the only length scale, and the inverse cubic dependence of the transverse stiffness of fibres in bending on this length played a significant role in understanding the bulk elastic behaviour of fibrous materials. By means of a scale transformation, a power-law relation was identified between the applied compressive stress and the length of fibre links, which was extended to the strain. Their power-law dependence was confirmed by measurement in the large strain region.

In the following sections, the details of various static bending models for fibrous media will be discussed. Initially, the structural behaviour of cellular materials will be reviewed, since it is useful to understand the structural difference between cellular and fibrous media on a theoretical basis. The work by Baudequin et al. [22] will then be

discussed further and its application as a structural "fitting model" for fibrous materials at high strain will be considered. The development of a series of bending models will next be described in detail. Their application to actual fibrous media, their limitations, and modifications to these models will also be described.

4.2 Cellular materials

Before further discussion of detailed models for fibrous materials, it is worth reviewing the current understanding of the structural behaviour of cellular materials. These materials play very similar roles to fibrous materials in their acoustic, thermal and mechanical applications. Comparison of the similarities and differences in mechanical behaviour between these two types of porous medium could be illuminating and will help to explain why different types of structural model need to be employed in each case. (Granular materials, a third type of porous medium, are sufficiently dissimilar to cellular and fibrous materials for them to be excluded from the present discussion.)

Cellular materials can be made from a variety of solids such as polymers, metals, ceramics and naturally-occurring materials such as wood [18]. The physical properties of foams depend on several factors which are mainly separated into material-related factors and test-related factors [17]. Apart from test-related factors, the structural behaviour of cellular materials in general is determined by their material-related factors and particularly by the way in which the cell frames respond to the applied stresses. The material-related factors are mainly connected with the geometric structure or cell connectivity of the bulk material and the properties of the solid-phase material. The solid density, Young's modulus and yield strength are important properties of a cell material. The bulk structural properties of foams are affected by the solid volume fraction, the degree of anisotropy, the interstitial fluid, and whether the cells are closed, open (i.e., "closed-cell" or "fully reticulated", respectively) or a combination of both ("partially reticulated").

In many applications, cellular materials are exposed to static compression. In such cases, their structural behaviour can be characterised by three distinctive regimes. Under low stresses, foams are likely to exhibit linear elasticity. As stresses increase, they undergo a structural collapse, and finally they experience an extreme densification which is associated with a sharp rise in stresses. These three regions are often referred to as "Hookean" (or "linear elasticity"), "plateau" (or "post collapse") and "densification" respectively, and can be separated by critical strains such as the "elastic collapse strain" and the "onset of densification strain". The former strain value is intended to draw a line between the elastic linear region and the structural collapse region. The latter distinguishes between the collapse region and the densification region [62, 63].

In the linear elasticity (Hookean) region, the mechanism of structural behaviour is determined by whether the cells are open or closed. The behaviour of open-cell foam is dominated mainly by the "bending" of cell frames especially if the foam has a low solid fraction. For open-cell foam with a high solid fraction, it is believed that the "axial" deformation of the cell frames needs to be taken into account. Closed-cell foam is likely to be governed by the "stretching" of cell membranes, although the axial and bending deformation of cell frames also need to be taken into account. Interstitial fluids are believed to affect the stiffness when their viscosity is high for open-cell foams, and when the cell membranes do not break in the case of closed-cell foams.

For isotropic low-density open-cell foams, an analogy can be found with fibrous materials under compression as long as the foams are in linear elastic region. Provided that the cell size is much smaller than the overall dimensions of the bulk foam, the bulk Young's modulus of foams under static compression can be evaluated from standard beam theory involving the linear elastic bending deflection of cell frames with a load applied at the midpoint [18, 64]. (This is closely related to the behaviour of an idealised fibrous model, which will be described in Section 4.4.) So long as stresses are small enough to keep the foam in the elastic region, the axial and shear deformations of cell frames are usually neglected as compared to the larger bending deflection. Gibson and Ashby [18] proposed the following relationship between the bulk Young's modulus E_b,

the modulus of the cell material E and the solid fraction Ψ_0 (equal to solid volume ÷total volume of solid plus fluid):

$$\frac{E_b}{E} \approx \Psi_0^2 . \tag{4.1}$$

The upper limit of the linear elastic region can be predicted by the "elastic collapse strain" ε_c (see the papers by Dement'ev and Tarakonov [62, 63]),

$$\varepsilon_c = \frac{\pi^2 \beta^2}{8(2+\beta)}. \tag{4.2}$$

This elastic collapse strain plays a key role in designing foam-based damping systems [18]. The solid fraction Ψ_0 is related to the parameter β (the ratio of the width to the length of a cell frame) by

$$\Psi_0 = \frac{3\sqrt{2}\beta^2}{(2+\beta)^2}. \tag{4.3}$$

In reality, when the compressive load applied to the bulk material increases, so does the axial component of stress along the frame members, which adds an extra moment in the case of bent frames. Thus the linear elastic region is not exactly linear, but involves a gradual decrease in the bulk modulus as the bulk stress increases.

As the compressive stress nears the upper end of the Hookean region, a plateau region is encountered, where stresses are parallel to the strain axis for open-cell foams or increase slightly for closed-cell foams during a significant rise of strain. The plateau is associated with the collapse of the cell structure, which is initiated by elastic bucking for elastomeric foams such as rubber and some types of polymer foams, by plastic yielding or hinges for metal foams such as porous aluminium, and by brittle crushing for ceramic foams (See Figure 2.1). As the compressive stress increases, so does the axial stress on cell frames. When the compressive load reaches the Euler load for bucking, the frames may be assumed to begin to buckle. Thus, for elastomeric open-cell foams, the plateau comes with the buckling of cell frames. The critical load of for buckling can be

determined by the use of Euler's formula and the elastic collapse stress σ_c is related to the solid fraction Ψ_0 and modulus E of solid material by [18]

$$\frac{\sigma_c}{E} \approx 0.05\Psi_0^2 \,. \tag{4.4}$$

In terms of strain, the plateau region is essentially bounded by the elastic collapse strain ε_c in equation (4.2) and the onset of densification strain ε_d (see Dement'ev and Tarakonov [62, 63]),

$$\varepsilon_d = 1 - \frac{\beta}{1+\beta/4}\cos(\pi/4) \,. \tag{4.5}$$

At significantly large compressive strains when the cell frames have almost completely collapsed, the adjacent and opposing frames of the cells touch one another and a densification region is followed (see also Figure 2.1). During densification, the strain increases rapidly to a "limiting strain" ε_l [18],

$$\varepsilon_l = 1 - 1.4\Psi_0 \,. \tag{4.6}$$

The limiting strain is not equivalent to but is less than the porosity, because there are still remaining pores even under extreme compression.

As an illustration of the preceding discussion, the nonlinear stress-strain behaviour of a 30 *mm* thick layer of open-cell foam material was measured by reading its deflection – with the use of a travelling microscope having a resolution of 0.01 *mm* – when it was loaded by weights placed on a thin aluminium plate, resting on top of the foam layer. Its fully-reticulated structure was confirmed by means of a 45× optical microscope (the image in Figure 2.1 is not for the fully-reticulated foam). The overall behaviour showed the expected three distinct regions of linear elasticity, post collapse and densification (Figure 4.2). The measured data were also fitted by the relations introduced in the earlier paragraphs. Dement'ev and Tarakonov's critical compressive strains were evaluated from equations (4.2) and (4.5), whose parameters are as follows: solid fraction, $\Psi_0 = 0.05$; elastic collapse strain, $\varepsilon_c = 0.03$; plateau stress, 3300 N/m^2;

onset of densification strain, ε_d = 0.67; and β = 0.245. In the process of fitting, the stress in the post-collapse region was assumed to lie parallel to the axis of strain [62, 63], although this assumption is not strictly realised as may be seen from the measured data. Although the density of the solid material comprising the cell elements was not known *a priori*, nor the solid fraction as a result, it was possible to determine these parameters by iterating several trial values of the solid fraction, evaluating two critical compressive strains, and determining the optimum solid fraction which places the plateau region in a proper position of the stress-strain curve. (Since it is the *strain-stress* relationship which is actually plotted in Figure 4.2, the term "plateau" might seem inappropriate, because the stress axis is placed in the abscissa. The generally accepted convention – of placing the stress in the ordinate and the strain in the abscissa – is not followed in this thesis, because stress is regarded as the independent variable in a measurement.)

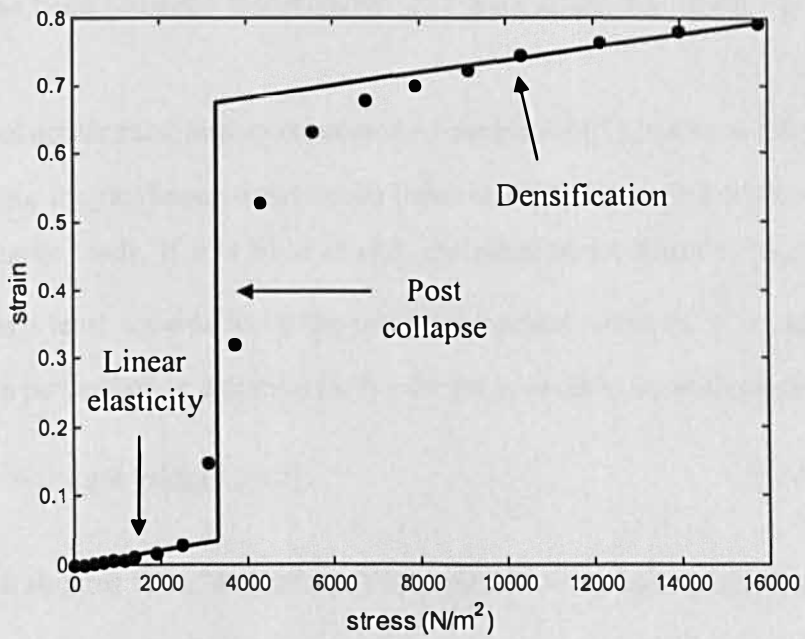

Figure 4.2 Measured and predicted behaviour of the nonlinear strain-stress relationship for open-cell foam with a bulk density of 30.2 *kg/m*^{3}. The solid circles denote measured data, and the solid line the prediction.

4.3 Power-law model

Before describing the bending models that have been developed in the present investigation, it is worth introducing an existing structural model for a fibrous material and discussing its application. It will also be helpful to explain how this and the bending models are different. Recently, a power-law relationship has been proposed [22] for the stress-strain behaviour of low density fibrous materials under large compressive strain:

$$\sigma = q(\varepsilon_{th} - \varepsilon)^p . \tag{4.7}$$

Here, ε_{th} is the threshold strain and q is a proportionality constant. The threshold strain is not mathematically related to any of strains mentioned in Section 4.2, but its physical meaning could be similar to the limiting strain in (4.6). The exponent p can be fixed at -1.5, which has been obtained theoretically [22], particularly for fibrous materials under compression.

The particular relationship expressed in equation (4.7) has been adopted here as a means of fitting the nonlinear stress-strain behaviour of fibrous materials when they are subjected to large loads. If p is fixed at -1.5, the other two unknowns, ε_{th} and q, can be obtained from a least squares fit by the use of numerical iteration. If linear regression is employed, the power law in equation (4.7) is better expressed logarithmically,

$$\log\sigma = \log q + p\log(\varepsilon_{th} - \varepsilon) . \tag{4.8}$$

To find a least squares fit, a "sum of squared residual" S can be expressed as below,

$$S = \sum_{i=1}^{n} \{\log\sigma_i - \log q - p\log(\varepsilon_{th} - \varepsilon_i)\}^2 , \tag{4.9}$$

where n is the number of measured data. It is necessary to minimise S with respect to both $\log q$ and ε_{th}, and the following equations result:

$$\frac{\partial S}{\partial(\log q)} = -2\sum_{i=1}^{n} \{\log\sigma_i - \log q - p\log(\varepsilon_{th} - \varepsilon_i)\} = 0 , \text{ and} \tag{4.10}$$

$$\frac{\partial S}{\partial \varepsilon_{th}} = -2p\sum_{i=1}^{n}\frac{1}{\varepsilon_{th}-\varepsilon_i}\{\log\sigma_i - \log q - p\log(\varepsilon_{th}-\varepsilon_i)\} = 0. \qquad (4.11)$$

Although q can be found explicitly from equation (4.10), the same is not true of ε_{th} in equation (4.11), and an iterative method of solution is therefore employed, as follows. A trial value of ε_{th} needs to be assumed to find q from the following equation (derived from equation (4.10)):

$$\log q = \frac{1}{n}\left\{\sum_{i=1}^{n}\log\sigma_i - p\sum_{i=1}^{n}\log(\varepsilon_{th}-\varepsilon_i)\right\}. \qquad (4.12)$$

The assumed value of ε_{th}, together with the value of $\log q$ resulting from equation (4.12), are inserted in equation (4.9) and a value of S is found. Successive values of S are then found by varying ε_{th} and the minimum value is thus determined by comparison, together with the corresponding iterated values of ε_{th} and q. As an example, the sum of squared residual S is plotted *versus* strain in Figure 4.3 for an acoustic duct-lining material (See Table 4.1 and 5.1). A regression process based on this procedure is illustrated in Figure 4.4 (note the log-log axes). For the regression process work properly, some measured data need to be excluded from the low strain range. The exclusions have been made according to the total number of data points and the deviations from the linear relationship shown in Figure 4.4. The final result of applying this power-law model to actual measured data in the stress-strain domain is shown in Figure 4.5. As it is seen, this fitting method applies only to the high strain region. Although the power-law model performs poorly at low strains, it is still useful especially in determining effects of the storage of low bulk density fibrous materials, which could cause a high strain. The parameters in the equation (4.7) for the acoustic duct-lining material are: q = 656.6; ε_{th} = 0.7802; and p = -1.5.

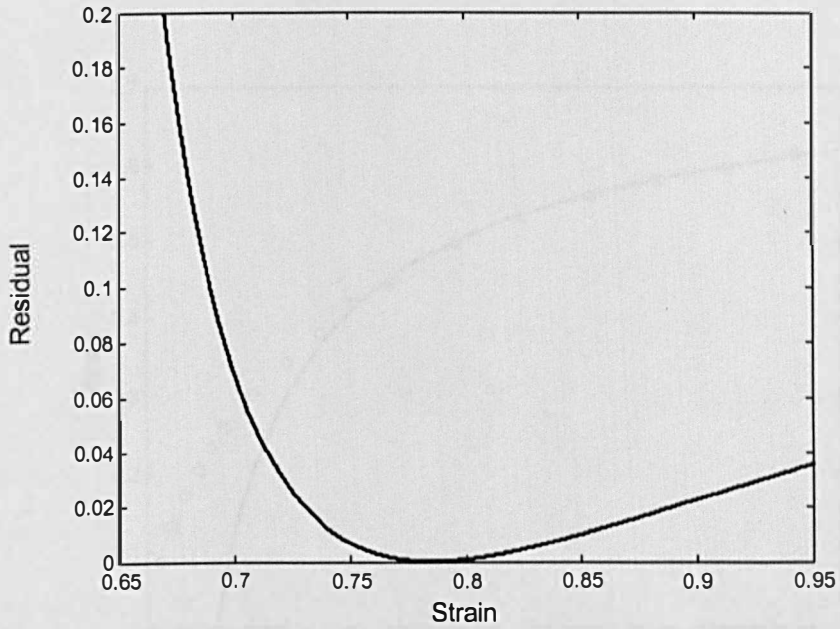

Figure 4.3 Sum of squared residual associated with equation (4.9), plotted against trial strain, for the acoustic duct lining material. The minimum value occurs at the threshold strain.

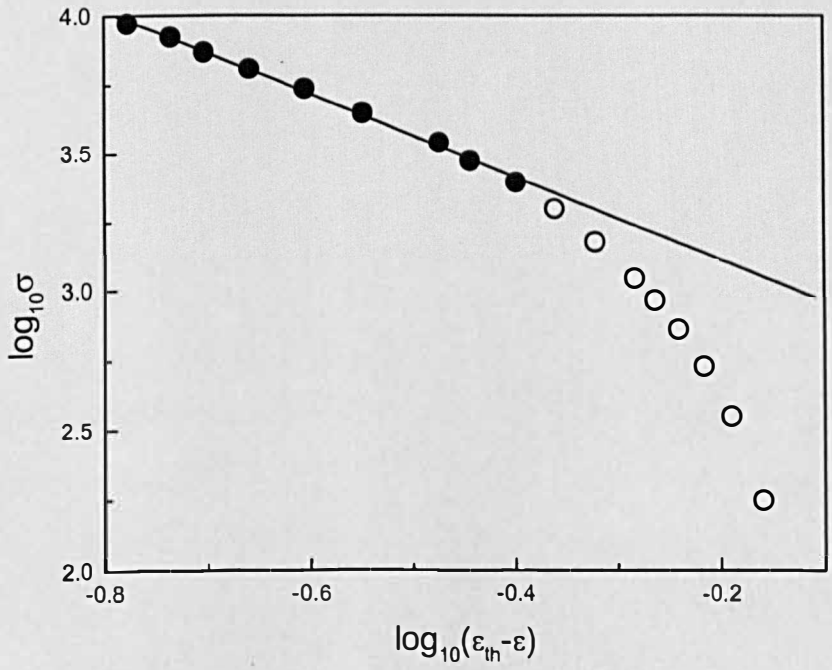

Figure 4.4 Regression procedure for the power-law model for the acoustic duct lining material. —, regression line; •, included measured data; ○, excluded measured data.

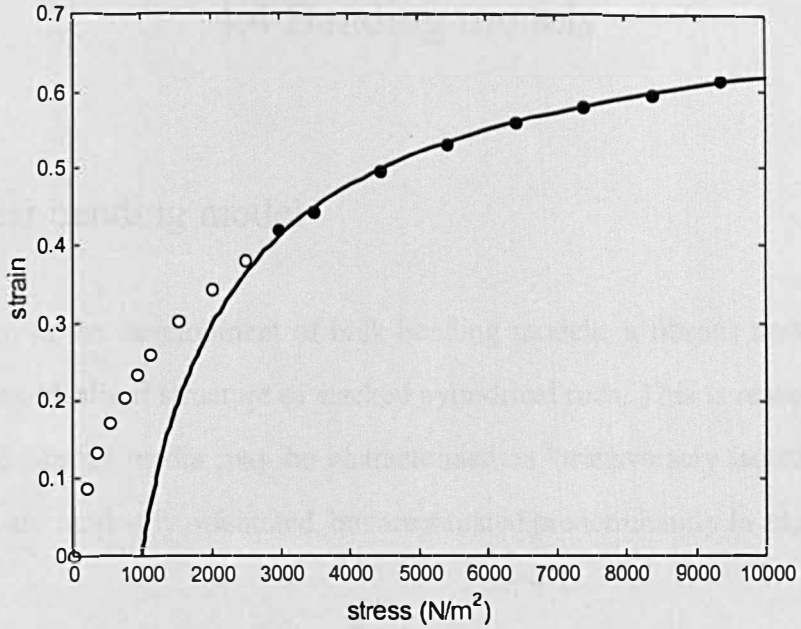

Figure 4.5 Measured and predicted strain/stress relationship for the duct lining material. The circles denote the measured data, and the solid line the power-law model.

4.4 Bending models

4.4.1 Linear bending model

As a first step in the development of bulk bending models, a fibrous material has been modelled as an idealised structure of stacked cylindrical rods. This is reasonable because many layered fibrous media may be characterised as "transversely isotropic". In other words, fibres are randomly orientated, but are situated predominantly in adjacent layers.

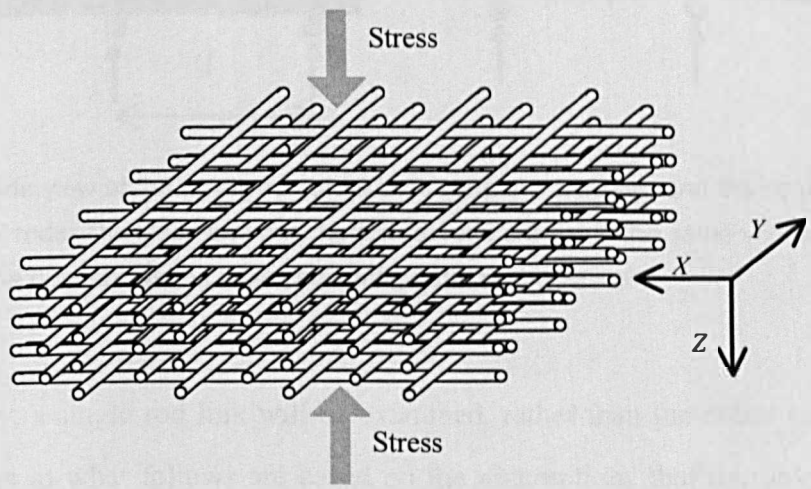

Figure 4.6 Idealised model for the bending behaviour of a fibrous material.

In the model depicted schematically in Figure 4.6, parallel elastic cylindrical rods form each layer, and successive layers are shifted by half a rod spacing (or fibre link) with respect to each other to allow the rods to bend. To make the model as simple as possible, the spacing between rods remains the same throughout the structure and the diameter is kept constant, thereby reducing the behaviour of the entire bulk model to that of a local structure. The deflection mechanisms for this model would be Hertzian and bending deflection. Hertzian deformation must occur at the contact points of adjacent rods, but it is assumed that this is negligible compared to the bending deflection of rods. Because of

its transversely isotropic geometry, the model can be regarded as two-dimensional. Thus, its compressional behaviour can be successfully identified as one producing uni-axial deflection, as shown in Figure 4.7. Therefore, the characteristic dimensions will be the rod diameter d and the "link length" l between adjacent cylindrical rods. These two dimensions are assumed to be fixed throughout the model, and are the defining geometric parameters.

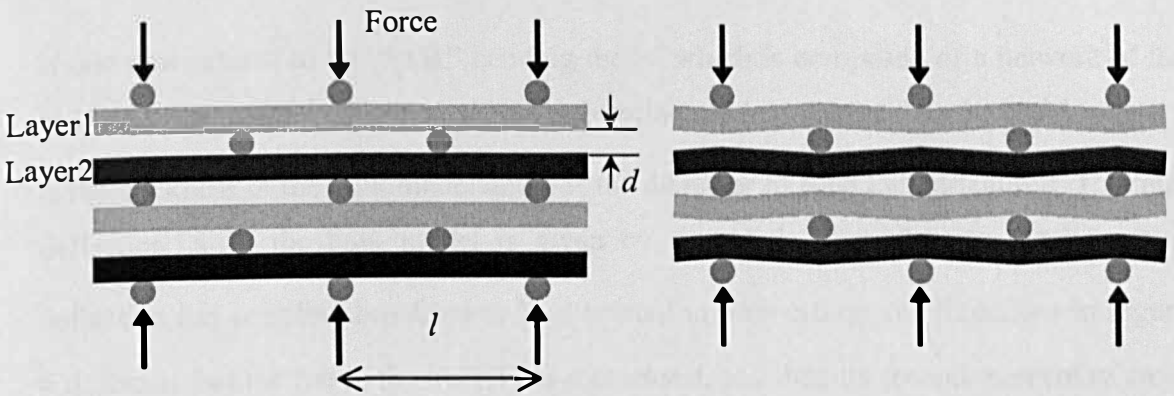

Figure 4.7 Side view of the idealised model, indicating the diameter and the contact points of the cylindrical rods. The black and grey horizontal rods are not in the same vertical plane. The diagram on the right shows the deflected configuration schematically.

Initially, a single rod link will be examined, rather than the entire bulk network. The procedures in what follows are based on the assumptions that the link has a fixed length, the force F is applied at its geometric centre, and its cross section is uniform along the length – and symmetric along the line of action – of the force, which permits a two dimensional representation of its behaviour. The fibre link in the model is also assumed to have the structural characteristic of a "linear" elastic beam that is symmetrical, relatively slender and hence predominantly subjected to pure bending. The material of the beam is supposed homogeneous enough to have a constant Young's modulus E. On the basis of these assumptions, the elastic energy W of the link, created by the bending moment M_b along the link, can be expressed by the following equation [61],

$$W = \int \frac{M_b^2}{2EI} dx = \frac{F^2 l^3}{384EI}, \tag{4.13}$$

where l is the link length of each rod and I is the second moment of the cross sectional area of a rod about the neutral axis. Although the assumed boundary condition here is simply supported, the symmetry inherent in an effectively infinite stack of rods will prevent any rotation of structural elements at the contact points. The deflection δ arising from the force F is obtained from Castigliano's theorem [61] as

$$\delta = \frac{\partial W}{\partial F} = \frac{Fl^3}{192EI}. \tag{4.14}$$

If one now returns to the "bulk" bending model which is composed of a network of the rod links, the number of layers N_l in the bending model is defined by $N_l = t/d$, where t is the thickness of the bulk model and d is the diameter of each cylindrical rod. The total deflection Δ of the bulk model is given by $\Delta = N_l \delta$. Note that the total bending deflection has contributions from rods orientated in both orthogonal directions in Figure 4.6. Recall that the rod in the model has diameter d, and then its second moment of cross sectional area I (about the neutral axis) is then given by $\pi d^4/64$. From the configuration of the model, the contact force F on the link is related to the force F_{ext} external to the model by $F = F_{ext} l^2/A$. Here, A is the surface area of the bulk model to which F_{ext} is applied. Thus, the quantity A/l^2 is the measure of the number of contacts per layer for this particular model. Finally, if it is recalled that the bulk strain ε is defined by $\varepsilon = \Delta/t$ and the bulk stress by $\sigma = F_{ext}/A$, then the parameters are reduced to $F = \sigma l^2$ and $\delta = d\varepsilon$. If these are inserted into (4.14), then the stress-strain relation for compression in the linear bending model may be expressed

$$\sigma = 3\pi E \left(\frac{d}{l}\right)^5 \varepsilon. \tag{4.15}$$

Based on the geometric structure in Figure 4.7, the ratio of the rod link length to the diameter is given in terms of the solid fraction Ψ_0 (solid volume / total volume of bulk medium) by

$$\frac{l}{d} = \frac{\pi}{4\Psi_0}. \tag{4.16}$$

Finally, if equations (4.15) and (4.16) are combined, the stress-strain relation based on the idealised linear bending model is written in terms of a macroscopic parameter Ψ_0,

$$\sigma = 3\pi E\left(\frac{4}{\pi}\Psi_0\right)^5 \varepsilon . \tag{4.17}$$

As expected, the bulk modulus here is independent of the stress and strain, and consequently equation (4.17) embodies a linear stress-strain relationship.

4.4.2 Simple Nonlinear Bending Model (SNBM)

Unlike the linear bending model described in the previous section, a bulk fibrous material is known to deflect nonlinearly under compression. In a real fibrous medium, this nonlinearity occurs predominantly by the increase in the number of inter-fibre contacts, as the material is compressed [22] (see also Chapter 2 concerning idealised macroscopic models). Based on the schematic view of the bending model in Figure 4.7, it is clear that there could be one more new contact per rod link (for example, layer 1 could make contact with layer 2) when the stress reaches the requisite value, but no further contacts on the basis of this particular geometry. Thus for this configuration, the stress-strain relation will be a piecewise linear curve composed of only two linear regions. Under normal compression, the strain increases as a function of the stress, and the solid fraction increases correspondingly. Since this compression process causes new contacts to occur, the length of each fibre link becomes shorter.

When the fibrous material is subjected to compression, the solid fraction Ψ and the bulk density ρ_b change correspondingly. If Hertzian deformation and volume change by bending of the fibres are neglected during the compression, the total fibre volume in the model is likely to remain essentially unchanged, especially in a fibrous material with a low solid fraction (or high porosity). For fibrous materials which are transversely isotropic in the horizontal direction of x and y (as in the model shown in Figure 4.6), the changing solid fraction Ψ' of the compressed material can be represented as follows, recalling that the total mass remains fixed,

$$\frac{\Psi_0}{\Psi} = \frac{\rho_{b0}/\rho_s}{\rho_b/\rho_s} = \frac{V}{V_0} = (1+\varepsilon_x)(1+\varepsilon_y)(1-\varepsilon_z) = (1+\nu_b\varepsilon_z)^2(1-\varepsilon_z)\,. \tag{4.18}$$

Here, ρ_s represents the density of the fibre material, V is the bulk volume (fibres plus voids), ν_b is the bulk Poisson's ratio and the subscript 0 denotes the initial value of a property without compression. Thus, the variable solid fraction is defined by the longitudinal strain ε_z (or ε if the subscript z is discarded), which is regarded as positive for compression, while ε_x and ε_y are considered positive in expansion. Equation (4.18) may be approximated by the simpler form

$$\Psi \approx \frac{\Psi_0}{1-\varepsilon}\,, \tag{4.19}$$

because ν_b is likely to be very small in a laminar material with a two-dimensional fibre arrangement and the term $\nu_b\varepsilon_z$ in (4.18) is therefore neglected.

In a real fibrous medium, the compression process is certain to cause new contacts to occur, which consequently reduces the average length of the fibre links. In addition, one may also conceive an increased solid fraction, based on the relation (4.16), which can be related to the strain in equation (4.19). Therefore, in the idealised model, one can imagine a link length which varies depending on the degree of compression. This process can be envisaged schematically as in Figure 4.8.

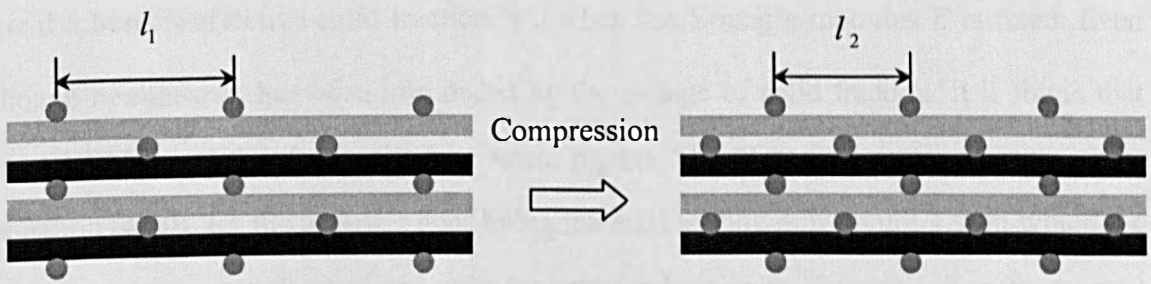

Figure 4.8 Schematic view, demonstrating the shortening of fibre links during compression.

But this seems technically impossible in the model, as mentioned in the first paragraph of this section, because the cylindrical rods are not allowed to move horizontally in any layer, but are assumed to deflect only vertically. Nevertheless, the intermediate states

with shortened characteristic fibre links can be conceived, irrespective of how they have occurred, and then only the consequence of this rearrangement on the deflected states need be considered. Therefore, the linear bending model may be applied at each stress-strain state, to create a nonlinear version, by inserting the effect of solid fraction change with strain (4.19) into the linear model (4.17):

$$\sigma = 3\pi E\left(\frac{4}{\pi}\frac{\Psi_0}{1-\varepsilon}\right)^5 \varepsilon . \tag{4.20}$$

In equation (4.20), the factor of $(1-\varepsilon)^{-5}$ appears because of the progressive change in structure of the linear stacked fibre model, as the strain increases. The net result is therefore a nonlinear bulk elastic behaviour which may also be interpreted as an integration of piecewise linear behaviours for each infinitesimal stress-strain region. The bulk Young's modulus may be found from $E_b = d\sigma/d\varepsilon$,

$$E_b = 3\pi E\left(\frac{4}{\pi}\frac{\Psi_0}{1-\varepsilon}\right)^5 \frac{1+4\varepsilon}{1-\varepsilon}. \tag{4.21}$$

These equations are adopted here to describe the nonlinear stress-strain behaviour of actual fibrous materials (see Section 4.5). The materials chosen for illustration are first, a thermal insulation blanket from an aircraft fuselage, and secondly an acoustic duct lining material. The measured data for these media have been inserted into equation (4.20) to yield a best-fit effective solid fraction Ψ_0 when the Young's modulus E is fixed. Even though nonlinearity has been introduced by the change of solid fraction, it is found that the SNBM is valid only for the low strain region. The "fitted" theoretical curve, from equation (4.20), for the acoustic duct lining material is shown in Figure 4.9, in which the measured data are well predicted only for strain values up to about 0.2. For the thermal insulation blanket, the fitted curve will be shown later, together with plots from other models.

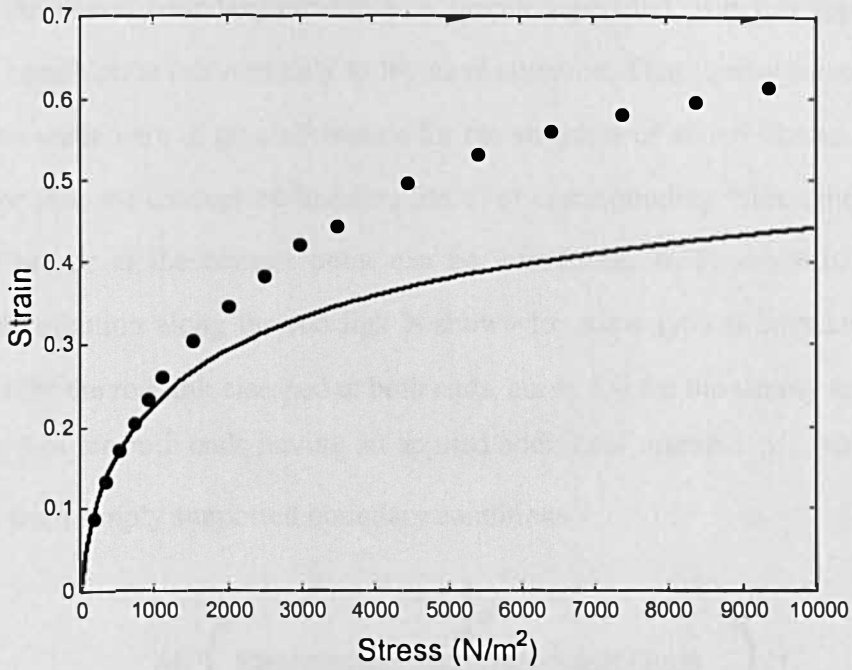

Figure 4.9 Measured and theoretical strain/stress relationship for the duct lining material. The circles are for the measured data, the line is for the SNBM.

4.4.3 Modified Nonlinear Bending Model (MNBM)

In the SNBM of the previous section, the effect of nonlinearity has been accounted for on the basis that the solid fraction changes according to the strain. As illustrated in Figure 4.9, however, the SNBM yields poor results at high strain. In the previous section, each elastic rod or fibre was considered to be initially straight with infinite length and to be bent during compression. Any change to the structure of the fibre itself in the sense that, in a realistic situation, the arrangement of fibres is different from that in the idealised model in Figure 4.6, has not been considered so far. It is certain that, in real fibrous media, the both-ends-clamped boundary conditions for each fibre link would no longer be valid.

The boundary conditions at the ends of each fibre link are a measure of the flexibility at those points. Based on the schematic view of the idealised model in Figure 4.6, as already mentioned in Section 4.4.1, the symmetry in an effectively infinite stack of elastic rods will not allow any rotation of structural elements at the contact points,

although the actual boundary condition is simply supported. But this type of clamped boundary condition is relevant only to the ideal situation. That is why some modification needs to be made here to give allowance for the structure of actual fibrous materials. To account for this, the concept of "binding force" or corresponding "flexibility" at the ends of each fibre or at the contact point can be introduced. In Figure 4.10, the bending moment distribution along the rod link is shown for some typical boundary conditions. Curve 1 is for the rod link clamped at both ends, curve 2 is for the simply supported ends, and curve 3 is for both ends having an applied additional moment M_0, representing the deviation from simply supported boundary conditions.

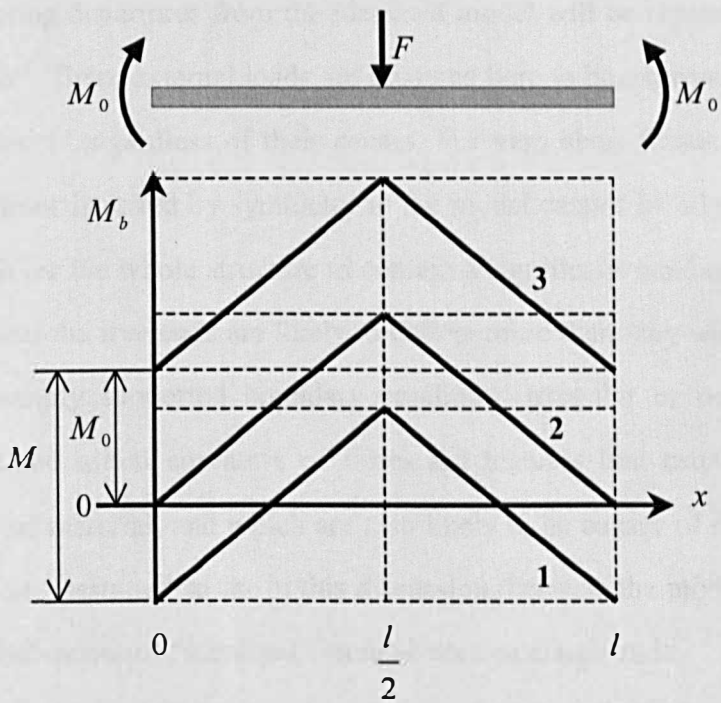

Figure 4.10 Diagram showing the bending moment along the fibre link.

It may be imagined that the binding force or binding restraint at the contact points is related to the rotation or flexibility at those points. No rotation is allowed for clamped ends, and the ends are free to rotate in the simply supported case. It is also worth noting that, in practice, simply supported ends lead to the largest peak value of bending moment among the possible combinations of various boundary conditions. Most of these peak values in an actual material are likely to vary between the minimum value associated with both-ends-clamped condition and the maximum value of the simply supported case.

Even though the entire structure would experience both-ends-clamped boundary conditions in the idealised model, some fibres in a real fibrous material would be exposed to the simply supported boundary condition because of the lack of constraint near the ends of the fibres. One may also conceive that, in certain situations, the ends may be likely to rotate more than they would in the simply supported case, especially when there are additional loads along the fibre link. Some of the possibilities for this concept are any deviation from an idealised situation such as the existence of relatively short fibres, irregular shapes or non-uniformity of fibre cross section, initial curvatures of the fibre and even damage to fibres. In the MNBM described in this section, all these various possibilities causing departures from the idealised model will be represented in terms of "additional loads". These external loads are assumed here to be expressed in terms of the "additional moment" regardless of their causes. For very short fibres, for example, the boundary conditions incurred by symmetry in the model cannot be adopted. If the fibres are short enough for the whole structure to contain a significant number of free ends, the parts of fibres near the free ends are likely to deflect more than they would in the case of the both-ends simply supported boundary condition. Irregular or non-uniform cross-sectional shape and initial curvature of fibres are features that usually exist to some extent in an actual material, and which are also likely to be causes of deviation from the boundary condition assumed so far in this discussion, because the model has been based on the bending behaviour of "idealised" circular-section elastic rods.

A single rod link will be examined here rather than the bulk network, as in the discussion in Section 4.4.1. One can imagine an additional moment M, representing the deviation from the clamped boundary condition, at the end of each fibre link. It is assumed that the additional moments are evenly distributed in both halves of the link, which are then assumed to be acted on by opposite moments, thereby reinforcing the effects of the acting force by ensuring greater rotation of the link. The elastic energy of the link, created by the bending moment, can be expressed by the following equation, provided that the same assumptions in Section 4.4.1 are used [61]:

$$W = \int \frac{M_b^2}{2EI} dx = \frac{1}{2EI}\left(\frac{F^2 l^3}{192} + M^2 l\right). \tag{4.22}$$

If it is assumed that the additional moment M arises solely from the force F acting on the centre of each link, the deflection of the link is straightforward to calculate by the use of the Castigliano's theorem [61]. This assumption seems reasonable because the entire behaviour within the model is actually activated by the external force F_{ext} and the force F is a manifestation of F_{ext} on the fibre link. The fibre rotation, as a feature of the internal behaviour of the model, will inevitably be related to the force F, in the sense that a higher load causes a greater rotation. So the additional moment M on the link can be related to the force F and further to the strain ε, in the sense that a higher strain is accompanied by a greater rotation or flexibility. M can also be written as a function of one of the characteristic dimensions of the model, the diameter d, as follows by the introduction of the new dimensionless parameters γ and ζ:

$$M = \gamma F d = \zeta \varepsilon F d. \tag{4.23}$$

If equation (4.23) is inserted into (4.22), the elastic energy of the link will be given by

$$W = \frac{1}{2EI}\left(\frac{F^2 l^3}{192} + (\zeta \varepsilon d)^2 F^2 l\right). \tag{4.24}$$

The deflection δ of a fibre link, arising from the force F, is obtained from Castigliano's theorem as

$$\delta = \frac{\partial W}{\partial F} = \frac{F}{EI}\left(\frac{l^3}{192} + (\zeta \varepsilon d)^2 l\right). \tag{4.25}$$

Secondly, if one focuses again on the bulk bending model comprising a stack of elastic rods, the bulk deflection can be defined in terms of the total external compressional force. The relationship between deflection and force in the microstructure can be expressed in terms of the bulk strain ε and stress σ and the microscopic dimensions of diameter and link length, through the same procedure as that described in Section 4.4.1 to give

$$\varepsilon = \frac{\sigma}{3\pi E}\left(\frac{l}{d}\right)^5 \left\{1+192(\zeta\,\varepsilon)^2\left(\frac{d}{l}\right)^2\right\} . \tag{4.26}$$

The relationship between the aspect ratio of the fibre link and the solid fraction in equation (4.16) is now inserted into (4.26) to replace the fibre aspect ratio d/l by the macroscopic parameter Ψ. The relationship in (4.19) is again adopted here to embody the nonlinear behaviour. The MNBM may, finally, be represented in the form of a bulk stress-bulk strain relationship,

$$\sigma = \frac{3\pi E\left(\frac{4}{\pi}\frac{\Psi_0}{1-\varepsilon}\right)^5 \varepsilon}{1+192\left(\zeta\,\varepsilon\frac{4}{\pi}\frac{\Psi_0}{1-\varepsilon}\right)^2} . \tag{4.27}$$

The bulk Young's modulus of the MNBM is given by $E_b = d\sigma/d\varepsilon$ as

$$E_b = \frac{3\pi E}{1-\varepsilon}\left(\frac{4}{\pi}\frac{\Psi_0}{1-\varepsilon}\right)^5 \frac{(4\varepsilon+1)+192\left(\zeta\,\varepsilon\frac{4}{\pi}\frac{\Psi_0}{1-\varepsilon}\right)^2(4\varepsilon-1)}{\left\{1+192\left(\zeta\,\varepsilon\frac{4}{\pi}\frac{\Psi_0}{1-\varepsilon}\right)^2\right\}^2} . \tag{4.28}$$

As seen in equations (4.27) and (4.28), the MNBM involves three parameters, the Young's modulus E of the solid material, the solid fraction of the undeflected material Ψ_0 and a newly introduced constant ζ. It is worth noting, at this stage that the solid fraction may have to be given an adjusted "effective value" because of the sensitivity brought about its high power dependence embodied in equation (4.27). Comparison between equation (4.27) and measured data together will be made in Section 4.5.2.

4.5 Measurements and comparison with theory

The results of deflection-force measurements on selected samples of fibrous materials were used to produce strain-stress plots, and comparison is made between these and predictions made by the use of the models described in Sections 4.3 and 4.4.

4.5.1 Method of measurement of stress/strain characteristics

The two materials examined in detail in this investigation were: first, a glass fibre thermal insulation blanket from an aircraft fuselage, and secondly a glass fibre acoustic duct lining material. The nominal bulk densities were 9 and 35 kg/m^3, respectively. Each of these materials was cut into a parallelepiped shape and glued to thin aluminium plates by the use of an adhesive spray. Equal groups of metal weights were positioned on the top plate at each corner and the corresponding deflection was measured by the use of a travelling microscope with a resolution of 0.01 *mm*. A short "sting" was glued to the centre of the plate, and the microscope was focussed on the tip of the sting. Figure 4.11 shows the measurement arrangement.

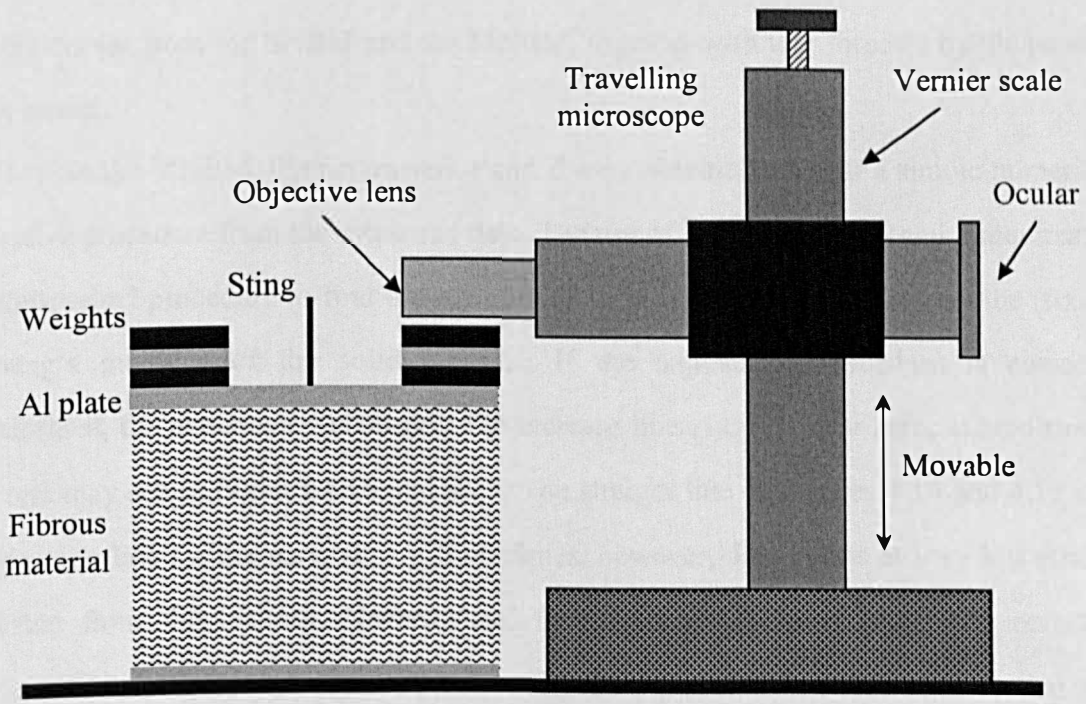

Figure 4.11 Schematic diagram showing the experimental setting for measuring the deflection of a fibrous material under static compression.

4.5.2 Comparison between experiment and theory

The strain-stress data measured on the thermal insulation blanket and the duct lining material are shown in Figures 4.12 and 4.13. In both cases, a highly nonlinear relationship is observed, with a very great increase in bulk stiffness occurring for high values of strain, as compared to the case where $\varepsilon \to 0$. (At this stage, it may be worth noting that a fibrous material behaves structurally in a different way from a cellular material (Figure 4.2), which has three distinct regimes.) The thermal insulation blanket was much more compliant than the duct lining, and it proved difficult to obtain data for stresses less than about 80 Pa, because of the fact that the aluminium top plate itself compressed the material quite significantly. The much denser – and stiffer – duct lining shows an early onset of nonlinearity, for $\varepsilon < 0.2$, with a progressive stiffening as the material is compressed. Also shown in Figures 4.12 and 4.13 are the predicted strain-stress curves from the SNBM and the MNBM, together with that forecast by the power-law model.

In the MNBM, the parameters γ and ζ were obtained through a simple numerical iterative procedure from the measured data. The use of the parameters γ and ζ requires an "adjustment" procedure to find the *effective* value of solid fraction, based on the (fixed) Young's modulus of the solid material. If the adjustment procedure is correctly performed, the parameter γ is observed to increase linearly from near zero, at zero strain, as one may see in Figures 4.14 and 4.15. The straight line in Figures 4.14 and 4.15 is a regression line for the parameter γ. Sometimes, however, data points at very low strains deviate from this pattern. Nevertheless, they do not adversely affect the essential behaviour of the model. This linearity without a significant offset ensures that the parameter ζ is approximately constant over the strain range of interest, because it can be regarded as the slope of γ.

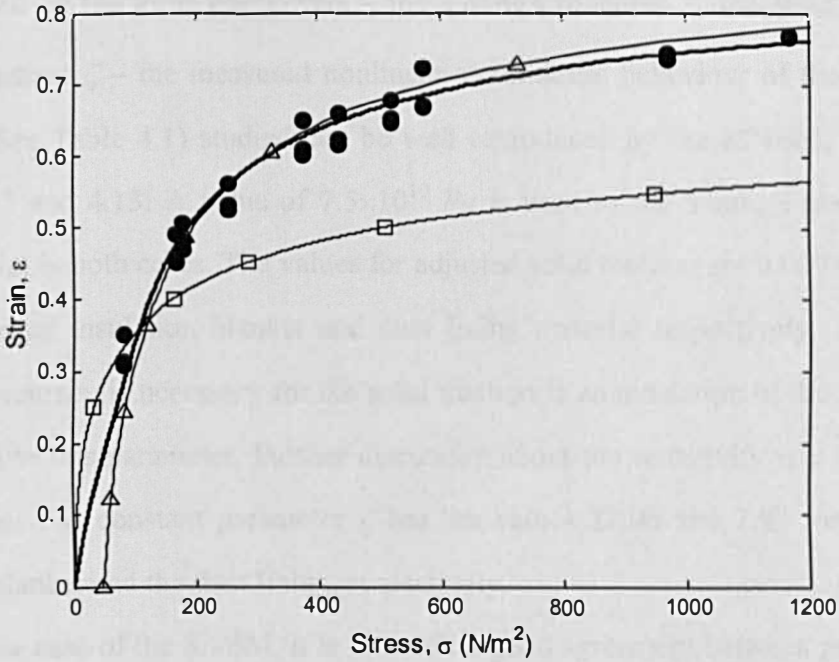

Figure 4.12 Strain-stress behaviour of the thermal insulation blanket. •, measurement; ——, MNBM; —□—, SNBM; —Δ—, power-law model.

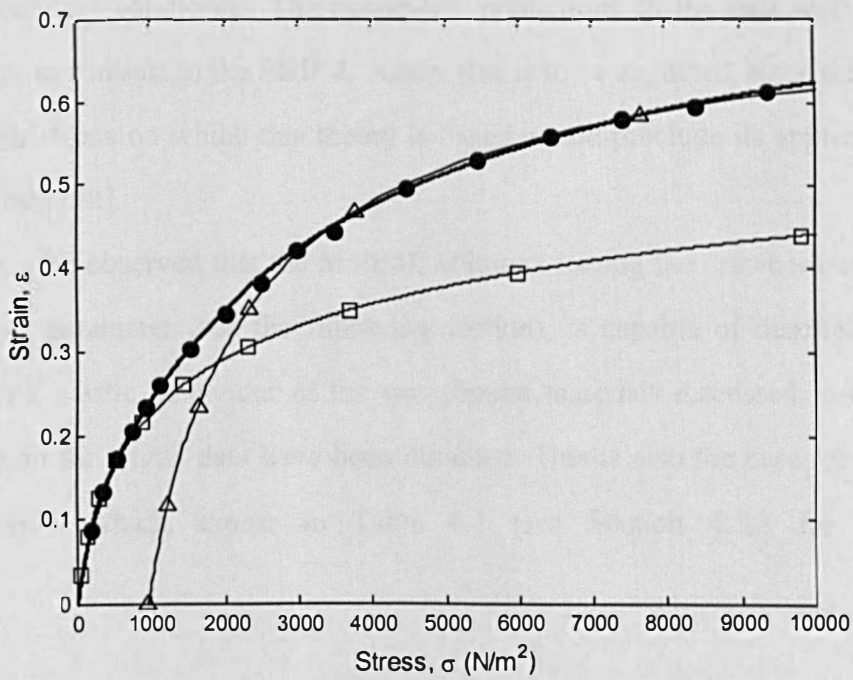

Figure 4.13 Strain-stress behaviour of the acoustic duct lining material. •, measurement; ——, MNBM; —□—, SNBM; —Δ—, power-law model.

Based on the three parameters – the Young's modulus E, the solid fraction Ψ_0 and the constant ζ – the measured nonlinear strain-stress behaviour of the two fibrous materials (See Table 4.1) studied can be well reproduced by the MNBM, as shown in Figures 4.12 and 4.13. A value of 7.5×10^{10} *Pa* is used as the Young's modulus of the solid material in both cases. The values for adjusted solid fraction are 0.0093 and 0.0144, for the thermal insulation blanket and duct lining material respectively. The fact that four-digit accuracy is necessary for the solid fraction is an indication of the sensitivity of the MNBM to this parameter. Further discussion about the sensitivity will follow in the next section. The constant parameter ζ has the values 22.06 and 7.92 for the thermal insulating blanket and the duct lining, respectively.

In the case of the SNBM, it is found that good agreement between prediction and measurement is observed only in the low strain region. This is because flexibility or rotation at the contact points or at the end of links has not been taken into account. Therefore, the discrepancy in the high strain regime is not surprising, considering that a greater load is more likely to result in situations which would violate the assumption of idealised boundary conditions. The power-law predictions fit the data well in the high strain region, in contrast to the SNBM. Again, this is to be expected, since the underlying physical restrictions on which this theory is based would preclude its application at low values of strain [22].

It may be observed that the MNBM, although having the drawback of containing an adjustable parameter (see the following section), is capable of describing well the observed bulk elastic behaviour of the two fibrous materials discussed, over the entire range of strain for which data have been obtained. This is also the case for a variety of other materials which appear in Table 4.1 (see Section 4.5.3 for discussion).

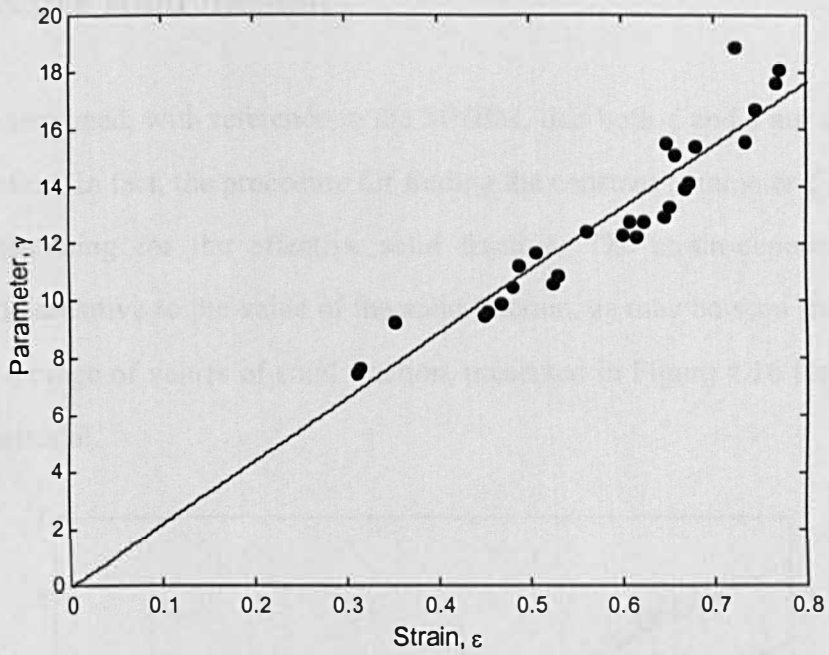

Figure 4.14 Parameter γ for the thermal insulation blanket. •, evaluated γ; ——, regression line.

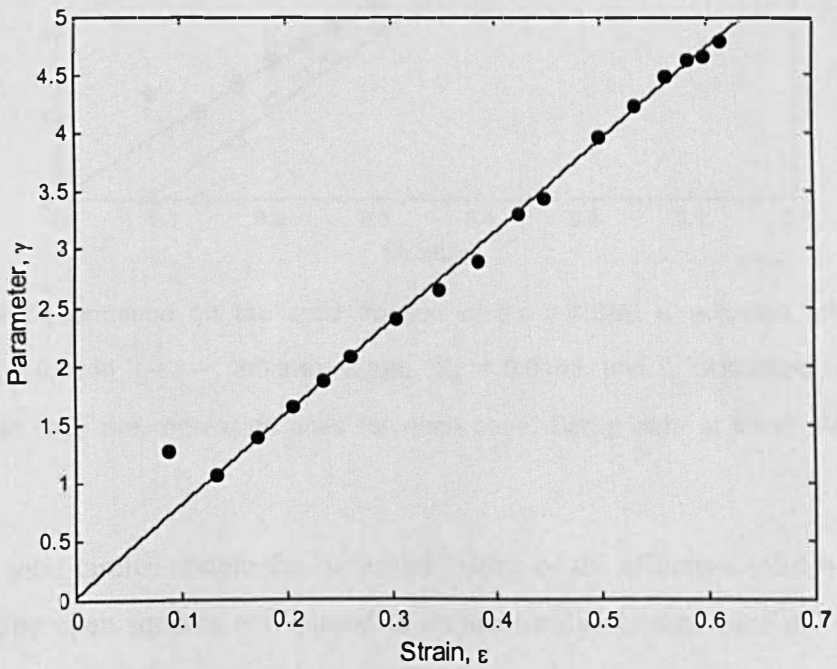

Figure 4.15 Parameter γ for the acoustic duct lining material. •, evaluated γ; ——, regression line.

4.5.3 Effective solid fraction

It has been mentioned, with reference to the MNBM, that both ζ and γ are dependent on the solid fraction. In fact, the procedure for finding the constant parameter ζ is equivalent to that in searching for the effective solid fraction. The strain-dependence of the parameter γ is sensitive to the value of the solid fraction, as may be seen from plots of γ versus ε for a range of values of solid fraction, presented in Figure 4.16 for the acoustic duct lining material.

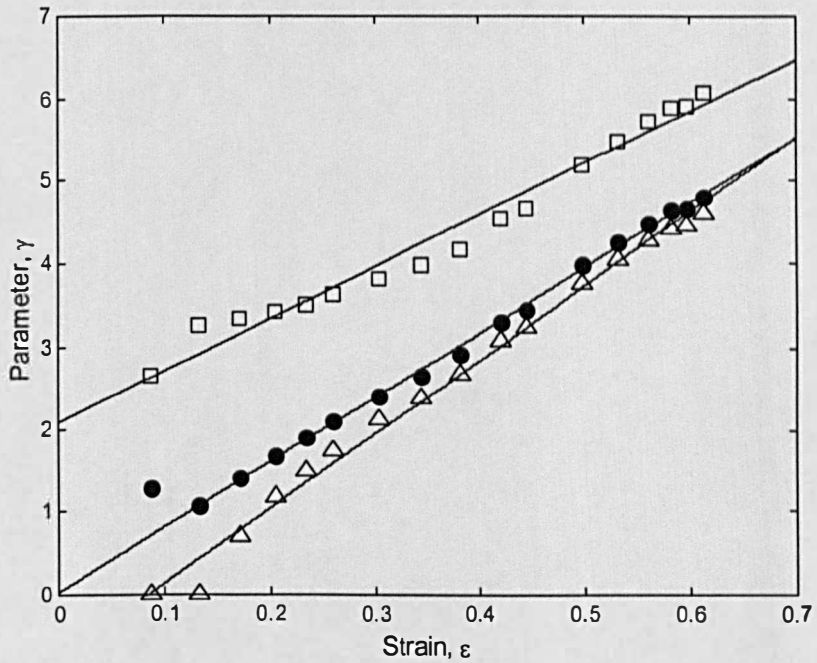

Figure 4.16 Dependence on the solid fraction of the MNBM. •, adjusted effective solid fraction, Ψ_0 = 0.0144; —□— , arbitrary value, Ψ_0 = 0.0165, and Δ, calculated value, Ψ_0 = 0.0140. Solid lines are regression lines for each case. Some data at lower strain are not counted.

The solid circles denote the "adjusted" value of the effective solid fraction, equal to 0.0144. The open squares correspond to an arbitrarily chosen value of Ψ_0 = 0.0165, which was about 15% higher than the adjusted value. The open triangles are matching to a calculated value of Ψ_0 = 0.140, based on an assumed solid density of 2500 kg/m^3 and the measured bulk density of 35 kg/m^3. It is worth noting that, in this case at least, the adjusted value of Ψ_0 is only about 2.9% higher than the calculated figure (which is

Property	Acoustic duct lining material	Aircraft thermal insulation	Rockwool 1	Rockwool 2	E-glass wool	Basalt wool	Glass fibre wool	Steel wool (circular section fibres)
Bulk density† kg/m^3	35.0	9.0	57.8	41.2	27.2	57.1	10.6	57.8
Solid density‡ kg/m^3	2500	2500	2500	2500	2570	2700	2500	7900
Young's modulus of frame‡, N/m^2	7.5×10^{10}	7.5×10^{10}	9.85×10^{10}	9.85×10^{10}	7.7×10^{10}	8.9×10^{10}	7.5×10^{10}	2.1×10^{11}
Adjusted solid fraction	0.0144	0.0093	0.0232	0.0188	0.0161	0.0115	0.0099	0.0100
Calculated solid fraction	0.014	0.0036	0.0231	0.0165	0.0106	0.0211	0.00424	0.00732
Parameter ζ	7.92	22.06	8.73	9.16	9.345	9.387	14.246	18.377

† Measured value

‡ Assumed value (based on published data)

Table 4.1 Various parameters for a range of fibrous materials related to the Modified Nonlinear Bending Model (equation(4.27)).

dependent on the assumed value of the solid density, itself subject to a degree of uncertainly in view of the unknown binder content of this material).

In all three of the cases presented in Figure 4.16, the parameter γ increases approximately linearly with ε, although the non-adjusted cases have offsets from the origin, preventing γ from being represented solely by its slope. It is worth noting again that the procedure for finding the effective solid fraction is equivalent to a search for the constant parameter ζ. This means that, once the solid fraction is adjusted, it will result in a unique value of the parameter ζ. The solid fraction is therefore actually the *only* adjustable parameter among the three in the equation (4.27).

It is, of course, possible for equation (4.27) to be re-defined such that it includes both the slope and the zero offset of the parameter γ. In this case, however, the total number of parameters will be increased by one. (This is clearly a disadvantage in the model, and one may conclude that the adjustment to find the effective solid fraction is worthwhile in order to minimise the total number of parameters.) If, however, the extra-parameter scheme is adopted and the adjustment procedure is discarded, the MNBM in equation (4.27) can be re-defined as

$$\sigma = \frac{3\pi E\left(\frac{4}{\pi}\frac{\Psi_0}{1-\varepsilon}\right)^5 \varepsilon}{1+192\left((a\varepsilon+b)\frac{4}{\pi}\frac{\Psi_0}{1-\varepsilon}\right)^2}. \tag{4.29}$$

The parameters a and b denote the slope and zero offset in Figure 4.16. For the adjusted case, the parameter a is equivalent to ζ, and the parameter b may be assumed to be zero. Predictions from equation (4.29) for the acoustic duct lining material are compared, in Figure 4.17, to those from the adjusted case of equation (4.27). It can be observed that, over the strain range of interest, both definitions adequately describe the nonlinear stress-strain relationship of a fibrous material.

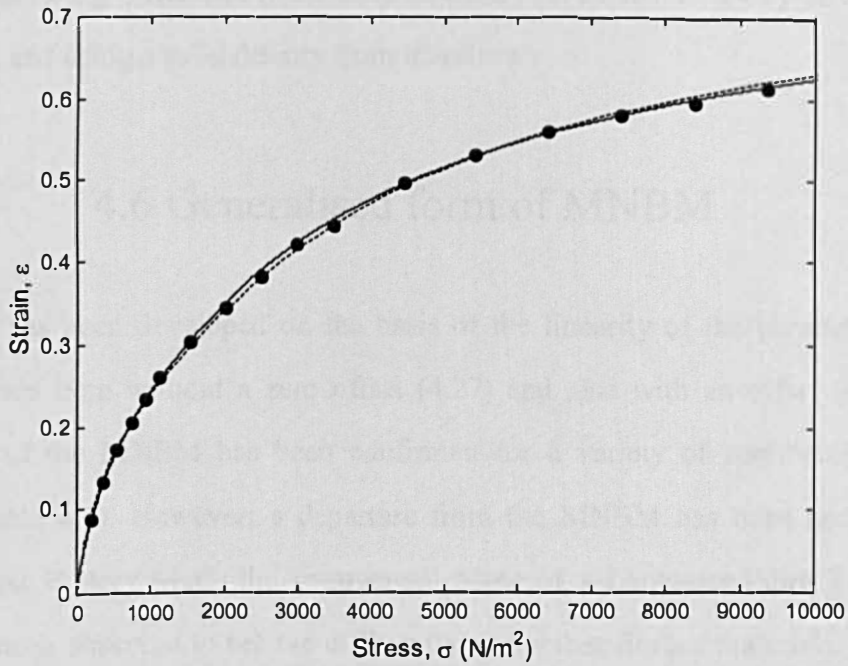

Figure 4.17 Strain-stress behaviour of the acoustic duct lining material. •, measurement; ------, equation (4.29) with four parameters and a measured solid fraction of 0.0140; ——, equation (4.27) with three parameters and an effective solid fraction of 0.0144.

It is of interest to see whether materials other than the duct liner exhibit such close correspondence between the values of adjusted and calculated solid fraction. In Table 4.1 such a comparison is given for a variety of fibrous media, and other relevant data are also included. It can be seen that the correspondence between adjusted and calculated solid fraction figures varies considerably, ranging from fair to excellent for five of the materials (duct lining, Rockwool 1, Rockwool 2, E-glass wool and steel wool) and being poor for the other three materials (thermal insulation, basalt wool and (lightweight) "glass fibre wool"). It is hard, at this stage, to speculate on the reasons for these disparities. However, it is worth noting that the calculated solid fractions in Table 4.1 are based on the published data for solid density of fibres. Thus, strictly, there could be difference between the values in the literature and the true solid densities. Also, the contribution of binding materials was not taken into account, although their effect is assumed small unless heavily used. In addition, the initial state of a fibrous material may need to be accounted for, if it has been already significantly compressed. However, this

might not make a big difference if the solid fraction is evaluated in a way of weighing a bulk material and using a solid density from literature.

4.6 Generalised form of MNBM

The MNBM has been developed on the basis of the linearity of the parameter γ with respect to strain both without a zero offset (4.27) and also with an offset (4.29). The applicability of the MNBM has been confirmed for a variety of commercial fibrous materials (Table 4.1). However, a departure from the MNBM has been noted in rare cases. "A-glass Battery Mat", the commercial name of a Lancaster Fibre Technology product, has been observed to behave differently from other fibrous materials. As can be seen in Figure 4.18, the parameter γ is not linearly related to the strain ε, but has a nonlinear curvature, which cannot be described by the MNBM regardless of whether it has an offset or not. However, it has been revealed that a linear relationship with strain may be found by the use of the relationship $\gamma = \zeta\,\varepsilon$ (in other words, the parameter ζ is assumed to be the *slope* of γ). Now, the parameter ζ may be observed to vary almost linearly with strain (Figure 4.19), after a trial-and-error choice of the solid fraction Ψ_0. (Note again that the parameter ζ is a constant in the MNBM.) Therefore, the nonlinear stress-strain performance of a fibrous material such as A-glass Battery Mat could be described by a generalised form of the MNBN,

$$\sigma = \frac{3\pi E\left(\frac{4}{\pi}\frac{\Psi_0}{1-\varepsilon}\right)^5 \varepsilon}{1+192\left((\alpha\,\varepsilon+\beta)\varepsilon\,\frac{4}{\pi}\frac{\Psi_0}{1-\varepsilon}\right)^2}. \tag{4.30}$$

(Because of the introduction of the generalised form of the MNBM in (4.30), it may be better to refer to the MNBN in (4.27) and (4.29) as the "original MNBN" to avoid confusion. A further distinction between (4.27) and (4.29) is clearly related to the offset.) The original MNBM without an offset in (4.27) can be deduced from the generalised MNBN when the parameter α goes to zero, in which case the parameter β will be

equivalent to ζ. Finally, when the parameters α and β are determined by the adjustment of the initial solid fraction with a prior knowledge of the Young's modulus of a fibrous material (See Table 4.2), the nonlinear stress-strain relationship of the A-glass Battery Mat can be described successfully as one may see from Figure 4.20.

	A-glass Battery Mat	A-glass non-adhesive bulk	E-glass non-adhesive bulk
Solid fraction	0.0160	0.0138	0.01375
Young's modulus of frame N/m^2	6.8×10^{10}	6.8×10^{10}	7.7×10^{10}
Parameter α	-16.453	-15.118	-20.653
Parameter β	13.892	10.240	14.835

	E-glass adhesive bulk	Layered stainless steel bulk	3-D stainless steel bulk
Solid fraction	0.01445	0.0100	0.0100
Young's modulus of frame N/m^2	7.7×10^{10}	21×10^{10}	21×10^{10}
Parameter α	-22.469	-74.176	Parameter ζ
Parameter β	14.589	73.492	18.377

Table 4.2 Parameters for various fibrous materials whose structural behaviour has been analysed by the generalised Modified Nonlinear Bending Model. Young's modulus of the frame is assumed (from literature). Solid fraction is adjusted. Parameters α and β are evaluated according to equation (4.30). The data for 3-D stainless steel bulk were taken from Table 4.1.

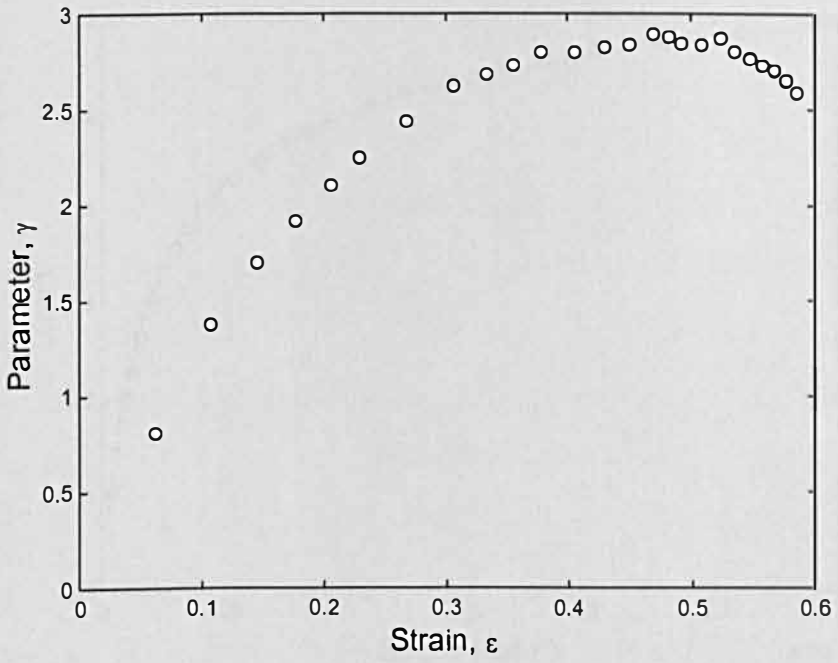

Figure 4.18 Nonlinear characteristics of the parameter γ for A-glass Battery Mat.

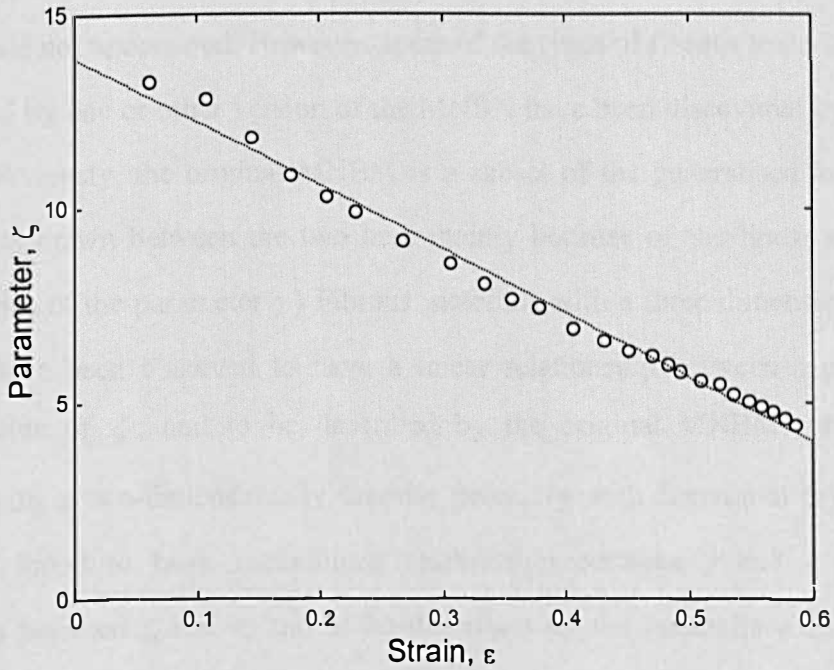

Figure 4.19 Linear variation of the parameter ζ for A-glass Battery Mat. The circles are for the evaluated values from the measurement data, and the dotted line is for linear regression.

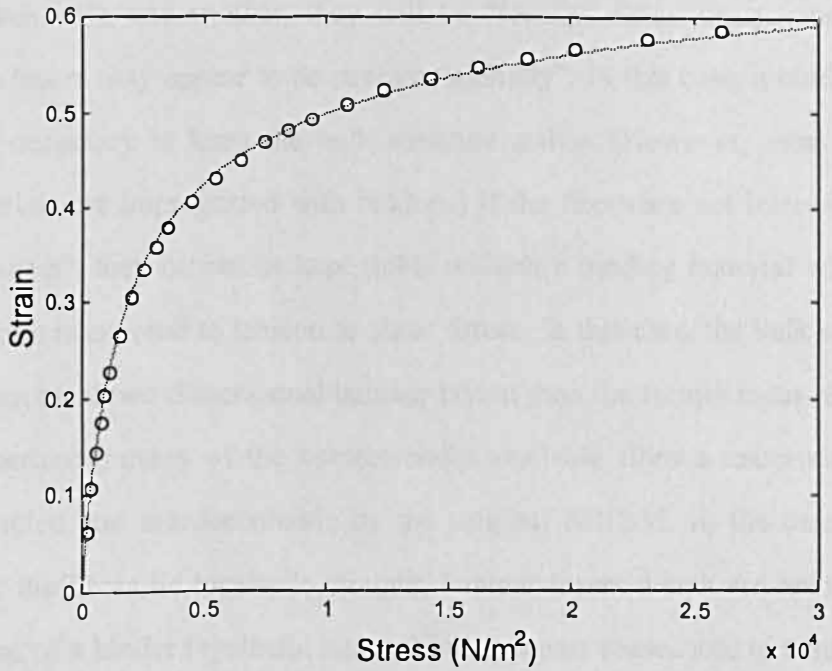

Figure 4.20 Measured and predicted nonlinear strain-stress relation of A-glass Battery Mat. The circles represent the measurement data and the dotted line the generalised MNBM predictions.

The physical reasons why such a generalised version of MNBM appears to be successful are not understood. However, some of the types of fibrous material which may be described by one or other version of the MNBN have been discovered by an heuristic process. (Obviously, the original MNBM is a subset of the generalised MNBM. But a distinction is drawn between the two here mainly because of the linear and nonlinear characteristics of the parameter γ.) Fibrous materials with a three-dimensionally tangled geometry have been observed to have a linear relationship between γ and ε, with a constant value of ζ, and to be described by the original MNBM, (4.27). Fibrous materials with a two-dimensionally laminar geometry with horizontal layers of fibres have been found to have a nonlinear relationship between γ and ε and a linear relationship between ζ and ε, and to be described by the generalised MNBM (4.30). Actually, whether the geometry is two-dimensional or three-dimensional may not be straightforward to decide and hence falls to the individual's judgement.

The author's own criterion is mainly based on whether fibres are interwoven and hence its bulk structure is stable without consolidation by a binding material. If the fibres

are interwoven with one another, they will be "locally" three-dimensionally tangled, although the layers may appear to be straight "globally". In this case, a binding material may not be necessary to keep the bulk structure stable. (However, most commercial fibrous materials are impregnated with binders.) If the fibres are not interwoven but are merely "piled up", they cannot be kept stable without a binding material when the bulk fibrous medium is exposed to tension or shear forces. In this case, the bulk structure will be closer to an ideal two-dimensional laminar layout than the former cases. Based on the author's experience, many of the commercially available fibrous materials have been "locally" tangled and are describable by the original MNBM. In the case of A-glass Battery Mat, the fibres lie locally in straight, laminar layers which are held together by the liberal use of a binder (synthetic latex). Thus it seems reasonable to assume that this is a two-dimensional laminar structure rather than a three-dimensional tangled structure. This argument concerning the categorisation of fibrous materials has been supported by further examination of fibrous materials which have been fabricated under laboratory conditions. It will be further discussed in the following sections.

4.6.1 Case study 1: the fibre component and the use of binder

Three bulk fibrous materials (made from glass fibres) have been fabricated by the author in the laboratory. Each layer of fibres was made by placing the fibres horizontally together, a few at a time. The structure is similar to that shown in the left-hand photo of Figure 4.24.Alternate sets, each of several layers, were orientated perpendicularly to one another to achieve a stable bulk structure. Both A-glass and E-glass fibres were used to construct the bulk structure. A- and E-glass are types of glass with different chemical compositions. With each type of glass fibre, two types of structure were made: one reinforced by spray type glue used as a binder, and the other without any binder. Thus, in terms of the categorisation introduced in the previous section, all the fabricated bulk fibrous materials had the general form of a two dimensional laminar structure. Comparisons between the experimental data and predictions have shown that these

materials are all describable by the generalised MNBM (4.30). In Figure 4.21 (which shows measured data from three of the materials), the parameter γ is observed to bear a nonlinear relationship to strain. In Figure 4.22, the parameter ζ is seen to vary linearly with the strain. In Figure 4.23, the nonlinear bulk strain-stress behaviour of these fabricated materials is observed to be well predicted by the use of the generalised MNBM. (See also Table 4.2 for parameters.) By observing that different types of material and the use of adhesive (non-adhesive A-glass, and adhesive/non-adhesive E-glass) do not make a significant difference to the general behaviour of the parameters, one may suggest that the need for the generalised MNBM was not brought about by such details of the structure of the material. Instead, the observation seems to support the author's assertion that the generalised MNBM is applicable particularly to materials having a two-dimensional laminar structure.

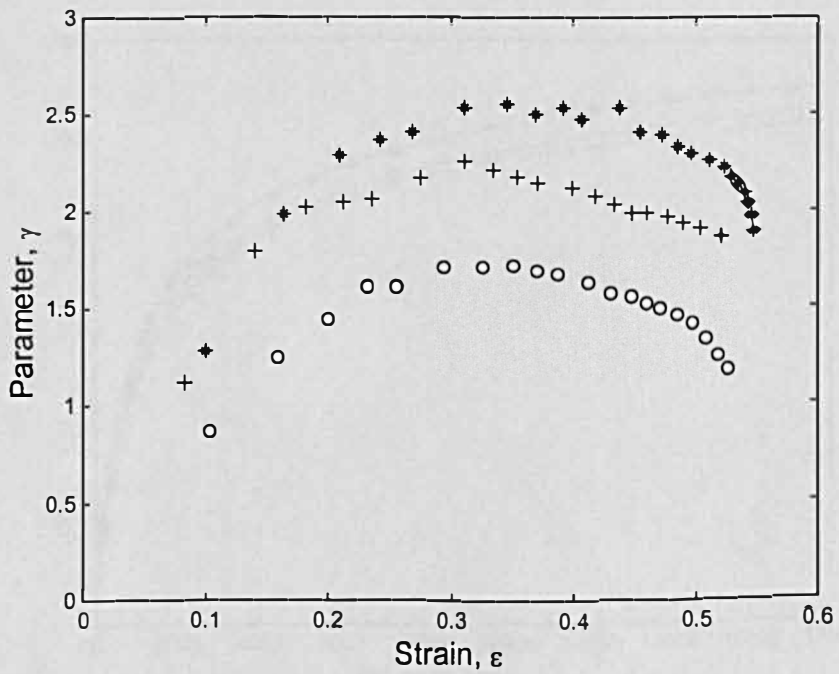

Figure 4.21 Nonlinear characteristics of the parameter γ for bulk fibrous materials manually fabricated by the author. The circles for the 31 *mm* thick A-glass bulk material without binder, the asterisks for 33 *mm* thick E-glass without binder and the crosses for 21 *mm* thick E-glass with binder.

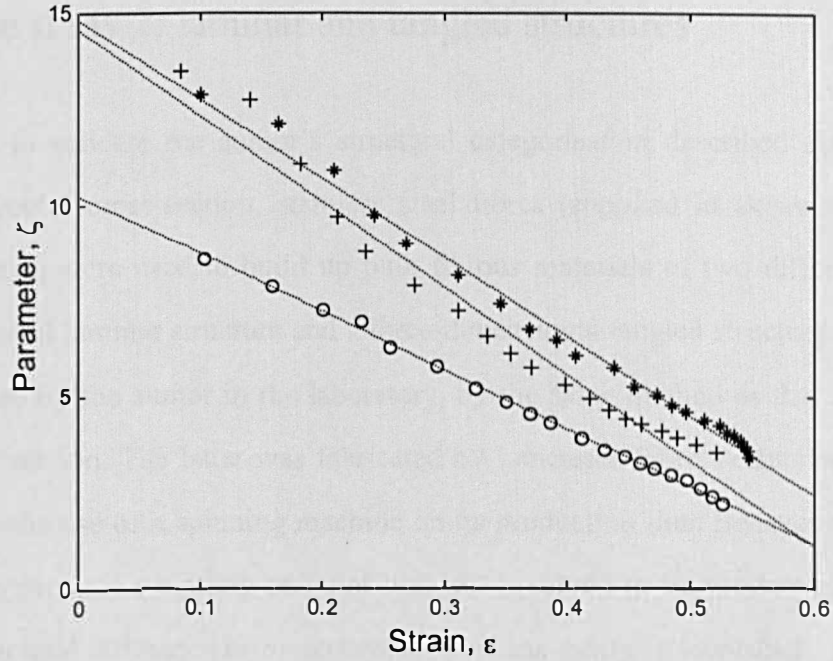

Figure 4.22 Linear variation of the parameter ζ for bulk fibrous materials manually fabricated by the author. The symbol notation is the same as that in Figure 4.21.

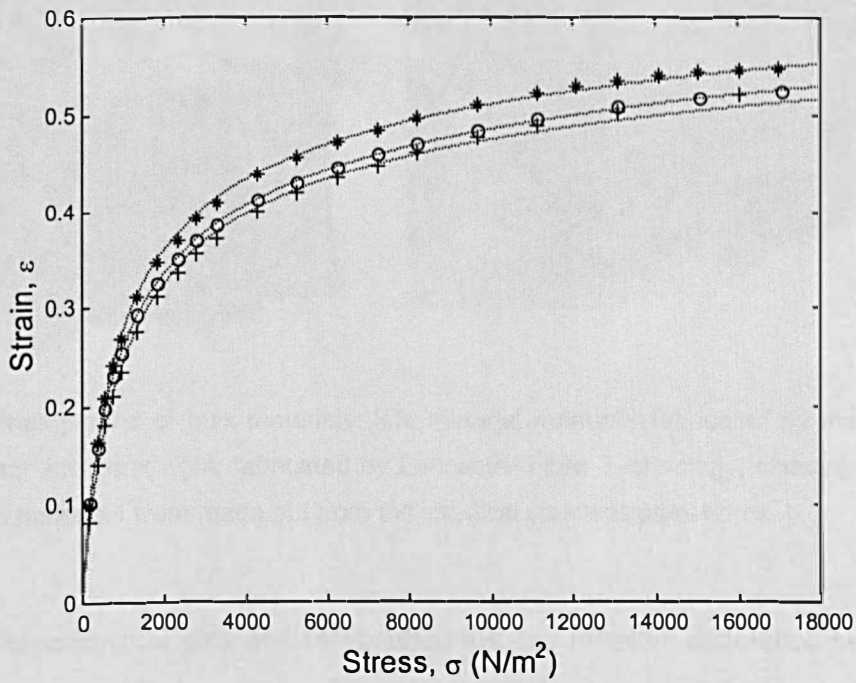

Figure 4.23 Measured and predicted nonlinear strain/stress relation of bulk fibrous materials manually fabricated by the author. The notation of discrete symbols is the same as in Figure 4.21, and the dotted line for the generalised MNBM for each material.

4.6.2 Case study 2: laminar and tangled structures

In an effort to validate the author's structural categorisation described above, 12 μm diameter, circular cross-section, stainless steel fibres (supplied in skeins of constant-diameter fibres) were used to build up bulk fibrous materials of two different types: a two-dimensional laminar structure and a three-dimensional tangled structure. The former was fabricated by the author in the laboratory, by the same method as that described in the previous section. The latter was fabricated by Lancaster Fibre Technology, and was produced by the use of a spinning machine on its production line. Because of its highly interwoven structure, a binding material was not involved in its production. In Figure 4.24, the structural difference between two samples can easily be identified.

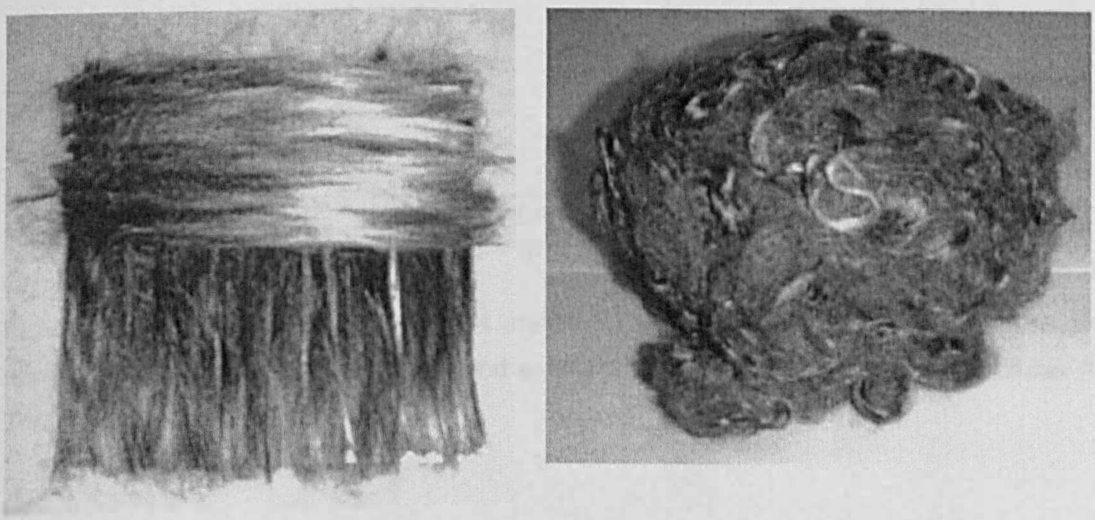

Figure 4.24 Photographs of bulk materials: left, material manually fabricated by the author, showing laminar structure; right, fabricated by Lancaster Fibre Technology, showing tangled structure. Both materials were made out from the identical stainless steel fibres.

In both the experimental data and the predictions, the intrinsic difference between two bulk materials is very evident. In Figure 4.25, the parameter γ for the tangled bulk material varies almost linearly with strain, while the layered bulk medium exhibits a very nonlinear relationship. In Figure 4.26, the parameter ζ for the tangled medium is evidently described by a constant value, while the layered medium requires a linearly

varying ζ. As a consequence, the nonlinear strain-stress behaviour of the two types of bulk material can be well described by the original MNBM for the tangled structure and by the generalised MNBM for the layered structure (See Figure 4.27 and Table 4.2). The findings in this and the previous case studies would seem to offer at least partial justification for the author's method of categorisation.

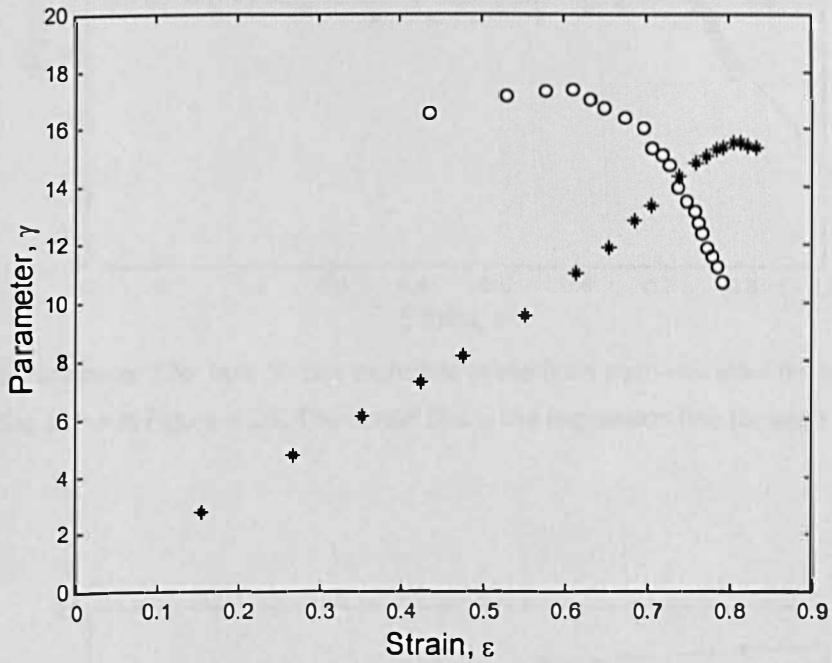

Figure 4.25 Parameter γ for bulk fibrous materials made from stainless steel fibre. The circles denote that fabricated by the author, and asterisks denote that fabricated by Lancaster Fibre Technology.

It is worth noting that, although this divergence in structural behaviour between the two categories of fibrous media seems to be supported by the experimental evidence, the very idea of the tangled and two-dimensional laminar categories appears to be contradictory to the ideas implicit in the bending models themselves, if one recalls that their development was based on the ideal laminar structure (Figure 4.6). For consistency with the bending model, the laminar type of fibrous materials, such as the ones in Case study 1 and in left-hand photo in Figure 4.24, should be predictable by the original MNBM, rather than by its generalised form. However, it is believed that such an inconsistency does not necessarily invalidate the ideas associated with the MNBM. That

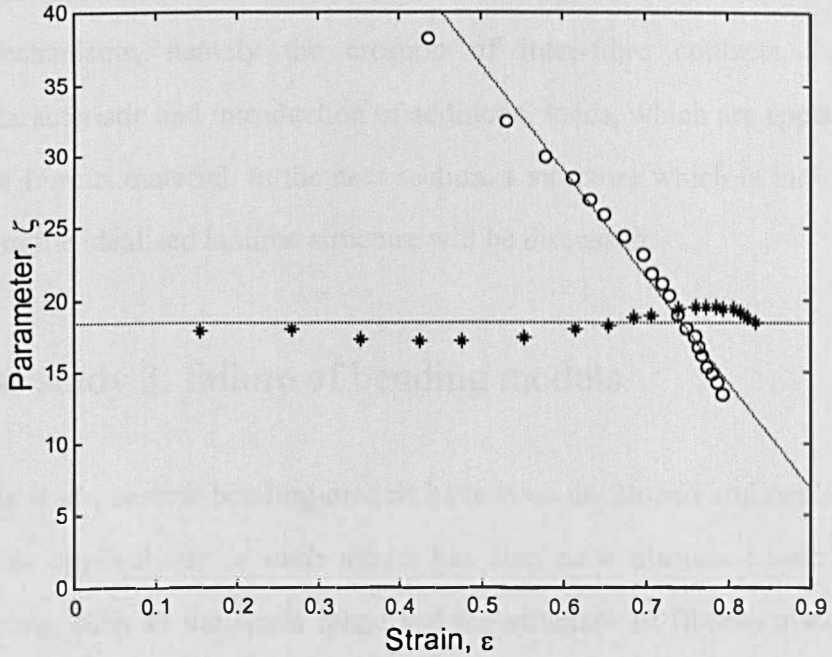

Figure 4.26 Parameter ζ for bulk fibrous materials made from stainless steel fibre. The symbol notation is the same in Figure 4.25. The dotted line is the regression line for each sample.

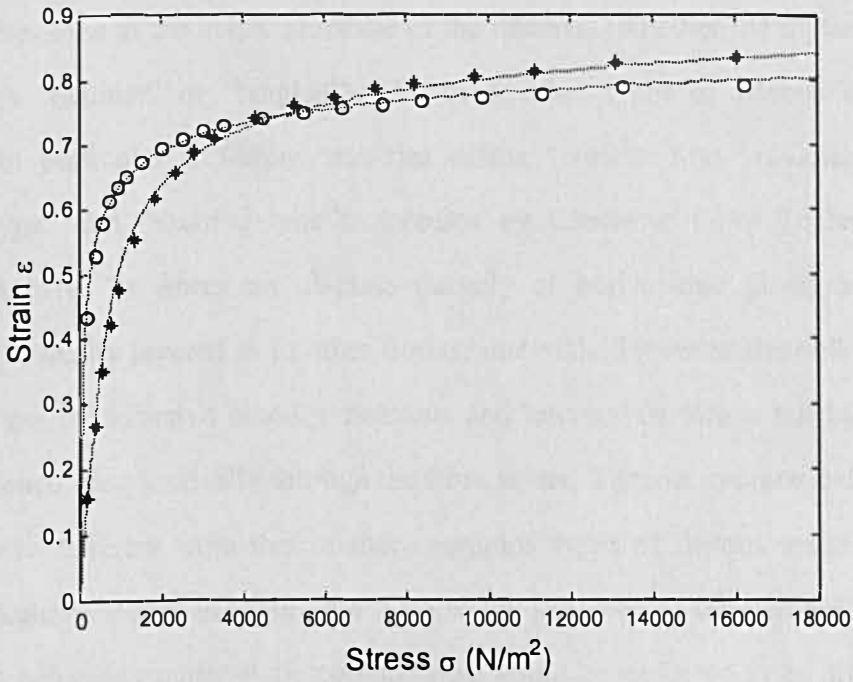

Figure 4.27 Measured and predicted nonlinear strain/stress relation for bulk fibrous materials out of stainless steel fibre. The notation for discrete symbols is the same as that in Figure 4.25. The dotted line denotes the generalised MNBM for each sample.

is because the fine details of the model are not so much at issue as the underlying physical mechanisms, namely the creation of inter-fibre contacts, corresponding nonlinear characteristic and introduction of additional loads, which are applicable to both categories of fibrous material. In the next section, a structure which is indisputably very different from the idealised laminar structure will be discussed.

4.6.3 Case study 3: failure of bending models

So far in this work, several bending models have been developed and applied to fibrous materials. The applicability of each model has also been discussed with reference to specific features such as the strain range and the structure of fibrous materials. In this section, however, both the applicability and the theoretical background will be considered for the bending models "as a whole". The SNBM and MNBM bending models are both based on a stacked cylinder model with an idealised laminar structure. So far, they have only been applied to real fibrous materials for which such a structure has some relevance to the actual structure of the material (whether the materials may be described as "laminar" or "tangled"). However, other types of fibrous material are available. In particular a fibrous material called "Needle Mat" (available as both "acoustic type" and "thermal type"), supplied by Lancaster Fibre Technology, was investigated here. Its fibres are E-glass (largely of borosilicate glass) and its bulk structure is basically layered as in other fibrous materials. However the bulk structure is kept stable not by adhesive binding materials and interwoven fibres, but by glass fibre "needles" penetrating vertically through the fibre layers. Thus its geometrical structure is fundamentally different from that of more common types of fibrous material and also from the idealised model in Figure 4.6. Due to the presence of the vertical needles, the stress-strain behaviour under static compression would be expected to be different. That is because the vertical needles will have a tendency to buckle or collapse (as shown schematically in Figure 4.28) when the critical compressive force is reached.

Examination of the strain-stress plots in Figure 4.29 reveals the effects of such a buckling effect, highlighted by dashed ellipses for acoustic-type and thermal-type Needle Mat.

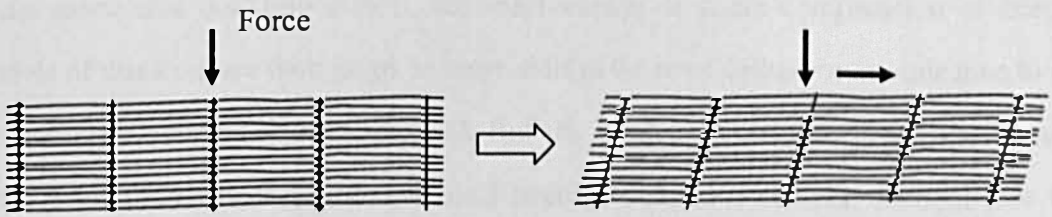

Figure 4.28 Schematic diagram depicting the structural behaviour of a fibrous material having vertical members under compression.

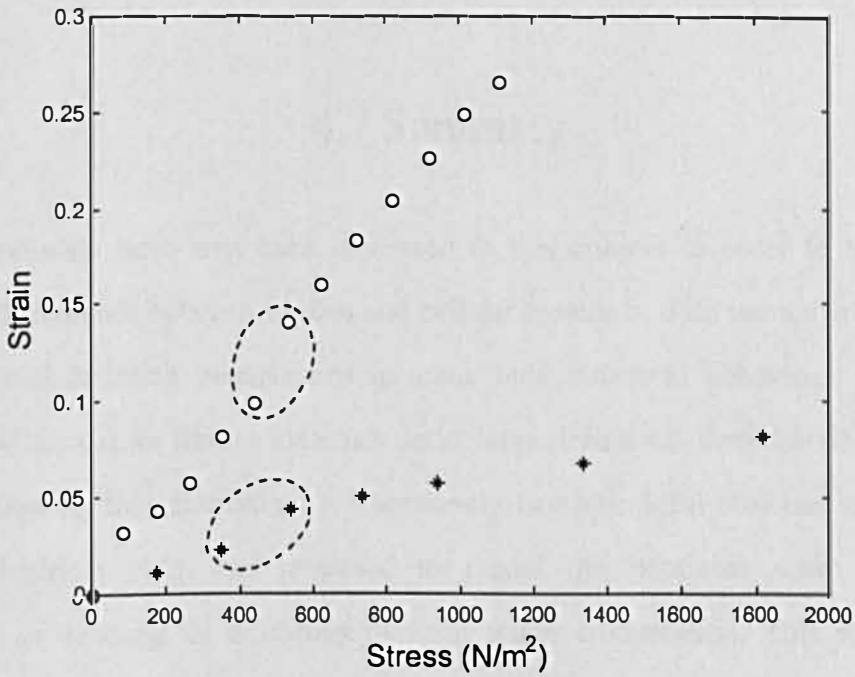

Figure 4.29 Measured strain-stress behaviour of Needle Mat fibrous materials. The circles are for an acoustic type material and asterisks for a thermal type material. The dashed ovals denote the regions where a structural buckling effect occurs.

The similarity in the stress at which buckling occurs is believed to imply that the critical force is about the same for both structures. Hence it is also deduced that the structural behaviour in compression normal to the plane of the material is mainly governed by the buckling of the vertical needles, not by the creation of new inter-fibre contacts, although there may be such an effect prior to collapse. Because of buckling, the strain-stress

relationship of needle mats is not thought to be describable by any of the bending models so far discussed. It may be noted that, because of the presence of vertical needle fibres and the associated buckling effects, the mechanisms of static compression of fibrous materials of this kind are thought to be more akin to those of cellular materials than to the more common types of fibrous material. But the degree of collapse is evidently much smaller in a fibrous material with vertical needles than in a cellular material (see the difference in the amount of the vertical jump of strain between Figures 4.2 and 4.29). That is, perhaps, because of an inherent structural difference related to the fairly close proximity between layered fibres and the relatively remote distance between cell frames (see Figure 2.1).

4.7 Summary

Cellular materials have first been discussed in this chapter in order to highlight the structural differences between fibrous and cellular materials, with particular reference to the associated differing mechanisms in static bulk structural behaviour. An existing "power-law" model for fibrous materials under large strains was then described.

Following this discussion, a transversely isotropic ideal structure consisting of elastic cylindrical rods was proposed to model the nonlinear static stress-strain behaviour, in bending, of a fibrous material under compression. This structure is a stacked cylinder model, incorporating staggered alternate layers in order to allow the components to bend. Initially, a model incorporating linear bending behaviour was described, and this was then extended to its nonlinear counterpart. In this second model, the concept of the shortening of micro-structural fibre links was introduced to account for the increase in the contact density between fibres upon compression of the material, a key mechanism of the nonlinearity. This shortening of link length was then related to a changing volumetric solid fraction, with strain, preserving the nonlinear stress-strain behaviour. The simplest model to take account of this nonlinearity effect, i.e. the simple nonlinear bending model (SNBM), was shown not to predict the nonlinear behaviour

well at high strain. A modified model (MNBM) was formulated to include fibre flexibility at the contact points at the ends of each fibre link. Finally a modified version of the nonlinear bending model was shown to be in good agreement with measured data, when the solid fraction is treated as an adjustable parameter because of the sensitivity of the model to the solid fraction at zero strain. It was also shown that the MNBM can be re-defined without the adjustment procedure but with one additional parameter. Predictions from these nonlinear bending models were also compared to from the power-law model. It was observed that the SNBM yields good predictions in the low strain region, the power-law model in the high strain region, and the MNBM throughout the strain range of interest.

Additionally a need to "generalise" the MNBM, and make it dependent on the material structure, arose. Support was given to the author's heuristic categorisation of fibrous materials by the results of tests on several fibrous materials fabricated in the laboratory. The behaviour of two-dimensionally layered fibrous materials appeared to deviate from that predicted by the original MNBN, but to be describable by a "generalised MNBM". Two case studies were used to illustrate the application of this latter model. In the third case study, the behaviour of a fibrous material with an unusual structure was examined, and it was concluded that fibre buckling effects were significant in its bulk elastic behaviour.

Among several forms of the MNBM, the preferable model would seem to be the MNBM with an adjusted solid fraction (i.e. the original MNBM without a zero offset in the strain-dependence of the parameter γ), since the predicted strain-stress relationships appear to be very similar in this case and in the case of the model with an offset (equation (4.29)). A range of commercial fibrous materials seems to be well described by the adjusted solid fraction approach.

Chapter 5

Connectivity in fibrous materials

The number of inter-fibre contacts in a fibrous material has been identified as one of the important mechanisms responsible for nonlinear bulk elastic behaviour in compression (see the bending models developed in Chapter 4). This effect has also been experimentally demonstrated in the series of idealised macro-scale models described in Chapter 2. The increase or decrease in contact number within a fibrous material is related to how individual fibres are connected one another. As previously stated (in Chapters 2, 3 and 4), it is impractical to devise complete models of fibrous materials, both taking into account all microstructural details and being applicable to the bulk structure. Therefore, a statistical and macroscopic approach is necessary. Apart from applications to fibrous media, such a connectivity phenomenon has been actively investigated in the field of "percolation theory". Its introduction therefore seems to be appropriate in order to assist in understanding further the structural behaviour of fibrous materials under static compression. It is impossible to do justice to the entire theory of percolation theory in just one chapter, of course, and here it is proposed to discuss only aspects which are relevant to the present investigation. The bending models in Chapter 4 will also be examined in terms of the way in which percolation theory is expressed. And the similarities and differences between the two cases will be discussed.

5.1 Percolation theory

In physics, the term "percolation" is used to describe a situation in which a transition occurs between a "locally-connected" (or "non-percolating") state and an "indefinitely-connected" (or "percolating") state. Such a transitional characteristic itself indicates that the idea of percolation shares features in common with a phase transition such as that of

condensation or evaporation of water at the critical temperature and pressure. Percolation may be seen as a geometrical analogy of a phase transition. However, the difference between the two is that a phase transition is a "dynamical" process which is an obstacle to the creation of a quantitative microscopic theory, but percolation is defined for "static" objects, which leads to an easier situation in developing a microscopic theory [66].

A percolation model may be regarded as an aggregation of points distributed in space. In its simplest form, this space may be idealised as a two-dimensional plane square lattice. Some of the points (or sites) are regarded as linked, adjacent or connected. Whether two points are linked is determined by a random mechanism, governed by types of models mentioned later. The linkage is mathematically determined for a given "probability". Each edge (or bond) in the lattice is thought of as either open (or connected) with a fixed probability p and closed (or disconnected) with a probability $1-p$. Physically, the open edges can be interpreted as inner paths in the lattice. The centre of the lattice can be regarded as placed at the end point of an "infinite" path, when a point near the centre is connected to those on the boundary through a series of open edges. The concept of linkage or path can also be expressed in terms of a "cluster".

A cluster is an aggregation of points, but is a part of the model. It is assumed that points in the same cluster are connected by given paths, but that no path can be found between points in different clusters. If an infinite path between points in different clusters could exist, this would imply the existence of a single, "infinitely connected", cluster. There is a critical value p_c of probability, at and beyond which there can exist such infinite clusters, which would pervade the entire structure of the lattice. Thus one may conceive a situation in which all open clusters are finite in connectivity when $p < p_c$, but where there are only infinitely connected open clusters when $p > p_c$, under which conditions the system is said to be in a percolating state.

In the critical region where the probability p approaches its critical value p_c from either direction, it is widely held that a "percolation quantity" Y behaves as a power of the difference between the two probabilities,

$$Y \approx (p - p_c)^{X_c}. \tag{5.1}$$

This is also known as a "universal power law" of percolation [65, 66]. The exponent X_c is usually known as a "critical exponent", which decides the "universality class" of a particular percolation quantity in a particular percolating system. The critical probability p_c is dependent on the dimension and structure of the model [65]. It is also affected by the type of the percolation model.

In engineering application, the percolation probability p can be replaced with other physical parameters, such as condensation, density, solid fraction, porosity or electric current density, which are all related to "connectivity". And the percolation quantity Y may refer to the effective electrical conductivity, elastic constants such as bulk Young's modulus, transport properties such as flow permeability and so on, and these are represented by the power law relation (5.1) in the critical region. The value of the critical exponent in these cases has been evaluated, together with the critical probability [67~76].

Various kinds of percolation model can be defined according to the connection and occupation rules for the basic elements (sites/points or bonds/edges, for example), which also determine the behaviour of the models as a consequence. Percolation can be divided into several subsets, which themselves can overlap one another. The simplest and most widely investigated is "bond percolation" [65]; the points may be fixed, and the path of random linkage between them is determined by whether the edges (or bonds) are open or closed. In "site percolation" it is sites, rather than bonds (or points), that are declared to be open or closed. Bond percolation can thus be seen as distinct from site percolation. "Mixed percolation" is a mixture of both site and bond percolation and is more often encountered in real systems. A bond/site percolating system is one which becomes un-percolated when its bonds/sites are (respectively) removed [78]. In an "anisotropic percolation" [67, 68, 75], different edges could have different probabilities of being open. Anisotropic percolation is believed to have wide application to disordered materials, in connection with their connectivity state such as elasticity or electrical conductivity. In "long-range percolation" [65], pairs of points may be connected although they are geometrically placed at a distance from one another. In "dependent percolation" (or "correlated percolation"), the probability of being open is not independent of the

surrounding sites and edges. The opposite of dependent percolation is "random percolation", in which sites and edges are occupied with a probability independent of the other elements. "Continuum percolation" [67, 73] deals with a collection of overlapping spheres, discs, rods, or other realistic elements. These elements are allowed to occupy any location within the model. In contrast, a regular lattice is a kind of "discrete percolation" [65], in which points are only defined at the vertices of the lattice. In "time-dependent percolation", the probability of points being open is a function of time. Among the above, bond *versus* site percolation, dependent *versus* random percolation and discrete *versus* continuum percolation may be regarded as the most significant pairs.

Percolation theory has been found to play an important role in the analysis of disordered media. In this application, it has been regarded as one of the simplest mathematical and physical tools with the minimum statistical dependence [65]. It is often stated that percolation theory emerged as a consequence of attempts to answer a simple question relating to the probability that the centre of a porous rock is wetted when the rock is immersed in water [65]. Intuitively, if the porous rock were composed entirely of closed cells, the water would not be absorbed at all. If, on the other hand, the rock had only open cells, then it would be simply a matter of time before the water reaches the centre of the rock. However, in a more realistic situation where the rock comprised a combination of both open and closed cells, the problem of calculating the probability would not be straightforward. Percolation models can be useful in dealing with the spread of an epidemic in an orchard [65]. Trees may be hypothetically positioned at the points of a lattice in the model. A probability, which is often a function of distance, can be assigned to the odds that a blighted tree would infect a healthy tree in its vicinity. The spacing between trees needs to be sufficiently greater than that associated with the critical probability in order to escape the catastrophic outcome that a small portion of the trees will eventually infect the majority of trees. In the same way, percolation theory can also be applied to the spread of bacteria and fire propagation in a forest. Another application is in telephone engineering, where all possible paths connecting a pair of callers can be made in the switching network. When lines are busy, a new call may be

blocked. Thus, in theory, a tolerable blocking probability is required in designing the network in order to keep the switching system economic and competitive.

5.2 Literature review

Critical transition behaviour in the percolation model has been investigated experimentally [67] and in simulations [68~71, 74, 75]. The percolation threshold p_c and the critical exponent X in equation (5.1) have attracted the greatest interest in investigations. Among the various possible critical behaviours, that of electrical conductivity has long been popular, because percolation is believed to be closely related to the onset of electric conduction in a composite material [67, 75, 75, 76]. The conductivity in a carbon-fibre polymer composite material has been the main subject in the percolation approach [67, 68, 75]. This type of material is renowned for excellent electromagnetic interference (EMI) shielding and other electromagnetic characteristics [75, 76]. It consists of a polymer as a matrix and "fibres" as particles inside. An epoxy resin (containing a hardener) is often used as a polymer and typically has very high resistivity, while carbon fibres have high conductivity and high elastic modulus. The fibres are mixed with resin in a controlled concentration (or solid fraction).

Carmona et al. [67] investigated the effect of anisotropy as a function of particle aspect ratio in a percolation model. Their percolation model of a carbon fibre/polymer composite embodied randomly disordered fibres but had a non-isotropic geometric property. The authors observed that a sharp drop of electrical resistivity occurred at a critical volume fraction, and that the percolation threshold was lower than that in an isotropic percolating system. Such a drop in resistivity is interpreted as the onset of electrical conduction, which is related to the existence of infinitely connected carbon fibres. When spheres are embedded in epoxy resin, this constitutes an isotropic system and the "number of contacts" per sphere is likely to be limited. Where the particles are long disordered fibres, a greater number of inter-particle contacts can be expected (depending on the aspect ratio) because of an increase in the total surface area. Thus, this

increase in the number of contacts leads to lowering the critical volume fraction in the composite. The authors' argument concerning the increased number of contacts for carbon fibres in the composite can be related to that of an increase in the number of contacts in a fibrous material under compression.

Boissonade, Barreau, and Carmona [68] used a three-dimensional cubic lattice to evaluate the critical exponent, X, in a Monte Carlo simulation. They determined the critical probability p_c as a function of the length of a "fibre". These authors reached the conclusion that their simulated anisotropic systems shared the same universality class as other isotropic percolating systems, on the basis that their critical exponents had about the same value as those typical of other three-dimensional random percolation processes. Although it was not explicitly stated, the critical probability in their anisotropic system might be expected to be different from those of isotropic cases, according to the results of other investigations [67, 73, 75].

Kantor [69, 74] investigated a two-dimensional square lattice by the use of the Monte Carlo method and demonstrated that geometrical properties can be useful in evaluating certain physical properties of a percolating system. Together with Webman [71], Kantor specifically focused on the macroscopic elastic modulus of an "elastic percolating system", with long thin rods having the properties of both bending and stretching. The critical behaviour of the effective elastic constant κ, which could be a bulk or shear modulus, was given by

$$\kappa = \kappa_0 (\Psi - \Psi_c)^{\tau}, \tag{5.2}$$

where κ_0 is a proportionality constant, τ is the critical exponent, and Ψ and Ψ_c are the solid volume fraction and its critical value respectively. He suggested values for the lower and upper bounds of the critical exponent in the cases of two-dimensional square and three-dimensional cubic lattices. It was also emphasised that the critical exponent of the macroscopic elastic stiffness was significantly larger than that in an electrical conductivity percolation model, and confirmed that the elastic behaviour belongs to a different universality class from that of conductivity.

Balberg, Bindenbaum and Wagner [70] examined a three-dimensional continuum system, characterised by the overlapping of regular objects such as spheres, cubes, and ellipsoids. The critical concentration was reported to be dependent on the aspect ratio of the objects and on the macroscopic anisotropy. Their study was limited to the critical threshold, and specific properties such as the electrical conductivity or elastic properties were not investigated. Although not explicitly stated by these authors, an inference may be drawn from their results concerning the dependence of the critical threshold on the aspect ratio and macroscopic anisotropy, leading to the conclusion that the critical probability of threshold is an "intrinsic property" of a material.

Deptuck, Harrison and Zawadzki [72] fabricated a set of "sintered, submicron, silver-powder beams" with pre-determined volume fractions Ψ. The silver powder was bonded by sintering to form a porous beam while heated in a stainless-steel mould in which the powder was distributed in a controlled solid volume fraction. Measurements were then performed to determine the Young's modulus E_b and electrical conductivity σ_e of the material. The authors observed that the beams behaved as percolation systems. In order to evaluate the percolative parameters near the critical region, the measured data were processed by means of least-squares fits conforming to the following linearised equations:

$$\ln \sigma_e = A + t \ln(\Psi - \Psi_c) \text{ for the conductivity,} \tag{5.3}$$

$$\ln E_b = B + \tau \ln(\Psi - \Psi_c) \text{ for the Young's modulus.} \tag{5.4}$$

A range of trial values for the critical volume fraction Ψ_c was iterated to evaluate the root-mean-squared residuals of the measurement data from the least-squared fit lines. Based on the minimum residual, both the critical exponents t and τ, together with the proportionality constants A and B were determined. No significant difference was observed in the critical volume fraction between the conductivity and the elastic modulus. The authors observed that the critical exponent for the elasticity, τ, is significantly larger than that for the conductivity, t, and this result is consistent with other

work [71]. The results in [72] again confirmed that the elasticity and conductivity belong to two different universality classes of percolation.

In a study of a continuum percolation system, Bug, Safran and Webman [73] showed the dependence of the critical percolation threshold on the aspect ratio of rods. They regarded their findings as a useful approximation for long rods with random distribution. They observed that their conclusion was not consistent with that of Carmona et al. [67] and suggested that the aspect ratio in this investigation was insufficiently large.

In the work of Ueda and Taya [75], the results from a Monte Carlo simulation were reported in the case of a percolation model in which short "fibres" were distributed in two-dimensional space. Macroscopic anisotropy of differing degrees was generated throughout the fibre structure, and the aspect ratio and distribution of fibres ranged from well-orientated to random. It was found out that the more random the fibre distribution and the larger the fibre aspect ratio, the smaller the critical volume fraction becomes. This trend is related to the connectivity, which in this case can be the "number of contacts" between fibres [67]. And the effective conductivity was also evaluated according to the universal power law of percolation in equation (5.1).

In the work of Ruschau and Newnham [76], conduction in "conductor-filled polymers" was investigated. Percolation behaviour was verified by observing that a sharp drop in resistivity occurred at the critical volume fraction. Such a decrease brings the resistivity of the polymer closer to the resistivity of the conducting filler than that of the matrix material. It was observed that the more nearly spherical the element is, the higher the critical volume fraction becomes, and also that the higher the aspect ratio of the fibre is, the smaller is the critical volume fraction. This result is consistent with those concerning the threshold parameter, presented by other workers [67, 75]. However, the critical volume fractions observed [76] were inconsistent with those found by other workers, and publications were cited in which it was concluded that the volume fraction can vary even within the same filler-polymer system. It was suggested that this inconsistency might occur because of the different packing geometries, types of lattice and the percolation model.

Although electrical conductivity (or resistivity) is an obvious indicator of percolation, it has been reported that conductivity in some materials does not yield a threshold phenomenon. One of them is a type of detrital sedimentary rocks that have been studied in geological physics. These rocks exhibit a power-law relationship between porosity and conductivity but do not have a threshold effect; this has been known as "Archie's law" [78]. The absence of a threshold is directly related to the microstructure of those rocks, which was determined by the way in which they had been formed. For such rocks, almost no isolated pockets or pores are reported and therefore every pore is already connected, hence there is no threshold. It has also been reported that it is relatively easy to fabricate a laboratory model showing a percolation threshold effect, because the threshold phenomenon is associated with the structure [78].

5.3 Fibrous materials

In Chapter 4, a series of static models was developed to describe the nonlinear structural behaviour of fibrous materials under compression. In the associated analysis, only the strain/stress relationship in the region of positive strain was considered. However, in this section, the behaviour of a hypothetical range of negative strain will be considered. Here, a negative strain is in the range in which a tensile stress is applied, since a normal compressive stress was defined as positive in Chapter 4.

By simply plotting the theoretical strain/stress relationship in the region of negative strain and stress, one can observe a "splitting apart" effect in fibrous media. In Figure 5.1, both the SNBM (dotted line) and the MNBM (dashed line) are plotted, together with measured data for positive strain and stress, in the hypothetical negative (third quadrant) and the "realistic" positive (first quadrant) strain/stress region. It is clear that the material is much "softer" in tension than its compressional counterpart, because of the apparent lengthening of fibre links. The third quadrant is expanded in Figure 5.2, to show clearly the apexes of curves, which may be taken as indicating the moment when a fibrous medium starts to "split apart" under tension. Although it shows mathematically

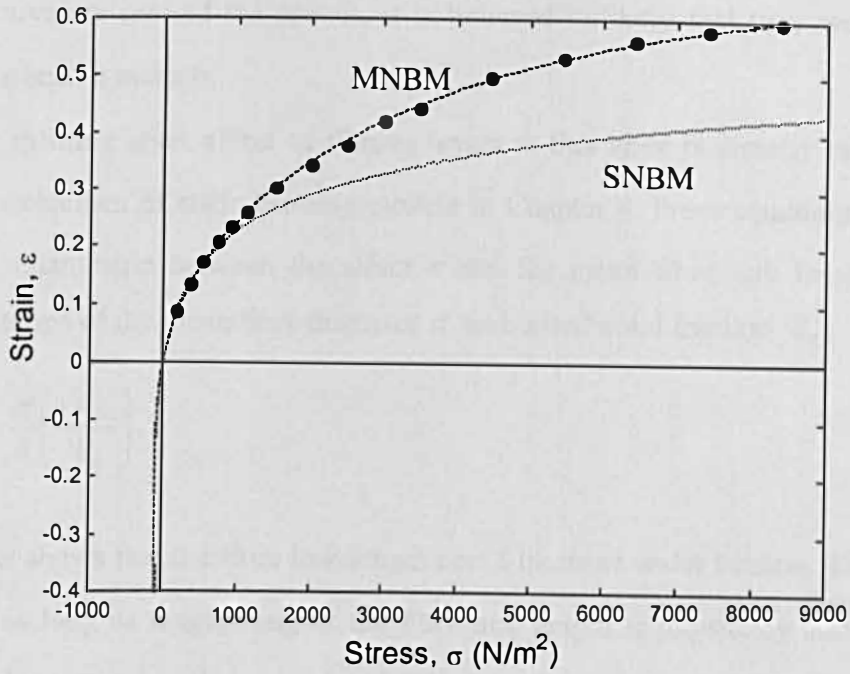

Figure 5.1 The extension of the SNBM (dotted line) and MNBM (dashed line) static models to negative stress, together with measured data on an acoustic duct lining material.

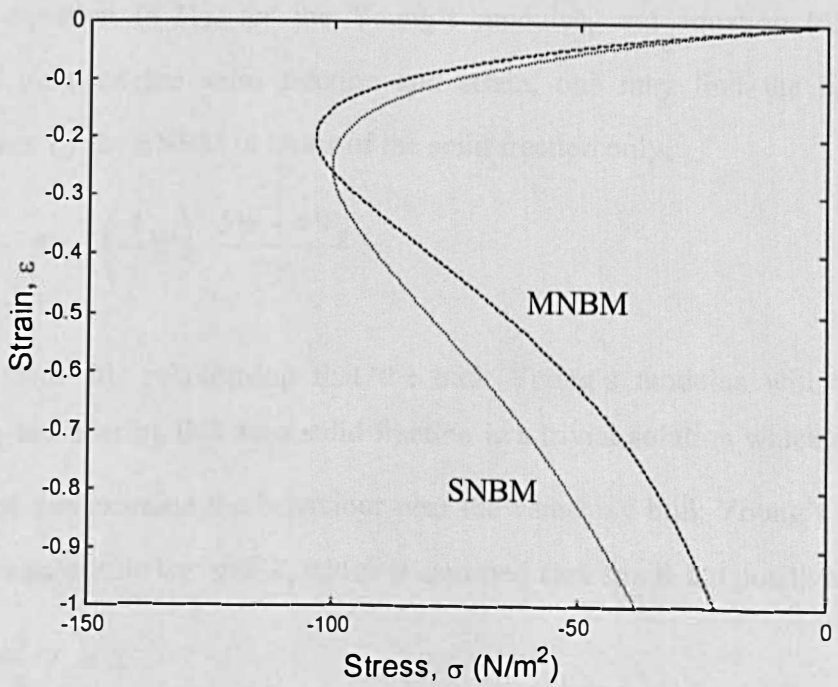

Figure 5.2 Expanded negative stress-strain portion of the Figure 5.1. The dotted line is for the SNBM, the dashed line for the MNBM.

a smooth curvature around the apexes, it is believed unlikely that they would behave physically in such a manner.

The splitting apart effect of fibrous layers at this apex is directly related to the nonlinear mechanism of static bending models in Chapter 4. From equations (4.16) and (4.19), the relationship between the strain ε and the mean fibre link length l can be obtained in terms of the mean fibre diameter d and initial solid fraction Ψ_0,

$$\frac{l}{d} = \frac{\pi}{4}\left(\frac{1-\varepsilon}{\Psi_0}\right). \tag{5.5}$$

The equation shows that the fibre link length could increase under tension. This increase will persist as long as lengthening of the fibre link length is physically sustainable. At some stage, however, it will pass a threshold where the length of a fibre link would be longer than that of the side of a given sample cross-section. Thus, the stable structure of a bulk fibrous material would no longer exist.

If both the SNBM and the MNBM are expressed in terms of the bulk Young's modulus, the interpretation of the split-apart behaviour is fairly straightforward. By combining equation (4.21), for the Young's modulus, and equation (4.19), for the relationship between the solid fraction and strain, one may find the bulk Young's modulus given by the SNBM in terms of the solid fraction only,

$$E_b = 3\pi E\left(\frac{4}{\pi}\Psi\right)^5 \frac{5\Psi - 4\Psi_0}{\Psi_0}. \tag{5.6}$$

It is clear from this relationship that the bulk Young's modulus will vanish when $\Psi = 0.8\Psi_0$, considering that zero solid fraction is a trivial solution which can never be attained. One can examine the behaviour near the vanishing bulk Young's modulus, by introducing a substitute variable X, which is assumed very small and positive,

$$\Psi = \frac{4}{5}\Psi_0 + X\ . \tag{5.7}$$

Insertion of (5.7) into (5.6) will yield, to a first order approximation,

$$E_b = \frac{15\pi E}{\Psi_0}\left(\frac{16}{5\pi}\Psi_0\right)^5\left(\Psi - \frac{4}{5}\Psi_0\right), \tag{5.8}$$

where terms of order X^2 and above are neglected. One can see that the bulk Young's modulus will follow a power-law relationship with an exponent of unity (i.e., a linear relation) near the region where it vanishes, and this may be termed a "threshold". An example of this power-law relationship is shown in Figure 5.3 for the SNBM applied to an acoustic duct-lining material (specified in Tables 4.1 and 5.1). The vertical dotted line indicates the initial solid fraction and hence implies that this power-law behaviour occurs mainly in the hypothetical tension region for this particular fibrous material. The inclined dashed line is the regression line, showing the power-law dependence, whose slope is 1.0564.

In the case of the MNBM, the bulk Young's modulus in equation (4.28) may be re-written in terms of the solid fraction,

$$E_b = \frac{3\pi E}{\Psi_0}\left(\frac{4}{\pi}\Psi\right)^5 \frac{5\Psi - 4\Psi_0 + 192\left(\zeta\frac{4}{\pi}\right)^2(\Psi-\Psi_0)^2(3\Psi-4\Psi_0)}{\left\{1+192\left(\zeta\frac{4}{\pi}\right)^2(\Psi-\Psi_0)^2\right\}^2}. \tag{5.9}$$

The threshold solid fraction Ψ_{th}, at which the Young's modulus vanishes, will be determined by the numerator of the right-hand quotient, provided that the trivial solution predicted by a zero solid fraction is ruled out. The threshold solid fraction will be given by a root of a third-order polynomial equation with real coefficients. Thus, the solution will be one real and two complex roots, three real roots with at least two of them equal, or three real unequal roots. Among these three options, the first one (of a single real and two complex roots) will be the most likely. If the single real root is denoted Ψ_{th} and a small positive variable X is defined by $\Psi = \Psi_{th} + X$, the behaviour of the bulk Young's modulus near the threshold may be represented as a first order approximation,

$$E_b = f(\Psi)(\Psi - \Psi_{th}), \tag{5.10}$$

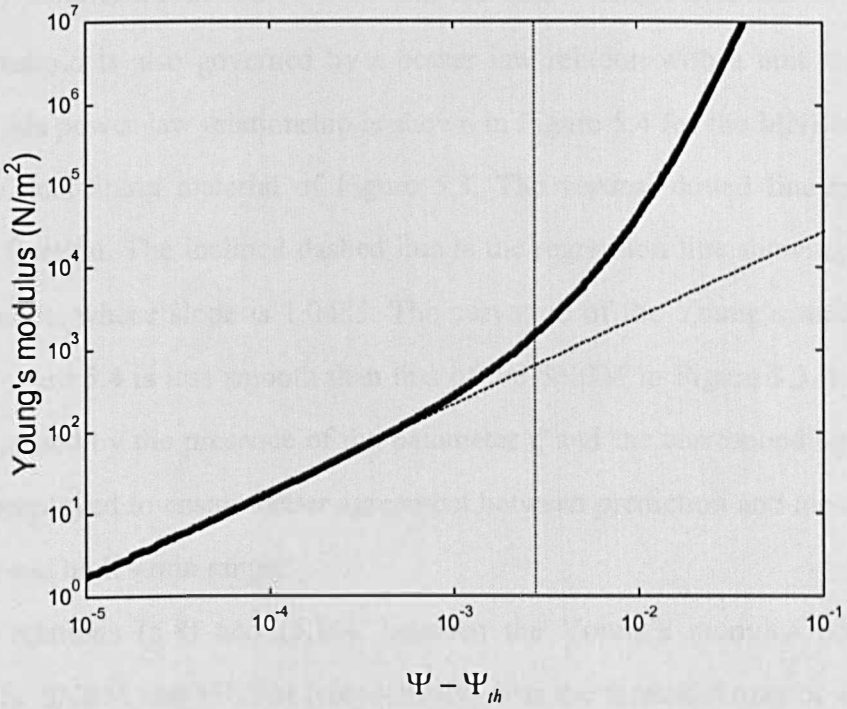

Figure 5.3 Power-law dependence of the SNBM near the solid fraction threshold for an acoustic duct lining material. The oblique dashed line is the regression line and the vertical dotted line indicates the initial solid fraction.

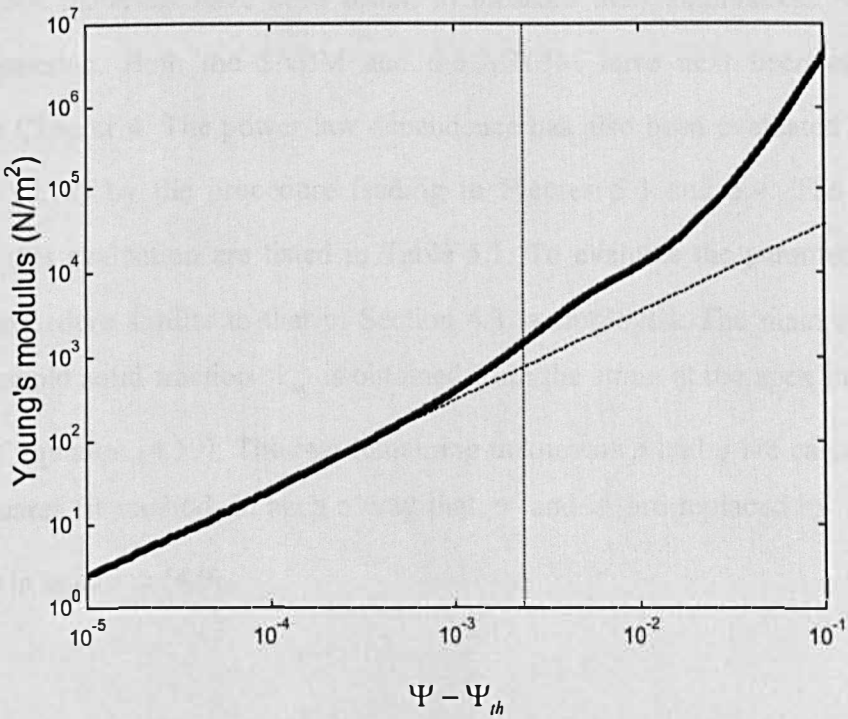

Figure 5.4 Power-law dependence of the MNBM near the solid fraction threshold for an acoustic duct lining material. The oblique dashed line is the regression line and the vertical dotted line indicates the initial solid fraction.

where $f(\Psi)$ denotes a function of Ψ. Thus, the bulk Young's modulus in the MNBM near the threshold is also governed by a power law relation with a unit exponent. An example of this power-law relationship is shown in Figure 5.4 for the MNBM applied to the acoustic duct-lining material of Figure 5.3. The vertical dotted line indicates the initial solid fraction. The inclined dashed line is the regression line showing the power-law dependence, whose slope is 1.0485. The curvature of the Young's modulus of the MNBN in Figure 5.4 is less smooth than that of the SNBM in Figure 5.3. It is believed that this is caused by the presence of the parameter ζ and the corresponding adjustment procedure, employed to ensure better agreement between prediction and measurement in the medium and high strain range.

The relations (5.8) and (5.10), between the Young's modulus and the solid fraction in the SNBM and MNBM (respectively) near the threshold may be expressed in a general power-law form as in equations (5.1) and (5.2),

$$E_b = Q\left(\Psi - \Psi_{th}\right)^P. \tag{5.11}$$

Several fibrous materials have been tested to measure their strain/stress relationships under compression. Both the SNBM and the MNBM have next been employed as described in Chapter 4. The power-law dependence has also been evaluated in the form of equation (5.11) by the procedure leading to Figures 5.3 and 5.4. The parameters involved in this evaluation are listed in Table 5.1. To evaluate the parameters, a basic numerical procedure similar to that in Section 4.3 is employed. The main difference is that the threshold solid fraction Ψ_{th} is obtained from the strain at the apex in Figure 5.2, by means of equation (4.19). The two remaining unknowns p and q are calculated using the least squares fit method, in such a way that σ and ε are replaced by E_b and Ψ, respectively in equation (4.9).

	Acoustic duct lining material		Aircraft thermal insulation material		Rockwool 1	
Bulk density (kg/m^3)	35.0		9.0		57.8	
Frame E (Pa)	7.5×10^{10}		7.5×10^{10}		9.85×10^{10}	
	SNBM	MNBM	SNBM	MNBM	SNBM	MNBM
Ψ_0	0.0139	0.0144	0.0067	0.0093	0.0233	0.0232
ζ	0	7.919	0	22.058	0	8.731
ε_{th}	-0.25	-0.1998	-0.25	-0.1548	-0.25	-0.156
Ψ_{th}	0.01112	0.01196	0.0054	0.0080	0.0186	0.020
P	**1.0564**	**1.0485**	**1.1116**	**1.1171**	**1.0346**	**1.0518**
Q (Pa)	3.08×10^5	4.12×10^5	1.32×10^5	2.03×10^5	2.09×10^6	5.11×10^6

	E-glass fibrous material		Glass mineral wool		Rockwool 2	
Bulk density (kg/m^3)	27.2		24.4		41.2	
Frame E (Pa)	7.7×10^{10}		8.0×10^{10}		9.85×10^{10}	
	SNBM	MNBM	SNBM	MNBM	SNBM	MNBM
Ψ_0	0.0160	0.0161	0.0116	0.0120	0.0189	0.0189
ζ	0	9.3455	0	10.216	0	9.167
ε_{th}	-0.25	-0.1797	-0.25	-0.1950	-0.25	-0.1688
Ψ_{th}	0.0128	0.0136	0.0093	0.010	0.0151	0.0161
P	**1.0991**	**1.0480**	**1.0661**	**1.0644**	**1.0459**	**1.0507**
Q (Pa)	7.08×10^5	7.73×10^6	1.75×10^5	2.57×10^5	1.03×10^6	2.04×10^6

Table 5.1 (To be continued.)

	Basalt wool		Glass fibrous material		Steel wool	
Bulk density (kg/m^3)	57.1		10.6		57.8	
Frame E (Pa)	8.9×10^{10}		7.5×10^{10}		2.1×10^{11}	
	SNBM	MNBM	SNBM	MNBM	SNBM	MNBM
Ψ_0	0.0110	0.0115	0.0080	0.0099	0.0079	0.0100
ζ	0	9.387	0	14.246	0	18.377
ε_{th}	-0.25	-0.2032	-0.25	-0.1847	-0.25	-0.1638
Ψ_{th}	0.00884	0.00956	0.0064	0.0084	0.00628	0.00859
P	**1.070**	**1.0937**	**1.0235**	**1.1094**	**1.0211**	**1.0916**
Q (Pa)	1.76×10^5	2.94×10^5	6.12×10^4	1.85×10^5	1.78×10^5	5.58×10^5

Table 5.1 Parameters involved in the evaluation of the power-law dependence of the SNBM and the MNBM near the threshold solid fraction in terms of the Young's modulus.

It can be observed that the exponents for all the materials listed are close to unity, as discussed in the preceding paragraphs. This same value of the exponent signifies that, from the percolation viewpoint, all the fibrous materials in Table 5.1 belong to the same universality class provided their Young's moduli are dealt with in a similar way to that in which the experiments described in Chapter 4 were conducted. An interesting aspect of the threshold value of strain may be noted. For the SNBM, regardless of the type of fibrous material, the threshold strain is found to be -0.25. This is obvious from equation (4.21), since the numerator is $1+4\varepsilon$. Such a fixed threshold may seem unrealistic.. The possible reason for a fixed threshold strain may originate from the fact that the nonlinear mechanism in the SNBM is related only to the spacing between the contacts, not with the binding forces appearing in real cases. On the other hand, binding forces or other factors

are included in the MNBM, and so the threshold strain turns out to be variable. Despite this variability of the threshold strain in the MNBM, some of the values in Table 5.1 may appear to be unrealistically small. If this is the case, it may be because entire layers in the model have been assumed to behave equally and identically, whereas in real situations, with local defects, this assumption might not be reasonable. Also, because of the presence of a binding agent or the "knotting together" of fibres, actual fibres might maintain their connection when they are under tension and at a small angle to the direction of the applied stress, which could dramatically increase the "negative" threshold strain. However, in bending models, this orientation of fibres is not allowed.

The existence of a threshold, as described above, is one of key concepts in percolation theory. Also, the power-law dependence is essential to describe the behaviour near the threshold. For simple percolation models, the theoretical values for the critical exponents are known [65, 66, 77]. Kantor and Webman [71] reported values of 3.6 and 3.55 for the critical exponent of *elastic modulus* in their "discrete" lattice network. In the case of realistic models in a field of "continuum" percolation, the values of critical exponents are believed to be different from those associated with idealised lattice percolation [77]. For a so-called Swiss cheese model, the exponent for the elastic modulus is reported to be larger than those of a standard lattice model by the amount of 1.5 and 2.5 in two and three dimensions, respectively [77].

However, the exponent of unity in the SNBM and the MNBM is well below those reported in the literature. Such a discrepancy may be explained by noting that the mechanisms involved in other percolating elastic systems [71, 72] are rather different from that prevailing in the fibrous materials studied in the present investigation. In the first place, it may seem that the threshold phenomenon is different in the two situations. In the case of fibrous materials, it is the formation of a bulk material without "splitting apart". In the case of percolation theory, it is the formation of infinitely connected paths between both sides of a specimen. Secondly, in the other investigations of percolation [71, 72], several specimens were prepared with different "pre-fixed" solid fractions. (These were achieved by varying the solid volume and keeping the bulk volume fixed.)

Thus a bulk material could exist even below the threshold. But *some* solid elements would not contribute to the elastic modulus below the threshold or even above it if they were isolated. In a fibrous material, the solid fraction would change gradually with strain. (The change of solid fraction occurs because of the change of bulk volume with a fixed volume of solid.) Below the threshold, a bulk fibrous material is not defined, because it would already have split apart. Thus *none* of the fibres contribute to the bulk Young's modulus below the threshold, and *all* of them do above the threshold. Previous publications on percolation [71, 72] concerned comparisons "across samples", whereas a single fibrous material under compression and hypothetical tension is related to the behaviour "within a sample". In order to achieve the "across-samples" situation for fibrous materials, one needs to prepare the samples with different initial solid fractions and a fixed bulk volume. One may need an interstitial component other than air, such as an epoxy resin, to keep the bulk structure stable. If an abrupt change of bulk Young's modulus is observed in a particular sample, the solid fraction at which the change occurs will be the threshold value for fibrous materials of that kind.

Based on the aforementioned findings, the following conclusions can be reached. Fibrous materials in general may be regarded as percolating systems. For example, a carbon-fibre polymer composite (see [67, 72, 75, 76]) may be regarded as a bulk fibrous material with two solid phases, and indeed is a percolating system. However, the treatment of hypothetical gradual static compression or tension does not appear to be a successful way of proving that a fibrous material is a percolating system, despite the behavioural similarity evident in equation (5.11) and Table 5.1. As previously suggested, other investigative approaches such as those in the literature previously cited [67, 71, 72] are required to demonstrate that a fibrous material having either acoustic, thermal or mechanical applications is also a percolating system.

5.4 Summary

The increase in the number of inter-fibre contacts occurring as a fibrous material is compressed is regarded as being of the utmost importance in the development of nonlinear structural models of fibrous materials. That is because the number of contacts per unit volume is directly related to the lengths of the fibre links, which in turn decides the degree of bending deflection of the fibres and hence the deflection of the bulk material. The inter-fibre contact density may also be regarded in terms of the connectivity between fibres. The degree of connectivity has been investigated in other areas of science. One of these is "percolation theory", the basis and applications of which have been introduced here.

Bending models such as the SNBM and MNBM have been expressed in the form of a power law near the threshold, as is common practice in percolation theory. In this process, both models have been re-written in terms of the bulk Young's modulus and the variation of solid fraction (See equations (5.6) and (5.9)). Both of them have also been extended to a hypothetical tension region, because fibrous materials are already stable (or well connected) and do not have any threshold effect when they are under compression. The discrepancy in the critical exponent, between the present bending models and the results of previous research on the elastic modulus of percolating fibre composite materials, has been pointed out. A set of possible reasons for fundamental differences in the way in which fibrous materials are treated, and their connectivity is established, has been outlined.

Finally, it is concluded that a fibrous material could be regarded as a percolating system. The bending models developed in Chapter 4 do not demonstrate percolating behaviour exactly, but address another type of connectivity. This is analogous to the fact that a phase transition is not exactly the same as percolation, but is similar to it. However, the variation of the number of inter-fibre contacts in a fibrous material has potential as a percolating system. This has been confirmed already in the laboratory, for electro-magnetic purposes, with fibre-composite materials [67]. A structural percolation

phenomenon has been observed for a porous beam [72]. Therefore, an experimental investigation of structural percolation could be a fruitful topic for fibrous materials used for vibro-acoustical and structural purposes. A different experimental approach is required for this purpose as described in the latter paragraphs of Section 5.3.

Chapter 6

Measurement of dynamic properties of porous elastic materials

Up until now, the static behaviour of fibrous materials has been addressed. The understanding of static performance itself is important for the use of fibrous materials, but usually their application involves a dynamic situation. This is true also for other types of poroelastic and viscoelastic materials, such as cellular materials and solid rubbers, respectively. To make the most of those materials in dynamic environments, their dynamic material properties need to be known in stages of design and development, or installation and application. Those dynamic properties are effectively characterised by the complex moduli in frequency domain and can be usually measured by means of a longitudinal harmonic excitation of a specimen. This chapter starts with reviews on a series of previous contributions to the methodology of how to measure the dynamic properties. Subsequently, one of the methods is discussed in detail, and a new method that employs conventional techniques is presented together with its applicability and limitation.

6.1 Reviews

There are several ways of classifying experimental methodologies for dynamic properties, especially for the longitudinal bulk Young's modulus. They can be described as "resonance methods" [15, 29, 30, 81~85, 87~90] or "non-resonance methods" [35, 36, 92], depending on the frequency of interest and according to the standing wave pattern that is excited inside a sample. For the resonance method, it is necessary to excite several

modes of longitudinal vibration. So a relatively long sample may be needed. Usually the properties are evaluated at the resonance and anti-resonance frequencies, so the resulting values are discrete in frequency domain. The non-resonance method targets the frequency below the first resonance of a sample, which may be short in length. Thus, as far as a frequency of interest is concerned, it is often referred to as a "quasi-static measurement".

Also the experimental methodologies can be classified into four groups according to what is measured i.e. transmissibility, compressional stiffness, mechanical impedance and dynamic mass measurements. The "transmissibility method" [15, 29, 30, 81~85, 87~89] captures the ratio of the same physical quantity (acceleration, velocity or displacement) between two measurement channels. The force transmissibility is often also measured [28]. Usually the transmissibility method is related to the resonance method. The "compressional stiffness method" [35, 36, 83, 93] measures the ratio of the force transmitted on one end to the displacement excited on the other end of a sample. It is a non-resonance method, therefore is usually restricted to frequencies below the fundamental resonance frequency. The "mechanical impedance method" analyses the ratio of the force transmitted to the velocity excited [16, 31]. It is also a non-resonance method. The "dynamic mass" [90] is obtained from the ratio of the force to the acceleration recorded at the excited end of a sample. It is a resonance method. A conventional method based on a transmissibility measurement and a novel method using both transmissibility and dynamic mass will be described in details later.

Nolle [79] investigated structural properties of viscoelastic materials such as rubber-like solid materials by means of acoustic measurement, which was not included in the groups identified previously. His technique was to measure the wavelength of a long narrow strip of a material stretched by a small weight and to convert the measured wavelength to the velocity of sound in the sample. The velocity was used to evaluate the elastic modulus by means of the relationship between the velocity, modulus and density. It was necessary to control the temperature to avoid it influencing the sound velocity.

The theoretical and experimental approaches to determination of the structural properties of poroelastic materials are related to the wave motion in vibration isolation mounts such as solid rubber. Harrison, Sykes and Martin [28] investigated the wave motions in isolation mounts. Longitudinal wave motion was mainly discussed by means of the magnitude of force transmissibility. They noticed that the vibration isolating properties of mounts could be changed by their wave motion which was not explained by an elemental vibration theory based on a spring-mass-damping system [26, 27]. So, they asserted that vibration isolation mount should be treated as a continuous medium with wave motion rather than as a lump-parameter system.

Pritz [29, 30, 81, 82, 84, 85, 87, 88] adopted a transfer function method to acoustic or viscoelastic materials. The term "transfer function" can be interpreted as equivalent to "transmissibility". He showed the transfer function technique was effective and useful in evaluating frequency-dependent complex modulus of vibroacoustic materials. His approach applied in two ways using: a spring-like specimen [29] and a rod-like specimen [30], respectively. The "spring-like specimen" was modelled as a lumped-parameter system of spring, mass and damping. Thus its dimensions need to be negligible compared with the wavelength. The high frequency limit of the method for a spring-like specimen was determined by a wave motion. The "rod-like specimen" was treated as a continuum with distributed parameters. Its dimensions could be comparable with the wavelength. The upper frequency limit for measurements on the rod-like specimen was imposed by the lateral wave motion which is apparent when a wavelength becomes smaller than the radial dimension of the sample. Between the two, the rod-like specimen approach was preferred [30], because (a) the wavelength of vibroacoustic materials is usually very small, (b) in some cases, the small ratio of the top-plate mass to the sample mass makes it difficult to assume a spring-like specimen, and (c) a wider frequency range can be covered by the rod-like specimen approach due to its series of high frequency resonances, compared to the single low frequency resonance of a spring-like specimen approach.

Wilson and Cummings [16, 31] have proposed a new experimental technique based on measuring the mechanical impedance of two samples of different length – one is twice as long as the other, which is equivalent to the "two thickness method" for determining acoustic impedance [33]. The method was suggested as an alternative to the widely accepted transfer function method [29, 30]. While the transfer function method assumes a frequency-independent static real density of the sample, the concept of complex dynamic density is acceptable in their mechanical impedance method.

6.2 The transfer function method

6.2.1 Methodology

The transfer function method is based on measuring the transmissibility of acceleration, velocity, or displacement between the excited end and the other free or loaded end of a sample under longitudinal excitation. Here, the case for a sample with a loading mass on its top will be addressed. Both end surfaces of a specimen are usually bonded to plates, which could be metal, wood, or plaster of Paris. The weight of the top plate plays a role as a loading mass and hence exerts a static stress. Sometimes, the weight needs to be chosen to match the actual stress to which the specimen is exposed in a practical application [29, 30]. When the sample is glued to the plates, the proper contact between the two is important to ensure a genuine transfer function induced by a sample not by the interaction between the two, such as a modal vibration of the plate itself. If an accelerometer is attached to the top plate, it is also included in the loading mass. Often, a non-contact capacitive probe [16] and non-contact laser velocity-meter are used as alternatives to avoid the loading effect of the accelerator and its cable. A sample is prepared to have a proper aspect ratio depending on a measurement requirement for it to be rod-like or spring-like. Sometimes a long slender sample is preferred to ensure a sufficient number of resonances. However such a sample may cause instability problem

when it is excited. The stability issue needs to be treated carefully, because the measurement is based on the ideal longitudinal vibration of a sample.

The transfer function method may be represented schematically in Figure 6.1. The sample is sandwiched between two plates as described in the previous paragraph and is excited through the bottom plate by an electro-dynamic shaker. The input signal could be a white noise, pink noise or sine sweep to excite a broad band spectrum.

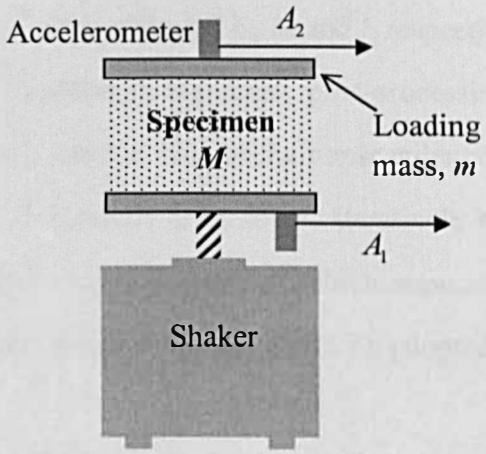

Figure 6.1 Schematic diagram showing the measurement setting for the transfer function method. In this setting, two accelerometers are placed out of phase.

The transfer function T is defined as the complex ratio of the vibration displacement D between two plates. Provided that the vibration is harmonic, the transfer function will be the same whether the ratio taken is for the velocity V or acceleration A. When accelerometers are used, the ratio of accelerations is preferred to other integrated signals, because of a possible signal-to-noise ratio problem.

$$T = \frac{A_2}{A_1} = \frac{V_2}{V_1} = \frac{D_2}{D_1} \tag{6.1}$$

The transfer function of a rod with a loading mass can be derived by solving a longitudinal wave equation [29, 30]. It can be presented in its complex form (6.2), or be divided to its magnitude $|T|$ and phase ϕ (6.3),

$$\frac{1}{T} = \cos kl - \frac{m}{M} kl \sin kl. \tag{6.2}$$

$$\frac{\cos\phi}{|T|} = \cosh\alpha l \cos\beta l + \frac{m}{M}(\alpha l \sinh\alpha l \cos\beta l - \beta l \cosh\alpha l \sin\beta l), \tag{6.3a}$$

$$-\frac{\sin\phi}{|T|} = \sinh\alpha l \sin\beta l + \frac{m}{M}(\alpha l \cosh\alpha l \sin\beta l - \beta l \sinh\alpha l \cos\beta l). \tag{6.3b}$$

The complex wave number k of a sample is defined by $k = \beta - j\alpha$, where β is the phase constant and α is the attenuation constant. The loading mass is denoted by m. The mass and length of a sample are represented by M and l, respectively.

When the transfer function is measured, post-processing is required to get the complex wave number k of a sample. Due to the transcendental nature of equations, the complex form of equation (6.2) needs to be solved iteratively by means of the Newton-Raphson method or Muller's method, both of which support complex manipulation. Alternatively the generalised Newton method could be adopted to solve the systems of equations (6.3).

Once α and β are known, the bulk complex dynamic modulus E_d can be calculated by using following relationships between the bulk Young's modulus and components of complex wave number [29, 30, 94],

$$E_d = E_0(1 + j\eta), \qquad E_0 = \rho\left(\frac{\omega}{\beta}\right)^2 \frac{1 - r_k^2}{(1 + r_k^2)^2}, \tag{6.4a}$$

$$\eta = \frac{2r_k}{1 - r_k^2}, \qquad r_k = \frac{\alpha}{\beta} \tag{6.4b}$$

where η is the loss factor. The static density of a sample and angular frequency are denoted by ρ and ω, respectively. However, it may be easily shown that the series of equations in (6.4) is nothing but the following single relation,

$$E_d = \rho\left(\frac{\omega}{k}\right)^2, \tag{6.5}$$

The transfer function method is often seen as a "resonance method". That is because the frequency and the magnitude of the transmissibility at the resonances could

lead to the bulk Young's modulus and loss factor at those frequencies [28, 84, 85, 88]. Based on a one-degree-of-freedom mass-spring-damping system, at the first resonant angular frequency ω_1, the bulk Young's modulus E_1 and loss factor η_1 are given by,

$$E_1 = M\frac{l\,\omega_1^2}{S}, \tag{6.6a}$$

$$\eta_1 \approx \frac{1}{|T_1|}, \tag{6.6b}$$

where $|T_1|$ is the magnitude of the transfer function at the first resonance and S is the cross-section area of a sample. These values from the resonance method could lead to good starting guesses for the complex wave number in solving the transcendental equations (6.2) and (6.3). It is also often useful as a single representative bulk Young's modulus of a material. This feature will be adopted in Section 7.2.3. At other (p-th order) resonances induced by longitudinal waves, the bulk Young's modulus and loss factor can be obtained by,

$$E_p = \rho\frac{l^2\,\omega_p^2}{(\beta l)_p^2}, \qquad (p = 2, 3, 4, \ldots) \tag{6.7a}$$

$$\eta_p \approx \frac{\Delta f_p}{f_p}, \tag{6.7b}$$

where Δf_p is the resonance bandwidth measured at $|T_p|/\sqrt{2}$, at p-th order. $|T_p|$ is the magnitude of the transfer function at the p-th order resonance. $(\beta l)_p$ is the p-th solution of the following transcendental equation,

$$\cot(\beta l)_p = \frac{M}{m}(\beta l)_p. \tag{6.7c}$$

6.2.2 Measurement

To demonstrate the transfer function method, a sample of fibrous material made out of E-glass was tested. The block diagram for the experiment is shown in Figure 6.2. A signal generator excites a signal which is amplified by a power amplifier and fed to a shaker inside a vacuum chamber. The accelerations on both plates are captured by accelerometers. The output signals are amplified by charge amplifiers and fed into a FFT analyser, which manipulates the transfer function between signals from two accelerometers.

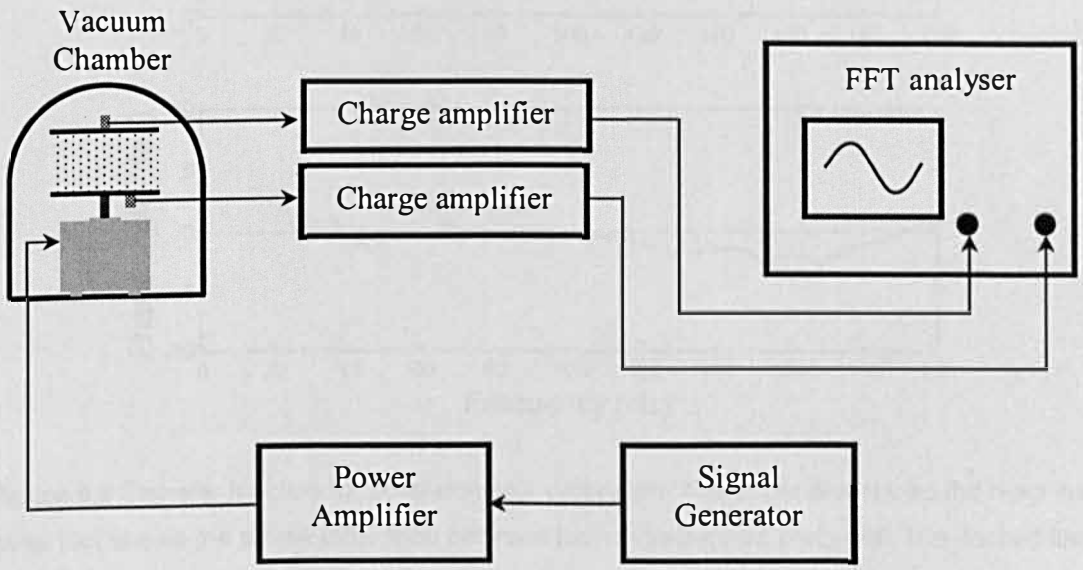

Figure 6.2 Block diagram of a measurement setting for the transfer function method.

First two accelerometers need to be calibrated. Usually the sensitivity information is supplied by a manufacturer. But it is still worth calibrating the measurement system, which include the accelerometers themselves, amplifiers and cables. That is because the transfer function is evaluated by the "ratio" of the signals captured by the system. The relative difference of their performance needs to be compensated, especially the phase difference. To do so, two accelerometers are placed in a balance on a flat plate which is excited by a shaker. In that case, two accelerometers are assumed to be under identical conditions and their signals are compared by evaluating the transfer function between the two. Figure 6.3 shows an example of a calibration transfer function ($T_{calibration}$). Simple

division enables the measured transfer function ($T_{measured}$) to be compensated for the transfer function between the accelerometers ($T_{compensated}$) by post-processing,

$$T_{compensated} = \frac{T_{measured}}{T_{calibration}}. \tag{6.8}$$

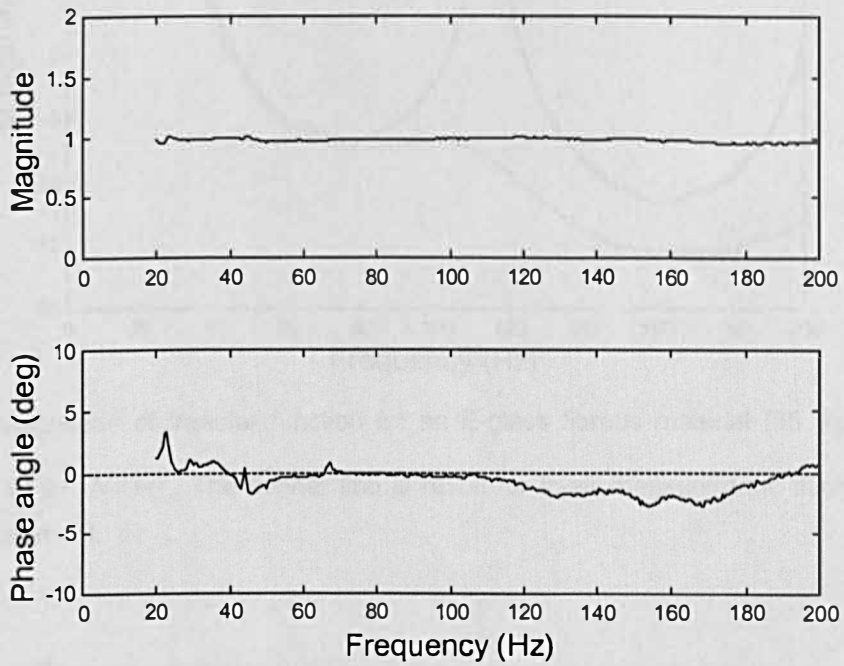

Figure 6.3 Transfer function for accelerometer calibration. The upper plot shows the magnitude; lower plot shows the phase difference between two-measurement channels. The dashed line in the lower plot denotes the zero phase difference.

The dynamic measurement is conducted in vacuum or in air depending on whether interest is in the structural properties or the air-structural coupling interaction. For the accurate evaluation of the "structural" loss factor, the air inside the pores of a material needs to be removed. In Figures 6.4 and 6.5, the magnitude and phase angle of the recorded transfer function for the E-glass fibrous material are shown. At the quasi-static frequencies, the phase angle is viewed out-of-phase. That is because the accelerometers are placed in a way to make such a phase difference as seen in Figure 6.1. Thus this out-of-phase should be corrected to give an in-phase in the analysis. The magnitude of the transfer function measured in vacuum of approximately 10^{-4} *Torr* is observed to have a sharper shape than that in-air measurement especially for the

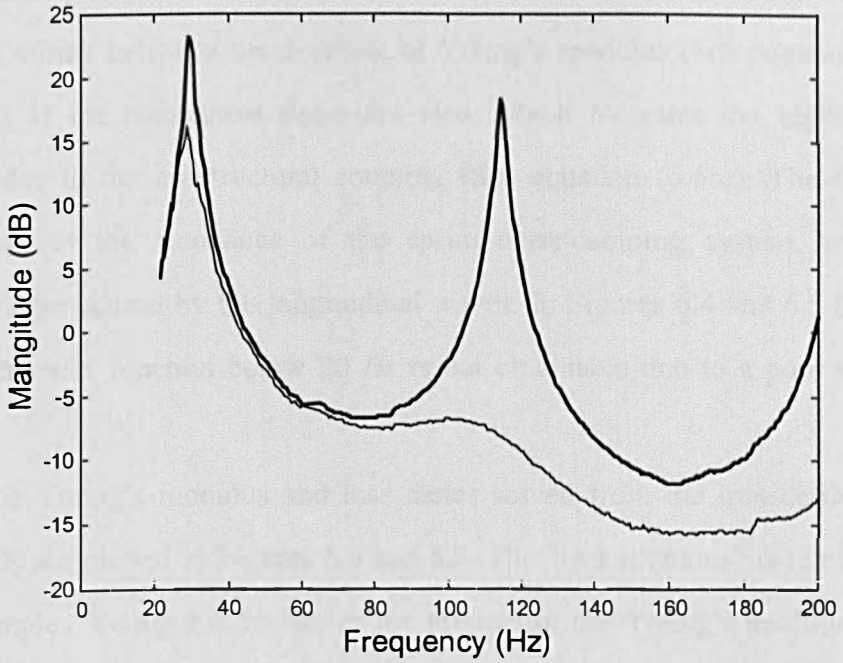

Figure 6.4 Magnitude of transfer function for an E-glass fibrous material (35 kg/m^3) with a static stress of 21 N/m^2. The thinner line is result for in-air measurement; thicker line for in-vacuo measurement.

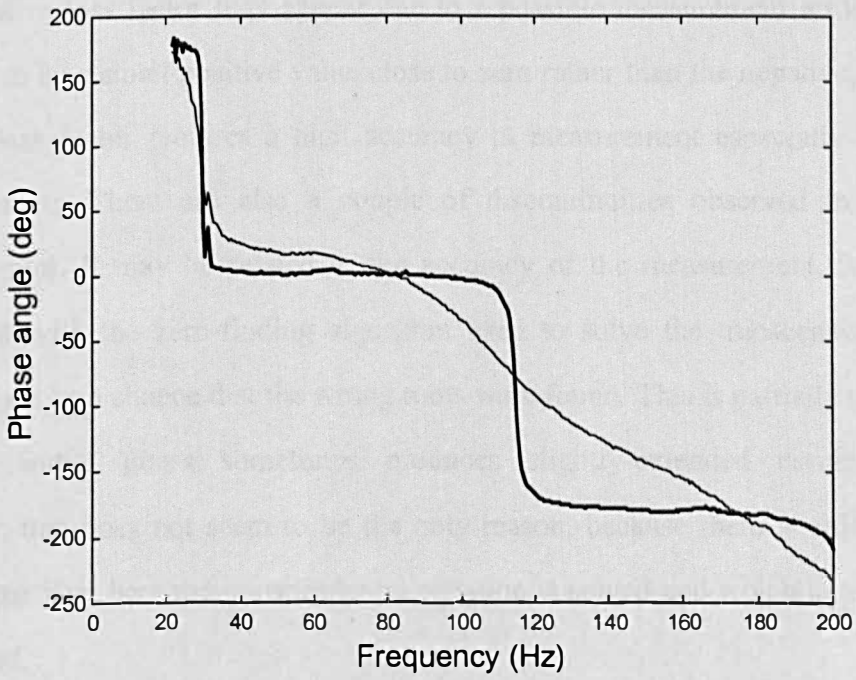

Figure 6.5 Unwrapped phase angle of transfer function for an E-glass fibrous material, with the same condition in Figure 6.4.

resonance frequencies. The resonant frequencies are seen to decrease in the atmospheric condition, which indicates the decrease of Young's modulus (See equation (6.6a)). The magnitude at the resonances decreases also, which indicates the higher loss factor, apparent due to the air-structural coupling (See equation (6.6b)). The first resonance corresponds to the resonance of the spring-mass-damping system, while the next resonances are caused by the longitudinal waves. In Figures 6.4 and 6.5 (also in Figure 6.3), the transfer function below 20 *Hz* is not obtainable due to a poor signal-to-noise ratio.

The Young's modulus and loss factor solved from the transcendental equation (6.2 or 6.3) are plotted in Figures 6.6 and 6.7. The "loss modulus" is the imaginary part of the complex Young's modulus, or the product of the Young's modulus and the loss factor. When in-vacuo results for Young's modulus are compared to those from in-air measurement, one can see the slight decrease, while a significant increase is observed for the loss factor and loss modulus. It is also seen that the loss factor passes at least one maximum in the atmospheric situation, as has been observed in other investigations [90]. The negative loss factor may appear due to a possible measurement error. Hence, it is assumed to be a small positive value close to zero rather than the negative, because such a small loss factor requires a high accuracy in measurement especially for the phase determination. There are also a couple of discontinuities observed in the Young's modulus plot. It may be related to the accuracy of the measurement. It may be also connected with the zero-finding algorithm used to solve the transcendental equation. There might be a chance that the wrong roots were found. This is partially true, because a different initial guess sometimes produces slightly-extended continuous results. However, that does not seem to be the only reason, because there is still discontinuity found regardless how the transcendental equation is solved and which initial guesses are introduced.

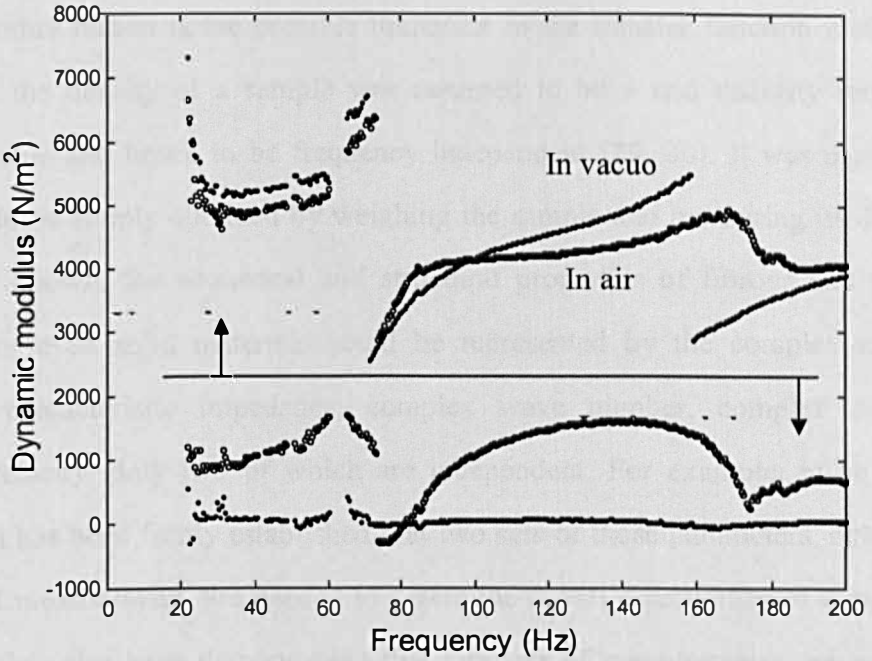

Figure 6.6 Dynamic Young's modulus (above the separation line) and loss modulus (below the line) of an E-glass fibrous material in Figure 6.4 and 6.5. The circles are results for in-air measurement; dots for in-vacuo measurement.

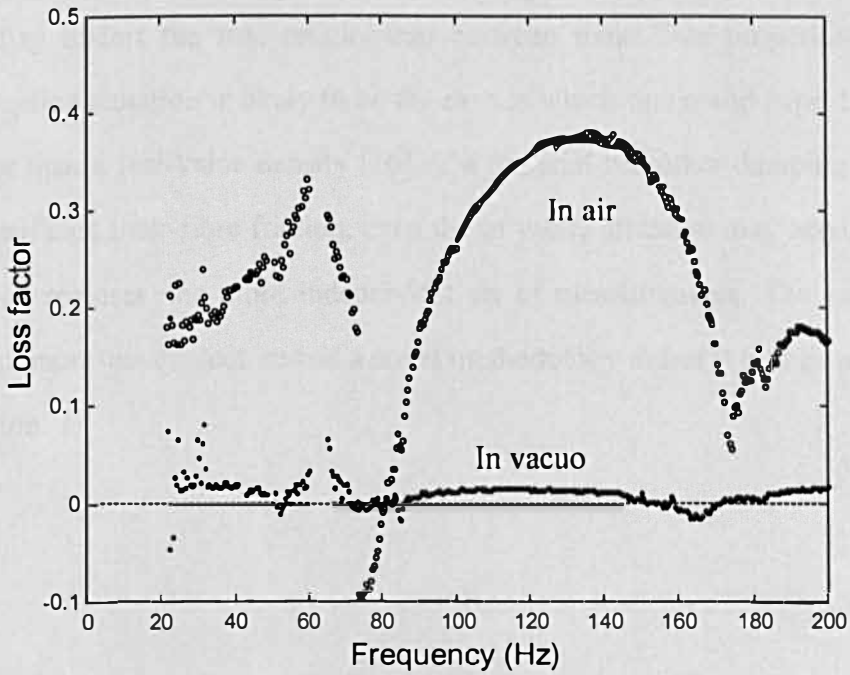

Figure 6.7 Loss factor of an E-glass fibrous material, with the same condition in Figure 6.6. The dashed line denotes zero.

Another reason is the possible limitation in the transfer function method. In its derivation, the density of a sample was assumed to be a real quantity rather than a complex value and hence to be frequency independent [29, 30]. It was *a priori* value which could be simply obtained by weighing the sample and measuring its dimensions. As widely known, the acoustical and structural properties of fibrous and poroelastic materials or even solid materials could be represented by the complex modulus of elasticity, characteristic impedance, complex wave number, complex density and complex velocity, only two of which are independent. For example, in an acoustical situation, it has been firmly established that two sets of those parameters, obtained from two sets of measurement, are needed to determine acoustic properties of a material [32, 33, 34]. It has also been demonstrated that two sets of measurements are necessary in determining mechanical properties without *a priori* knowledge [16, 31, 35, 36, 92]. Because the static density is assumed in the transfer function method [29, 30], only one measurable property, which is the complex wave number in this case, is used to calculate the dynamic Young's modulus (See equation (6.5)). However, in some cases, it may be an excessive assumption to take a real-value frequency-independent density for granted, because it may distort the true relationship between those five properties. The air-structural coupling situation is likely to be the case in which one could expect a complex density rather than a real-value density [16]. If a material has other damping conditions such as a significant inter-fibre friction, even the in-vacuo situation may need a complex density, which requires one more independent set of measurements. The experimental evidence to support this conjecture and a novel methodology to test it will be presented in the next section.

6.3 Transmissibility-dynamic mass method

A new method for measuring the dynamic properties of fibrous materials has been developed. The basic concept combines the advantages of the existing methods. The transfer function method [29, 30] is a very robust and efficient method, however its assumption of a frequency-independent real-value density of a sample might not be appropriate for some cases, where the complex density is required. It also demands a numerical iteration to solve the transcendental equation to get the complex wave number, from which the bulk Young's modulus can be extracted. The mechanical impedance method [16, 31] does not have an assumption about a density, but requires two samples of a material, one of which should be twice as long as the other, to avoid solving the transcendental equation. Preparing two samples is sometimes not straightforward and may lose consistency as a result. This may sometimes hamper the evaluation of the true properties.

The new method exploits the advantages of both methods. There is no need to assume the density of a material as a real-value one. The complex wave number is determined by solving an analytical equation rather than by the numerical iteration required for the transfer function method. So the simplicity of the post-calculation can be expected. Moreover the measurement is carried out on a single sample of a material, just like in the transfer function method. Thus any inhomogeneity related to two different samples can be avoided, unlike the mechanical impedance method. Once the measurement set-up is complete, the only extra requirement may be to change the measurement channels, which might not even be necessary if a facility is available for the simultaneous processing of three channels.

6.3.1 Development of the method

The configuration of a new method is shown in Figure 6.8. A longitudinal sample with a mass on its top is considered to have a constant cross-section. The material of a sample is also homogenous and isotropic or at least transversely isotropic. It is assumed that the lateral motion is not prevented at the ends bonded to the plates. The radial dimension is preferred to be much smaller that the wavelength. Thus a linear relation between the stress and strain can be assumed. Based on these assumptions, the longitudinal wave motion in the elastic sample can be given by a one-dimensional wave equation [26, 27, 28, 61, 86, 95],

$$\frac{\partial^2 \xi}{\partial t^2} = \frac{E_d}{\rho_d} \frac{\partial^2 \xi}{\partial x^2} \,. \tag{6.9}$$

The symbol ξ is the displacement of the sample under longitudinal excitation in the dimension x and time t. The dynamic bulk Young's modulus E_d and dynamic bulk density ρ_d may be complex to deal with viscosity or internal losses in the material.

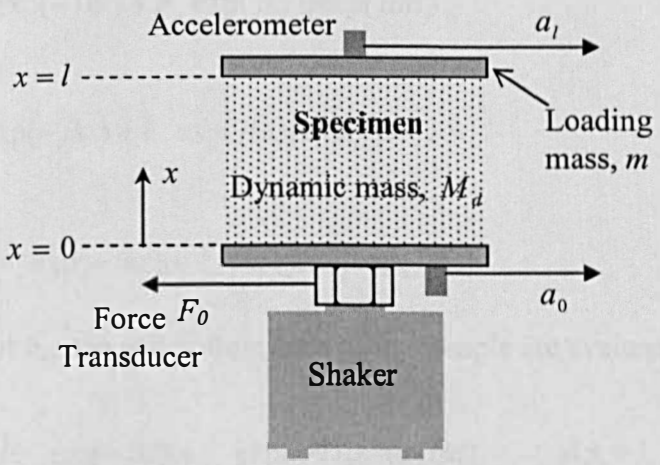

Figure 6.8 Schematic diagram showing the measurement setting for the novel method.

A simple harmonic vibration characterised by $\exp(j\omega t - jkx)$ with a complex wave number k can be a solution to (6.9). When the specimen is excited longitudinally, it experiences stress and strain, which can also be represented by the force and velocity.

Under the harmonic vibration, the components of the force and velocity travelling in both directions of the material may be defined by;

$$F_+ = \hat{F}_+ \exp(j\omega t - jkx), \qquad F_- = \hat{F}_- \exp(j\omega t + jkx), \tag{6.10a}$$

$$v_+ = \hat{v}_+ \exp(j\omega t - jkx), \qquad v_- = \hat{v}_- \exp(j\omega t + jkx). \tag{6.10b}$$

The subscript + and – denote the positive and negative direction, and the symbol $\wedge$ over the character represents the magnitude of the quantity. Thus the mechanical characteristic impedance Z is given by the ratio of the force and velocity,

$$Z = \frac{F_+}{v_+} = -\frac{F_-}{v_-}. \tag{6.11}$$

The negative sign appears due to the opposite direction of the travel. The material will experience the combination of the forward and backward propagating components. So, the force F and velocity v together with acceleration a could be written again, bearing in mind $\partial / \partial t = j\omega$,

$$F = \left\{\hat{F}_+ \exp(-jkx) + \hat{F}_- \exp(jkx)\right\}\exp(j\omega t), \tag{6.12a}$$

$$v = \left\{\hat{v}_+ \exp(-jkx) + \hat{v}_- \exp(jkx)\right\}\exp(j\omega t), \tag{6.12b}$$

$$a = j\omega \left\{\hat{v}_+ \exp(-jkx) + \hat{v}_- \exp(jkx)\right\}\exp(j\omega t). \tag{6.12c}$$

The accleration at the top and bottom ends of the sample are evaluated as,

$$a_l = j\omega \left\{\hat{v}_+ \exp(-jkl) + \hat{v}_- \exp(jkl)\right\}\exp(j\omega t) \qquad \text{at } x = l, \tag{6.13a}$$

$$a_0 = j\omega \left\{\hat{v}_+ + \hat{v}_-\right\}\exp(j\omega t) \qquad \text{at } x = 0. \tag{6.13b}$$

From the two values above, the transfer function T is defined,

$$T = \frac{a_l}{a_0} = \frac{\hat{v}_+ \exp(-jkl) + \hat{v}_- \exp(jkl)}{\hat{v}_+ + \hat{v}_-}. \tag{6.14}$$

The force reflection coefficient r_F may be introduced,

$$r_F = \frac{F_-}{F_+} = \frac{\hat{F}_-}{\hat{F}_+} = \frac{-Z \cdot \hat{v}_-}{Z \cdot \hat{v}_+} = -\frac{\hat{v}_-}{\hat{v}_+}. \tag{6.15}$$

Therefore, the transmissibility of accelerations between ends of the sample are represented by the complex wave number k and the reflection coefficient r_F as follows,

$$T = \frac{\exp(-jkl) - r_F \exp(jkl)}{1 - r_F}. \tag{6.16}$$

The forces measurable at the top and bottom ends of the sample can also be represented by the product of the mass and associated acceleration,

$$F_l = m \cdot a_l = \left\{\hat{F}_+ \exp(-jkl) + \hat{F}_- \exp(jkl)\right\}\exp(j\omega t), \tag{6.17a}$$

$$F_0 = M \cdot a_0 = \left\{\hat{F}_+ + \hat{F}_-\right\}\exp(j\omega t). \tag{6.17b}$$

Here m denotes the mass of the top plate plus an accelerometer and M_d will be interpreted as a dynamic mass of the system, which includes the sample itself, two plates and the two accelerometers. From these two relations in (6.17), the transfer function of acceleration can be obtained again,

$$T = \frac{a_l}{a_0} = \frac{M_d}{m}\frac{\hat{F}_+ \exp(-jkl) + \hat{F}_- \exp(jkl)}{\hat{F}_+ + \hat{F}_-} = \frac{M_d}{m}\frac{\exp(-jkl) + r_F \cdot \exp(jkl)}{1 + r_F}. \tag{6.18}$$

Finally, using equations (6.16) and (6.18) produces the following analytical formula relating the complex wave number k to the transmissibility T and dynamic mass M_d,

$$\cos kl = \frac{mT^2 + M_d}{(m + M_d)T}. \tag{6.19}$$

Therefore, to work out the complex wave number, two pieces of measurement information are essential. They are the transmissibility T from two accelerometers and

dynamic mass M_d from the force transducer and accelerometer on the bottom plate. It is essential to be aware that the inverse cosine is "multi-valued". So it needs to be "unwrapped" to produce the complex wave number belonging to a proper branch. Failing to do so will end up with a non-reasonable discontinous complex wave number which will also lead to a wrong evaulation of other dyamic properties, especially at high frequency after a branch cut.

6.3.2 Four-pole representation

The relationship (6.19) between the complex wave number k, transimissiblity T, and dynamic mass M_d can also be derived by the well-known four-pole representation [80, 86], where a force F_0 and velocity v_0 at the input terminal give rise to a force F_l and velocity v_l at the output terminal of a system. The force-velocity relation can be expressed by a four-pole equation as below,

$$v_l = v_0 \cos kl - j\frac{F_0}{Z}\sin kl, \tag{6.20a}$$

$$F_l = -jZv_0 \sin kl + F_0 \cos kl. \tag{6.20b}$$

The subcripts *0* and *l* represent the input and output terminals spaced with the distance *l* for the current setting (Figure 6.8). The characteristic mechanical impedance is denoted by Z. The symbol $\wedge$ over a character denoting the magnitude of the physical quantities is omitted for a virtue of brevity. All the forces and velocities need to be represented by the accelerations through the top-end mass m and dynamic mass M_d,

$$F_l = ma_l, \qquad F_0 = M_d a_0, \tag{6.21a}$$

$$v_l = \frac{a_l}{j\omega}, \qquad v_0 = \frac{a_0}{j\omega}. \tag{6.21b}$$

If the four-pole equations are re-written in the terms of acceleration, then

$$a_l = a_0 \cos kl + \frac{M_d \omega a_0}{Z} \sin kl\,, \tag{6.22a}$$

$$\omega m a_l = -Z a_0 \sin kl + M_d\, \omega a_0 \cos kl\,. \tag{6.22b}$$

If the transmissibility $T = a_l / a_0$ is introduced, then

$$T = \cos kl + \frac{M_d \omega}{Z} \sin kl\,, \tag{6.23a}$$

$$\omega m T = -Z \sin kl + M_d\, \omega \cos kl\,. \tag{6.23b}$$

Therefore, the analytical equation connecting the complex wave number k with the transmissibility T and dynamic mass M_d is confirmed again,

$$\cos kl = \frac{mT^2 + M_d}{(m + M_d)T}\,. \tag{6.19}$$

The mechanical characteristic impedance of the material can be retrieved as,

$$Z = \frac{M_d \omega \sin kl}{T - \cos kl}, \text{ or } Z = \frac{M_d \omega \cos kl - \omega m T}{\sin kl}\,. \tag{6.24}$$

The other dynamic properties including complex Young's modulus E_d, complex density ρ_d, and complex wave velocity c can be obtained by means of following arithmetic manipulation.

$$E_d = \frac{Z\omega}{k}, \tag{6.25}$$

$$\rho_d = \frac{Zk}{\omega}, \tag{6.26}$$

$$c = \sqrt{\frac{E_d}{\rho_d}}\,. \tag{6.27}$$

6.3.3 Experiment

Unlike the transmissibilty measurement, the dynamic mass measurement requires more caution in calibrating transducers. That is because the transmissibility is worked out based on the ratio of the identical physical amounts, and hence only the relative quantity does matter, not the absolute quantity of each transducer signal. However, the dynamic mass is the ratio of two different measurements, which are force and acceleration. Thus the sensitivity of each transducer must be known precisely. The sensitivity is supposed to be supplied by manufacturers. Nevertheless, it is recommended to check whether the initially provided sensitivity still holds. Calibration of the accelerometer is quite straightforward. Any commercially available calibration excitator can be adopted as the way that a piston phone is used for a microphone. However, a force transducer demands a two-step procedure for the senstivity calibration [96]. A force transducer needs to be subjected to the same acceleration level a, which is fed by a calibration excitator, with two known weights m_1 and m_2 attached on its top in a row. Putting two weights is essential because a force transducer itself has an inertial mass inside and hence just one mass does not produce a proper value for the calibration. A scale factor K will be determined in the following way,

$$K = \frac{F_2 - F_1}{(m_2 - m_1)a}. \tag{6.28}$$

Here, F_2 and F_1 are the measured forces associated with the mass m_2 and m_1, respectively. If the initial senstivity has been intact, the scale factor will be unity, otherwise it needs to be multiplied to the provided sensitivity to produce a rectified one.

After the sensitivity information is secured, the main round of experiment can be conducted in the following way. The schematic diagram for the proposed method has been already shown in Figure 6.8. The specimen is bonded to the top and bottom plates, both of which house an accelerometer. The sample is excited through a force transducer which is placed between the shaker and the bottom plate of the sample. The transmissibility of two accelerometers is to be obtained in the exactly same way in the

transfer function method. The dynamic mass of a sample will be measured by the ratio of signals between the force transducer and the accelerometer on the bottom plate. However, the measured ratio of the force to the acceleration on the bottom plate is not actually what is sought as a dynamic mass of the specimen plus loading mass. That is because a force transducer is supposed to capture the signal induced by the combined effect of a sample with loading mass and a bottom plate with an accelerometer. Therefore, in order to get a genuine dynamic mass contributed by the sample with loading mass, the mass of the bottom plate and accelerometer should be taken into account. Thus the dynamic mass M_d will be in the following form,

$$M_d = \frac{F_0}{a_0} - m_0 . \tag{6.29}$$

The symbol m_0 denotes the extra mass contributed by the bottom plate and accelerometer on it. A block diagram for the measurement will not be much different from that in Figure 6.2 for the transfer function method, only to include one more channel for a force transducer.

To demonstrate the proposed method, a sample fibrous material made out of E-glass, which is identical to that shown for the transfer function method in Section 6.2, has been tested. Figures 6.9 and 6.10 show the measured dynamic mass. It is normalised by the static mass of the specimen plus the top mass. The real part is seen to approach to the static mass at near-zero frequency, despite the non-availability of data due to a poor signal-to-noise ratio. The measured transmissibility between two accelerometers has already been shown in Figures 6.4 and 6.5 for the transfer function method.

Figure 6.11 shows the function $\cos kl$ evaluated from the measurements of dynamic mass and transmissibility. As anticipated from equation (6.19), the real part of $\cos kl$ approaches unity and the imaginary part approaches zero as for the static situation, where the transmissibility T is supposed to be unity. This trend is also evident in Figure 6.11. For in-vacuo situation with a negligible loss, it is expected that the function $\cos kl$, especially its real part, is bounded between –1 and +1, to produce a typical graph of a cosine. However, it is observed that the function deviates from this especially at high

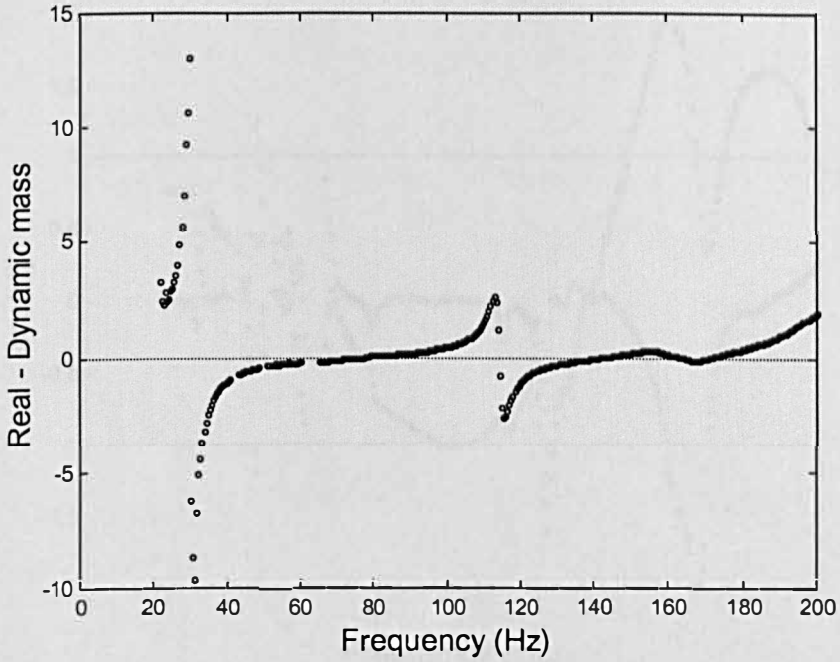

Figure 6.9 Real part of the measured dynamic mass of an E-glass fibrous material sample tested *in vacuo*. The dotted line shows the zero.

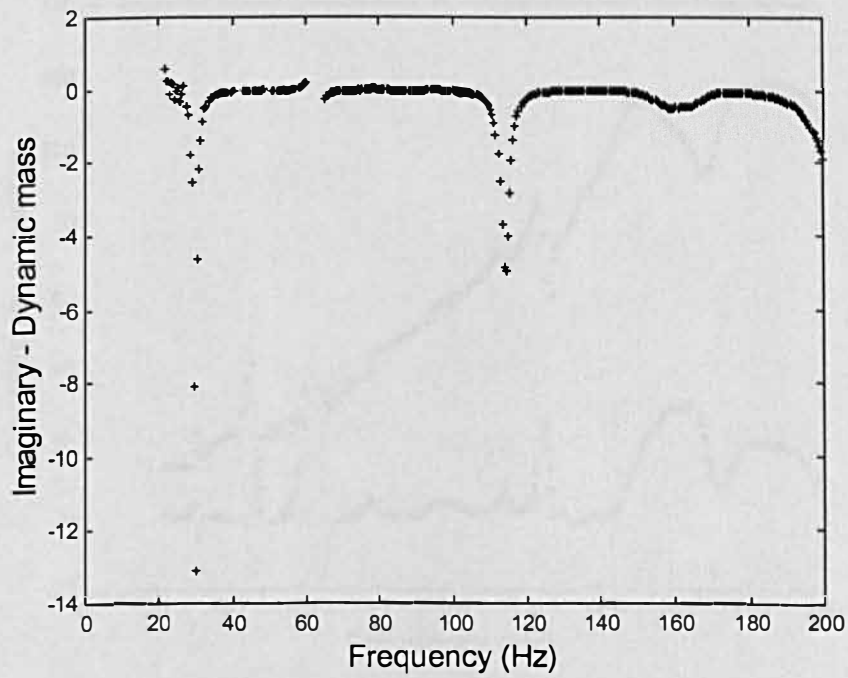

Figure 6.10 Imaginary part of the measured dynamic mass of an E-glass fibrous material sample tested *in vacuo*.

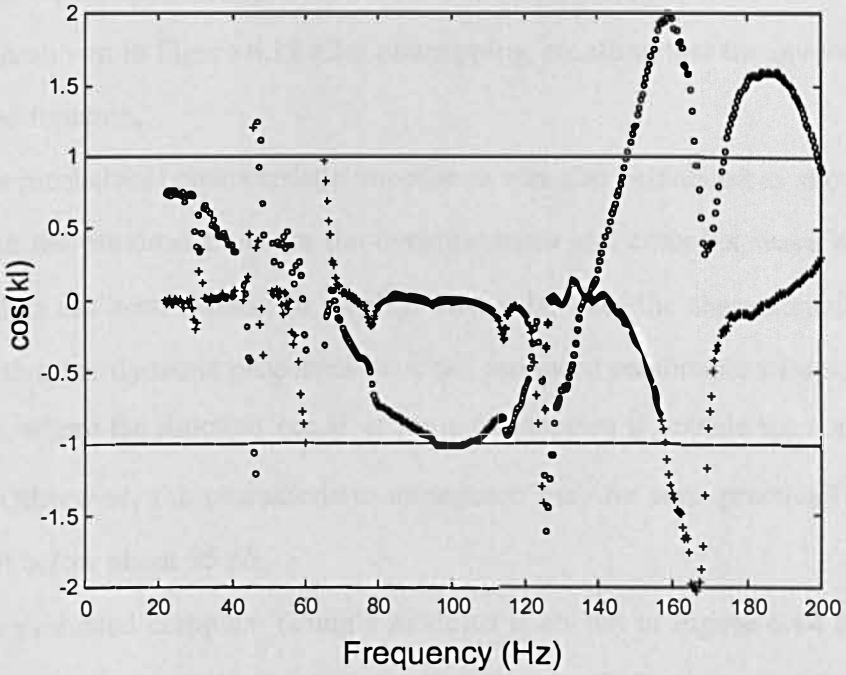

Figure 6.11 Function $\cos kl$ evaluated from the measured transmissibility and dynamic mass of an E-glass fibrous material sample tested *in vacuo*. The circles denote its real part and the crosses represent its imaginary part. The solid lines show the boundaries within which the function is valid.

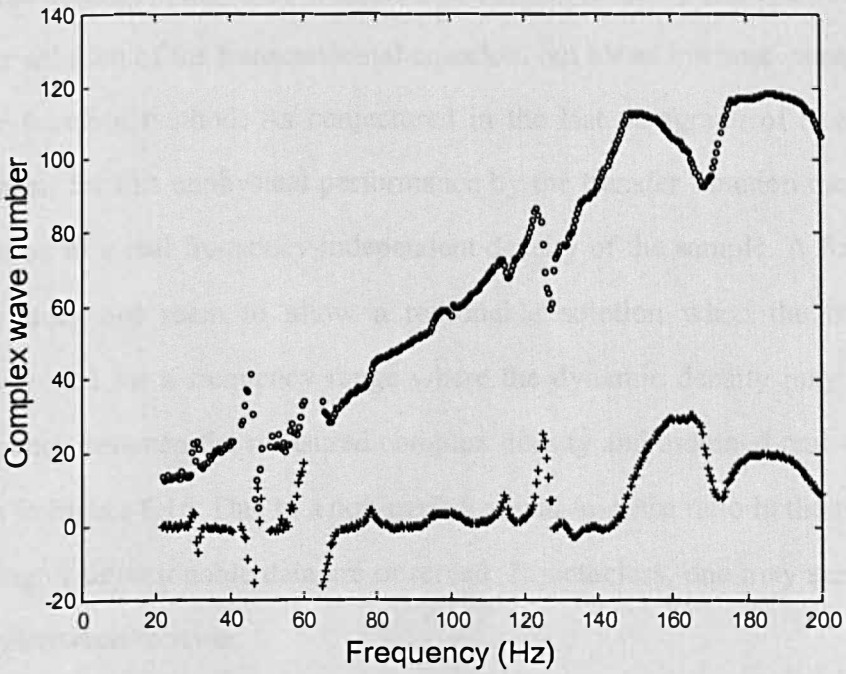

Figure 6.12 Complex wave number evaluated from the function $\cos kl$ for an E-glass fibrous material sample tested *in vacuo*. The circles denote the phase constant and the crosses represent the attenuation constant.

frequencies, where the validity of data is suspect. The complex wave number evaluated in vacuum is shown in Figure 6.12 after unwrapping, recalling that the inverse cosine is a multi-valued function.

The mechanical characteristic impedance was also calculated as shown in Figure 6.13. Unlike the previous plots for the dynamic mass and complex wave number, only portion of data has been chosen for display. That is because the characteristic impedance together with other dynamic properties have not produced reasonable values, as hinted in Figure 6.11, where the function $\cos kl$ at some frequencies is outside the zone between – 1 and +1. Otherwise, the characteristic impedance may be seen practically frequency-independent below about 95 *Hz*.

The evaluated complex Young's modulus is shown in Figure 6.14 together with the counterpart obtained by the transfer function method. A reasonable agreement between the two is observed below 60 *Hz* and then a sudden drop of the modulus by the transfer function method is notified. The relative continuity of the modulus by the new method may suggest that the behaviour of the solution in the transfer function method may be unreasonable. It may also indicate that the discontinuity has not been caused by an improper solution of the transcendental equation, but by an intrinsic cause involved in the transfer function method. As conjectured in the last paragraph of Section 6.2.2, a possible reason for this unphysical performance by the transfer function method may be the assumption of a real frequency-independent density of the sample. A fixed value for the density does not seem to allow a reasonable solution when the transcendental equation is solved for a frequency range where the dynamic density may be complex. The discrepancy between the measured complex density and assumed real-value density can be seen in Figure 6.15. Due to a non-perfect signal-to-noise ratio in the measurement, some missing or unreasonable data are observed. Nonetheless, one may see the intrinsic discrepancy between the two.

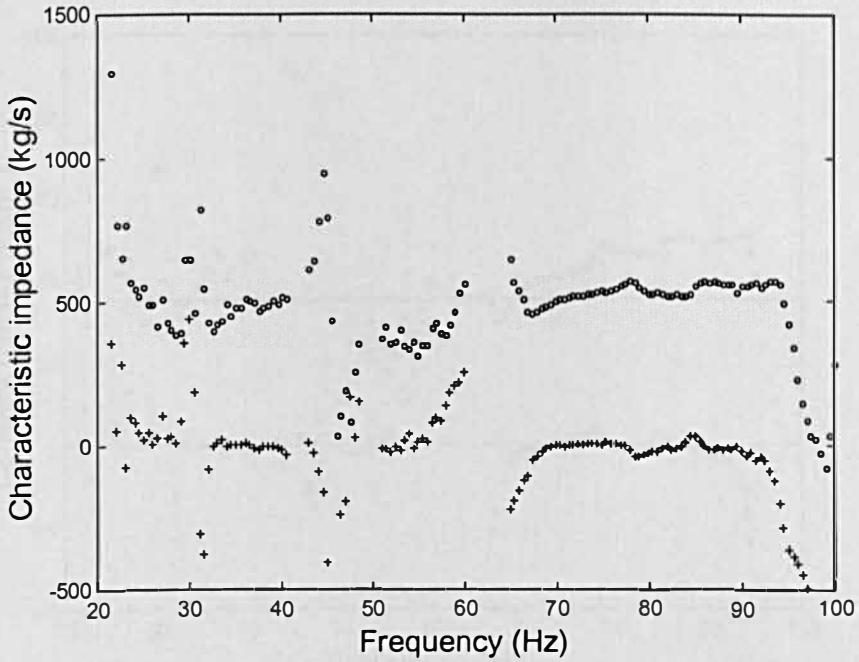

Figure 6.13 Mechanical characteristic impedance of an E-glass fibrous material sample tested *in vacuo*. The circles denote its real part and the crosses represent its imaginary part.

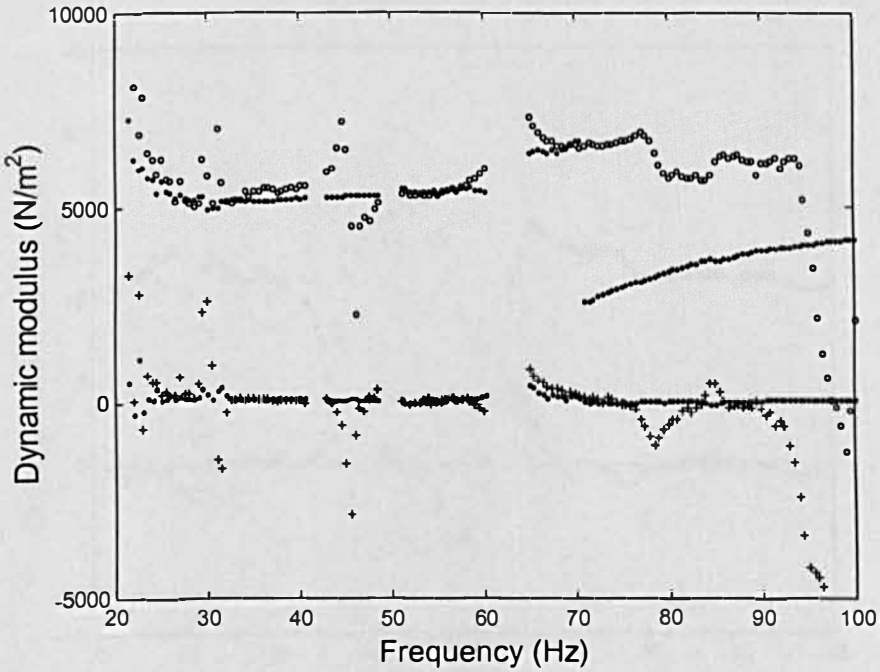

Figure 6.14 Complex Young's modulus for an E-glass fibrous material sample tested *in vacuo*. The circles denote its real part and the crosses represent its imaginary part from the new method. The dots shows those obtained by the transfer function method; upper lines of dots is for Young's modulus; lower lines for loss modulus.

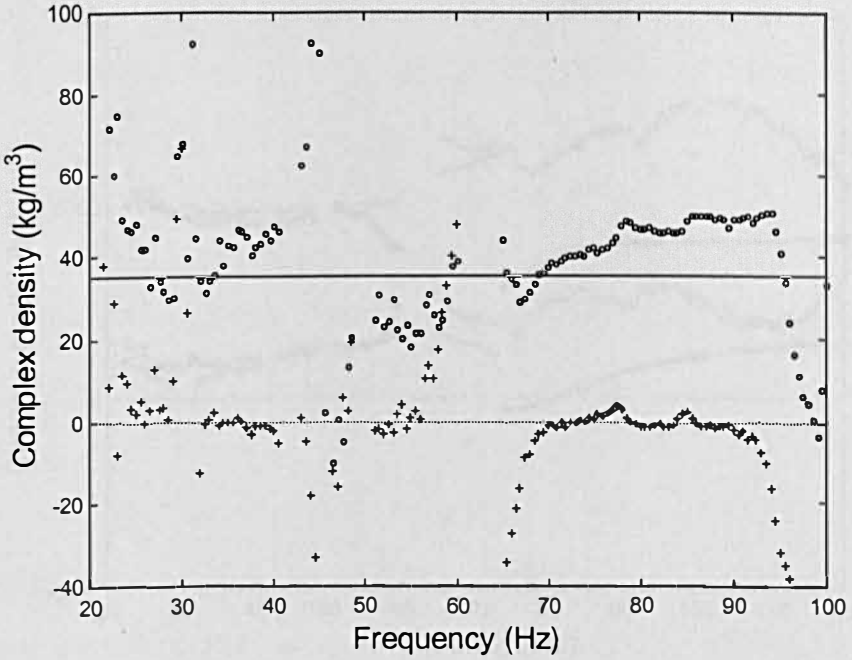

Figure 6.15 Complex density evaluated for an E-glass fibrous sample tested *in vacuo*. The circles denote its real part and the crosses represent its imaginary part by the novel method. The solid line and dotted line denote the weighed static value used in the transfer function method.

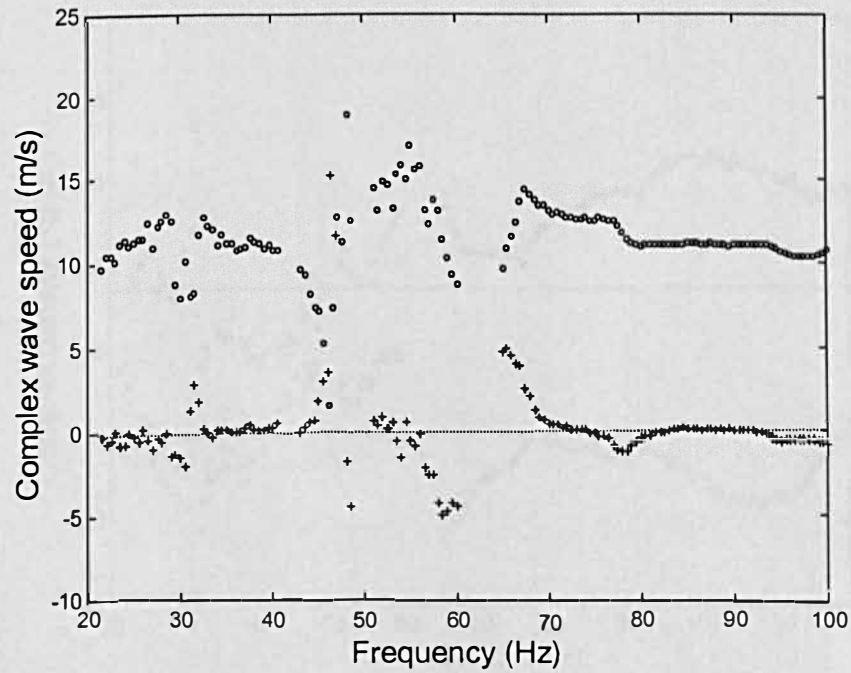

Figure 6.16 Complex wave speed evaluated for an E-glass fibrous material sample tested *in vacuo*. The circles denote its real part and the crosses represent its imaginary part. The dotted line denotes zero.

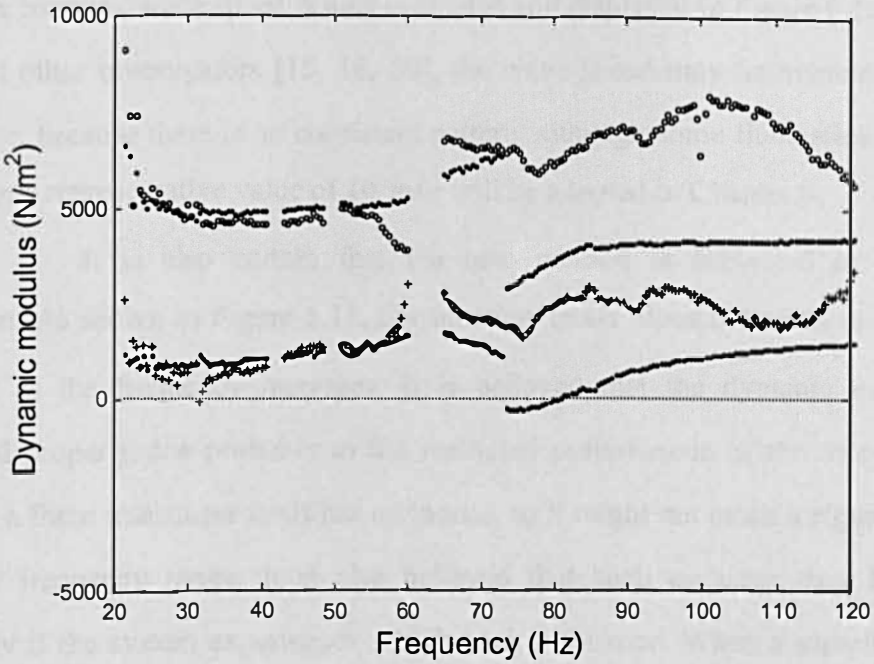

Figure 6.17 Complex Young's modulus for an E-glass fibrous material sample tested *in air*. The circles denote its real part and the crosses represent its imaginary part from the new method. The dots show those obtained by the transfer function method; upper line of dots is for Young's modulus; lower line for loss modulus. The straight dotted line shows zero.

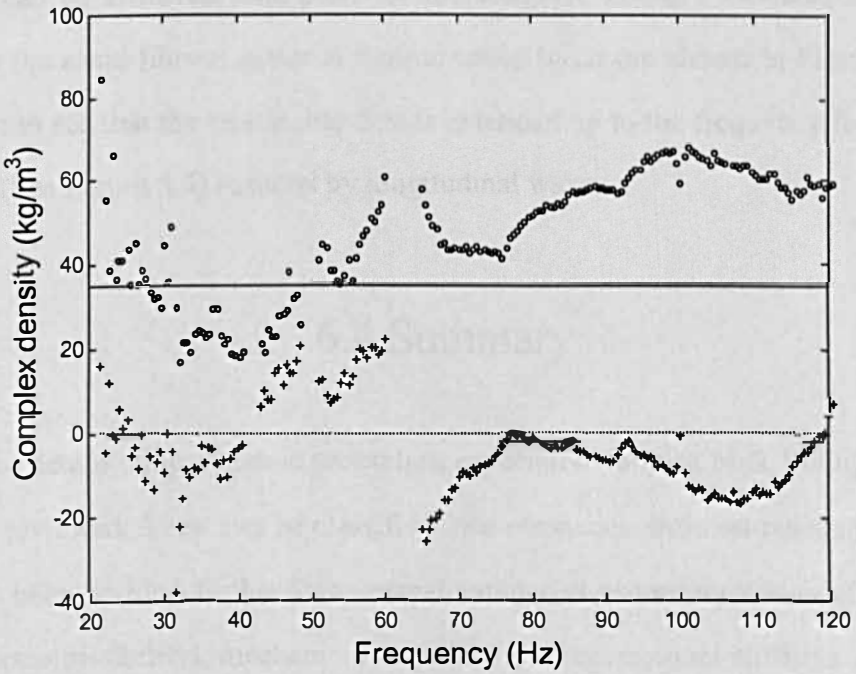

Figure 6.18 Complex density evaluated for an E-glass fibrous material sample tested *in air*. The circles denote its real part and the crosses represent its imaginary part. The solid line and dotted line denote the weighed static value used in the transfer function method.

A complex wave speed is also evaluated and displayed in Figure 6.16. Like in the works of other investigators [15, 16, 89], the wave speed may be assumed to be non-dispersive, because there is no consistent pattern, although some fluctuation is observed. So, a single representative value of 10 m/s will be adopted in Chapter 8.

It is also certain that the new method is subjected to a frequency limitation. As shown in Figure 6.11, the function $\cos kl$ does not seem to be evaluated properly as the frequency increases. It is believed that the dynamic mass was not measured properly due probably to the restricted performance of the force transducer. Usually, a force transducer itself has an inertia, so it might not catch a signal properly in a higher frequency range. It is also believed that such an error may be worsened especially if the system experiences a high-peak resonance. When a sample is tested in the atmospheric condition rather than in a vacuum, the level of a resonance is supposed to be reduced, as seen in Figure 6.4, due to a higher loss induced by an air-structural coupling effect. In such a case, a force transducer seems to record a signal better than otherwise high-peak cases, and as a consequence, an extended curve for the dynamic properties can be achieved. The plots for the complex Young's modulus and complex density for the same fibrous material sample tested in air are shown in Figures 6.17 and 6.18. One can see that the reasonable data is extended up to the frequency for the second resonance (See Figure 6.4) induced by longitudinal waves.

6.4 Summary

Methods for determining dynamic properties, especially complex bulk Young's modulus, have been reviewed. They can be classified into resonance and non-resonance methods. They have been divided further into several categories according which of the transfer function (transmissibility), mechanical impedance, compressional stiffness and dynamic mass have been measured. In particular, the transfer function method has been reviewed intensively. A new method has been developed that combines the advantages of conventional methods. It is based on the measurement of transmissibility and dynamic

mass. It benefits from a simple manipulation of an analytical equation rather than solving a transcendental equation by a numerical iteration, which is encountered in the transfer function method. By requiring only one specimen, it can also avoid a potential difficulty in experiment and its sequential evaluation occurred by any inhomogeneity related to two pieces of samples, which is the case for the mechanical impedance method. Most of all, its ability to deal with a complex density seems to give an alternative to the transfer function method which relies on the assumption of a real-value frequency-independent static density, which is often suspected to produce unreasonable values for dynamic properties. However, despite all the benefits it can bring to the evaluation for dynamic structural properties, it seems to suffer a limitation in its applicabilty, especially as the frequency increases. It is assumed that this is because the measurement of a dynamic mass is not as good as the transmissibility in those frequency regions. Therefore, methods of increasing the applicability of the novel method may need to be the subject of a further work.

Chapter 7

Dynamic structural behaviour of fibrous materials

In Chapter 6, methodologies were reviewed for measurement of the dynamic properties of porous materials in the direction normal to the surface. No limitation was imposed on the type of porous material tested. In this chapter, however, attention is focussed on fibrous materials. Published works on their dynamic behaviour are reviewed and experimental data are presented. Finally, a dynamic model for idealised fibrous materials will be proposed.

7.1 Review of previous works

Nolle [79] noted that the dynamic modulus of rubber-like materials is often much larger than the static modulus (in contrast to the case of ideal crystalline materials). The difference between dynamic and static moduli was also recognised by Zwikker and Kosten (See p. 76 in [5]) stating: "It seems plausible that a statical measurement of the stiffness of a sample should give us the modulus of K_1 (modulus of the frame). However it is a rather well-known fact that the dynamical modulus may be several times the statical one."

Pritz [29, 30, 81, 84, 87, 88] observed that almost every vibroacoustic material exhibits nonlinear elastic behaviour as the amplitude of excitation increases. However, in order to determine the *linear* dynamic properties (which are of some practical importance) it was emphasised that the dynamic strain in measurements should be kept below the limiting value at which nonlinear effects appear. It was also mentioned that the limiting strain could act as a material property, but no theoretical or systematically determined experimental value was reported [82, 87]. The "dynamic strain" was also

investigated only theoretically for a viscoelastic rod-like specimen under longitudinal excitation [30, 82], and was assumed to be non-uniform (unlike the case of a spring-like specimen [29]), changing its value according to the standing wave pattern inside the sample.

Pritz also investigated the *in vacuo* dynamic Young's modulus and loss factor of mineral and glass wools containing binding materials [84, 85, 87]. Based on experimental results over the frequency range of architectural interest (100-3000 *Hz*), the frame properties were reported to be independent of frequency [84]. The loss factor was reported to be less than 0.01. In addition, the nonlinearity of the bulk dynamic properties was investigated [85, 87]. The resonant frequency and resonant magnitude of the transfer function were both observed to decrease with increasing strain amplitude. Accordingly the dynamic modulus was observed to decrease and the loss factor to increase, through a maximum, with increasing strain amplitude. The pattern of changing resonant frequency against strain was fitted by a polynomial [87].

Fibrous materials for thermal insulation, used in aircraft fuselage structures, have been intensively investigated in experiments concerning the frequency and amplitude dependence of their dynamic properties [15, 16, 89]. For dynamic excitation, these materials were observed to behave nonlinearly, with the same pattern as that reported for mineral and glass wool used for architectural purposes, by Pritz [89]. At very high levels of excitation, the dynamic modulus approached its static counterpart. It was confirmed that the dynamic modulus was also related to the degree of static "pre-stress" (induced by the mass of a plate placed on top of the sample). The modulus was observed to increase as the static stress increased, which showed the stiffening effect of a sample under increasing static loading [89]. It was also suggested that the character of the frequency dependence in thermal insulation materials might be different, depending on the type of excitation. From experiments with three different types of excitation spectrum involving constant acceleration, velocity, and displacement, it was inferred that the dynamic modulus could be regarded as frequency-independent only when the excitation spectrum was of constant velocity, rather than constant acceleration or displacement [15].

Apart from fibrous materials, Pritz also investigated, in detail, cellular materials such as polyethylene and polystyrene foams [88]. The bulk dynamic Young's modulus and loss factor of these materials were measured as a function of the frequency and amplitude of excitation. The bulk Young's modulus of two types of foam was reported to slightly increase with frequency, in contrast to the frequency independence of polyurethane foam [29]. Beyond the linear upper limit of dynamic strain, the cellular materials were observed to behave nonlinearly like fibrous materials as reported in [85, 87, 89]. Although fibrous materials and cellular materials showed the same trend of nonlinear behaviour, a much larger excitation amplitude was necessary to initiate nonlinearity in the foams, than in their fibrous counterparts. The reason for this was not explained by Pritz. However, the different level of linearity limitation for the two types of materials does not seem to be surprising to the present author. This is because it was demonstrated in Chapter 4 that nonlinearity in fibrous materials is initiated by bending of their fibre components, while frame buckling in cellular materials causes their nonlinearity. As may easily be seen, buckling by the axial component of force is much harder to achieve than bending by the transverse component of force. Therefore, in general, cellular materials are expected to have higher threshold values of nonlinearity than fibrous materials.

7.2 Experimental investigation

Nonlinear dynamic behaviour in fibrous materials needs to be investigated carefully especially when the Young's modulus is measured. Some of the aforementioned characteristics will be confirmed by the results of experiments, reported here. Among several measurement methods, a resonance method [29, 30] has been used. The classical transfer function method (Section 6.2) has been used rather than the newly proposed transmissibility-dynamic mass method (Section 6.3) because the experiments reported in this chapter had been conducted before the new method was developed. However, the

transfer function method proved to be adequate to measure the dynamic nonlinear behaviour of interest for the purposes of this chapter.

7.2.1 Nonlinearity by excitation level

A mineral wool material with a nominal bulk density of 24 kg/m^3 and a thickness of 50 *mm* was subjected to a series of *in vacuo* measurement in which the excitation level was varied. A square sample with the cross-sectional area of 100×100 mm^2 was loaded with a 1.5 *mm* thick aluminium plate weighing approximately 24 *g*. The weight of the plates varies because they were not exactly 100×100 mm^2. Aluminium plates were bonded to both sides of the sample by means of spray-type glue. The fibrous material then was vibrationally excited by white noise, generated by an electro-dynamic shaker.

When the excitation level is low enough to suppress nonlinearity, the measured transmissibility may be expected to be repeatable. However, as illustrated in Figure 7.1, at higher levels the transmissibility plot changes: as the level increases, the resonance peaks decrease both in frequency and magnitude. This is the same trend of observation as that previously reported [85, 87, 89]. In Figure 7.2 it may be noted that, as the level increases, the phase angle does not change as rapidly around resonances as it does at a lower level. In Figure 7.3, the frequency variation of dynamic elastic modulus is plotted. It can be observed that the bulk Young's modulus decreases and the loss modulus – the product of Young's modulus and loss factor – increases with the excitation level. It is also interesting to note that the bulk Young's modulus varies little with frequency when the excitation level is in the linear range, though it increases with frequency under higher excitation levels. Figure 7.4 shows the excitation level measured by the accelerometer on the bottom plate connected to the shaker. It may be concluded from the data that the nonlinear behaviour of the mineral wool can be caused simply by a several-fold increase in the excitation level. (This will be discussed in more detail in a later section.)

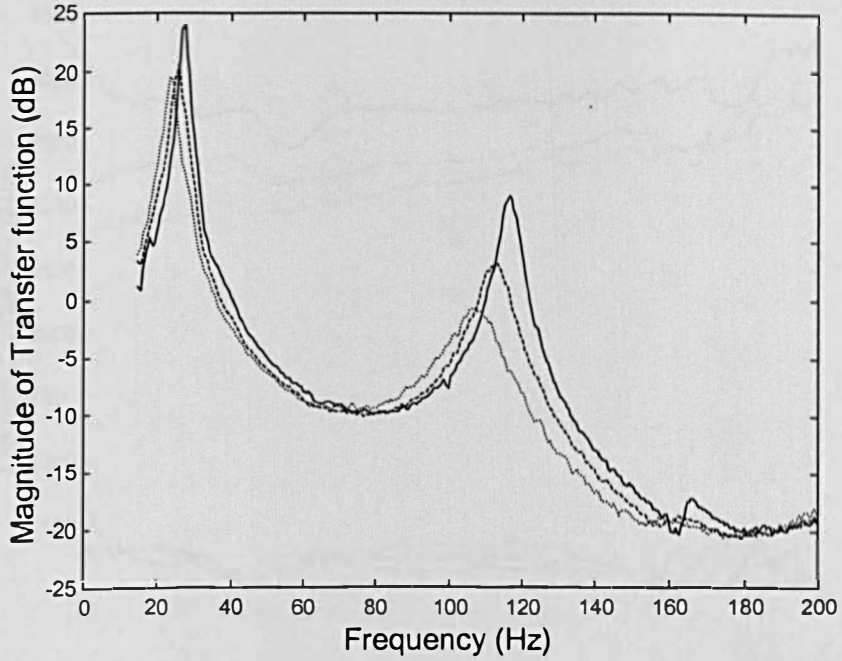

Figure 7.1 Magnitude of the transfer function, showing its dependence on excitation level with white noise, for a mineral wool material. The solid line is for the lowest level and the dotted for the highest.

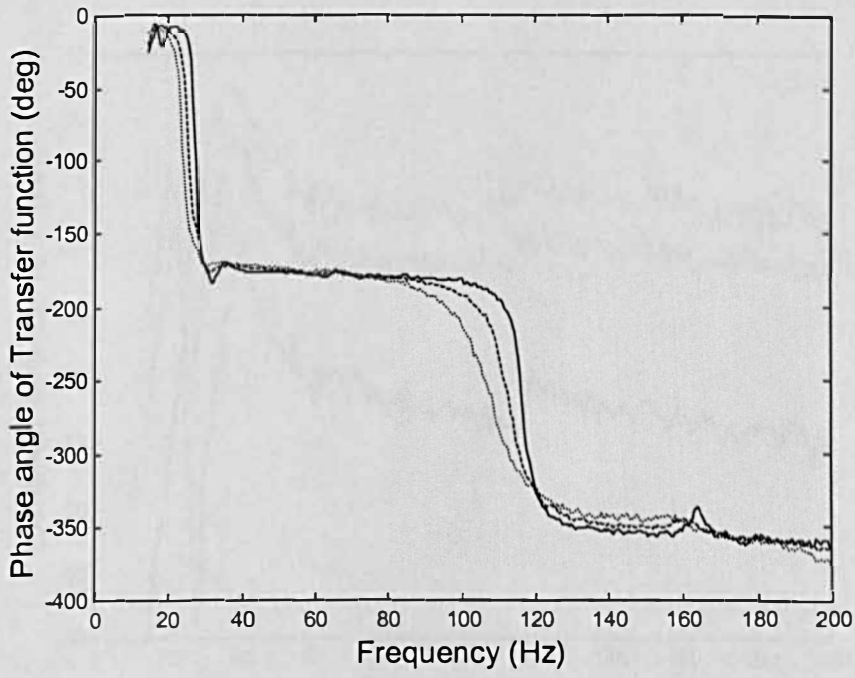

Figure 7.2 Unwrapped phase angle of the transfer functions, showing its dependence on excitation level with white noise, for a mineral wool material. The solid line is for the lowest level and the dotted for the highest.

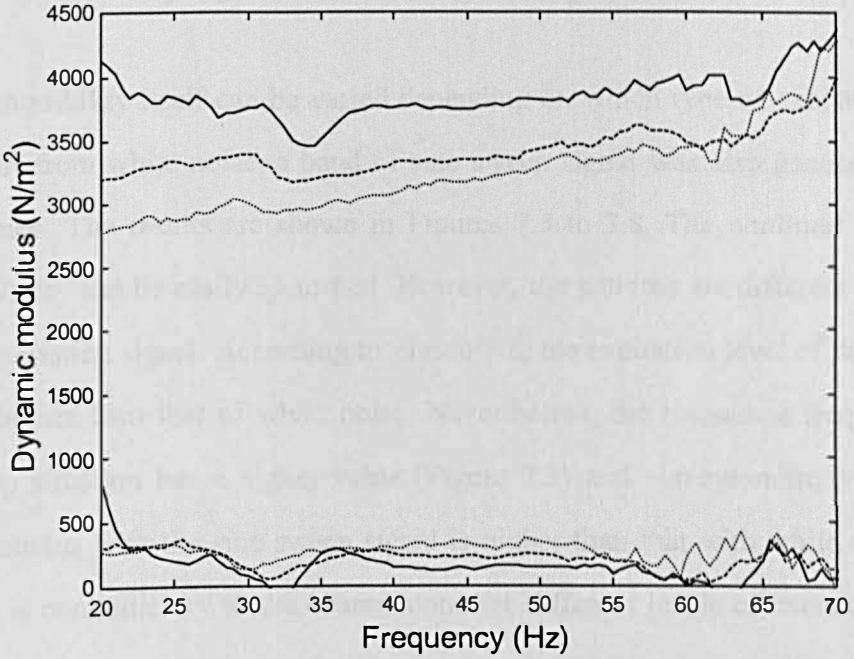

Figure 7.3 Frequency dependence of the dynamic modulus, for different levels of excitation with white noise, for a mineral wool material. The solid line is for the lowest level, and the dotted for the highest. The group of upper curves is for Young's modulus and the lower for loss modulus.

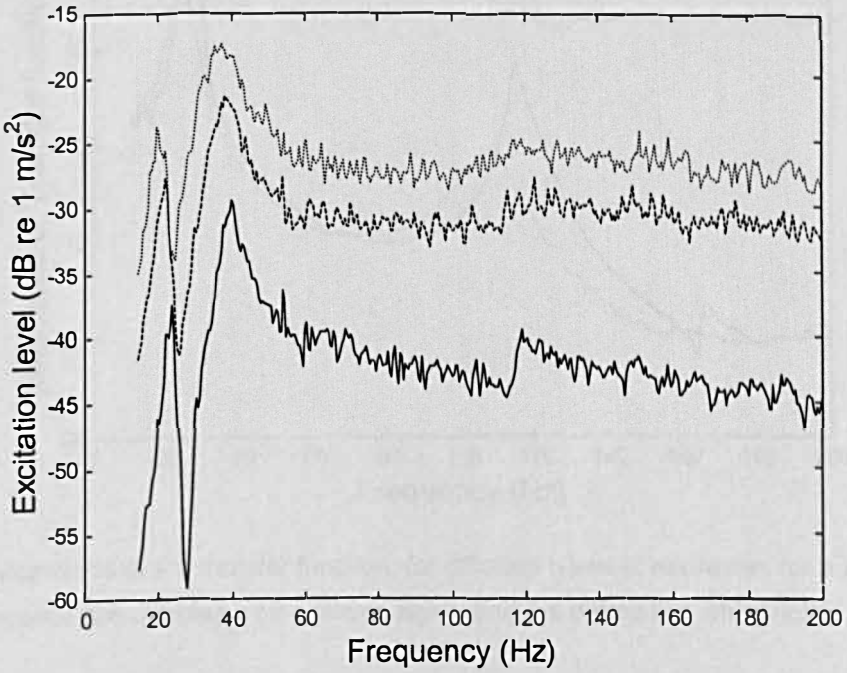

Figure 7.4 Acceleration levels of the bottom plate with white noise excitation. The solid, dashed and dotted lines conform to those of Figures 7.1 to 7.3.

7.2.2 Nonlinearity by excitation signal type

The transmissibility itself can be varied depending on which type of excitation signal is used. Apart from white noise, a band of sine sweep signal was also generated to excite the specimen. The results are shown in Figures 7.5 to 7.8. The nonlinear distortion in transmissibility can be easily identified. However, the patterns are different with the two types of excitation signal. According to Figure 7.8, the excitation level of the sine sweep signal is higher than that of white noise. Nevertheless, the resonance frequency in the sine sweep situation has a higher value (Figure 7.5) and correspondingly the inferred overall modulus with the sine sweep signal is higher than that with white noise (Figure 7.7). This is contradictory to the observations for different levels of excitation by white noise.

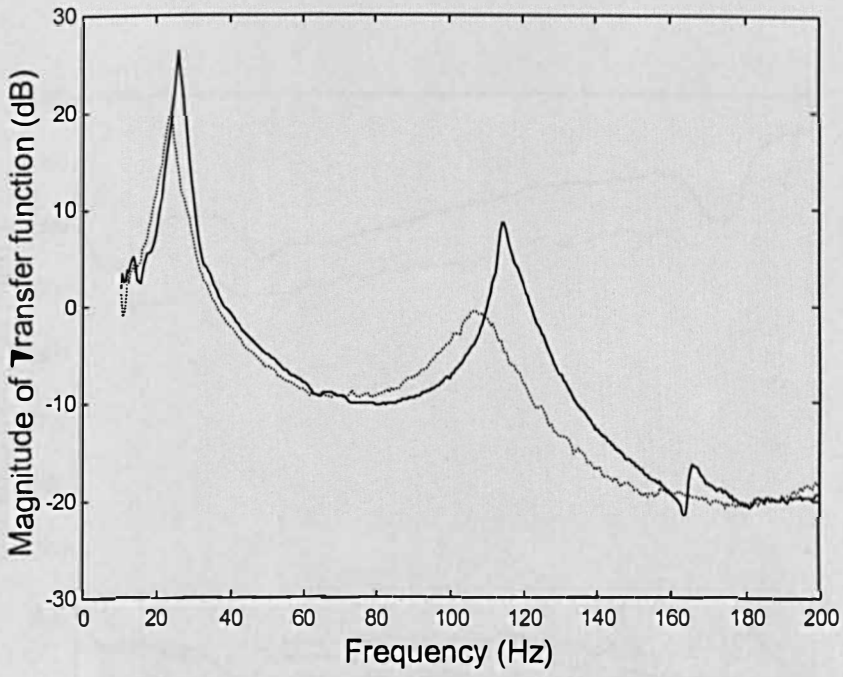

Figure 7.5 Magnitude of the transfer function, for different types of excitation, for a mineral wool material. The solid line denotes a sine sweep signal and the dotted line white noise.

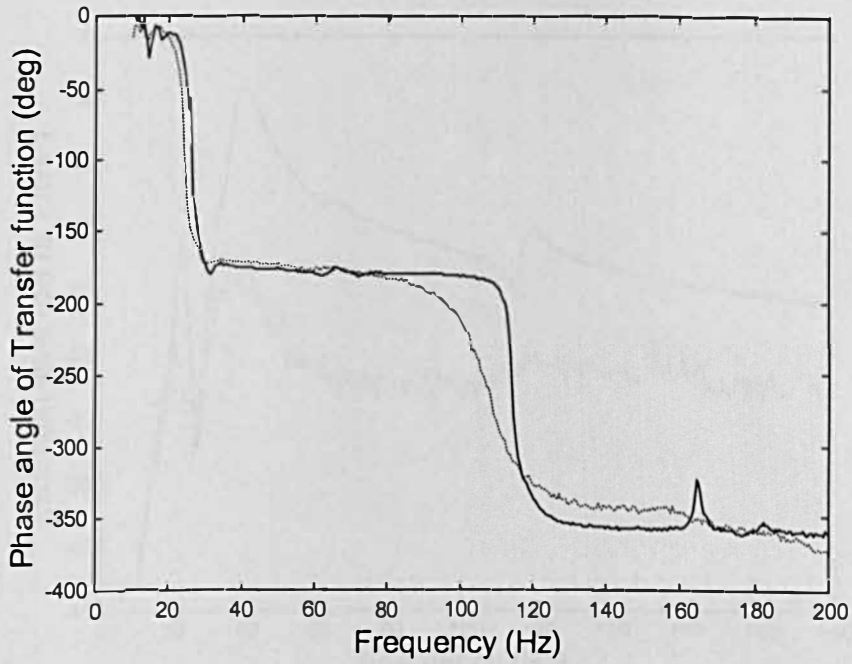

Figure 7.6 Phase angle of the transfer function, for different types of excitation, for a mineral wool material. The solid line denotes a sine sweep signal and the dotted line white noise.

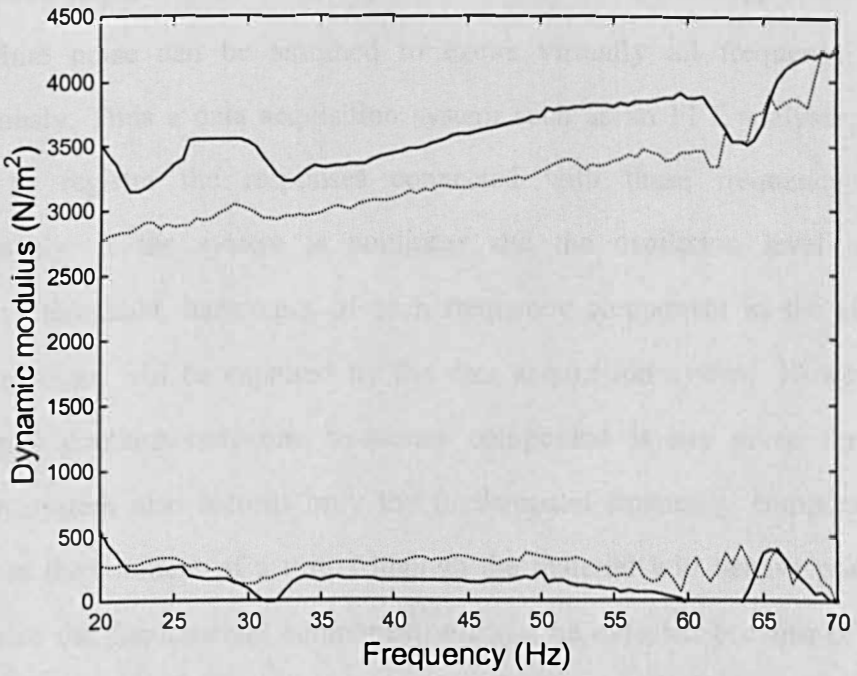

Figure 7.7 Frequency dependence of the dynamic modulus, for different types of excitation, for a mineral wool material. The solid line is for a sine sweep, and the dotted for white noise. The two upper curves are for the bulk Young's modulus, and the lower two are for the loss modulus.

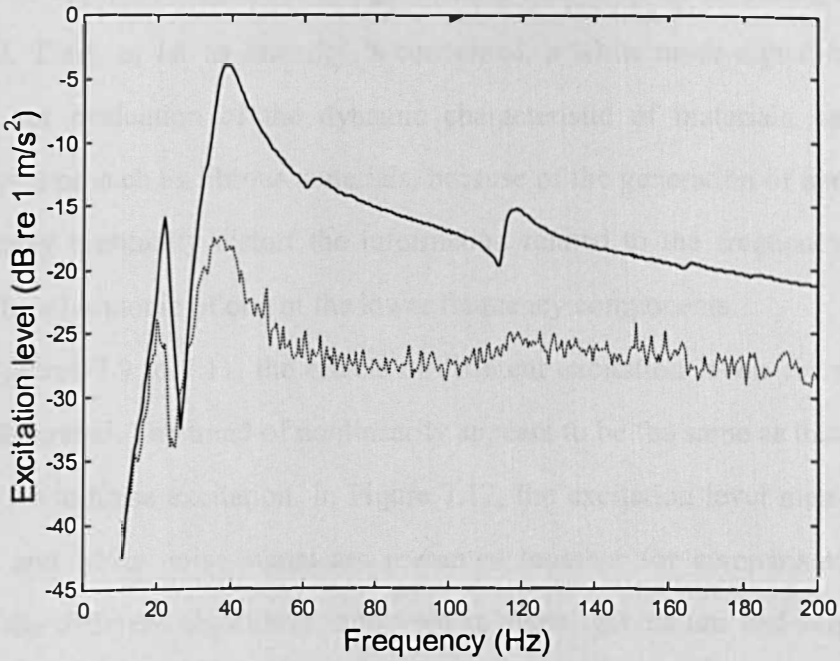

Figure 7.8 Acceleration levels on the bottom plate with different types of excitation. The solid line denotes a sine sweep signal and the dotted line white noise.

At this stage, some differences related to the nature of both types of signal may be noted. White noise can be assumed to excite virtually all frequency components simultaneously. Thus a data acquisition system such as an FFT analyser may also be expected to register the responses connected with these frequency components simultaneously. If the system is nonlinear and the excitation level is above the nonlinearity threshold, harmonics of each frequency component in the signal will be excited and these will be captured by the data acquisition system. However, the sine sweep signal contains only one frequency component at any given time. The data acquisition system also records only the fundamental frequency component which is generated at the moment of a test. Although the material will behave nonlinearly, the harmonics of the fundamental component will not be detected because of the inherent characteristics of a sine sweep algorithm. Therefore, the effects of nonlinearity in the sine sweep signal are less than those in the case of white noise, although the level of excitation is apparently greater in the sine sweep signal than in the white noise signal. Although the nonlinear behaviour of fibrous materials is the main topic in this chapter, in

many practical applications such as design work, the linear value of Young's modulus is often useful. Thus, as far as linearity is concerned, a white noise signal might not be appropriate for evaluation of the dynamic characteristic of materials, especially for nonlinear systems such as fibrous materials, because of the generation of harmonics. The harmonics may eventually distort the information related to the frequency of interest, which may be a harmonic of one of the lower frequency components.

In Figures 7.9 to 7.11, the effects of different excitation levels for a sine sweep signal are illustrated. The trend of nonlinearity appears to be the same as that observed in the case of white noise excitation. In Figure 7.12, the excitation level measured for the sine sweep and white noise signal are presented together for comparison. Therefore, because of the different algorithms employed in signal generation and acquisition, the mixed use of different types of signal is not recommended for the evaluation of nonlinear behaviour in fibrous materials.

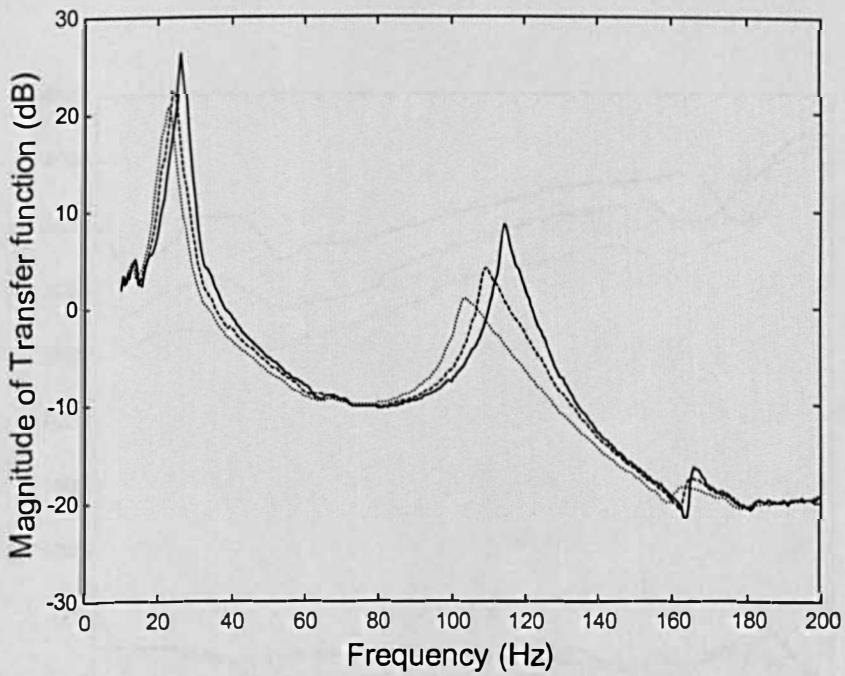

Figure 7.9 Magnitude of the transfer function, for different excitation level of sine sweep signals, for a mineral wool material. The solid line is for the lowest level and the dotted for the highest.

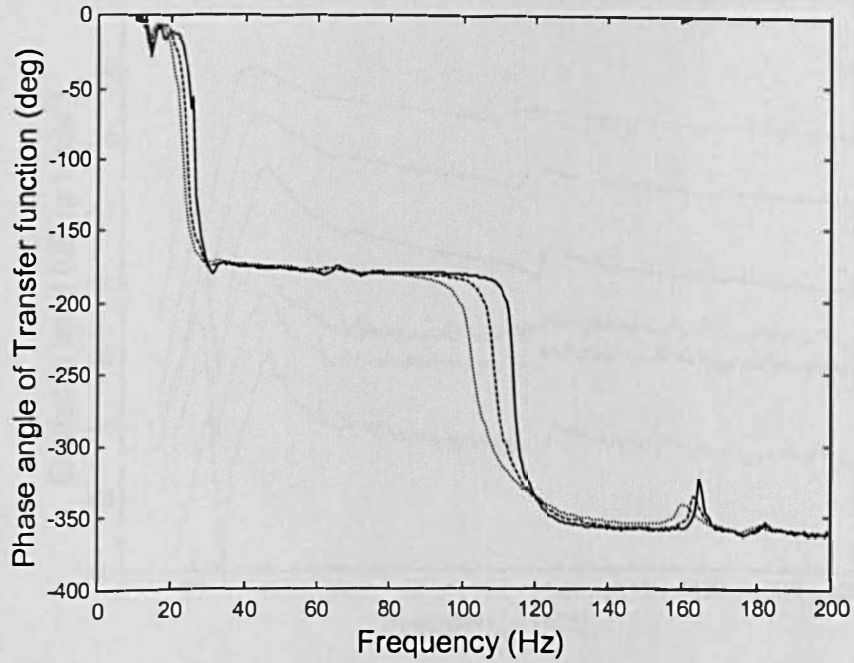

Figure 7.10 Phase angle of the transfer function, for different excitation level of sine sweep signals, for a mineral wool material. The solid line is for the lowest level and the dotted for the highest.

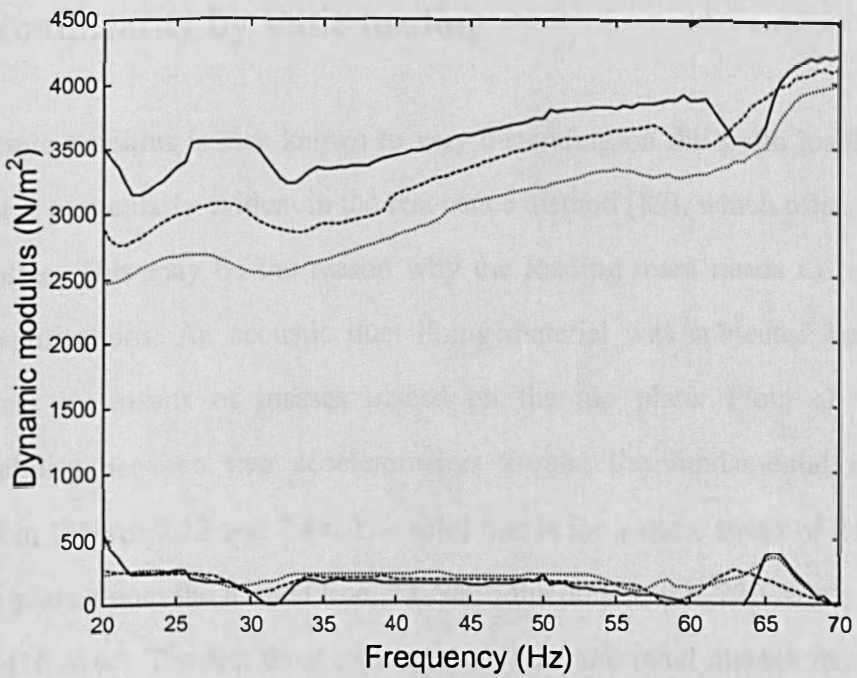

Figure 7.11 Frequency dependence of the dynamic modulus, for different excitation level of sine sweep signals, for a mineral wool material. The solid line is for the lowest level and the dotted for the highest. The upper three curves are for the Young's modulus and the lower three are for the loss modulus.

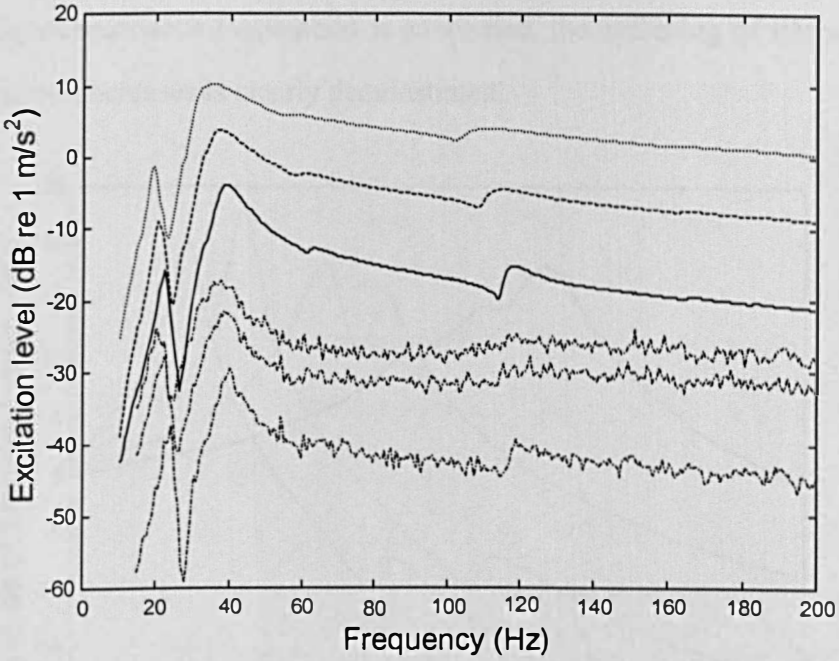

Figure 7.12 Acceleration levels on the bottom plate. The solid, dashed and dotted lines are for sine sweep signals and conform to those in Figures 7.9 to 7.11. The bottom three dash-dot lines are those for white noise, shown in Figure 7.4.

7.2.3 Nonlinearity by static loading

The dynamic modulus is also known to vary depending on the static loading mass, and this effect is particularly evident in the resonance method [89], which often requires a top loading plate. This may be the reason why the loading mass needs to be selected for specific applications. An acoustic duct lining material was subjected here to varying static stress by means of masses placed on the top plate. Plots of the *in vacuo* transmissibility between two accelerometers around the fundamental resonance are presented in Figures 7.13 and 7.14. The solid line is for a static stress of 24 N/m^2, which is the top plate alone; the dashed line, 73 N/m^2; the dotted line, 220 N/m^2; and the dash-dot line, 416 N/m^2. The last three cases include the additional masses together with the aluminium top plate. The presence of the double peak for 73 N/m^2 is believed to be related to an imbalance occurring when masses were placed on the top plate, causing additional degrees of freedom in the motion of the system to be excited. However, as far

as the shifting of resonance frequencies is concerned, the stiffening of fibrous materials as the static stress increases is clearly demonstrated.

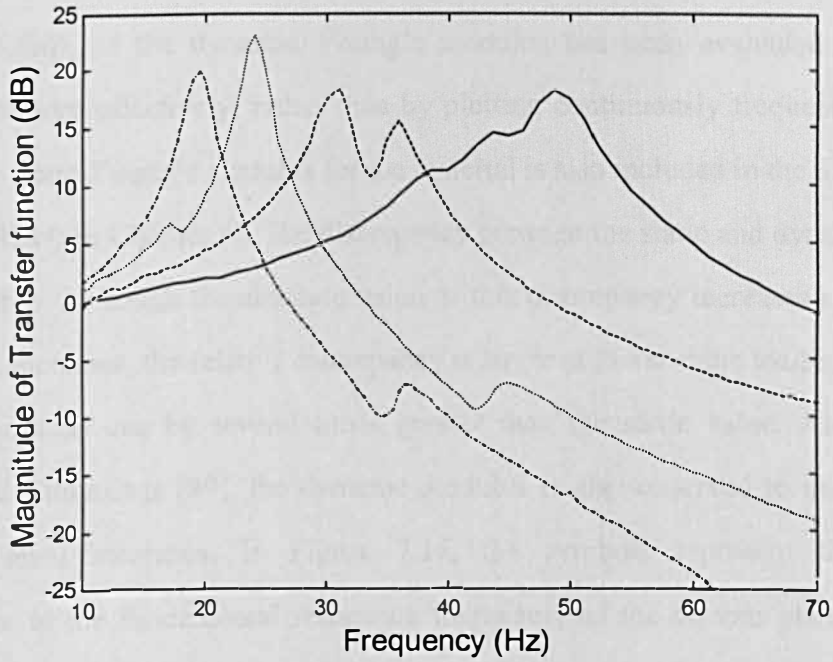

Figure 7.13 Magnitude of the transfer function, showing its dependence on the static loading, for an acoustic duct lining material. The solid line is for 24 N/m^2; the dashed line, 73 N/m^2; the dotted line, 220 N/m^2; and the dash-dot line, 416 N/m^2.

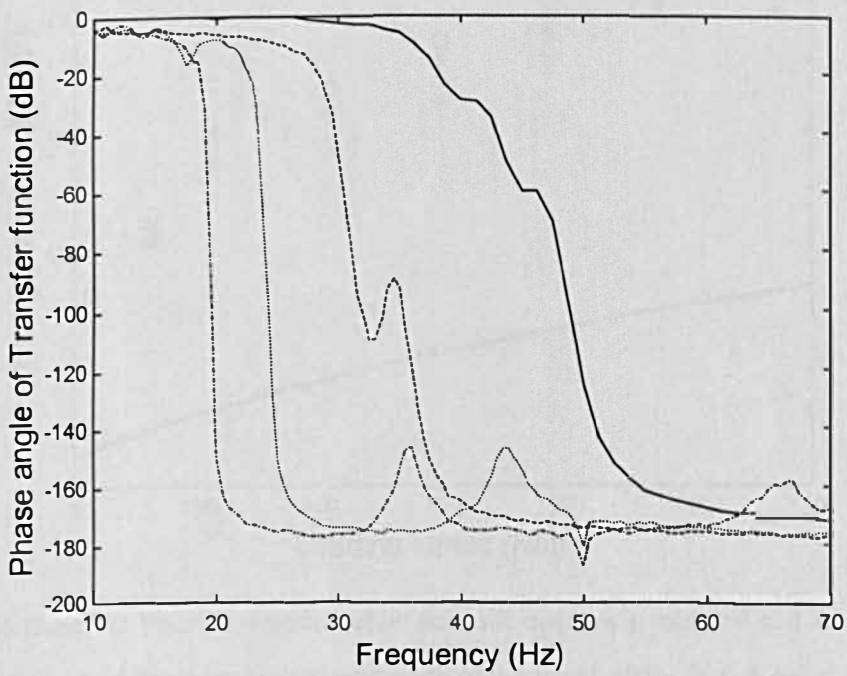

Figure 7.14 Phase angle of the transfer function, showing its dependence on static loading, for an acoustic duct lining material. The line definitions are as in Figure 7.13.

In Figure 7.15, a variation of excitation levels is superimposed upon the relationship between the bulk Young's modulus and the static loading stress. A single representative value, obtained at the resonance frequency for each loading stress (see equation (6.6a)), of the dynamic Young's modulus has been evaluated to show the relationship more effectively, rather than by plotting continuously frequency-dependent values. The static Young's modulus for the material is also included in the plot by the use of the MNBM (see Chapter 4). The discrepancy between the static and dynamic values is plainly visible. Although the absolute value of this discrepancy increases slightly as the static stress increases, the relative discrepancy is larger at lower static loadings, where the dynamic modulus can be several times greater than the static value. As reported by Watson and Cummings [89], the dynamic modulus is also observed to decrease as the excitation level increases. In Figure 7.15, the symbols represent the measured acceleration, at the fundamental resonance frequency, of the bottom plate, which was bonded to the specimen. The stiffening effect of the material is confirmed through a range of excitation levels as the static loading stress increases.

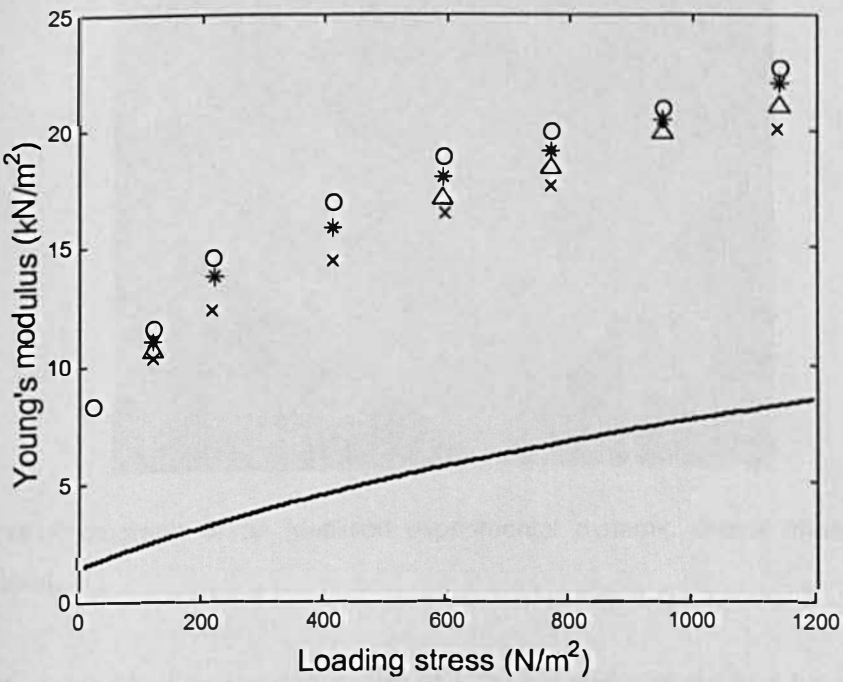

Figure 7.15 Dynamic Young's modulus of an acoustic duct-lining material and its dependence on static loading and the acceleration amplitude of the lower plate. O, 0.3 m/s^2 ; ✳, 0.6; Δ, 0.9; and X, 1.2, respectively. The solid line is for the static Young's modulus according to the MNBM.

7.2.4 Idealised dynamic models

Nonlinearity in fibrous materials under static loading has been shown to occur as a result of an increase in the number of inter-fibre contacts (see Chapters 2 and 4). The same concept can be applied to the dynamic situation. A number of what may be termed "idealised dynamic models" have been formulated here to support this idea experimentally. Straight, uniform, circular rods such as welding rods and glass capillary tubes were cut to a fixed length. They were then stacked in order to build a bulk structure. Rods were placed at an equal spacing in each layer. Each new layer was placed at 90° to the layer below and was shifted by a half spacing between rods, relative to the next layer but one below, to allow bending to occur. This structure is essentially the same as that of the idealised static bending models described in Chapter 4. As an example, a photograph of a model composed of glass capillary tubes is shown in Figure 7.16.

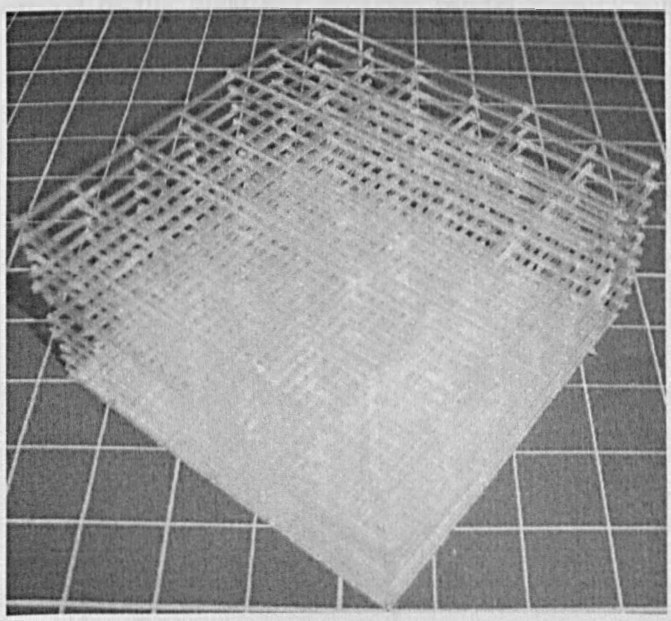

Figure 7.16 Photograph of an idealised experimental dynamic model made from glass capillary tubes.

Each capillary tube had an outer diameter of 1.26 *mm* and was cut to a length of 100 *mm*. The nominal spacing between the rods was 33.3 *mm*, and there were 42 layers. The bulk density of the structure was 31.7 kg/m^3. Thus the solid fraction was 0.0127, based on a

density of 2500 kg/m^3 for glass. Given the nature of the idealised structure, there would not be a change in the number of inter-rod contacts, even if the excitation level were high. However, if the level were great enough, there could be a possibility of intermittent contact between layers. The measured transfer function of the idealised model is shown in Figures 7.17 to 7.18, and the excitation levels with white noise and sine sweep signals are shown in Figure 7.19. It can be seen that there is no difference whatsoever in the transmissibility between white noise and sine sweep excitation (Figures 7.17 and 7.18). Taking into account that the difference in the excitation level between two signals is about 50 *dB* (Figure 7.19), one may regard the idealised model as a true linear system. This suggests that a nonlinear mechanism in fibrous materials is a change in the number of inter-fibre contacts in the dynamic situation as well as for static loading. It may be worth noting again that, in real fibrous materials, an increase in the excitation level of only 10 *dB* is enough to bring about nonlinear behaviour (Figure 7.8), while no nonlinearity is observed in the idealised dynamic model despite a large change in the excitation level.

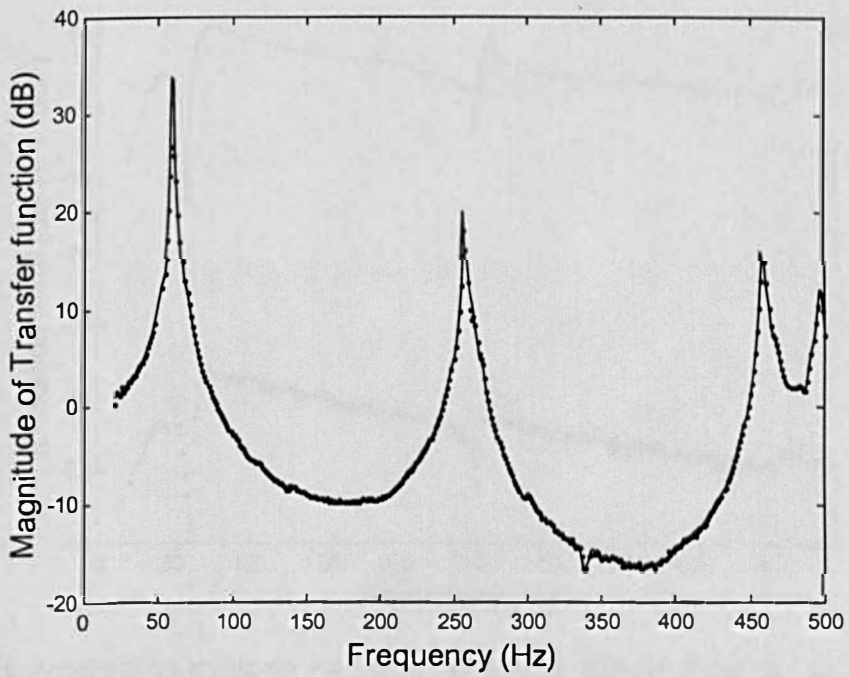

Figure 7.17 Magnitude of the transfer function, showing its dependence on signal type, for an idealised dynamic model made from glass capillary tubes. The solid line denotes a sine sweep signal, and the dots white noise.

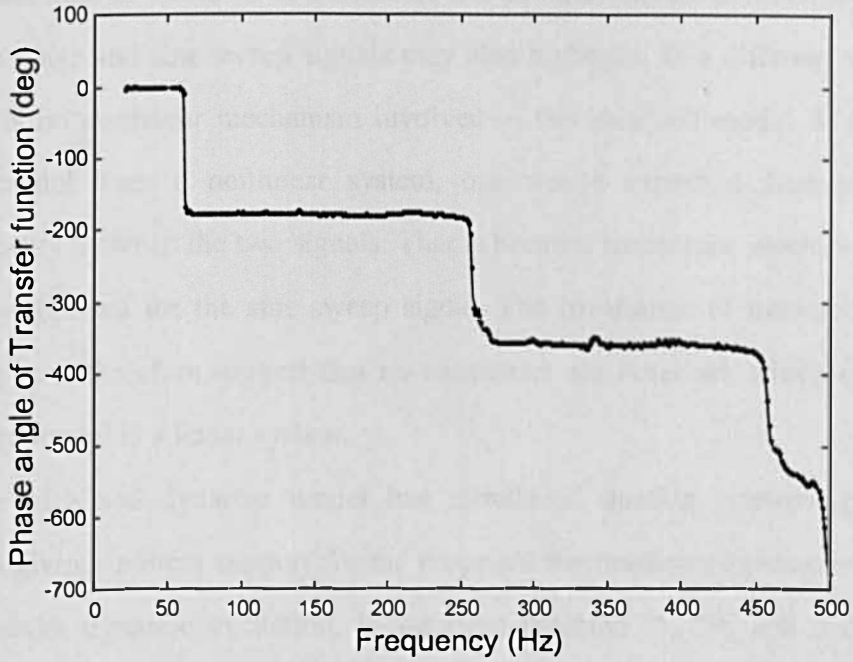

Figure 7.18 Unwrapped phase angle of the transfer function, showing its dependence on signal type, for an idealised dynamic model made from glass capillary tubes. The solid line denotes a sine sweep signal and the dots white noise.

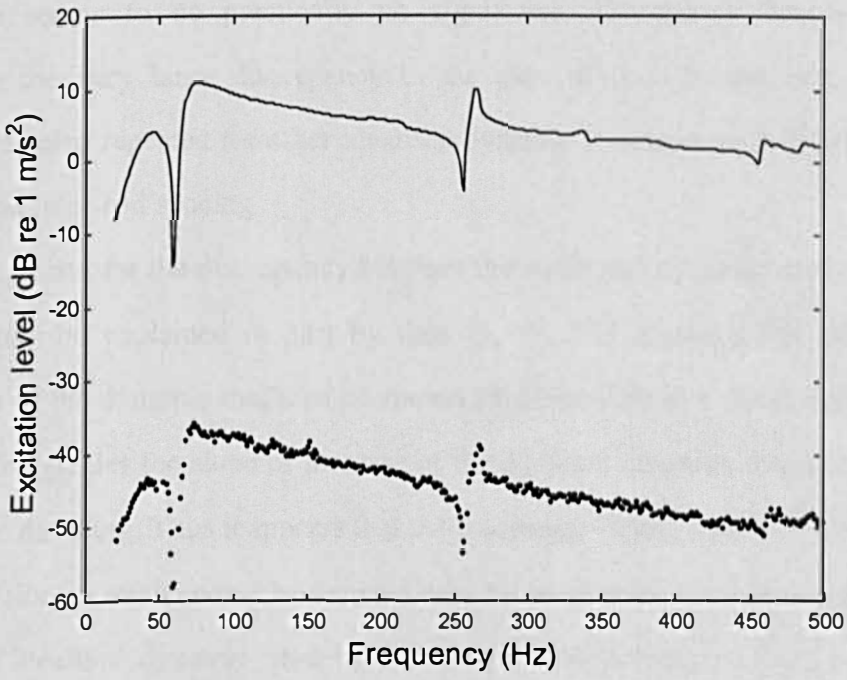

Figure 7.19 Acceleration levels on the bottom plate with different types of excitation, for an idealised dynamic model made from glass capillary tubes. The solid line denotes a sine sweep signal and the dots white noise.

In addition to the level of excitation, the fact that the transmissibility is identical with white noise and sine sweep signals may also highlight, in a different way, the fact that there is no nonlinear mechanism involved in the idealised model. If the idealised dynamic model were a nonlinear system, one would expect a discrepancy in the transmissibility between the two signals. That is because harmonics would be present for white noise, but not for the sine sweep signal. The invariance of transmissibility with signal type may therefore suggest that no harmonics are involved, which indicates that the idealised model is a linear system.

The idealised dynamic model has introduced another interesting feature, in addition to giving indirect support for the proposed the nonlinear mechanism of fibrous materials under dynamic excitation. It has been reported [5, 79] and confirmed here experimentally (Figure 7.15) that the dynamic Young's modulus of poroelastic materials is usually much higher than its static counterpart. However, in Figure 7.20, the dynamic Young's modulus of an idealised structure is seen to be very close to its static counterpart, which is measured in a separate static test and denoted by the dashed line. Thus there seems to be practically no significant discrepancy between the two, considering the very large discrepancy in the case of real fibrous materials. These findings were also repeated for other idealised dynamic structures with different element materials and inter-rod spacing.

The reason for the discrepancy between the static and dynamic moduli of fibrous materials may be explained in part by data [5, 97, 98] showing that the frequency dependence of the dynamic modulus of viscoelastic materials is a direct consequence of damping. The greater the slope of increase of the dynamic modulus-frequency curve, the higher is the damping. Thus it appears that the frequency independence of the bulk elastic modulus of fibrous media could be realised only for ideal elasticity with no damping. For the case of idealised dynamic models, the frequency dependence of the modulus (see Figure 7.20) may be regarded "weak" in the sense that it does not show a gradual increase or decrease. The loss factor in air (see Figure 7.21) is small and falls to the order of 0.01 in most cases. It is believed that the low-loss nature of the idealised dynamic

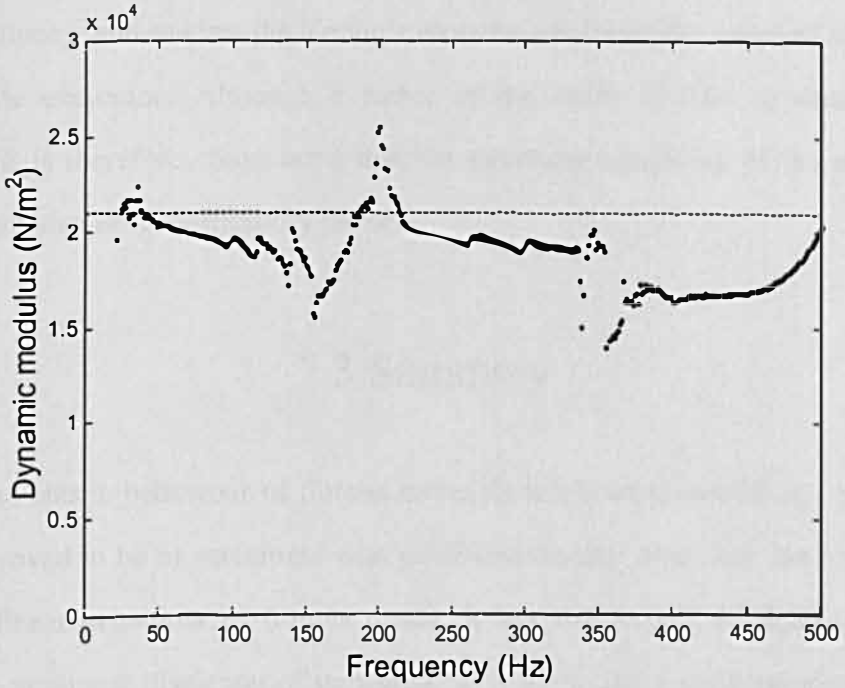

Figure 7.20 Dynamic Young's modulus of an idealised dynamic model made from glass capillary tubes. The dashed line denotes the static Young's modulus.

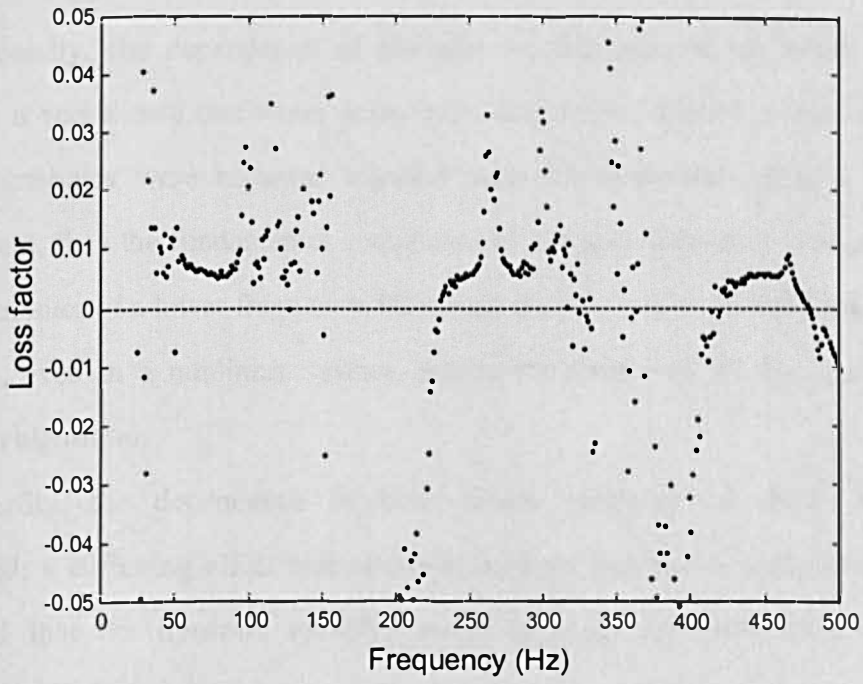

Figure 7.21 Loss factor of an idealised dynamic model made from glass capillary tubes. The dashed line denotes zero.

models extends the frequency independence of the dynamic bulk elastic modulus down to zero frequency, and renders the Young's modulus similar in the cases of static loading and dynamic excitation. Although a factor of the order of 0.01 is small, it is not negligible. It is therefore conjectured that the structural simplicity of the experimental models might also be a contributory factor.

7.3 Summary

The dynamic elastic behaviour of fibrous materials has been reviewed and experimental data have proved to be in agreement with published results. Attention has been focussed on the nonlinear behaviour of fibrous media. It has first been confirmed that one can observe the nonlinear distortion of transmissibility plots and a corresponding change in the complex Young's modulus as a function of excitation level. The trend is that, with increasing excitation amplitude, the dynamic modulus decreases and the loss factor increases; this is detectable by a decrease of resonant peaks in the transmissibility both in frequency and magnitude.

Secondly, the dependence of modulus on the type of excitation signal was examined. It was shown that white noise and a sine sweep showed a clear difference in results. Harmonics were recorded together with fundamentals during a white-noise measurement, thus the fundamental component of a higher frequency was contaminated by the harmonics of a lower frequency. However, the sine sweep procedure did not detect harmonics, even in a nonlinear system, due to the nature of its data generation and acquisition algorithm.

Thirdly, the dependence of bulk elastic modulus on static loading was investigated; a stiffening effect was observed with an increase in static loading. It was also noted that the dynamic modulus could approach its static counterpart, with increasing excitation.

Finally, an idealised experimental dynamic model was introduced. It had the same transversely isotropic layered structure as that used in previous static bending models. It

has been shown that the dynamic behaviour of this structure is independent of the level of excitation and the type of signal. This therefore seems to suggest that the nonlinear mechanism in the dynamic situation is similar to that in the static situation, namely a change in the number of inter-fibre contacts. Tests on the idealised experimental model have also demonstrated that its dynamic modulus is very close to its static modulus. It is believed that its inherent low loss factor as well as its idealised simple structure could explain this feature.

Chapter 8

A differential equation for the nonlinear dynamic structural behaviour of fibrous materials

The dynamic behaviour of bulk fibrous materials, including nonlinear effects, has been discussed in Chapter 7. It was observed that nonlinear characteristics could be identified in "raw" measured data such as the transmissibility as well as in corresponding "post-processed" data such as the complex bulk Young's modulus. Despite this nonlinearity, the linear wave equation has been used to determine the bulk properties in the nonlinear region (see the development of methods in Chapter 6 and other references [16, 28, 29, 30, 85, 87]). It is therefore appropriate that the nonlinear behaviour of bulk fibrous materials should be investigated by means of a nonlinear formulation of the *in vacuo* structural wave equation. The development of such an equation and its interpretation and application to bulk fibrous materials are described in this chapter.

8.1 The differential equation governing longitudinal motion

When porous or homogeneous solid materials are at rest, the stress-strain relationship is governed by the equations of equilibrium. However, in a dynamic situation where actions such as force, displacement, velocity or acceleration are applied to parts of the structure, the equations of equilibrium need to be replaced by equations of motion. Usually it takes time for such changes to travel to all parts of the structure. This is because the "information" or "signal" represented by changes in stress or strain, is transmitted as a form of wave with finite propagation speed [61].

The following wave equation governs the linear dynamic behaviour of plane waves in solid or porous media, represented by the particle displacement ξ, when there are no body forces [61, 86, 100, 101, 102, 104],

$$\frac{\partial^2 \xi}{\partial t^2} = c^2 \frac{\partial^2 \xi}{\partial x^2}. \tag{8.1}$$

Depending on how solids resist changes in both volume and shape (storing energy in both compression and shear), there are several types of waves with different propagation speeds c. These are compressional (longitudinal) waves, transverse (shear) waves, torsional waves, flexural (bending) waves and Rayleigh surface waves [102]. Especially for longitudinal and transverse waves in isotropic solid or porous materials, the phase speed c of those waves can be written [61, 86, 100, 101, 102, 104]

$$c = \sqrt{\frac{\lambda + 2G}{\rho}} \quad \text{for pure longitudinal waves,} \tag{8.2a}$$

$$c = \sqrt{\frac{G}{\rho}} \quad \text{for transverse waves,} \tag{8.2b}$$

$$c = \sqrt{\frac{E}{\rho}} \quad \text{for quasi-longitudinal waves,} \tag{8.2c}$$

where the symbol λ denotes a Lamé constant and G is the modulus of elasticity in shear, or simply the modulus of rigidity. The modulus of elasticity in tension or compression is E (i.e., the Young's modulus), and the material density is ρ. In the case of a porous material the Young's modulus, shear modulus and density should be for the bulk structure rather than for the solid comprising the frame of the material. The bulk parameters are usually much smaller than those for the solid material. For isotropic materials, the parameters appearing in equation (8.2) are related to one another by

$$\lambda = \frac{\nu}{(1+\nu)(1-2\nu)} E, \tag{8.3a}$$

$$G = \frac{E}{2(1+\nu)}. \tag{8.3b}$$

Here, ν denotes the Poisson's ratio.

The distinction between the pure and quasi-longitudinal waves can be explained in the following manner. Theoretically a pure longitudinal wave can be realised only for a structure whose extent in all directions is much greater than a wavelength. Thus, lateral dimensions are not free from stress. Instead, lateral strains are usually set to zero – which does not necessarily imply an infinitesimal Poisson's ratio – to produce the relations (8.2a) and (8.3a). However, in many engineering applications, most structures or materials in use have at least one of the dimensions smaller than the wavelength of interest. This is the case, for example, in plates, beams, rods and bars [86]. Thus, a pure longitudinal wave is hard to realise in practice. The lateral strains experience periodic variations because of effects related to Poisson's ratio. The absence of lateral stresses makes the wave speed in practice smaller than that of a pure longitudinal wave. According to the definition of Young's modulus as the ratio of stress to strain in tension or compression with no lateral stresses, the phase speed of a quasi-longitudinal wave is directly related to Young's modulus as forecast by equation (8.2c) [86]. However, the relation for a quasi-longitudinal wave is an approximation of so-called "Love theory" [81, 90, 100], which partially takes into account the lateral motion,

$$\frac{\partial^2 \xi}{\partial t^2} - (\nu r_G)^2 \frac{\partial^4 \xi}{\partial x^2 \partial t^2} = \frac{E}{\rho} \frac{\partial^2 \xi}{\partial x^2}. \tag{8.4}$$

Here r_G represents the radius of gyration about the direction of the propagation, the x axis in this case. Thus, for a long slender rod, the second term on the left-hand side of equation (8.4) may be negligible, justifying the approximation of quasi-longitudinal wave motion.

8.2 The governing differential equation for fibrous materials

So far in this chapter, the isotropy of solid media has been taken for granted. As a consequence, simple relationships have been established between Young's modulus, shear modulus and Poisson's ratio (in equation (8.3)) and the phase speed of waves (in equation (8.2)). However, fibrous media – which are the main subject of this thesis – are not, in the first place, isotropic materials. Therefore, the true nature of the structural behaviour of typical fibrous materials needs to be investigated with the inclusion of anisotropy.

By analogy, it may be useful to note that three basic equations are required to derive a wave equation in acoustics [95]. These are usually called the equation of continuity, the equation of motion and the equation of state. Similarly, three basic relationships are also needed to develop a structural wave equation in a solid body. They are the equation of motion, the displacement-strain relation and the stress-strain relation. The stress-strain relationship is also known – in the case of linear elasticity – as Hooke's law. The first two relationships will be the same regardless of whether or not the material is isotropic.

Consider a parallelepiped element of material, with stress components acting on its six sides. The equations of motion are easily obtained by equating the external force acting on this element to the inertial force in each orthogonal direction. Provided that there are no body forces, the differential equations for small displacements are [61]

$$\frac{\partial \sigma_x}{\partial x}+\frac{\partial \tau_{xy}}{\partial y}+\frac{\partial \tau_{xz}}{\partial z}=\rho\frac{\partial^2 \xi_x}{\partial t^2} \tag{8.5a}$$

$$\frac{\partial \tau_{yx}}{\partial x}+\frac{\partial \sigma_y}{\partial y}+\frac{\partial \tau_{yz}}{\partial z}=\rho\frac{\partial^2 \xi_y}{\partial t^2} \tag{8.5b}$$

$$\frac{\partial \tau_{zx}}{\partial x}+\frac{\partial \tau_{zy}}{\partial y}+\frac{\partial \sigma_z}{\partial z}=\rho\frac{\partial^2 \xi_z}{\partial t^2}. \tag{8.5b}$$

The normal stress is denoted σ, the shear stress τ, the particle displacement ξ and the density ρ. For stresses, the single subscript indicates that the first and second subscripts are equal. The first subscript denotes the side of the parallelepiped to which the stress is applied and the second denotes the direction of the stress, as is usual in the stress tensor. For displacements, the single subscript denotes the direction of the displacement.

For small displacements, strain can be related to displacement by a first order approximation of the partial derivatives of displacements. Thus the relationships can be expressed as follows (under the assumption that the strains are small compared with unity [51, 61]),

$$\varepsilon_x = \frac{\partial \xi_x}{\partial x}, \qquad \varepsilon_y = \frac{\partial \xi_y}{\partial y}, \qquad \varepsilon_z = \frac{\partial \xi_z}{\partial z}, \text{ and} \tag{8.6a}$$

$$\gamma_{xy} = \frac{\partial \xi_x}{\partial y} + \frac{\partial \xi_y}{\partial x}, \qquad \gamma_{yz} = \frac{\partial \xi_y}{\partial z} + \frac{\partial \xi_z}{\partial y}, \qquad \gamma_{zx} = \frac{\partial \xi_z}{\partial x} + \frac{\partial \xi_x}{\partial z}. \tag{8.6b}$$

In equations (8.6a,b), the normal strains are denoted ε and the shear strains γ.

For isotropic materials, three elastic constants such as Young's modulus, shear modulus and Poisson's ratio suffice to describe the linear structural relationships between stresses and strains. For anisotropic materials, the number of elastic constants could be as large as 21. This number is reduced when the material has a particular symmetry, and is equal to three in the isotropic case [103]. Although fibrous materials are generally regarded as anisotropic, they have a certain symmetry which has the effect of reducing the necessary number of elastic constants (provided the macroscopic volume is chosen to be large enough to overcome the potential inhomogeneity related to the microstructure). They may at first seem to be orthotropic materials, because their structures all appear to be identical after a 180° rotation about any of the three orthogonal coordinate axes. Secondly, one of the three orthogonal axes is the axis of symmetry, and any plane containing it is the plane of symmetry. So they can be further simplified as transversely isotropic materials or hexagonal materials. The transversely isotropic nature of typical layered fibrous materials is depicted in simplified form in Figure 8.1.

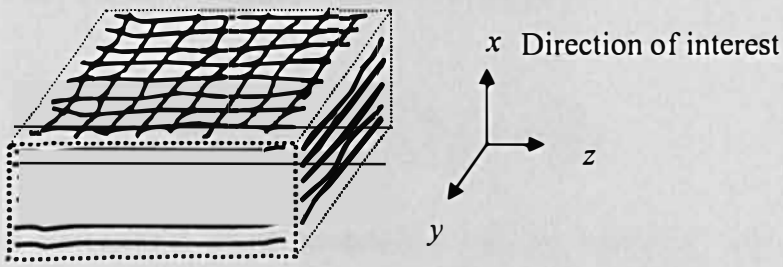

Figure 8.1 Schematic diagram of a typical layered fibrous material. Its transverse isotropy is exaggerated.

The simplicity brought by the symmetry of orthotropic media is that there is no interaction between the normal and shear stress and strain components, which reduces the number of elastic constants to nine. Furthermore, no distinction is made for other two axes (y and z in Figure 8.1) in the case of transversely isotropic materials, which requires only 6 elastic constants [51, 103]. Therefore, the relation between strain and stress in linear elastic fibrous materials may be expressed in the following,

$$\begin{bmatrix} \varepsilon_x \\ \varepsilon_y \\ \varepsilon_z \\ \gamma_{xy} \\ \gamma_{yz} \\ \gamma_{zx} \end{bmatrix} = \begin{bmatrix} S_{11} & -\nu_1 S_{11} & -\nu_1 S_{11} & & & \\ -\nu_1 S_{11} & S_{22} & -\nu_2 S_{22} & & & \\ -\nu_1 S_{11} & -\nu_2 S_{22} & S_{22} & & & \\ & & & S_{44} & & \\ & & & & S_{55} & \\ & & & & & S_{44} \end{bmatrix} \begin{bmatrix} \sigma_x \\ \sigma_y \\ \sigma_z \\ \tau_{xy} \\ \tau_{yz} \\ \tau_{zx} \end{bmatrix}. \tag{8.7}$$

Here, S is an elastic constant which is inversely proportional to elastic modulus. Subscripts represents directions, 1 to 3 for x to z in normal components, and 4 to 6 for x to z in shear components (see Figure 8.1). Symmetry has already been allowed for in subscripts and blank elements. The blank in the matrix shows there are no relations for particular strain-stress components.

Provided that all the elements in the stiffness matrix (8.7) are linear, the equation of motion (8.5a) turns out to be the following expression, after three basic equations for structural motion for fibrous materials are combined together,

$$\frac{-\nu_1}{(\nu_2-1)S_{22}+2\nu_1^2 S_{11}}\nabla^2\xi_x+\frac{(\nu_2-1)S_{22}+\nu_1 S_{11}}{S_{11}\{(\nu_2-1)S_{22}+2\nu_1^2 S_{11}\}}\frac{\partial^2\xi_x}{\partial x^2}+\cdots$$

$$\cdots+\frac{1}{S_{44}}\left\{\frac{\partial^2\xi_x}{\partial y^2}+\frac{\partial^2\xi_x}{\partial z^2}+\frac{\partial^2\xi_y}{\partial x\partial y}+\frac{\partial^2\xi_z}{\partial x\partial z}\right\}=\rho\frac{\partial^2\xi_x}{\partial t^2}. \tag{8.8}$$

In the case of one-dimensional plane longitudinal waves, where $\xi_y=\xi_z=0$ and $\xi_x=\xi_x(x)$ (the main case of interest of this chapter) the above relation further simplifies to

$$\frac{(\nu_2-1)S_{22}}{S_{11}\{(\nu_2-1)S_{22}+2\nu_1^2 S_{11}\}}\frac{\partial^2\xi_x}{\partial x^2}=\rho\frac{\partial^2\xi_x}{\partial t^2} \tag{8.9}$$

The bulk Poisson's ratio ν_1 of typical fibrous materials is likely to be close to zero, but the other Poisson's ratio ν_2 relating the two transverse directions is not negligible. Recall that the elastic constant S_{11} is exactly the inverse of the Young's modulus E_x in the x-direction; then the differential equation for the longitudinal plane wave in a fibrous material is expressible in the form

$$\frac{\partial^2\xi_x}{\partial t^2}=\frac{E_x}{\rho}\frac{\partial^2\xi_x}{\partial x^2}. \tag{8.10}$$

Most interestingly, equation (8.10) reveals that, for fibrous materials which are transversely isotropic and have a zero Poisson's ratio associated with the main axis of symmetry, there is no distinction between longitudinal plane waves, in contrast to the situation encountered in isotropic materials. In other words, there is only one type of longitudinal plane wave in typical fibrous materials, regardless of their relative bulk dimensions with respect to wavelength, while isotropic materials have three different wave types: a pure longitudinal wave, a quasi-longitudinal wave, and a Love-type longitudinal wave. These findings will justify the use of equation (8.10) in measuring the dynamic properties of fibrous materials with finite lateral dimensions (see equation (6.9) in the derivation of a novel method). In Chapters 6 and 7, typical fibrous material samples for use in tests had dimensions of 5 *cm* (thickness) × 10 *cm* × 10 *cm*.

8.3 Lossy differential equation

So far, only perfectly elastic materials have been considered. Because internal friction in the structure would be present in practice, the wave equation for viscoelastic materials may need to be employed. The behaviour of such materials is also governed by the three basic equations which have been used in Section 8.2 for perfectly elastic materials. There may be two ways to approach this viscoelastic problem. The first, which is more rigorous, is apply a type of "causality condition" to the relationship between stress and strain, which states that there are no stresses and strains before the onset of motion. Thus the one-sided Laplace transform in the time domain may be applied to a stress-strain relation such as equation (8.7), given that stresses $\sigma(x,t)$, strains $\varepsilon(x,t)$ and all the elastic constants are time-dependent, while the other two basic equations for motion and displacement-strain remain unaltered [100]. The other method, which is somewhat heuristic though simple and efficient, is to modify the equation of motion directly, while maintaining the other two basic equations. Keeping in mind that the viscous force is associated with the time rate of strain change, one can assume that the viscous force $F_{v,x}$ in the x direction in longitudinal wave propagation may be expressed

$$F_{v,x} \propto -\frac{\partial^2 \xi_x}{\partial t \partial x}. \tag{8.11}$$

Thus the equation of motion (8.5a) becomes

$$\frac{\partial \sigma_x}{\partial x}+\frac{\partial \tau_{xy}}{\partial y}+\frac{\partial \tau_{zx}}{\partial z}+\frac{\partial}{\partial x}\left(\eta_x \frac{\partial^2 \xi_x}{\partial t \partial x}\right)=\rho \frac{\partial^2 \xi_x}{\partial t^2}. \tag{8.5a'}$$

Here, η denotes a structural coefficient of viscosity. Provided that the viscosity is constant, then the differential equation for a longitudinal plane wave for viscoelastic fibrous material may be expressed

$$\rho \frac{\partial^2 \xi_x}{\partial t^2} = E_x \frac{\partial^2 \xi_x}{\partial x^2} + \eta_x \frac{\partial^3 \xi_x}{\partial t \partial^2 x}. \tag{8.12a}$$

The above expression is identical to those previously adopted [28, 79]. In the case of a linear solution with harmonic motion, the "lossy" wave equation can be represented in the same form as the lossless wave equation by introducing the complex Young's modulus E_c,

$$\rho \frac{\partial^2 \xi_x}{\partial t^2} = (E_x + j\omega\eta_x)\frac{\partial^2 \xi_x}{\partial x^2} = E_c \frac{\partial^2 \xi_x}{\partial x^2}. \tag{8.12b}$$

This equation is the basis for the determination of the Young's modulus E and the loss modulus $\omega\eta_x$ by the experiments described in Chapters 6 and 7.

8.4 The governing nonlinear differential equation for fibrous materials

Fibrous materials are known to be more prone to nonlinearity than cellular porous materials [88]. When vibration levels in fibrous materials exceed a threshold value, nonlinear effects have been reported [15, 16, 85, 87] (also see Chapter 7). In such cases, a linear wave equation may be inappropriate to describe the structural motion of fibrous materials. In the development of the linear wave equation for the one-dimensional motion of fibrous materials, the amplitude has been assumed to be small enough to belong to the linear regime. Thus, among the three basic equations leading to the wave equation for structural motion, the equation of motion and the strain-displacement relationship were linearised on the basis of a first-order approximation. If the amplitude is finite, both approximations need to be amended to include higher order terms [51]. In addition, the nonlinear contribution is also required in the stress-strain relationship, in which the elastic constant (or stiffness matrix) would not be fixed, but would vary spatially in a bulk material. Among the three basic equations, the stress-strain relationship is considered to be the most important in terms of nonlinear effects, and it might be sufficient to consider only the dependence of elastic moduli on the space dimension in order to derive the nonlinear differential equation for longitudinal wave motion. This

argument can be justified by the way in which nonlinearity is usually treated in high-intensity acoustics. As mentioned earlier in this chapter, the acoustic wave equation is derived from three basic equations: the equations of continuity, motion, and state. They are all actually obtained by the use of first order approximations. When nonlinear effects are modelled in the acoustics of single-phase gaseous media, the equations of continuity and motion are not normally expanded to the higher order terms. Only the equation of state which links the acoustic pressure p to the density ρ (or condensation s) of air is expanded [37, 42] beyond the second order terms,

$$p = A\,s + \frac{B}{2!}s^2 + \frac{C}{3!}s^3 + \ldots, \tag{8.13a}$$

$$s = \frac{\rho - \rho_0}{\rho_0}. \tag{8.13b}$$

Here the subscript 0 denotes the equilibrium state. Usually, the second order approximation is adopted, and the coefficient of nonlinearity β^* is defined [37] as

$$\beta^* = 1 + \frac{B}{2A}. \tag{8.14}$$

Where nonlinear effects prevail, Hooke's law does not apply and the compliance matrix in is no longer constant. The linear wave equation (8.10) for one-dimensional longitudinal plane waves may be modified to include nonlinear effects [26, 27] by the use of equations (8.5), (8.6) and (8.7) (where the elements of the compliance matrix in equation (8.7) are dependent on the space coordinate):

$$\rho\frac{\partial^2\xi}{\partial t^2} = \frac{\partial}{\partial x}\left[E_b(x)\frac{\partial\xi}{\partial x}\right]. \tag{8.15}$$

Here, Young's modulus E_x is replaced by the bulk Young's modulus $E_b(x)$ to emphasise its dependence on x, and the subscript x is now omitted from ξ, since the motion is one-dimensional. Unlike the Young's modulus, the density is regarded as being invariant with the space coordinate. The bulk Young's modulus is effectively dependent

on the strain in the material. Especially in the case of fibrous materials, the nonlinear stress-strain relationship may be obtained according to the modified nonlinear bending model (MNBM, equation (4.27)) in Chapter 4. Although the MNBN has been derived for static compression, it has also been shown to be applicable in the case of tension (Chapter 5). It is also likely that it could be applied to a quasi-static dynamic situation (this will be discussed further, later in this chapter). The bulk Young's modulus, based on the MNBM, has been shown to be a function of strain ε (see equation (4.28)) and hence it is also a function of the longitudinal displacement ξ. Thus it is no longer constant, but variable depending on the displacement amplitude. Therefore the governing equation may be further expanded via the chain rule,

$$\frac{\partial^2 \xi}{\partial t^2} = \frac{1}{\rho}\frac{\partial}{\partial x}\{E_b(\varepsilon)\varepsilon\} = \frac{1}{\rho}\frac{d}{d\varepsilon}\{E_b(\varepsilon)\varepsilon\}\frac{\partial \varepsilon}{\partial x} = \frac{1}{\rho}\left\{\frac{dE_b}{d\varepsilon}\frac{\partial \xi}{\partial x} + E_b\right\}\frac{\partial^2 \xi}{\partial x^2}. \quad (8.16)$$

The combination of equation (4.28) and (8.16) leads to a nonlinear partial differential equation for one-dimensional longitudinal plane wave motion in a fibrous material. At this stage, the Taylor series expansion with respect to $\varepsilon = 0$ (i.e., the Maclaurin series) is adopted for the bulk Young's modulus,

$$E_b = A + B\varepsilon + C\varepsilon^2 + \cdots, \quad (8.17a)$$

$$\frac{dE_b}{d\varepsilon} = B + 2C\varepsilon + \cdots. \quad (8.17b)$$

Coefficients A, B and C, for a solid fraction Ψ_0 and parameter ζ from the MNBM are:

$$A \equiv 3\pi E\left(\frac{4}{\pi}\Psi_0\right)^5, \quad (8.18a)$$

$$B \equiv 10A, \quad (8.18b)$$

$$C \equiv 9A\left\{5 - 64\left(\frac{4}{\pi}\zeta\Psi_0\right)^2\right\}. \quad (8.18c)$$

In the first instance, the second order approximation may be adopted to produce the following nonlinear partial differential equation,

$$\frac{\partial^2 \xi}{\partial t^2} = \frac{1}{\rho}\left\{A + 2B\frac{\partial \xi}{\partial x} + 3C\left(\frac{\partial \xi}{\partial x}\right)^2 + \cdots\right\}\frac{\partial^2 \xi}{\partial x^2}. \tag{8.19}$$

However, provided the dynamic strain is very small, the following first order approximation may be sufficient:

$$\frac{\partial^2 \xi}{\partial t^2} = \frac{1}{\rho}\left\{A + 2B\frac{\partial \xi}{\partial x}\right\}\frac{\partial^2 \xi}{\partial x^2}. \tag{8.20a}$$

This may also be expressed as

$$\frac{\partial^2 \xi}{\partial t^2} = \frac{A}{\rho}\left\{1 - 20\frac{\partial \xi}{\partial x}\right\}\frac{\partial^2 \xi}{\partial x^2}. \tag{8.20b}$$

The error of the first order approximation of Taylor's series (8.17) is 0.3% for $\varepsilon = 0.01$, 1.2% for $\varepsilon = 0.02$ and 2.3% for $\varepsilon = 0.03$, in the case of an acoustic duct-lining absorber (properties specified in Tables 4.1 and 5.1). A strain of order of 10^{-2} is regarded as being very high in the dynamic situation, so the use of the first-order approximation is justified. In equation (8.20b), the negative sign in the nonlinearity term appears because of the sign convention for the MNBM, in which compressive strain is chosen to be positive. The sign convention therefore needs to be inverted in equation (8.20b), in which tension is regarded as positive. It is also worth noting that the value of -20 is fixed as long as the material is a fibrous medium with quasi-static motion.

It is also interesting to observe that equations (8.20) are independent of the parameter ζ, because only the coefficient C in the second order term is related to it. Recall that the parameter ζ was adopted to take into account the flexibility of fibre links (Section 4.4.3); this independence from ζ is then consistent with the SNBM, which applies only in the low strain region – as does equation (8.20) – and does not contain ζ.

Second order partial differential equations can be grouped into three categories, depending on the roots of its characteristic equation. When a partial differential equation is generalised in the form

$$a\frac{\partial^2\xi}{\partial t^2}+b\frac{\partial^2\xi}{\partial t\partial x}+c\frac{\partial^2\xi}{\partial x^2}+d\frac{\partial\xi}{\partial t}+e\frac{\partial\xi}{\partial x}+f\xi+g=0, \tag{8.21}$$

it is said to be hyperbolic, parabolic or elliptic, with the "discriminant" of the equation, b^2-4ac, respectively greater than, equal to, or less than, zero [105, 106, 107]. In a physical sense, a hyperbolic type of equation is required to guarantee a simple wave which is not discontinuous [106], such as a wave equation. In case of fibrous materials, the requirement would be

$$b^2-4ac=4\frac{A}{\rho_b}\left\{1-20\frac{\partial\xi}{\partial x}\right\}>0, \tag{8.22a}$$

$$\text{i.e.}\quad \left|\frac{\partial\xi}{\partial x}\right|<0.05\ . \tag{8.22b}$$

For displacements of practical interest, it may be expected that the equation will remain hyperbolic, because a strain higher than 0.05 is very unlikely to occur.

Based on these findings, the governing equation (8.20) has been derived to explain the nonlinear dynamic behaviour of fibrous materials. Throughout the development, the loss mechanism has not been included because of a lack of knowledge of the nonlinear dissipation mechanism. However, use of the lossless nonlinear governing equation for a structural wave may be justified, because the loss factor of typical fibrous material is known to be very small in a vacuum. A range of typical values has been reported to be 0.001 to 0.01 [84, 87].

Some doubt has, however, been raised here about the applicability of the MNBM to a dynamic problem, because it has been developed for static compression. The main difficulty originated in how to reconcile the local deflection of a fibre layer with that of the bulk fibrous material. In the MNBN, because of its static characteristics, the change

of strain or displacement was treated as being invariant across the specimen, which can be easily confirmed from wave equations such as (8.10) or (8.15), where the inertia term is set to zero for static equilibrium. Thus the deflection of each layer in the MNBN contributes equally to that in the bulk fibrous model. However, this is not the case in the dynamic situation, where the local strain and displacement experience peaks and troughs [30, 82]. Thus, it seems likely that the MNBM is not applicable to the dynamic situation in the first instance. Nonetheless, two positive points may be raised at this stage. First, the MNBN may still be valid in the low frequency region where the motion is quasi-static and where dynamic effects are not significant. Such a quasi-static approach is often adopted, for example, in the experimental determination of Young's modulus by means of the so-called stiffness method [35, 36, 92, 93]. Secondly, the concept of strain dependence in the Young's modulus may still be useful in describing nonlinear effects on the Young' modulus in a fibrous material. Thus the Taylor series expansion scheme according to in equation (8.17) might still be valid even at higher frequencies.

At high frequencies, where the MNBM is clearly not applicable, equation (8.20) may be generalised by the use of equation (8.16) in the form

$$\frac{\partial^2 \xi}{\partial t^2} = \frac{E_b}{\rho}\left(1+\beta\frac{\partial \xi}{\partial x}\right)\frac{\partial^2 \xi}{\partial x^2}. \tag{8.23}$$

Here, β represents the degree of nonlinearity, which can be interpreted as the coefficient of nonlinearity,

$$\beta \equiv \frac{1}{E_b}\frac{dE_b}{d\varepsilon}. \tag{8.24}$$

This is equivalent to the nonlinear parameter β^* in equation (8.14) as $\beta \equiv -2\beta^*$. It therefore represents the dimensionless rate of change of the bulk Young' modulus E_b with strain ε. It is obvious that there will be no nonlinearity if the Young's modulus is not affected by the strain.

Interestingly, an analogy can be found when the nonlinear governing differential equation for fibrous material is expressed in the form of equation (8.23). The propagation

of a pure longitudinal ultrasonic sound wave with finite amplitude in an isotropic solid is known [37, 39, 40] to be governed by

$$\rho\frac{\partial^2\xi}{\partial t^2}=K_2\left(1+\frac{3K_2+K_3}{K_2}\frac{\partial\xi}{\partial x}\right)\frac{\partial^2\xi}{\partial x^2}, \tag{8.25}$$

where K_2 and K_3 are conventional combinations of the second and third order elastic constants in orthotropic directions in crystal lattices. As in equation (8.23), ξ denotes particle displacement. The propagation of a finite amplitude longitudinal wave in a fluid is described [37] by

$$\frac{\partial^2\xi}{\partial t^2}=c_0^2\frac{\partial^2\xi}{\partial x^2}\left(1+\frac{\partial\xi}{\partial x}\right)^{-2-B/A}. \tag{8.26}$$

The symbol c_0 is the speed of sound for small amplitude waves. The constants A and B represent the degree of nonlinearity according to equations (8.13) and (8.14). The nonlinear partial differential equation governing finite amplitude sound propagation in an ideal gas is [37, 42, 108]

$$\frac{\partial^2\xi}{\partial t^2}=c_0^2\frac{\partial^2\xi}{\partial x^2}\left(1+\frac{\partial\xi}{\partial x}\right)^{-1-\gamma}. \tag{8.27}$$

Here, γ denotes the ratio of principal specific heats. When expanded in binomial series, both equations (8.26) and (8.27) can be expressed in the same form as equations (8.23) or (8.25). Therefore, according to these four nonlinear differential equations, it can be concluded that nonlinearity in longitudinal waves with finite amplitude (or high intensity) is related to the spatial derivative of displacement or strain.

8.5 Solution of nonlinear differential equations

The analytical solution of the lossless or inviscid type of equation (such as (8.25), (8.26) or (8.27)) is known for the case of a single travelling wave [37, 39, 40, 42, 108, 110, 111]. In these references, the application was to high-amplitude sound waves propagating

in air or a liquid and to the propagation of ultrasound in solid materials, but the application to *in vacuo* structural waves in fibrous materials (equation (8.23)) has not yet been reported. Because of the isomorphism in the governing differential equations, this solution should be applicable to fibrous materials. In the following sub-sections, two ways to approach this solution will be examined. One is perturbation analysis, and the other is known as the "Fubini solution" or the "Bessel-Fubini solution".

Because of the reduction in the number of parameters, it may be more convenient to carry out the mathematical manipulation if equation (8.23) is re-written in the form

$$\frac{\partial^2 \xi}{\partial t^2} = c^2 \frac{\partial^2 \xi}{\partial x^2} + \alpha \frac{\partial \xi}{\partial x} \frac{\partial^2 \xi}{\partial x^2}, \tag{8.28a}$$

where $\alpha = c^2 \beta$, and $c^2 = \frac{E_b}{\rho}$. (8.28b)

8.5.1 Perturbation analysis

Perturbation analysis [107, 113] is an analytical method for finding an approximate solution of a weakly nonlinear differential equation. Accordingly, the perturbed system is regarded as being slightly different from a known standard linear system. Such a difference is represented by the expansion of the nonlinear system in terms of a perturbation or nonlinear parameter, which is α in the case of the equation (8.28). Because its absence would make equation (8.28) linear, the parameter α can be treated as a measure of the extent to which equation (8.28) deviates from its linear counterpart. Thus a candidate for the solution may be expressed

$$\xi(x,t) = \xi_0(x,t) + \alpha \xi_1(x,t) + \alpha^2 \xi_2(x,t) + \cdots. \tag{8.29}$$

It is usually assumed that either the parameter α is small, or either the effect of nonlinear terms such as $\alpha \xi_1(x,t)$ is small or smaller than that of the linear term such as $\xi_0(x,t)$. For a fibrous material, the effect will be addressed later in this section. In the case of

wave propagation in germanium [40], the value of α was -6.5×10^{7} in *mks* units. However, the displacement was usually of the order of 1Å = 10^{-10} *m*.

Each term in equation (8.29) can be evaluated by satisfying the initial conditions or the boundary conditions. Upon inserting equation (8.29) into (8.28a) and collecting together terms in powers of α, one finds

$$\frac{\partial^2\xi_0}{\partial t^2}+\alpha\frac{\partial^2\xi_0}{\partial t^2}+\alpha^2\frac{\partial^2\xi_0}{\partial t^2} \tag{8.30}$$

$$=c^2\frac{\partial^2\xi_0}{\partial x^2}+\alpha\left(c^2\frac{\partial^2\xi_1}{\partial x^2}+\frac{\partial\xi_0}{\partial x}\frac{\partial^2\xi_0}{\partial x^2}\right)+\alpha^2\left(c^2\frac{\partial^2\xi_2}{\partial x^2}+\frac{\partial\xi_0}{\partial x}\frac{\partial^2\xi_1}{\partial x^2}+\frac{\partial\xi_1}{\partial x}\frac{\partial^2\xi_0}{\partial x^2}\right)+\cdots.$$

The coefficient of each power of the nonlinear parameter α should be matched in order that equation (8.30) should be satisfied identically in terms of α. This process produces the following system of equations:

$$\frac{\partial^2\xi_0}{\partial t^2}=c^2\frac{\partial^2\xi_0}{\partial x^2}, \tag{8.31a}$$

$$\frac{\partial^2\xi_1}{\partial t^2}=c^2\frac{\partial^2\xi_1}{\partial x^2}+\frac{\partial\xi_0}{\partial x}\frac{\partial^2\xi_0}{\partial x^2}, \tag{8.31b}$$

$$\frac{\partial^2\xi_2}{\partial t^2}=c^2\frac{\partial^2\xi_2}{\partial x^2}+\frac{\partial\xi_0}{\partial x}\frac{\partial^2\xi_1}{\partial x^2}+\frac{\partial\xi_1}{\partial x}\frac{\partial^2\xi_0}{\partial x^2}. \tag{8.31c}$$

The first equation is homogeneous and the other two are inhomogeneous. The three equations constitute a linear system, because the inhomogeneous lower-order terms are determined at previous stages. Suppose the following sinusoidal boundary condition is considered at the driving point:

$$\xi(0,t)=\hat{\xi}\sin(-\omega t). \tag{8.32}$$

Here, the forcing frequency is denoted by ω and the corresponding wave number will be $k=\omega/c$. The symbol ^ represents the magnitude of the quantity. The solution of

equation (8.31a) can now be straightforwardly obtained by using the substitution $\theta \equiv kx - \omega t$,

$$\xi_0 = \hat{\xi} \sin\theta . \tag{8.33}$$

Upon inserting (8.33) into (8.31b), one obtains the inhomogeneous partial differential equation

$$\frac{\partial^2 \xi_1}{\partial t^2} = c^2 \frac{\partial^2 \xi_1}{\partial x^2} - \frac{\hat{\xi}^2 k^3}{2} \sin 2\theta . \tag{8.34}$$

The particular solution of equation (8.34) can be found by using a trial solution

$$\xi_1 = B x \sin 2\theta + D x \cos 2\theta , \tag{8.35}$$

where B and D are arbitrary coefficients. Then the particular solution can be obtained,

$$\xi_1 = -\frac{\hat{\xi}^2 k^2}{8c^2} x \cos 2\theta . \tag{8.36}$$

By the use of the above results, equation (8.31c) now assumes the form

$$\frac{\partial^2 \xi_2}{\partial t^2} = c^2 \frac{\partial^2 \xi_2}{\partial x^2} + \frac{\hat{\xi}^3 k^4}{16c^2} [3 \sin\theta + 5 \sin 3\theta + 2k x \cos\theta + 6k x \cos 3\theta]. \tag{8.37}$$

The following trial solution may be employed in order to obtain a particular solution of (8.37):

$$\xi_2 = p x \sin\theta + q x \cos\theta + r x \sin 3\theta + s x \cos 3\theta \quad \cdots$$

$$+ d x^2 \sin\theta + l x^2 \cos\theta + m x^2 \sin 3\theta + n x^2 \cos 3\theta , \tag{8.38}$$

where p, q, r, s, d, l, m and n are arbitrary constants. After some manipulation, one finds a solution

$$\xi_2 = \frac{\hat{\xi}^3 k^3}{16c^4} \left(x \cos\theta + \frac{2}{3} x \cos 3\theta \right) - \frac{\hat{\xi}^3 k^4}{32c^4} \left(x^2 \sin\theta + x^2 \sin 3\theta \right). \tag{8.39}$$

Finally, the perturbation solution of equation (8.28a) can be determined in the following form up to second order in α, by inserting (8.33), (8.36) and (8.38) into (8.29):

$$\xi = \hat{\xi}\sin(kx-\omega t) - \alpha\frac{\hat{\xi}^2k^2}{8c^2}x\cos 2(kx-\omega t)$$

$$-\alpha^2\frac{\hat{\xi}^3k^4}{32c^4}x^2\{\sin(kx-\omega t)+\sin 3(kx-\omega t)\} \qquad (8.40)$$

$$+\ \alpha^2\frac{\hat{\xi}^3k^3}{16c^4}x\left\{\cos(kx-\omega t)+\frac{2}{3}\cos 3(kx-\omega t)\right\}\cdots$$

This solution clearly shows the generation of harmonics as the wave travels, and also demonstrates that the intensity of the lower harmonics is reduced by "leakage" into higher harmonics. If the first order approximation is adopted, then the amplitude of the second harmonic appears to be proportional to the square of that of the fundamental component. These two terms are often employed to determine the nonlinearity parameter of a system [37]. The amplitude of the fundamental displacement component $A_1 = \hat{\xi}$ and that of the second harmonic A_2 need to be measured. (Here the difference between ξ_i and A_j is that ξ_i appears in the perturbation expansion, whereas A_j denotes the amplitude of the jth harmonic. The magnitude of ξ_i can therefore have a combination of several A_j terms.) Then the nonlinearity parameter α can be determined from

$$A_2 = -\alpha\frac{A_1^2k^2x}{8c^2} = -\alpha\frac{A_1^2\omega^2x}{8c^4}. \qquad (8.41)$$

The nonlinearity parameter α has a negative value in equation (8.28a). Although α is in itself not small, it appears to be compensated for by a weak excitation in the form of a power of the small amplitude A_1. For example, the result of Section 8.6 can be used: for a 30 *Hz* sinusoidal excitation with an amplitude of -40 *dB* re 1 *mm* on a 5 *cm* thick fibrous material (which means $\alpha = -20c^2$ from equations (8.20b) and (8.28b)), the product of the second harmonic A_2 and the nonlinear parameter α (or the magnitude of $\alpha\xi_1(x,t)$ in equation (8.29)) will be 8.8×10^{-6} *m*. This is 12% less than the fundamental

amplitude A_1 and hence one can expect that the magnitude of the next higher order term, $\alpha^2 \xi_2(x,t)$, in equation (8.29) should be much less than that. Thus, the perturbation analysis seems to be applicable where the effect of the nonlinear terms are small, provided that x, the distance travelled from the source, and the driving frequency ω are not too great.

8.5.2 Fubini solution

The exact solution for the particle velocity V in an inviscid fluid governed by equation (8.27) is known in terms of a Bessel function, and is termed the (Bessel-) Fubini solution [40, 42]. This solution is based on the condition of weak nonlinearity,

$$V_0 << \frac{2c_0}{\gamma+1}, \tag{8.42a}$$

corresponding to

$$V_0 << \frac{2c}{\beta} \tag{8.42b}$$

in equations (8.23) and (8.28a), and this is easily satisfied for the case of structural wave nonlinearity in fibrous materials. Here, V_0 is the amplitude of the particle velocity. In equations (8.42a,b), γ is the ratio of principal specific heats, and c_0, c are the wave speeds in the *linear* regime in the case of the fluid and structure respectively. For a sinusoidal particle velocity signal

$$V(0,t) = V_0 \sin(\omega t) \tag{8.43}$$

at the driving point, Fubini [40, 42] gave the following velocity-based form of an exact solution which satisfies the governing equation of particle displacement (8.27):

$$V = 2V_0 \sum_{n=1}^{\infty} \frac{J_n(n x/x^*)}{n x/x^*} \sin\{n(\omega t - kx)\}. \tag{8.44}$$

Here, $J_n(\,)$ is a Bessel function of the first kind of order n, x^* represents a "discontinuity distance", at which a discontinuity in the first derivatives of the displacement (i.e., the velocity) is assumed to occur as the wave propagates in a nonlinear system, given by [42]

$$x^* = \frac{2c_0^2}{(\gamma+1)\omega V_0}. \tag{8.45a}$$

Although the solution (8.44) was derived for the case of an inviscid fluid, its equivalent should be equally applicable to the case of fibrous media [40]. Thus, fibrous materials (see equations (8.23) and (8.28)) have a discontinuity distance

$$x^* = \frac{2c^2}{-\beta\omega V_0} = -\frac{2c^2}{\beta\omega^2 \hat{\xi}}. \tag{8.45b}$$

Because the solution (8.44) is expressed in terms of particle velocity, integration is required to obtain a solution in terms of particle displacement. Term-by-term integration yields

$$\xi = -2\hat{\xi}\sum_{n=1}^{\infty} \frac{J_n(nx/x^*)}{n^2 x/x^*}\cos\{n(\omega t - kx)\}, \tag{8.46}$$

where the displacement amplitude $\hat{\xi}$ and the velocity amplitude V_0 are related by $V_0 = \omega\hat{\xi}$, as indicated in (8.45b).

A comparison between the two solutions from the perturbation analysis (8.40) and the Fubini method (8.46) requires a power series expansion of the Bessel function in (8.46),

$$J_n(y) = \sum_{p=0}^{\infty} \frac{(-1)^p \left(\frac{y}{2}\right)^{n+2p}}{p!\,\Gamma(n+p+1)}. \tag{8.47}$$

The solution will be the sum of the fundamental and its harmonics,

$$V = V_1 + V_2 + V_3 + \cdots, \tag{8.48a}$$

expressed by the following series:

$$V_1 = V_0 \sin(\omega t - kx)\left[1 - \frac{1}{8}\left(\frac{x}{x^*}\right)^2 + \frac{1}{192}\left(\frac{x}{x^*}\right)^4 - \cdots\right], \tag{8.48b}$$

$$V_2 = V_0 \sin\{2(\omega t - kx)\}\left[\frac{1}{2}\left(\frac{x}{x^*}\right) - \frac{1}{6}\left(\frac{x}{x^*}\right)^3 + \frac{1}{48}\left(\frac{x}{x^*}\right)^5 - \cdots\right], \tag{8.48c}$$

$$V_3 = V_0 \sin\{3(\omega t - kx)\}\left[\frac{3}{8}\left(\frac{x}{x^*}\right)^2 - \frac{27}{128}\left(\frac{x}{x^*}\right)^4 + \frac{243}{5120}\left(\frac{x}{x^*}\right)^6 - \cdots\right]. \tag{8.48d}$$

To rectify the difference between the displacement and velocity boundary conditions, a phase shift is required. Thus the argument $\omega t - kx$ in (8.48) needs to be replaced by $3\pi/2 - (\omega t - kx)$. The solution represented by (8.47) and (8.48) may be re-written

$$\begin{aligned}\xi = {} & \hat{\xi}\sin(kx - \omega t) - \alpha\frac{\hat{\xi}^2 k^2}{8c^2}x\cos 2(kx - \omega t) \\ & - \alpha^2\frac{\hat{\xi}^3 k^4}{32c^4}x^2\{\sin(kx - \omega t) + \sin 3(kx - \omega t)\} \\ & + \alpha^3\frac{\hat{\xi}^4 k^6}{96c^6}x^3\cos 2(kx - \omega t) + \alpha^4\frac{9\hat{\xi}^5 k^8}{2048\,c^8}x^4\sin 3(kx - \omega t)\cdots\end{aligned} \tag{8.49}$$

if the first two terms of each harmonics are retained. Upon comparison between (8.40) and (8.49), one can easily see that the first four terms of each solution are identical to one another. The differences in the higher order terms may be explained by the fact that the perturbation solution has been based on a binomially-expanded version (8.23, 8.25) of the governing equation (8.26, 8.27) in the Fubini solution.

8.6 Experimental investigation

Experimental results concerning the generation of harmonics in nonlinear structural waves propagating in a fibrous material (E-glass) will be described in this section. According to the solution of equations (8.40) and (8.49) the amplitude of the second harmonic, A_2, is proportional to the square of that of the fundamental component, A_1, especially for a weakly nonlinear travelling wave.

Figures 8.2 and 8.3 show the displacement amplitudes measured on the top and bottom plates respectively when a layer of E-glass fibrous material (placed between the two plates in a vacuum) was excited by a shaker fed with a sinusoidal signal at 30 *Hz*, which is close to the mass-spring resonance frequency of the material and top plate together. The selection of a frequency near resonance was made on the basis that the displacement of the top plate will be relatively high, thereby giving the best likelihood of observation of nonlinear effects. Figure 8.4 shows the displacement of the shaker alone, in order to illustrate the nonlinearity of the shaker itself. The dotted lines in Figures 8.2 to 8.4 have a slope of two, corresponding to the relationship $A_2 \propto A_1^2$.

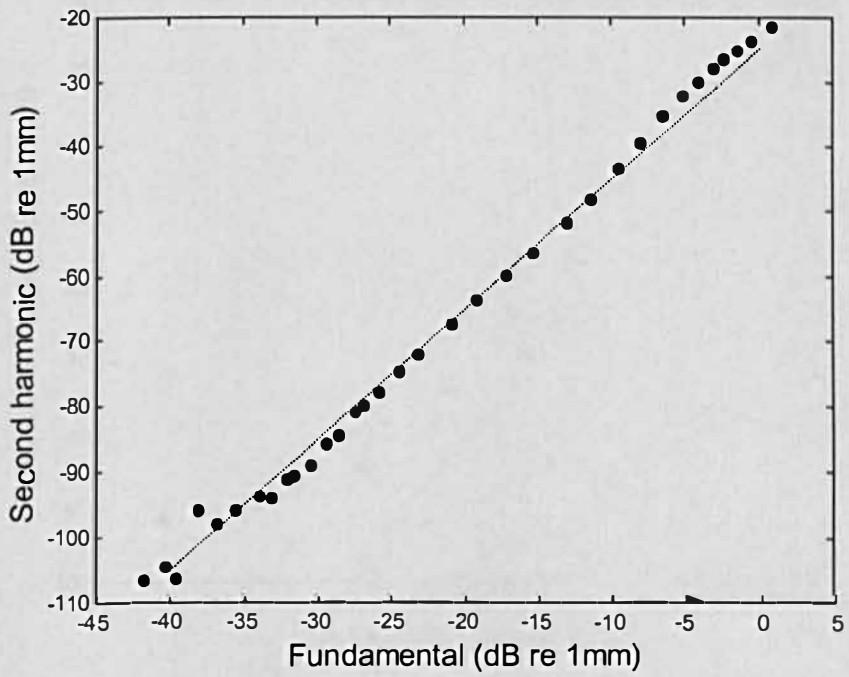

Figure 8.2 Nonlinear behaviour of bulk E-glass fibrous material under longitudinal excitation at 30 *Hz*. The relationship between the displacement amplitudes of the second harmonic and the fundamental component on the *top plate* is plotted. The dotted line is the fitted line with a slope of two.

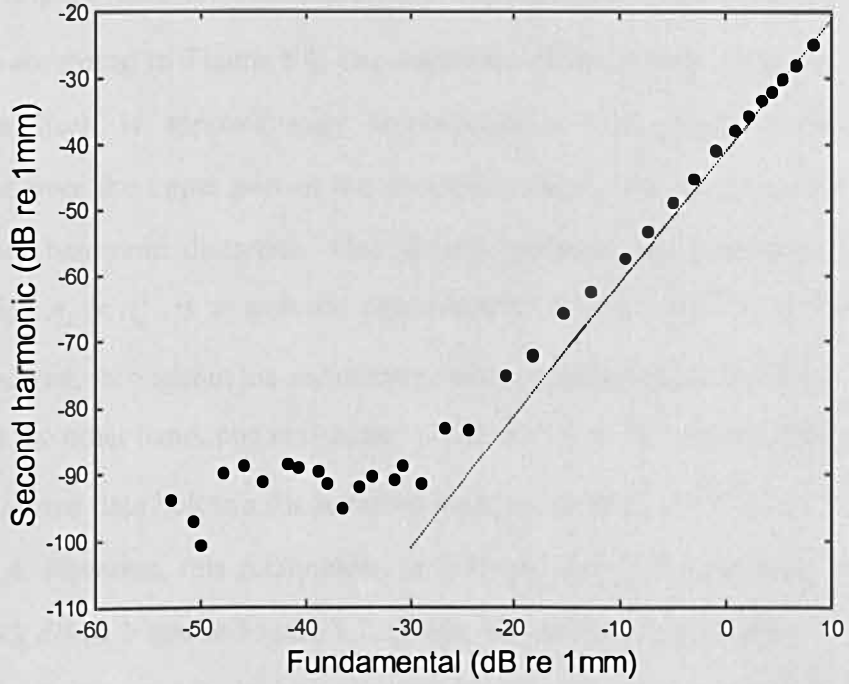

Figure 8.3 Nonlinear behaviour of bulk E-glass fibrous material under longitudinal excitation at 30 *Hz*. The relationship between the displacement amplitudes of the second harmonic and the fundamental component on the *bottom plate* is plotted. The dotted line has a slope of two.

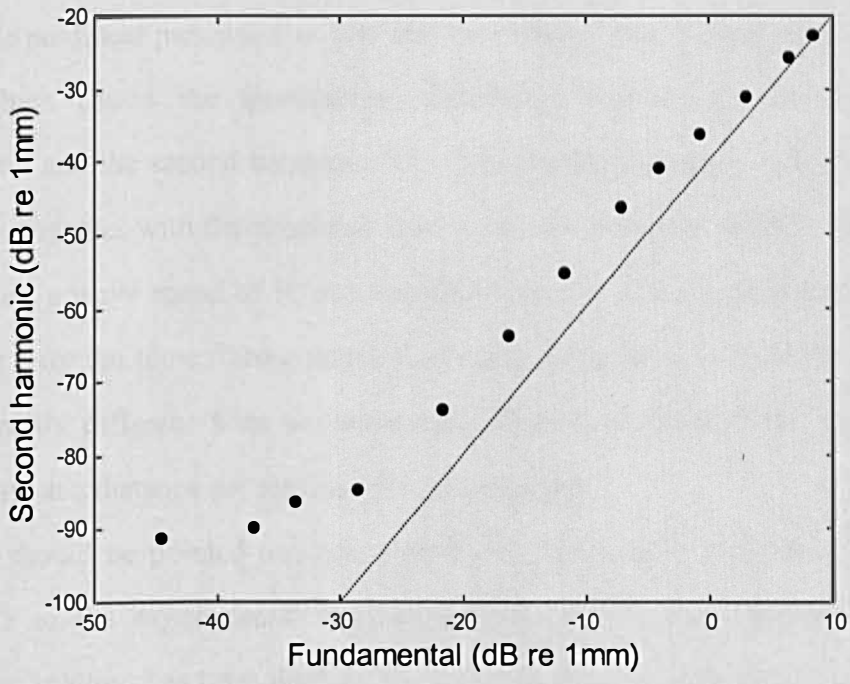

Figure 8.4 Harmonic distortion in the shaker at 30 *Hz*, with no specimen in place. The dotted line has a slope of two.

In Figure 8.2, the measured data closely follow the relationship $A_2 \propto A_1^2$. However, according to Figure 8.4, the amplitude of the second harmonic generated by the shaker itself is approximately proportional to the square of the fundamental component over the upper part of the excitation range. The forcing function evidently also suffers harmonic distortion. One should, perhaps, not therefore assert that the relationship $A_2 \propto A_1^2$ is a genuine characteristic of the nonlinear behaviour of this fibrous material, throughout the *entire* range of excitation level in the tests.

On the other hand, one may observe that the $A_2 \propto A_1^2$ relationship is not followed by the measured data below a fundamental component level of -20 *dB* re 1 *mm* in Figure 8.3 and 8.4. However, this relationship is followed down to a fundamental component level of -43 *dB* re 1 *mm* in Figure 8.2. (Note, however, that the level of -25 *dB* for the fundamental in Figure 8.2 corresponds approximately to a level of -20 *dB* in Figures 8.3 and 8.4.) Therefore, in the region of weak nonlinearity, the relation $A_2 \propto A_1^2$ can be observed experimentally, and is predicted theoretically (see equations (8.40) and (8.49)). These observations are consistent with those of other workers for a porous material made from a polymer [48, 112].

The nonlinear parameter α was also measured. It can be evaluated from equation (8.41), which shows the quantitative relationship between the amplitudes of the fundamental and the second harmonic. The dynamically measured values are plotted in Figure 8.5, together with the predicted value based on the static MNBM. In determining these values, a wave speed of 10 *m/s* was assumed; this was determined experimentally in Chapter 6 for the same fibrous material. As seen in Figure 8.5, the MNBM predictions are not greatly different from the measured values over most of the region of weak nonlinearity, at a distance not far from the driving point.

It should be pointed out here that the above theoretical solution might not be appropriate to the experimental equipment which has been employed here. This is because the solution has been derived under the assumption of a single travelling wave, whereas waves travelling in both directions were present in the experimental arrangement. Nevertheless, it is believed that the theoretical solution and results obtained

here are at least indicative of the relative amplitudes between the fundamental component and its harmonics, together with the corresponding nonlinear parameter.

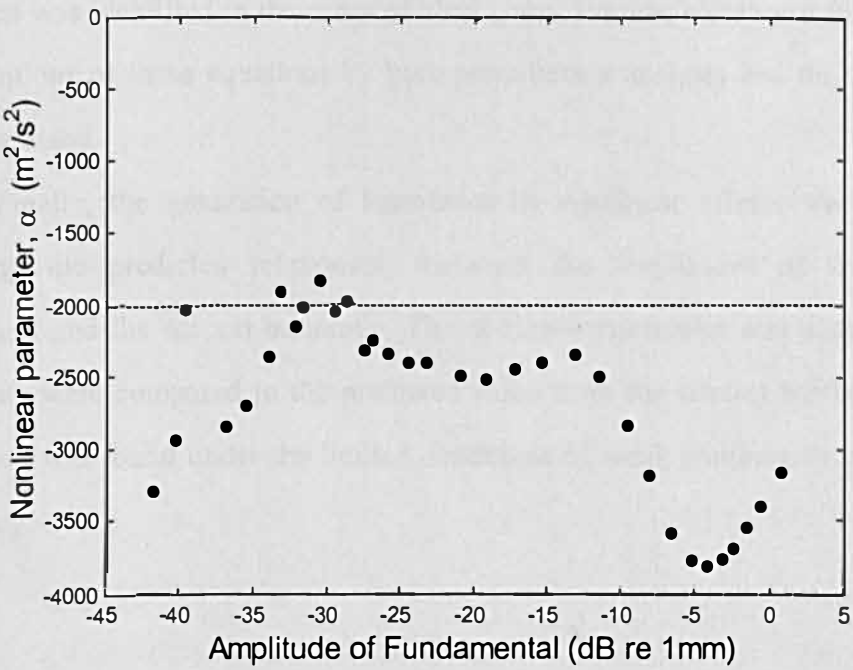

Figure 8.5 The measured nonlinear parameter α of bulk E-glass fibrous material with longitudinal sinusoidal excitation at 30 *Hz*. The dashed line is the predicted value from the static Modified Nonlinear Bending Model.

8.7 Summary

The nonlinear nature of the *in vacuo* structural wave in fibrous materials has been investigated in this section. Structural wave equations for different types of waves were first discussed in the case of isotropic media. The linear partial differential equation governing one-dimensional plane longitudinal waves was then derived for a fibrous material with a transversely isotropic structure. By means of the strain dependence of the bulk Young's modulus from the Modified Nonlinear Bending Model (MNBM), the linear governing differential equation for fibrous materials was extended to its nonlinear counterpart. Despite the static nature of the MNBM, it appears that it could be applicable to a quasi-static dynamic situation. Moreover, the same form of the nonlinear equation

can be applied at higher frequencies, as long as the strain dependence of the bulk Young's modulus is specified.

For dynamic excitation with finite amplitude, an analogy between the governing equations was identified in the cases of ideal gases, liquids, solids and fibrous materials. The solutions of these equations by both perturbation analysis and the Fubini solution were discussed.

Finally, the generation of harmonics by nonlinear effects was confirmed by observing the predicted relationship between the amplitudes of the fundamental component and the second harmonic. The nonlinear parameter was also measured and these data were compared to the predicted value from the (static) MNBM. Reasonable agreement was found under the limited conditions of weak nonlinearity and quasi-static frequency.

Chapter 9

Conclusions

This thesis is concerned with the static and dynamic structural properties of bulk fibrous materials. The first half of the thesis (Chapters 2 ~ 5) is devoted to the static elastic behaviour of fibrous media and the remainder (Chapters 6 ~ 8) is focused on their dynamic properties. Several themes have run through each chapter and some of these have revealed new aspects of fibrous materials, as follows.

1. The nonlinear mechanism in the structural behaviour of fibrous materials has been successfully identified: it is the change in the number of inter-fibre contacts with bulk strain. This number may be supposed to increase monotonically when the material is subjected to static compression, but to oscillate in the dynamic case. The idealised experimental models which have been fabricated support this idea in the cases of both static loading (where stacks of silver steel rods were used, See Chapter 2) and dynamic loading (where stacks of glass capillary tubes or welding rods were built, See Section 7.2.4).

2. Two predictive static bending models have been developed to describe the nonlinear bulk elastic properties of fibrous media under compression. Both have the configuration of an ideal transversely isotropic structure consisting of elastic cylindrical rods (See Figure 4.6). These static models have been based on the findings about the nonlinear mechanism involving inter-fibre contacts. Of the two models, the modified nonlinear bending model (MNBM, Section 4.4.3) has been shown to describe well a high degree of nonlinearity, ranging from low strain to high strain, by means of a single equation, while the application of the simple nonlinear bending model (SNBM, Section 4.4.2) is confined to low strain. Both models are presented

not only by the stress-strain relation (equation (4.20) and (4.27)) but also by the bulk Young's modulus-strain relation (equation (4.21) and equation (4.28)).

3. The change in the number of inter-fibre contacts has been further investigated. Percolation theory has been introduced in this study, and this has led to questions regarding the relationship between percolation theory and the behaviour of fibrous material under static compression. In doing so, the bulk Young's modulus-strain relations of static models have been converted to the bulk Young's modulus-solid fraction relations (equation (5.6) and equation (5.9)). Similarities and differences were discussed, and it has been determined that the particular aspects examined in this thesis are not directly related to percolation theory. However, it is believed that a fibrous material is potentially a percolating system, and a method of approach which would resolve this question has been suggested.

4. A novel method has been developed, to measure the dynamic bulk Young's modulus of a fibrous material under longitudinal excitation. It combines the features of conventional methods such as the transfer function method and the mechanical impedance method. Although it is very robust, the transfer function method requires an assumption about a bulk density and yields a transcendental equation (equation (6.2)) for a complex wave number. The mechanical impedance method appears, at first sight, to overcome the difficulties occasioned by the transfer function method. However, its execution involved difficulties in practice, because of the need for the use of two samples of different lengths. In contrast, the novel method does not demand the assumed density or the use of two samples, but produces a straightforward analytical solution (equation (6.19)) for a complex wave number.

5. A nonlinear partial differential governing equation (equation 8.23) has been developed to describe the dynamic structural behaviour of fibrous materials under longitudinal excitation. Unlike other types of poroelastic or non-porous materials, it

has been shown that there is only one type of a longitudinal wave for fibrous materials (equation (8.10)). Its derivation has been tailored especially for fibrous media, although it is analogous to that for finite-amplitude wave propagation in other types of media such as ideal gases, fluids and solids. The occurrence of a second harmonic component of a sine wave has been identified experimentally (Figure 8.2). The *static* modified nonlinear bending model (MNBM) has been shown to be capable of estimating the nonlinear parameter so long as both the excitation frequency and the propagation distance are small (See Figure 8.5).

6. An idealised experimental dynamic model (Figure 7.16) has been constructed initially to investigate the nonlinear mechanism in the dynamic case. In addition, it has yielded the interesting feature that there is no significant discrepancy between its bulk static and dynamic bulk moduli (Figure 7.20), unlike a real fibrous material. The low loss factor and simple structure of the model are believed to be responsible for this phenomenon.

In the course of this research, certain topics have not been investigated in as much detail as had been originally planned. Three of these are as follows.

1. A macro-scale experimental and predictive model investigation, based on idealised representations of the microscopic geometry of a bulk fibrous material, has been shown to be a useful tool for investigation of the principal mechanisms responsible for the bulk structural behaviour. However, a more ambitious goal involving the assembly of many such models as "modules" in an idealised bulk material has led to practical problems involving the sheer size and complication of the mechanical structure which could, for example, lead to a series of statically indeterminate systems. This was also highlighted during the finite-element analysis (Section 2.3). Although the FE approach is being used in the analysis of a cellular porous material

such as a replica bone, its implementation to an idealised fibrous material is not an easy task, not alone a real bulk fibrous material. The difference could be easily explained, in terms of "connectivity" that, in a cellular material, its morphology does not change much, even though its frames experience buckling. However, in a fibrous material, there is no way to predict where fresh contacts are formed. Even though one has a means to know the contact locations, after every single new contact, one needs to make sure that contact forces could pass through them, which requires the merge of contact nodes in a FE analysis. Apart from the investigation on mechanical aspects, the electrical contact resistance on idealised models together with bulk electrical conductivity on a steel wool was investigated as a means of measuring the inter-fibre contact density. However, various practical difficulties have been highlighted, related to the extremely complex nature of the electrical circuit.

2. Dissipation mechanisms in the structural motion of fibrous materials have not been treated theoretically in this thesis. In the case of static compression, possibly because of the laminar configuration of the idealised structure, theoretical models without a loss mechanism satisfactorily describe the nonlinear stress-strain relationship. In a test for the dynamic elastic properties of fibrous materials, the loss component was also measured; but this was no more than an empirical approach. However, in the development of the nonlinear governing partial differential equation, only the inviscid form of the nonlinear equation was derived and solved to describe the dynamic behaviour of a fibrous material.

3. Although a novel method was devised as an alternative way of measuring the dynamic bulk Young's modulus of a fibrous material under longitudinal excitation, there appears to be a limitation in its applicability, especially regarding the frequency range. However the reasons for this are not completely understood, apart from their seeming to be related to the measurement of the dynamic mass.

Items 2 (dissipation mechanism) and 3 (improvement of the new method) are obvious topics for future research. Other ideas for future work are:

1. The static models (SNBM and MNBM) are only concerned about the normal compression. However it should be possible to extend this work to provide a static model of the "shear" behaviour of a fibrous material. First, it would be necessary to investigate the shear mechanisms, about less is known than the normal compression behaviour. It could involve inter-fibre friction, and the contribution of binder materials could be a lot more significant than it is for the normal compression.

2. The investigation of a fibrous material as a percolating system will be no doubt an interesting task. To do so, fibrous materials need to be prepared with different pre-fixed solid fractions. Their elastic properties such as bulk Young's modulus could be key issues, but their electric properties such as conductivity could also be worth investigating especially for a steel wool. Their percolation behaviour could be a useful design guide, for example, to optimise the amount of fibres required, especially for fibre-reinforced structures, which require interstitial materials. This percolation approach could be applied not only to fibrous materials, but also to other types of porous materials such as unconsolidated granular materials with different interstitial elements.

3. According to equations (4.17), (4.21) and (4.28), the bulk Young's modulus E_b without compression (i.e. $\varepsilon = 0$) is dependent on the "fifth power" of the initial solid fraction Ψ_0 as follows,

$$E_b = 3\pi E\left(\frac{4}{\pi}\Psi_0\right)^5. \tag{9.1}$$

Therefore, an experimental investigation of the power-law dependence would be an exciting topic in the future. Practically, high-precision equipment [22], rather

than a set of travelling microscope and weights, might be necessary to measure the deflection and force for this purpose, because fibrous materials are supposed to behave nonlinearly no matter how small the loading force. Once it is confirmed, such knowledge would be very useful in the design stage of fibrous materials, because it would tell manufacturers how to control the solid fraction of fibrous materials to achieve the specific bulk Young's modulus required by a commercial market. More interestingly, this work could be done in line with the measurements to investigate the percolating behaviour of fibrous materials, because both require the same types of sample materials, which would be constructed with different initial solid fractions. The difference might be the fact that a non-air interstitial substance is not required for the purpose of confirming the power law dependence.

4. In the dynamic measurements, an electro-dynamic shaker was used as a means of exciting sample materials, involving direct contact between the shaker and the sample. However, care needs to be taken because improper contact could affect the longitudinal excitation and lead to measurement error. On the other hand, non-contact probes have been used to avoid the extra loading effect of accelerometers. So, one possible way to get around the source-sample contact situation may be to use a non-contact source. It could be implemented by means of a high-amplitude shock wave, which can be generated by focusing a high-powered laser beam [114]. An unpublished trial by the author has found that laser-generated acoustic shocks contain sufficient energy to move particles. Thus, this new source of excitation could be a means of improving the measurement quality in future.

5. Another topic that would exploit laser-generated shock waves would be to use it as a one-way wave. Because they are pulses, it should be possible to arrange for forward and backward travelling waves to be separated. Therefore, the high-

amplitude shock pulses would be an effective means to obtain data for finite-amplitude response to compare with the solution (equation (8.40) and (8.49)) based on a one-way wave.

6. The thesis has addressed only the structural motion. Therefore its expansion to a structural-fluid coupling model, such as Biot theory [10, 11], would be another attractive future work. The nonlinear equation (8.23) in Ch8 was derived especially for a fibrous material with a transversely-isotropic structure. However, the process in Ch8 was simplified only to the longitudinal direction. Therefore, it would be interesting to derive the nonlinear equations for all directions of "transversely-isotropic" or even "anisotropic" structure, as well as their solutions. It could be a step-forward from "nonlinear" version of Biot theory, which only concerns "isotropic" structure despite its superb physical insight. For this task, the knowledge from the item 1 (shear behaviour) of future works would be useful in investigating other directions than the longitudinal direction, even though it would concern the static behaviour in the first instance.

Finally, it may be remarked that the findings in this thesis are believed to contribute to the enhancement of our *fundamental* understanding of the structural behaviour of bulk fibrous materials. For example, the static models may be employed to describe the nonlinear behaviour of fibrous material in static applications. The proposed test method for the dynamic Young's modulus could improve the efficiency of measurement techniques. Finally, application of the governing nonlinear differential equation derived in Chapter 8 should cast light on methods of approach to the structural behaviour of fibrous materials subjected to high amplitude excitation.

References

1. ALLARD, J.F. 1993. Sound propagation in porous materials having a rigid frame. In: *Propagation of Sound in Porous Media: Modelling Sound Absorbing Materials.* London: Elsevier Science Publishers LTD. Chapter 5.

2. ALLARD, J.F. 1993. Biot theory of sound propagation in porous materials having an elastic frame. In: *Propagation of Sound in Porous Media: Modelling Sound Absorbing Materials.* London: Elsevier Science Publishers LTD. Chapter 6.

3. LAI, H., KATRAGADDA, BOLTON, J.S. and ALEXANDER, J. H. 1997. Layered fibrous treatments for a sound absorption and sound transmission. Proceedings of the 1997 Noise and Vibration Conference, Society of Automotive Engineers, pp.1553-1560.

4. STRUTT, J.W. (3rd Baron of Rayleigh) 1926. *The Theory of Sound.* 2nd ed. London: Macmillan

5. ZWIKKER, C. and KOSTEN, C.W. 1949. *Sound Absorbing Materials.* London: Elsevier Publishing Company, Inc.

6. JOHNSHON, D.L, KOPLIK, J. and DASHEN, R. 1987. Theory of dynamic permeability and tortuosity on fluid-saturated porous media. *Journal of Fluid Mechanics,* **176**. pp.379-402.

7. ATTENBOROUGH, K. 1987. On the acoustic slow wave in air-filled granular media. *Journal of the Acoustical Society of America*, **81**. pp.93-102.

8. CHAMPOUX, Y. and ALLARD, J.-F. 1991. Dynamic tortuosity and bulk modulus in air-saturated porous media. *Journal of the Acoustical Society of America*, **70**(4). pp.1975-1979.

9. DELANY, M.E and BAZLEY, E.N. 1970. Acoustical properties of fibrous absorbent materials. *Applied Acoustics*, **3**. pp.105-116.

10. BIOT, M. A. 1956. Theory of propagation of elastic waves in a fluid-saturated porous solid. I. Low-frequency range. *Journal of the Acoustical Society of America*, **28**(2). pp.168-178.

11. BIOT, M. A. 1956. Theory of propagation of elastic waves in a fluid-saturated porous solid. II. Higher frequency range. *Journal of the Acoustical Society of America*, **28**(2). pp.179-191.

12. KAWASIMA, Y. 1960. Sound propagation in a fibre block as a composite medium. *Acustica*, **10**. pp.208-217.

13. DAHL, M.D., RICE, E.J. and GROESBECK, D.E. 1990. Effects of fiber motion on the acoustic behavior of an anisotropic, flexible fibrous material. *Journal of the Acoustical Society of America*, **87**(1). pp.54-66

14. LAMBERT, R.F. 1993. Acoustic resonance in highly porous, flexible, layered fine fiber materials. *Journal of the Acoustical Society of America*, **93**(3). pp.1227-1234.

15. WATSON, A.P. and CUMMINGS, A. 1994. Equivalent fluid behaviour and further mechanical properties of the thermal insulation materials. *Brite/Aero Contract no. CT92 0032*, deliverable no. 8.

16. WILSON, R., CUMMINGS, A. and RICE, H. 1994. Investigation of thermal insulation non-linearity. *Brite/Aero Contract no. CT92 0032*, deliverable no. 14.

17. CUNNINGHAM, A. and HILYARD, N. C. 1994. Physical behaviour of polymeric foams – an overview. In: Hilyard, N.C. and Cunningham, A., ed. *Low density cellular plastics: physical basis of behaviour.* London; Chapman & Hall. Chapter 1.

18. GIBSON, L. J. and ASHBY, M. F. 1997. *Cellular solids: structure and properties.* 2nd ed. Cambridge: Cambridge University Press.

19. SIDES, D.J., ATTENBOROUGH, K. and MULHOLLAND, K.A. 1971. Application of a generalized acoustic propagation theory to fibrous absorbents. *Journal of Sound and Vibration*, **19**(1). pp.49-64.

20. ROSEN, B.W., BAGCHI, D. and KIBLER, J. 1974. Analytical study of rigidized fibrous materials. *N.A.S.A. Contractor Report*, NASA CR-2371.

21. SHERWOOD, J.D. and VAN DAMME, H. 1994. Nonlinear compaction of an assembly of highly deformable platelike particles. *Physical review E*, **50**(5). pp.3834-3840.

22. BAUDEQUIN, M., RYSCHENKOW, G. and ROUX, S. 1999. Non-linear elastic behavior of light fibrous materials. *European Physical Journal B*, **12**. pp.157-162.

23. MEAD, D.J. 1982. Vibration control (I). In: White, R.G. and Walker J.G, ed. *Noise and Vibration.* Chichester: Ellis Horwood Limited. Chapter 25.

24. UNGAR, E.E. 1992. Vibration isolation. In: Beranek L.L. and Vér I.L. ed. *Noise and Vibration Control Engineering: Principles and Applications.* New York: John Wiley & Sons, Inc. Chapter 11.

25. WHITE, R.G. 1982. Vibration control (II). In: White, R.G. and Walker J.G, ed. *Noise and Vibration.* Chichester: Ellis Horwood Limited. Chapter 26.

26. STEIDEL, R.F, Jr. 1989. *An introduction to mechanical vibrations*. 3rd ed. New York: John Wiley & Sons.

27. MEIROVITCH, L. 1967. *Analytical methods in vibrations*. New York: Macmillan Publishing Co., Inc.

28. HARRISON, M., SYKES, A.O. and MARTIN, M. 1952. Wave effects in isolation mounts. *Journal of the Acoustical Society of America*, **24**(1). pp.62-71.

29. PRITZ, T. 1980. Transfer function method for investigating the complex modulus of acoustic materials: spring-like specimen. *Journal of Sound and Vibration*, **72**(3). pp.317-341.

30. PRITZ, T. 1982. Transfer function method for investigating the complex modulus of acoustic materials: rod-like specimen. *Journal of Sound and Vibration*, **81**(3). pp.359-376.

31. WILSON, R. and CUMMINGS, A. 1996. An impedance technique for determining the dynamic structural properties of a porous material. In: Hill, F.A. and Lawrence, R., ed. *Proceedings of the 1996 International Congress on Noise Control Engineering*, Liverpool, U.K.: Institute of Acoustics. **1**. pp.269-272.

32. YANIV, S. L. 1973. Impedance tube measurement of propagation constant and characteristic impedance of porous acoustical material. *Journal of the Acoustical Society of America*, **54**(5). pp.1138-1142.

33. SMITH, C.D. and PARROTT, T.L. 1983. Comparison of three methods for measuring acoustic properties of bulk materials. *Journal of the Acoustical Society of America*, **74**(5). pp.1577-1582.

34. UTSUNO, H. et al. 1989. Transfer function method for measuring characteristic impedance and propagation constant of porous materials. *Journal of the Acoustical Society of America*, **86**(2). pp.637-643.

35. SAHRAOUI, S., MARIEZ, E. and ETCHESSAHAR, M. 2001. Mechanical testing of polymeric foams at low frequency. *Polymer Testing*, **20**. pp.93-96.

36. LANGLOIS, C., PANNETON, R. and ATALLA N. 2001. Polynomial relations for quasi-static mechanical characterization of isotropic poroelastic materials. *Journal of the Acoustical Society of America*, **110**(6). pp.3032-3040.

37. BREAZEALE, M.A. 1998. Finite-amplitude waves in solids. In: CROCKER, M.J., ed. *Handbook of acoustics*. New York: John Wiley & Sons, Inc. Chapter 19.

38. ZIELIŃSKI, P., ŁODZIANA, Z. and SROKOWSKI, T. 1999. Harmonics generation and chaos in scattering of phonons from anharmonic surfaces. *European Physical Journal B*, **9**. pp.525-532.

39. MELNGAILIS, J., MARADUDIN, A.A., and SEEGER, A. 1963. Diffraction of light by ultrasound in anharmonic crystals. *Physical Review*, **131**(5). pp.1972-1975.

40. BREAZEALE, M.A. and FORD, J. 1965. Ultrasonic studies of the nonlinear behaviour of solids. *Journal of Applied Physics*, **36**(11). pp.3486-3490.

41. BREAZEALE, M.A. and THOMPSON, D.O. 1963. Finite-amplitude ultrasonic waves in aluminum. *Journal of Applied Physics*, **36**(11). pp.3486-3490.

42. KECK, W. and BEYER, R.T. 1960. Frequency spectrum of finite amplitude ultrasonic waves in liquids. *The Physics of Fluids*, **3**(3). pp.346-352.

43. BETCHOV, R.. 1958. Nonlinear oscillation of a column of gas. *The Physics of Fluids*, **1**(3). pp.205-212.

44. CRUIKSHANK, D.B. Jr. 1972. Experimental investigation of finite-amplitude acoustic oscillations in a closed tube. *Journal of the Acoustical Society of America*, **52**(3). pp.1024-1036.

45. CHESTER, W. 1964. Resonant oscillations in closed tubes. *Journal of Fluid Mechanics*, **18**(1). pp.44-64.

46. JIMENEZ, J. 1973. Nonlinear gas oscillations in pipes. Part 1. Theory. *Journal of Fluid Mechanics*, **59**(1). pp.23-46.

47. STURTEVANT, B. 1974. Nonlinear gas oscillations in pipes. Part 2. Experiment. *Journal of Fluid Mechanics*, **63**(1). pp.97-120.

48. BELYAEVA, I.Y., OSTROVSKY, L.A. and ZAITSEV, V.Y. 1994. Nonlinear acoustoelastic properties of media with complex structure. In: Naugol'nykh K.A. and Ostrovsky, L.A., ed. *Research Trends in Physics: Nonlinear Acoustics*. New York; American Institute of Physics. pp.1-27.

49. JOHNSON, K. L. 1985. *Contact mechanics*. Cambridge: Cambridge University Press.

50. SHIGLEY, J. E. and MISCHKE, C. R. 1989. *Mechanical engineering design*. 5th and international ed. New York: McGraw-Hill Book Company.

51. CRANDALL, S.H., DAHL, N.C., and LARDNER, T.J. 1978. *An introduction to the mechanics of solids*. 2nd ed. Singapore: McGraw-Hill Book Company.

52. On-line manual of ANSYS, version 5.5.

53. EISBERG, R. M. and LERNER, L. S. 1981. *Physics: foundations and applications*. New York: McGraw-Hill Book Company.

54. BOWDEN, F. P. and TABOR, D. 1956. *Friction and lubrication*. London: Methuen & Co. Ltd.

55. HOWELL, H.G. 1953. The laws of static friction. *Textile research journal*, (August). pp.589-591.

56. GUPTA, B.S. and MOGAHZY, Y.E.E. 1991. Friction in fibrous materials. Part I: Structural model. *Textile research journal*, **61**(9). pp.547-555.

57. MOGAHZY, Y.E.E. and GUPTA, B.S. 1993. Friction in fibrous materials. Part II: Experimental study of the effects of structural and morphological factors. *Textile research journal*, **63**(4). pp.219-230.

58. HOLM, R. 1981. *Electric contacts: theory and application.* 4th ed. Berlin: Springer-Verlag.

59. HOWELL, H.G. 1954. The friction of a fibre round a cylinder and its dependence upon cylinder radius. *Textile research journal*, **45**(8). pp.575-579.

60. GREEN, P. 1973. *Anisotropy in the scratch hardness of crystals.* Ph.D. thesis, Department of Engineering Science, University of Exeter.

61. TIMOSHENKO, S.P and GOODIER, J.N. 1970. *Theory of elasticity.* 3rd ed. London: McGraw-Hill Book Company.

62. DEMENT'EV, A. G. and TARAKANOV, O. G. 1970. Effect of cellular structure on the mechanical properties of plastic foams. *Polymer Mech. USA*, **6**(4). pp.519-525.

63. DEMENT'EV, A. G. and TARAKANOV, O. G. 1973. Deformative properties of flexible plastic foam in compression. *Polymer Mech. USA*, **9**(3). pp.395-400.

64. KRAYNIK, A.M. and WARREN, W.E. 1994. The elastic behavior of low-density cellular plastics. In: Hilyard, N.C. and Cunningham, A., ed. *Low density cellular plastics: physical basis of behaviour.* London; Chapman & Hall. Chapter 7.

65. GRIMMETT, G. 1989. *Percolation.* New York: Springer-Verlag.

66. ESSAM, J.W. 1980. Percolation theory. In: Blin-Stoyle, R.J., ed. *Reports on progress in physics.* London: The Institute of Physics. pp.833-912.

67. CARMONA, F., BARREAU, F., DELHAES, P. and CANET, R. 1980. An experimental model for studying the effect of anisotropy on percolative conduction. *J. Physique Letters*. **41**. pp.L531-L534.

68. BOISSONADE, J. BARREAU, F. and CARMONA, F. 1983. The percolation of fibres with random orientations: a Monte Carlo study. *J. Phys. A: Math. Gen.*, **16**, 2777-2787.

69. KANTOR, Y. 1984. Geometrical properties of singly connected bonds in percolation clusters. *J. Phys. A: Math. Gen.*, **17**, L843-L847.

70. BALBERG, I., BINENBAUM, N. and WAGNER, N. 1984. Percolation thresholds in the three-dimensional sticks system. *Physical Review Letters*, **52**(17). pp.1465-1468.

71. KANTOR, Y. and WEBMAN, I. 1984. Elastic properties of random percolating systems. *Physical Review Letters*, **52**(21). pp.1891-1984.

72. DEPTUCK, D., HARRISON, J.P. and ZAWADZKI, P. 1985. Measurement of elasticity and conductivity of a three-dimensional percolation system. *Physical Review Letters*, **54**(9). pp.913-916.

73. BUG, A. L.R., SAFRAN, S.A. and WEBMAN, I. 1985. Continuum percolation of rods. *Physical Review Letters*, **54**(13). pp.1412-1415.

74. KANTOR, Y. 1986. Statistical properties of low-connectivity bonds in percolation clusters. *Journal of Physics A – Mathematical and General*, **19**, L497-L503.

75. UEDA, N. and TAYA, M. 1986. Prediction of the electrical conductivity of two-dimensionally misoriented short fiber composites by a percolation model. *Journal of Applied Physics*, **60**(1). pp.459-461.

76. RUSCHAU, G.R. and NEWNHAM R.E. 1992. Critical volume fractions in conductive composites. *Journal of Composite Materials*, **26**(18), 2727-2735.

77. TORQUATO, S. 2002. *Random heterogeneous materials: Microstructure and macroscopic properties*. New York: Springer-Verlag.

78. SEN, P.N, SCALA, C., COHEN, M.H. 1981. A self-similar model for sedimentary rocks with application to the dielectric constant of fused glass beads. *Geophysics*, **46**(5). pp.781-795.

79. NOLLE, A.W. 1947. Acoustic determination of the physical constants of rubber-like materials. *Journal of the Acoustical Society of America*, **19**(1). pp.194-201.

80. SNOWDON, J.C. 1971. Mechanical four-pole parameters and their application. *Journal of Sound and Vibration*, **15**(3). pp.307-323.

81. PRITZ, T. 1981. Apparent complex Young's modulus of a longitudinally vibrating viscoelastic rod. *Journal of Sound and Vibration*, **77**(1). pp.93-100.

82. PRITZ, T. 1982. Dynamic strain of a longitudinally vibrating viscoelastic rod with an end mass. *Journal of Sound and Vibration*, **85**(2). pp.151-167.

83. OYADIJI, S.O. and TOMLINSON, G.R. 1985. Determination of the complex moduli of viscoelastic structural elements by resonance and non-resonance methods. *Journal of Sound and Vibration*, **101**(3). pp.277-298.

84. PRITZ, T. 1986. Frequency dependence of frame dynamic characteristics of mineral and glass wool materials. *Journal of Sound and Vibration*, **106**(1). pp.161-169.

85. PRITZ, T. 1987. Nonlinearity of dynamic modulus of mineral wool slabs. In: Peizi. L., ed. *Proceedings of the 1987 International Conference on Noise Control Engineering (Internoise)*, Beijing, China: Institute of Acoustics. **2**. pp.1367-1370.

86. CREMER, L., HECKL, M. and UNGAR, E.E. 1988. *Structural-borne sound*. 2th ed. Berlin: Springer-Verlag.

87. PRITZ, T. 1990. Non-linearity of frame dynamic characteristics of mineral and glass wool materials. *Journal of Sound and Vibration*, **136**(2). pp.263-274.

88. PRITZ, T. 1994. Dynamic Young's modulus and loss factor of plastic foams for impact sound isolation. *Journal of Sound and Vibration*, **178**(3). pp.315-322.

89. WATSON, A.P. and CUMMINGS, A. 1994. Results of the experimental investigation of the compressional behaviour of thermal insulation. *Brite/Aero Contract no. CT92 0032*, deliverable no. 11.

90. SFAOUI, A. 1995. On the viscoelasticity of the polyurethane foam. *Journal of the Acoustical Society of America*, **97**(2). pp.1046-1052.

91. RODRIGUEZ-PEREZ, M.A. and DE SAJA, J.A. 2000. Dynamic mechanical analysis applied to the characterisation of closed cell polyolefin foams. *Polymer Testing*, **19**. pp.831-848.

92. PANNETON, R., LANGLOIS, C. and ATALLA, N. 2001. Mechanical characterization of poroelastic materials. *17th ICA*, Rome, Italy.

93. PILON, D., PANNETON, R., and SGARD F.C. 2001. Effect of boundary conditions on acoustical measurements in the standing wave tube. *17th ICA*, Rome, Italy.

94. SNOWDON, J.C. 1968. *Vibration and shock in damped mechanical systems.* New York: John Wiley and Son.

95. KINSLER, L.E. et al. 1980. *Fundamentals of acoustics.* 3rd ed. New York: John Wiley and Son.

96. Technical documentation, Force transducers types 8200 and 8201. Brüel & Kjær.

97. PRITZ, T. 1996. Analysis of four-parameter fractional derivative model of real solid materials. *Journal of Sound and Vibration*, **195**(1). pp.103-115.

98. PRITZ, T. 1998. Frequency dependence of complex moduli and complex Poisson's ratio of real solid materials. *Journal of Sound and Vibration*, **214**(1). pp.83-104.

99. PRITZ, T. 2001. Loss factor peak of viscoelastic materials: magnitude to width relations. *Journal of Sound and Vibration*, **246**(2). pp.265-280.

100. NOWACKI, W. 1963. *Dynamics of elastic systems.* London: Chapman & Hall Ltd.

101. FAHY, F.J. 1985. *Sound and structural vibration: radiation, transmission and response.* London: Academic Press.

102. VÉR, I.L. 1992. Interaction of sound waves with solid structures. In: Beranek, L.L, ed. *Noise and vibration control engineering: principles and applications.* New York: John Wiley & Sons Inc., Chapter 9.

103. TING, T.C.T. 1996. *Anisotropic elasticity: theory and application.* Oxford: Oxford University Press.

104. LANGHAAR, H.L. 1962. *Energy methods in applied mechanics.* New York, John Wiley and Sons, Inc.

105. SMITH, G. D. 1978. *Numerical solution of partial differential equations: Finite Difference Methods.* Second edition. Oxford: Clarendon Press.

106. JEFFREY, A. and TANIUTI, T. 1964. *Non-linear wave propagation: with applications to physics and magnetohydrodynamics (Mathematics in science and engineering, volume 9).* London: Academic Press Inc.

107. AMES, W.F. 1965. *Nonlinear partial differential equations in engineering (Mathematics in science and engineering, volume 18).* London: Academic Press Inc.

108. MCDANIEL, O.H. 1975. *Propagation of sound at moderate and high intensities in absorbent and hard-walled cylindrical ducts.* Ph.D. thesis, The Pennsylvania State University.

109. RUDENKO, O.V. 2002. Nonlinear acoustics. In: MECHEL, F.P, ed. *Formulas of acoustics.* Berlin: Springer-Verlag. Chapter S.

110. LAMB, H. 1925. *The dynamical theory of sound.* 2th ed. London: Edward Arnold & Co.

111. KUNTZ, H.L. II. 1982. High-intensity sound in air saturated fibrous bulk porous materials. National Aeronautics and Space Administration Office of Naval Research.

112. BELYAEVA, I.Y., and TIMANIN, E.M. 1992. Experimental study of the nonlinear properties of porous elastic media. *Soviet Physics Acoustics*, **37**(5) pp.533-534.

113. JORDAN, D.W. and SMITH, P. 1987. *Nonlinear ordinary differential equations.* 2nd ed. Oxford: Oxford University Press.

114. QIN, Q. and ATTENBOROUGH, K. 2004. Characteristics and Application of laser-generated acoustic shocks in air. *Applied Acoustics*, **65** (4) pp.325 – 340.